LBL-11519 c.2

Lawrence Berkeley Laboratory
UNIVERSITY OF CALIFORNIA

Materials & Molecular Research Division

RECEIVED
LAWRENCE
BERKELEY LABORATORY
SEP 30 1982
LIBRARY AND
DOCUMENTS SECTION

NONLINEAR EFFECTS OF MATERIALS IN LASER CAVITIES

Raymond H. Hsu
(Ph.D. thesis)

August 1982

TWO-WEEK LOAN COPY

This is a Library Circulating Copy which may be borrowed for two weeks. For a personal retention copy, call Tech. Info. Division, Ext. 6782.

LBL-11519 c.2

Prepared for the U.S. Department of Energy under Contract DE-AC03-76SF00098

DISCLAIMER

This document was prepared as an account of work sponsored by the United States Government. While this document is believed to contain correct information, neither the United States Government nor any agency thereof, nor the Regents of the University of California, nor any of their employees, makes any warranty, express or implied, or assumes any legal responsibility for the accuracy, completeness, or usefulness of any information, apparatus, product, or process disclosed, or represents that its use would not infringe privately owned rights. Reference herein to any specific commercial product, process, or service by its trade name, trademark, manufacturer, or otherwise, does not necessarily constitute or imply its endorsement, recommendation, or favoring by the United States Government or any agency thereof, or the Regents of the University of California. The views and opinions of authors expressed herein do not necessarily state or reflect those of the United States Government or any agency thereof or the Regents of the University of California.

LBL-11519

NONLINEAR EFFECTS OF MATERIALS IN LASER CAVITIES

Raymond H. Hsu

Ph.D. Thesis

August 1982

Materials and Molecular Research Division
Lawrence Berkeley Laboratory
University of California
Berkeley, CA 94720

This work was supported by the Division of Materials Sciences, Office of Basic Energy Sciences of the U.S. Department of Energy under Contract DE-AC03-76SF00098, and by the National Science Foundation under Grant DMR78-18826.

NONLINEAR EFFECTS OF MATERIALS IN LASER CAVITIES

Raymond H. Hsu

Abstract

The concept of adding intensity dependent losses to a laser cavity in order to control output pulse shape is reviewed. Background theory and models for Kerr liquids using ellipse rotation to achieve these inducible losses are developed. Detailed calculations and experiments are performed using the liquid crystal MBBA in a ruby laser cavity. The results support the theories and model. The proper choices of parameters to optimize the technique is discussed.

Self focusing inside a laser resonator was found to play an important role in the lasing process. Its effects on laser output were investigated. Three regimes occur. In the weak regime, self focusing can be used to improve mode structure and reduce beam divergence. The intermediate regime results in inducible loss allowing self focusing to be used for pulse shaping. No lasing is possible in the strong regime and thus this regime must be avoided. The uses and drawbacks of self focusing in a laser resonator are discussed. The interaction between ellipse rotation and self focusing and the proper selection of materials and parameters to achieve desired laser characteristics are determined.

Acknowledgements

There are many people whose efforts contributed to the completion of this work. I would particularly like to thank:

Professor Y. R. Shen for his patience and guidance during the entire course of my research and for his insistence upon a careful, in depth approach to any project;

Dr. Toni Bischofberger and Dr. Eric Hanson, who helped me acquire the skills necessary to experimental physics;

Dr. Tai Chiang and Robert Smtih, who through example, illuminated the road I followed, helping me to avoid the worst of the rocks;

Chenson Chen, Gary Boyd, Steve Durbin, and Alex Jacobson for valuable discussions that broadened my knowledge and improved my well being;

Rita Jones and Gloria Pelatowski for their expert assistance in preparing this manuscript.

This work was supported by the National Science Foundation under Grant DMR78-18826 and by the Division of Materials Sciences, Office of Basic Energy Sciences, U. S. Department of Energy, under contract No. DE-AC03-76SF00098.

Table of Contents

	Page
I. Introduction	1
II. Background Theory	7
III. Ellipse Rotation Inducible Loss	65
IV. Self Focusing in a Laser Cavity - Model	136
V. Self Focusing Experimental Set Ups and Data	152
VI. Self Focusing - Comparison of Data with Proposed Model	201
VII. Conclusions	224
References	229

I. INTRODUCTION

A Kerr liquid typically will exhibit several related nonlinear effects. Two of these effects, ellipse rotation and self focusing, play important roles when a Kerr liquid is placed in a laser cavity. Ellipse rotation refers to circular birefringence induced by an applied optical field. If this field is elliptically polarized, the induced birefringence will result in a rotation of the polarization state with no change in ellipticity. Self focusing refers to an induced gradient in the index of refraction of the liquid due to an applied optical field, which then acts as a lens to focus the applied field.[1-3]

A liquid crystal consists of long molecules.[4] In the isotropic phase, these molecules exhibit a random orientation. Because of the large dielectric anisotropy associated with many liquid crystals, an applied optical field $E(\omega)$ can induce molecular alignment in the isotropic phase. This induced ordering leads to the same nonlinear effects as seen in Kerr liquids. These effects have been studied in many liquid crystals, including N-[p-methoxybenzylidene]-p-butylaniline (MBBA).[3,5,6] See Fig. 1 for molecular structure of MBBA.

Because of the similarity in effects seen in Kerr liquids and MBBA, it is customary to refer to MBBA as a Kerr liquid. It is important, however, to keep in mind the difference in both response time and temperature dependence for MBBA as compared to the typical Kerr liquid. Since the nonlinear effects being studied arise from molecular ordering in MBBA,[2] the phase transition from the isotropic to the nematic phase at $T^* = 314.7°K$ becomes critical. As will be seen in Section II, the induced anisotropy in the index of refraction δn will exhibit a critic-

ally divergent behavior as $T \rightarrow T^*$:

$$\delta n = C|E|^2/(T - T^*) \tag{1}$$

where C is a constant and T^* is the critical temperature for a second order isotropic $\rightarrow$ nematic transition in the mean field approximation. Similar divergent behavior results in both the relaxation time τ ($\sim 10^{-8}$ seconds) and the nonlinear constants for MBBA being larger than in an ordinary Kerr liquid ($\tau \sim 10^{-11}$ seconds). This behavior is especially pronounced near $T = T^*$.[7]

Kerr liquids were first used in a laser cavity for mode locking by Comly et al.[8] They used α-chloronaphthalene and nitrobenzene as the Kerr liquid. As predicted by an earlier theoretical calculation,[9] mode locking was only seen for relaxation times

$$\tau \leqslant 1/(\Delta\nu)_{gain} \tag{2}$$

where $(\Delta\nu)$ is the gain linewidth for the laser. Physically, this says that the Kerr liquid must be able to respond to the beat frequencies resulting from any of the modes lying within the gain envelope, a reasonable requirement for full mode locking. The authors also reported an improvement in the quality of output as compared with mode locking with a saturable absorber. This improvement was attributed to the decrease in formation of filimentary structure in the laser output. The mode locking referred to above is longitudinal mode locking where the various longitudinal cavity modes (mode spacing is given by $\Delta\omega = c/2\ell$ where ℓ is the laser cavity length) have their phases locked to each

other — hence the term mode locking. The result of this mode locking in frequency space manifests itself in the time domain as a train of pulses whose width $\sim 1/(\Delta\nu)_{gain}$ and whose separation $\sim 2\ell/c$. Very short pulses can be obtained in this fashion making the technique highly useful.[10]

Dahlström made use directly of the nonlinear effects of Kerr liquids by using ellipse rotation to couple part of the laser cavity fields out of the cavity.[11] His work was motivated by a need for an output coupler to be used in resonators where prisms have replaced the usual mirrors. Such a resonator eliminates the problem of minor damage due to the high powers present in a mode locked train of pulses. The techniques use the ellipse rotation induced by the cavity fields to change the polarization state of the cavity fields. A glan prism polarizer was then used to couple out the cavity fields. At low cavity intensities, little ellipse rotation is induced, resulting in only a small change in polarization state and small output coupling. At large intensities, the ellipse rotation becomes substantial, leading to a large change in polarization state and a correspondingly large output coupling. By appropriate changes in optical components, Dahlström was able to couple out the one or two largest pulses in the mode locked train, thus demonstrating a passive switching technique for obtaining single picosecond pulses. Other configurations allowed the entire mode locked train to be coupled out.

Cavity dumping is a process for extracting the cavity energy quickly. Typically, cavity dumping is achieved by starting with a Q-switched laser with very small output coupling, waiting until the cavity fields reach a maximum and then introducing large output coupling. In the ex-

treme case the cavity energy is "dumped" in one round trip time of the cavity.[12] Most techniques involve active switching and are subject to jitter — it being hard to predict precisely when the cavity fields will peak. Examination of Dahlström's set-up reveals that his technique should also have application as an intensity dependent passive cavity dumping scheme. Indeed, Dahlström recognized this and successfully demonstrated the effect.[13] He obtained cavity dumped output energies of 15%-50% of the non cavity dumped output energies, with pulse lengths 4-10 times shorter for the cavity dumped output. This technique offers greater simplicity by virtue of its passive nature, and greater freedom from jitter by virtue of the intensity dependence which uses the actual cavity intensities to control the dumping.

A thorough theoretical treatment for using the ellipse rotation of Kerr liquids in laser cavities has been done and experimentally tested.[14] One application is the use of the ellipse rotation to generate an inducible loss in the cavity. An inducible loss is one for which the loss increases nonlinearly with incident intensity — the counterpart to a saturable absorber.

Work has been done, initially by using 2 photon absorption as the inducible loss[15] and later using ellipse rotation in liquid crystals as the inducible loss,[16] showing that the introduction of an inducible loss into a slowly Q-switched laser cavity results in pulse durations that vary with the pump power while the pulse intensity remains constant. A rotation prism (at 400 Hz) was used as the Q-switching device. It should be pointed out that this is so slow as to be nearly free running.[17] Faster Q-switching leads to complications which will be discussed below. As in the free running case, the laser output energy in-

creases with the pump energy.[18] The inducible loss acts to limit cavity intensities and thereby forces the extra output energy to appear in the form of a longer pulse — hence the increase in pulse duration with pump energy.

It has been suggested that combining an inducible loss with a saturable absorber Q-switch could lead to clamping of the laser output intensities at a predetermined level.[19] The saturable absorber determines the lowest allowed cavity intensity and the inducible loss determines the highest. This has obvious applications. Saturable absorber Q-switching is a fast Q-switch, however, with laser pulse behavior different from that seen with slow Q-switching. With fast Q-switching the laser output energy does not depend strongly on pump energy.[18] This characteristic remains when an inducible loss is added to the cavity and the pulse duration is independent of pump energy, though longer than the case where no inducible loss is present.[20] These differences resulting from differences in Q-switching technique prompted a thorough theoretical examination of how the Q-switching speed, inducible loss mechanism and laser gain media coupled together.[21] The results indicate that though the output energy does not vary with pump power, it is still possible to increase pulse duration by clamping the cavity intensities at a suitably low level — essentially releasing the energy more slowly.

Because it is not possible to use pump energy to vary the pulse length with saturable absorber Q-switching, another means of easily varying the pulse length is needed. Ellipse rotation inducible loss is attractive because the amount of loss is easily changed by changing the configuration of the set-up without a need to change the nonlinear material. Liquid crystals as the nonlinear material are an obvious choice

both for their large nonlinear constants and the ability to vary these constants near $T = T^*$, the isotropic-nematic phase transition. In this work, the liquid crystal MBBA is placed in the cavity as the inducible loss material. It is found that a new loss mechanism, self focusing in the laser cavity, predominates over the inducible loss. This process of self focusing in the laser cavity is carefully studied and close agreement with theory is found.

In Chapter II, some background theory is presented. Chapter III discusses the theory of ellipse rotation inducible cavity loss. Chapter IV presents a qualitative model of self focusing in a laser cavity and discusses how this leads to inducible cavity loss and improvement of cavity mode structure. Experimental results are presented in Chapter V and analyzed in Chapter VI. Finally, conclusions are drawn in Chapter VII.

II. BACKGROUND THEORY

A. Liquid Crystals

The behavior of liquid crystals in the isotropic phase near the isotropic-nematic phase transition is referred to as pretransitional behavior. This behavior has been carefully measured for MBBA[2,22] and other liquid crystals.[23] The results obtained agree well with the Landau-de Gennes model based on Landau's theory of second order phase transitions.[24] What follows is a brief description of this model.

As emphasized by de Gennes, any tensorial property of the liquid crystal may be used to define an order parameter. (An order parameter indicates the degree of alignment of the molecules.) It is convenient to use optical susceptibilities to define the order parameter Q_{ij}.

$$\chi_{ij} = \bar{\chi}\delta_{ij} + \frac{2}{3}\Delta\chi Q_{ij} \tag{3}$$

$$\bar{\chi} = \frac{1}{3}\sum_i \chi_{ii} \tag{4}$$

where $\Delta\chi$ is the anisotropy in χ_{ij} with perfect molecular alignment. The free energy per unit volume in the isotropic phase (Q_{ij} all small) can be written as

$$F = F_o + \frac{1}{2}AQ_{ij}Q_{ji} + \frac{1}{3}BQ_{ij}Q_{jk}Q_{ki} + \frac{1}{4}DQ_{ij}Q_{jk}Q_{k\ell}Q_{\ell i}$$

$$- \frac{1}{8}\chi_{ij}(\omega)[E_i^*(\omega)E_j(\omega) + c.c.] \tag{5}$$

where F_o is independent of Q_{ij}, and A, B, D are constants.

Landau assumes the constants B and D vary slowly with temperature when compared with the constant A. Above the phase transition ($T > T^*$) the minimal free energy must occur at $Q_{ij} = 0$ (no applied field), since the material is isotropic. Below the phase transition ($T < T^*$) the minimal free energy must occur at some finite value for Q_{ij} (again, no applied field), since the material is in the nematic phase. Figure 2[4] shows some typical free energy curves for a liquid crystal where the third order term is absent ($B = 0$). The case where $B \neq 0$ is similar and shown in Fig. 3.[4] The important feature to recognize is that A must change sign at $T = T^*$ in order for the minimum in F to shift away from $Q_{ij} = 0$ for $T < T^*$ while still remaining at $Q_{ij} = 0$ for $T > T^*$. Thus, A must have the form

$$A = a(T - T^*) \tag{6}$$

which is how Figs. 2 and 3 were obtained.

Of interest is the middle curve for Fig. 3. There a second stable state has appeared at a finite value of Q_{ij}. One would expect that fluctuations would play a major role in the phase transition dynamics in the presence of such a state. This is indeed so and the Landau theory does not adequately handle this situation. However, in most liquid crystals, the temperature at which this meta stable state first occurs is < 1°C above T^*. At temperatures higher than this, the Landau theory works quite well.

Thus one expects in the isotropic state that the Q_{ij} will be sufficiently small so that the $Q_{ij}^{(3)}$ and $Q_{ij}^{(4)}$ terms in Eq. (5) can be neglected for temperatures far enough above the critical temperature T^*. The

steady state value of Q_{ij} induced by the field can be obtained using Eq. (3) and minimizing the free energy F with respect to the Q_{ij} for Eq. (5). We make use of the fact that Q_{ij} is symmetric ($Q_{\alpha\beta} = Q_{\beta\alpha}$) and traceless ($Q_{11} + Q_{22} + Q_{33} = 0$). For $\alpha \neq \beta$, we have

$$0 = \frac{\partial F}{\partial Q_{\alpha\beta}} = 2AQ_{\alpha\beta} - \frac{1}{6}\Delta\chi[E_i^*(\omega)E_j(\omega) + c.c.] \tag{7}$$

while for $\alpha = \beta$, we have

$$0 = \frac{\partial F}{\partial Q_{11}} = 2AQ_{11} + AQ_{22} - \frac{\Delta\chi}{6}[|E_1(\omega)|^2 - |E_3(\omega)|^2] \tag{8}$$

$$0 = \frac{\partial F}{\partial Q_{22}} = AQ_{11} + 2AQ_{22} - \frac{\Delta\chi}{6}[|E_2(\omega)|^2 - |E_3(\omega)|^2] \tag{9}$$

where the fact that only two of the Q_{ii} are independent has been used. We can solve Eqs. (7)-(9) to get

$$Q_{ij} = \frac{f_{ij}}{a(T - T^*)} \tag{10}$$

$$f_{ij} = \frac{\Delta\chi}{12}\cdot[(E_i^*(\omega)E_j(\omega) - \frac{1}{3}|E(\omega)|^2\delta_{ij}) + c.c.]. \tag{11}$$

For linearly polarized light, with the polarization along $\hat{x}$, Eq. (11) reduces to

$$Q_{xx} = -2Q_{yy} = -2Q_{zz} = \frac{\Delta\chi|E(\omega)|^2}{9a(T - T^*)}. \tag{12}$$

The induced anisotropy in the index of refraction δn is then given by

$$\delta n = \frac{2\pi}{n}\,\delta\chi = \frac{2\pi}{n}\left(\frac{2}{3}\,\Delta\chi\right)(Q_{xx} - Q_{yy})$$

$$= \frac{2\pi}{n}\,\frac{(\Delta\chi)^2|E(\omega)|^2}{9a(T - T^*)} \tag{13}$$

where $\delta\chi = \chi_{xx} - \chi_{yy}$ is the induced anisotropy in the optical susceptibility. This is the result claimed for Eq. (1).

For a sufficiently short optical pulse, the order parameter will not be able to respond instantaneously. The dynamic equation governing this transient response can be obtained as

$$\nu\,\frac{dQ_{\alpha\beta}}{dt} + \frac{\partial F}{\partial Q_{\beta\alpha}} = \sum_{\ell=1}^{4} \lambda_\ell\,\frac{\partial f_\ell}{\partial Q_{\beta\alpha}} \tag{14}$$

$$f_1 = Q_{12} - Q_{21} = 0$$

$$f_2 = Q_{23} - Q_{32} = 0$$

$$f_3 = Q_{13} - Q_{31} = 0$$

$$f_4 = Q_{11} + Q_{22} + Q_{33} = 0 \tag{15}$$

where we have used the standard technique of Lagrange multipliers to treat the fact that not all the Q_{ij} are independent. ν is a viscosity coefficient. Substituting for F and treating all the Q_{ij} as independent when taking the derivatives (since we have accounted for any dependence via the Lagrange multipliers), we get for $\alpha \neq \beta$

$$\nu \frac{dQ_{\alpha\beta}}{dt} + a(T - T^*)Q_{\alpha\beta} - \frac{\Delta\chi}{12} [E_\alpha^*(\omega)E_\beta(\omega) + c.c.] = \lambda$$

$$\nu \frac{dQ_{\beta\alpha}}{dt} + a(T - T^*)Q_{\beta\alpha} - \frac{\Delta\chi}{12} [E_\beta^*(\omega)E_\alpha(\omega) + c.c.] = - \lambda. \qquad (16)$$

Since $Q_{\alpha\beta} = Q_{\beta\alpha}$ this clearly means $\lambda = 0$. For $\alpha = \beta$ we get

$$\nu \frac{dQ_{11}}{dt} + a(T - T^*)Q_{11} - \frac{\Delta\chi}{6} |E_1(\omega)|^2 = \lambda$$

$$\nu \frac{dQ_{22}}{dt} + a(T - T^*)Q_{22} - \frac{\Delta\chi}{6} |E_2(\omega)|^2 = \lambda$$

$$\nu \frac{dQ_{33}}{dt} + a(T - T^*)Q_{33} - \frac{\Delta\chi}{6} |E_3(\omega)|^2 = \lambda. \qquad (17)$$

We eliminate λ to get the equation of motion for $Q_{\alpha\alpha}$

$$\nu \frac{dQ_{\alpha\alpha}}{dt} + a(T - T^*)Q_{\alpha\alpha} = \frac{\Delta\chi}{6} [|E_\alpha(\omega)|^2 - \frac{1}{3} |E(\omega)|^2]. \qquad (18)$$

Equations (16) and (18) can be combined as

$$\nu \frac{dQ_{ij}}{dt} + a(T - T^*)Q_{ij} = f_{ij}$$

$$f_{ij} = \frac{\Delta\chi}{12} [(E_i^*(\omega)E_j(\omega) - \frac{1}{3} |E(\omega)|^2\delta_{ij}) + c.c.]. \qquad (19)$$

The solution to Eq. (19) is immediate:

$$Q_{ij}(t) = \int_{-\infty}^{t} \frac{f_{ij}(t')}{\nu} e^{-(t-t')/\tau_M} dt' \qquad (20)$$

$$\tau_M = \frac{\nu}{a(T - T^*)} \tag{21}$$

where τ_M is the orientational relaxation time. The ratio ν/a has been well measured for MBBA and the results for τ_M are shown in Fig. 4,[2] and Table 1.

The connection of these liquid crystal parameters to the third order nonlinear susceptibility tensor is made in the next section of this chapter.

B. Third Order Optical Susceptibilities in Isotropic Liquid Crystals

The optical susceptibilities used in the first part of this section have been measured quite accurately for MBBA.[2,22] To make use of these measurements, it is necessary to relate the optical susceptibilities to the underlying nonlinear susceptibility tensor. The polarization $\vec{P}$ of the material may be expanded in a power series

$$\vec{P} = \vec{P}^{(0)} + \vec{P}^{(1)} + \vec{P}^{(2)} + \vec{P}^{(3)} + \ldots$$

$$\vec{P}^{(n)} \propto (E)^n. \tag{22}$$

For media with inversion symmetry, only the odd terms will be nonzero. $\vec{P}^{(1)}$ is the linear term used in classical optics. $\vec{P}^{(3)}$ is the lowest order nonlinear term, and gives rise to the nonlinear phenomena mentioned in Chapter I.

Since the applied field is quasimonochromatic, it is convenient to work with the Fourier decomposition of $\vec{P}$ and $\vec{E}$, in which case

$$P_i^{(3)}(\omega_o) = 6\chi_{ijk\ell}^{(3)}(\omega_o = \omega_1 + \omega_2 + \omega_3)E_j(\omega_2)E_k(\omega_2)E_\ell(\omega_3) \tag{23}$$

where $\chi_{ijk\ell}(\omega_o = \omega_1 + \omega_2 + \omega_3)$ is the third order susceptibility and where by convention, the factor of 6 is explicitly retained. This factor of 6 comes from the expansion of

$$[\vec{E}(t)]^3 = \left[\vec{E}(\omega_1)e^{-i\omega_1 t} + \vec{E}(\omega_2)e^{-i\omega_2 t} + \vec{E}(\omega_3)e^{-i\omega_3 t}\right]^3$$

$$= 6\vec{E}(\omega_1)\vec{E}(\omega_2)\vec{E}(\omega_3)e^{-i(\omega_1+\omega_2+\omega_3)t} + \text{other terms} \tag{24}$$

where the omitted terms do not give the proper frequency response for the polarization. The $\chi_{ijk\ell}^{(3)}$ is the symmetrized χ defined by Maker and Tehrune. The decision to use the symmetrized χ, retaining the explicit degeneracy factor means that as the frequencies ω_1, ω_2, ω_3 become degenerate, this factor of 6 is replaced by $3(\omega_1 = \omega_2 \neq \omega_3)$ or $1(\omega_2 = \omega_2 = \omega_3)$. Of course, the $\chi_{ijk\ell}^{(3)}$ are continuous.[25] Though it is perhaps unwieldly to require a different definition of χ for the different cases of degeneracy, the benefits of permutation symmetry (due to the symmetrized χ) and consistency between the time and frequency domains more than compensates.[26]

Of course, the susceptibility tensor must obey the symmetry properties of the material. For isotropic media, there are only 21 nonzero elements in the susceptibility tensor, only 3 of which are independent.[27] These nonvanishing elements are

$$\chi_{1122} = \chi_{iijj} \text{ (6 elements)}$$

cont'd

$$\chi_{1212} = \chi_{ijij} \text{ (6 elements)}$$

$$\chi_{1221} = \chi_{ijji} \text{ (6 elements)}$$

$$\chi_{1111} = \chi_{iiii} = \chi_{1212} + \chi_{1122} + \chi_{1221} \text{ (3 elements).} \tag{25}$$

For the case where $\omega_1 = \omega_2$, then by permutation symmetry

$$\chi^{(3)}_{iijj}(\omega_o = \omega_1 + \omega_1 + \omega_2) = \chi^{(3)}_{ijij}(\omega_o = \omega_1 + \omega_1 + \omega_2). \tag{26}$$

This reduces the number of independent elements to two which are by convention χ_{1122} and χ_{1221}. Note that this convention requires we write the frequencies in the order $\omega_o = \omega_1 + \omega_1 + \omega_2$. $\chi^{(3)}_{ijk\ell}$ $(\omega_o = \omega_1 + \omega_2 + \omega_3)$ can thus be written

$$\chi^{(3)}_{ijk\ell} = \chi_{1122}\delta_{ij}\delta_{k\ell} + \chi_{1212}\delta_{ik}\delta_{j\ell} + \chi_{1221}\delta_{i\ell}\delta_{jk} \tag{27}$$

where $\delta_{ij} = 1$ if $i = j$ and 0 otherwise. The situation of interest is that of self induced nonlinear effects where $(\omega_o = \omega + \omega - \omega)$. Then

$$P^{(3)}_i(\omega) = 3\chi^{(3)}_{ijk\ell}(\omega = \omega + \omega - \omega)E_j(\omega)E_k(\omega)E^*_\ell(\omega) \tag{28}$$

$$= \delta\chi_{ij}(\omega,\omega)E_j(\omega). \tag{29}$$

Equation (29) is of course the definition for the induced optical susceptibility $\delta\chi_{ij}(\omega,\omega)$, which can be rewritten

$$\delta\chi_{ij}(\omega,\omega) = 3\chi^{(3)}_{ijk\ell}(\omega = \omega + \omega - \omega)E_k(\omega)E^*_\ell(\omega). \tag{30}$$

The $\chi_{ijk\ell}$ of Eq. (28) can be expressed in terms of the Born Oppenheimer coefficients σ, A_o, B_o as defined by Hellwarth.[26] σ is the electronic contribution, while A_o and B_o are the nuclear contributions to $\chi^{(3)}$. Roughly speaking, A_o represents the isotropic contribution and B_o the anisotropic contribution.

$$12\chi^{(3)}_{1122}(\omega = \omega + \omega - \omega) = \sigma + 2A_o + B_o$$

$$12\chi_{1221}(\omega = \omega + \omega - \omega) = \sigma + 2B_o.$$

$$\chi_{1212}(\omega = \omega + \omega - \omega) = \chi_{1122}(\omega = \omega + \omega - \omega) \tag{31}$$

where we have used the symmetry properties of $\chi^{(3)}$ (Eqs. (25) and (26)). The induced optical susceptibility then takes the form

$$\delta\chi_{ij}(\omega,\omega) = 3[2\chi_{1122}(\omega = \omega + \omega - \omega)|E(\omega)|^2\delta_{ij}$$

$$+ \chi_{1221}(\omega = \omega + \omega - \omega)E_j(\omega)E^*_i(\omega)]. \tag{32}$$

The anisotropic part of the $\delta\chi_{ij}(\omega,\omega)$ is immediately

$$\delta\chi_{ij}(\omega,\omega)_A = 3\chi_{1221}(\omega = \omega + \omega - \omega)E_j(\omega)E^*_i(\omega). \tag{33}$$

For pulsed lasers, it is necessary to include the time response of the material. If the field E is given by

$$E_i(\omega,t) = (\hat{i}^* \cdot \hat{e})\mathcal{E}(t)e^{i\vec{k}\cdot\vec{r}-i\omega t} \tag{34}$$

then the convoluted form for Eq. (33) becomes

$$\delta\chi_{ij}(\omega,\omega,t)_A = \int_{-\infty}^{t} 3\chi_{1221}(\omega = \omega + \omega - \omega; t - t')E_j(\omega,t')E_i^*(\omega,t')dt'. \tag{35}$$

For liquid crystals the electronic contribution to $\chi^{(3)}$ is negligible[2] so we have $\sigma \ll B_o$ and combining Eqs. (3) and (20)

$$\delta\chi_{ij}(\omega,\omega,t)_A = \frac{(\Delta\chi)^2}{18\nu}\int_{-\infty}^{t} e^{-(t-t')/\tau_M}[E_j(\omega,t)E_i^*(\omega,t) + c.c.]dt'. \tag{36}$$

Comparing Eq. (35) to Eq. (36) with $\sigma = 0$ gives

$$3\chi_{1221}^{(3)}(\omega = \omega + \omega - \omega; t) = \frac{\beta}{2\tau_M} e^{-t/\tau_M}$$

$$\beta = \frac{2(\Delta\chi)^2}{9a(T - T^*)} = B_o. \tag{37}$$

Now the connection has been established between the liquid crystal parameters and the nonlinear susceptibility tensor. The values of β and τ_M have been measured[2] for MBBA. They are given in Eq. (38) for convenience.

$$\beta = \frac{2.7 \times 10^{-9}}{T - T^*} \quad \text{(esu)}$$

$$\tau_M = \frac{9.1 \times 10^{-11}}{T - T^*} e^{2800/T} \text{ sec} \tag{38}$$

where the viscosity ν takes the form suggested by Stinson and Litster[28]

$$\nu = \nu_o e^{W/T}$$

$$W = 2800°K \tag{39}$$

where B_o is replaced by β to provide consistency with other works on the subject.[1,2,22,23]

Examination of the isotropic portion $\delta\chi_{ij}$ in Eq. (32) and comparison with the isotropic part of $\delta\chi_{ij}$ obtained from Eqs. (3) and (20) gives

$$\chi_{1122} = 1/6\ \chi_{1221}. \tag{40}$$

For liquid crystals where $\sigma = 0$, this means

$$\alpha = A_o = -\beta/3 \tag{41}$$

where again the α replaces the A_o for consistency.

C. Self Induced Ellipse Rotation (SIER)

Having determined the liquid crystal parameters in terms of the nonlinear susceptibility tensor, it remains to determine the size of the expected SIER and self focusing for later use. The expressions involved may be derived from either the nonlinear susceptibility tensor[1,2] or directly from the optical susceptibility χ_{ij}.[23] The use of optical susceptibilities directly is simpler and followed here. Using the nonlinear susceptibility tensor would give the same results.

The f_{ij} of Eq. (19) have been chosen for $i,j = \hat{x},\hat{y},\hat{z}$. The corres-

ponding $\tilde{f}_{ij}$ for $i,j = \hat{e}_+, \hat{e}_-, \hat{z}$ where

$$\hat{e}_+ = \frac{1}{\sqrt{2}}(\hat{x} + i\hat{y})$$

$$\hat{e}_- = \frac{1}{\sqrt{2}}(\hat{x} - i\hat{y}) \tag{42}$$

are obtained by applying the transformation tensor

$$T = \begin{pmatrix} 1 & 1 & 0 \\ i & -i & 0 \\ 0 & 0 & 1 \end{pmatrix} \tag{43}$$

$$\tilde{f}_{ij} = T^{-1} f_{ij} T$$

$$= \begin{pmatrix} \frac{1}{2}[f_{xx} + f_{yy} + i(f_{xy} - f_{yx})] , & \frac{1}{2}[f_{xx} - f_{yy} - i(f_{xy} + f_{yx})] , & 0 \\ \frac{1}{2}[f_{xx} - f_{yy} + i(f_{xy} - f_{yx})] , & \frac{1}{2}[f_{xx} + f_{yy} - i(f_{xy} - f_{yx})] , & 0 \\ 0 , & 0 , & f_{zz} \end{pmatrix}. \tag{44}$$

For ellipse rotation the incident field is elliptically polarized

$$\vec{E}(\omega,t) = (\hat{e}_+ E_+ + \hat{e}_- E_-) e^{ikz - i\omega t} \mathcal{E}(x,y,t)$$

$$|E_+|^2 + |E_-|^2 = 1 \tag{45}$$

where $\mathcal{E}(x,y,t)$ is the pulse envelope. Then the f_{ij} are

$$f_{ij} = \frac{\Delta\chi}{12} |\mathcal{E}(x,y,t)|^2 \begin{pmatrix} \frac{|E|^2}{3} + E_+^* E_- + E_-^* E_+ & i(E_-^* E_+ - E_- E_+^*) & 0 \\ i(E_-^* E_+ - E_- E_+^*) & \frac{|E|^2}{3} - E_+^* E_- - E_-^* E_+ & 0 \\ 0 & 0 & -\frac{2|E|^2}{3} \end{pmatrix} \tag{46}$$

and the corresponding $\tilde{f}_{ij}$ is

$$\tilde{f}_{ij} = \frac{\Delta\chi}{12} \begin{pmatrix} \frac{1}{3}|E|^2 & 2E_-^* E_+ & 0 \\ 2E_- E_+^* & \frac{1}{3}|E|^2 & 0 \\ 0 & 0 & -\frac{2}{3}|E|^2 \end{pmatrix} |\mathcal{E}(x,y,t)|^2 \tag{47}$$

where $|E|^2 = |E_+|^2 + |E_-|^2 = 1$. The corresponding $\tilde{\chi}_{ij}$ is then (where ~ refers to circular coordinants)

$$\tilde{\chi}_{ij} = \bar{\chi}\tilde{\delta}_{ij} + \frac{(\Delta\chi)^2}{18a(T - T^*)} \begin{pmatrix} \frac{1}{3}|E|^2 & 2E_-^* E_+ & 0 \\ 2E_- E_+^* & \frac{1}{3}|E|^2 & 0 \\ 0 & 0 & -\frac{2}{3}|E|^2 \end{pmatrix} \int_{-\infty}^{t} \frac{1}{\tau_M} e^{-(t-t')/\tau_M}$$

$$\times |\mathcal{E}(x,y,t')|^2 dt'. \tag{48}$$

The polarization induced is

$$P_\pm(\omega,t) = \left\{ \left[\bar{\chi} + \frac{(\Delta\chi)^2}{54a(T - T^*)} g(t) \right] + \left[\frac{(\Delta\chi)^2 |E_\mp|^2}{9a(T - T^*)} g(t) \right] \right\} E_\pm(\omega,t)$$

$$g(x,y,t) = \frac{1}{\tau_M} \int_{-\infty}^{t} |\mathcal{E}(x,y,t')|^2 e^{-(t-t')/\tau_M} dt'. \tag{49}$$

The terms have been written in a form that separates the field polariza-

tion dependent part from the field polarization independent part for $P_{\pm}(\omega,t)$. We get immediately from the field polarization dependent term:

$$\delta\chi_{\pm} = \frac{(\Delta\chi)^2 |E_{\mp}|^2}{9a(T - T^*)} g(t). \tag{50}$$

The corresponding circular birefringence is

$$\delta n_c = \frac{2\pi}{n} (\delta\chi_- - \delta\chi_+)$$

$$= \frac{2\pi}{n} \frac{(\Delta\chi)^2}{9a(T - T^*)} g(t)[|E_+|^2 - |E_-|^2]. \tag{51}$$

Using Eq. (37) this reduces to

$$\delta n_c = \frac{\pi}{n} \beta g(t)[|E_+|^2 - |E_-|^2]. \tag{52}$$

The phase shift induced between the $\hat{e}_+$ and $\hat{e}_-$ polarizations is given by $d\phi/dz = \delta n_c\ \omega/c$. Thus the ellipse rotation angle θ is given by

$$\frac{d\theta}{dz} = \frac{\omega}{2c} \delta n_c \tag{53}$$

where θ is the angle through which the elliptical polarization is rotated by the material.

Actual values for $d\theta/dz$ require that the field be specified. For many cases the applied field is a laser pulse that can be approximated by a Gaussian

$$\mathcal{E}(x,y,t) = \mathcal{E}_o\ e^{-b^2t^2/2}\ e^{-r^2/w^2} \tag{54}$$

where

$$r = \sqrt{x^2 + y^2}$$

$$b = [1/e \text{ width of Gaussian time profile (intensity)}]^{-1}$$

$$w = 1/e \text{ width of Gaussian spatial field distribution.}$$

The expression for g(x,y,t) defined in Eq. (49) becomes

$$g(x,y,t) = \frac{1}{\tau_M} \int_{-\infty}^{t} |\mathcal{E}_o|^2 \, e^{-b^2 t'^2} \, e^{-2r^2/w^2} \, e^{-(t-t')/\tau_M} \, dt'$$

$$= \frac{\sqrt{\pi} \, |\mathcal{E}_o|^2}{2\tau_M b} \, e^{-t/\tau_M} \, e^{-2r^2/w^2} e^{\left(\frac{1}{2b\tau_M}\right)^2} \left\{1 + \operatorname{erf}\left[bt - \frac{1}{2b\tau_M}\right]\right\} . \quad (55)$$

This will be evaluated further when the actual laser intensities can be specified.

D. Self Focusing in Liquid Crystals

In any Kerr liquid, it is always important to consider the process of self focusing. Liquid crystals with their enhanced nonlinear coefficients are particularly susceptible to self focusing. Under most circumstances, this concern is primarily one of eliminating the self focusing, thereby avoiding the damage or breakdown that frequently accompanies it.[3] However, work with transient self focusing, where the duration of the applied field $\lesssim$ the response time of the material, has shown that the self focusing process need not be catastrophic.[5,6] We will examine self focusing for MBBA in a ruby laser cavity in Chapters IV-VI. In this section, the basic theory of transient self focusing is described, and an expression for the effects of self focusing is determined for the

weak focusing limit.

In the fully transient limit (duration of laser pulse $\tau_p \ll$ response time of the material T_m), it was found that an input laser pulse evolves as it propagates into a characteristic horn shape, which then can continue to propagate for long distances, essentially unchanged.[5] The actual shape the horn takes is determined by the total power present in the pulse. The amount of material the pulse must travel through to attain this shape depends on pulse intensity. And the distance the horn-shaped pulse will travel without appreciable change is approximately a diffraction length of the original unfocused pulse. For a given pulse intensity and total power, there is a corresponding minimum length of material needed for the pulse to deform completely to the horn shape. For cells longer than this minimum length, the output will depend only weakly on cell length, while for cells shorter than this minimum, the output will depend strongly on cell length. This can be seen graphically in Fig. 5. The evolution of the pulse as it deforms to the horn shape is seen in Fig. 6 (from Shen[3]).

The limiting beam radius seen in Fig. 5 depends on power available in the pulse. This limiting beam radius occurs at the neck of the horn, and its value represents the beam size where the increased diffraction (due to the smaller beam size) is able to compensate for the induced focusing. For a given pulse power, this balance between diffraction and induced focusing occurs at a specific beam radius. As the available power increases, the intensity for a given radius increases. The increased intensity results in greater induced focusing so this limiting beam radius decreases. The decrease of limiting beam size with increased power is ultimately limited by the onset of competing nonlinear

processes, such as two-photon absorption, Brillouin scattering or Raman scattering. These competing processes work by depleting the power as the beam focuses, maintaining the pulse intensity at a level near the threshold for the particular process. Since the focused pulse intensity determines the induced focusing, the limiting beam size will be determined by the lowest threshold intensity of these competing processes. Of course, the pulse power must be great enough for the focused pulse intensities to reach the threshold to see this effect. Figure 7 shows the behavior of the limiting beam radius as a function of pulse power. P_{CR} is the theoretical steady state power at which self focusing should first become observable.

The quasi-transient situation ($\tau_P \lesssim \tau_M$) resembles the fully transient case. Qualitatively, the behavior is described by the picture presented above for the fully transient limit and need not be repeated. The only qualitative difference between the fully transient and quasi-transient self focusing lies in the characteristic horn shape where the neck region develops the flared shape seen in Fig. 8.[6] This flaring becomes more noticeable as $\tau_P \gtrsim \tau_M$.

A complete solution for the self focusing problem is quite complicated, and has not been done analytically. To solve the problem, approximations must be made. For weak self focusing, the problem becomes considerably more tractable than for the full blown case. Referring to Fig. 5, it is clear that for small enough cell lengths, the output beam radius will not differ substantially from the input radius. With low input pulse intensities, the cell length can be quite large before appreciable change in beam radius is seen at the output. Under these conditions, it is possible to ignore the spatial redistribution of fields

that complicates the full self focusing calculation. One can then calculate the induced δn seen by the pulse. Naturally, the induced δn is not uniform but will depend on the spatial variation of the input pulse in the plane normal to the direction of propagation. Below we calculate this δn and estimate its effects on the inducing pulse. The notation used has been introduced in Sections IIA and IIB and the approach is similar to that used in Section IIC.

We assume an input field of the form

$$\vec{E}(r,t) = \mathcal{E}(x,y,t)e^{ikz-i\omega t}\,\hat{x} \tag{56}$$

where $\mathcal{E}(x,y,t)$ contains the spatial variation of the fields in the x,y plane and the slowly varying time envelope for the pulse. The nonzero $f_{ij}(x,y,t)$ for Eq. (19) are then

$$f_{xx}(x,y,t) = \frac{\Delta\chi}{9}\,|\mathcal{E}(x,y,t)|^2 \tag{57}$$

$$f_{yy}(x,y,t) = f_{zz}(x,y,t) = -\frac{\Delta\chi}{18}\,|\mathcal{E}(x,y,t)|^2. \tag{58}$$

The resulting χ_{ij} are then by Eqs. (3) and (20)

$$\chi_{xx}(x,y,t) = \bar{\chi} + \frac{2}{3}(\Delta\chi)\int_{-\infty}^{t}\frac{\Delta\chi}{9\nu}\,|\mathcal{E}(x,y,t')|^2\,e^{-(t-t')/\tau_M}\,dt' \tag{59}$$

$$\chi_{yy}(x,y,t) = \bar{\chi} + \frac{2}{3}(\Delta\chi)\int_{-\infty}^{t}-\frac{\Delta\chi}{18\nu}\,|\mathcal{E}(x,y,t')|^2\,e^{-(t-t')/\tau_M}\,dt'. \tag{60}$$

Since only the $\hat{x}$ polarization is present, the relevant δn is

$$\delta n(x,y,t) = \frac{2\pi}{n}\,\delta\chi_{xx}(x,y)$$

$$= \frac{4\pi(\Delta\chi)^2}{27\nu n}\int_{-\infty}^{t} |\mathcal{E}(x,y,t')|^2\, e^{-(t-t')/\tau_M}\, dt'$$

$$= \frac{2\pi}{3n}\,\beta g(x,y,t) \tag{61}$$

where the definition of β in Eq. (37) has been used. The $g(x,y,t)$ is that of Eq. (49), reproduced here for convenience

$$g(x,y,t) = \frac{1}{\tau_M}\int_{-\infty}^{t} |\mathcal{E}(x,y,t')|^2\, e^{-(t-t')/\tau_M}\, dt'. \tag{62}$$

The value of $g(x,y,t)$ for a single mode pulse is given by Eq. (55).

The effect of the induced δn (Eq. (59)) is to change the phase velocity of the various sections of the pulse wavefront, producing distortions. These distortions are shown in Fig. 9, exaggerated for clarity. The shape of the distorted wavefront can be calculated from the phase velocity of each section. ℓ is the length of material passed through.

$$\nu_P = c/n \tag{63}$$

after the pulse has left the material, the edges of the wavefront will lead the center. We define $\delta(x,y)$ as the position of the wavefront along the z axis. δ_o will be this position for the center of the wavefront. We have with $r = \sqrt{x^2 + y^2}$, using Fig. 10,

$$\ell n(r = 0) + \delta_o = \ell n(r) + \delta(r) \tag{64}$$

where we have assumed air (n = 1) outside the self focusing material. This of course reduces to

$$\delta(r) = \ell[n(0) - n(r)] + \delta_o. \tag{65}$$

It is clear from Eqs. (61) and (62) that a converging Gaussian wavefront is formed. The optics of a Gaussian beam profile with a Gaussian wavefront are complicated. We use the paraxial approximation to simplify the calculation. With this approximation, we replace the Gaussian wavefront with a parabolic wavefront while retaining a Gaussian beam profile. Since $\delta(r)$ is given by Eq. (65), the paraxial approximation is equivalent to replacing the Gaussian δn profile with a parabolic profile

$$\begin{aligned} \delta n(r) &= \delta n(r = 0)e^{-2r^2/w^2} \\ &\approx \delta n(0)\left(1 - \frac{2\nu^2}{w^2}\right) \end{aligned} \tag{66}$$

where w is the 1/e width of the incident Gaussian beam.

Propagation of Gaussian beams through quadratic index media can be described using the so-called "ABCD matrices."[29] Propagation of Gaussian beams and use of the ABCD matrices are discussed in the following section. For future reference, we give here the ABCD matrix for the parabolic index media (Eq. (66)), which is a special case of quadratic index media.[29]

$$\begin{bmatrix} AB \\ CD \end{bmatrix} =$$

$$\begin{bmatrix} \cos\left(\frac{2\ell}{w}\sqrt{\frac{\delta n(0)}{\bar{n} + \delta n(0)}}\right) & \frac{w}{2}\sqrt{\frac{\bar{n} + \delta n(0)}{\delta n(0)}}\,\sin\left(\frac{2\ell}{w}\sqrt{\frac{\delta n(0)}{\bar{n} + \delta n(0)}}\right) \\ -\frac{2}{w}\sqrt{\frac{\delta n(0)}{\bar{n} + \delta n(0)}}\,\sin\left(\frac{2\ell}{w}\sqrt{\frac{\delta n(0)}{\bar{n} + \delta n(0)}}\right) & \cos\left(\frac{2\ell}{w}\sqrt{\frac{\delta n(0)}{\bar{n} + \delta n(0)}}\right) \end{bmatrix}. \tag{67}$$

Here $\bar{n}$ is the index of refraction for the MBBA with no applied field.

E. Laser Cavity Theory

Sections IIA-IID have given needed background theory for the liquid crystal. In this section, some laser cavity theory will be presented. We begin with a discussion of the laser rate equations and progress to mode selection and cavity losses. A working knowledge of laser systems and terminology is assumed. For a review of these subjects see Ref. 18 or similar works.

The treatment of laser rate equations will be directed towards a three level system such as the ruby laser. A four level laser system is similar, and the extension is straightforward. The three level laser energy level diagram is seen in Fig. 11, along with the definition of certain parameters. The lifetime τ_{32} is very short compared with τ_{21} so the total population density is

$$\mathcal{N}_{tot} \approx \mathcal{N}_1 + \mathcal{N}_2. \tag{68}$$

For a working three level laser, the physical situation can be viewed as a two level system since the decay from state 3 to state 2 is so rapid. The dynamics of such a system is described resonably by a set of coupled

rate equations.[18]

$$\frac{\partial \mathcal{N}_1}{dt} = \left(\mathcal{N}_2 - \frac{g_2}{g_1}\mathcal{N}_1\right)c\phi\sigma + \frac{\mathcal{N}_2}{\tau_{21}} - W_p\mathcal{N}_1$$

$$\frac{\partial \mathcal{N}_2}{dt} = -\frac{\partial \mathcal{N}_1}{\partial t}$$

$$\frac{\partial \phi}{\partial t} = c\phi\sigma\left(\mathcal{N}_2 - \frac{g_2}{g_1}\mathcal{N}_1\right) - \frac{\phi}{\tau_c} + S \tag{69}$$

where ϕ is the photon density, σ is the stimulated emission cross section, τ_c is the average photon lifetime in the cavity, S is the spontaneous emission contribution to ϕ, and W_p is the effective pump rate given by

$$W_p = \frac{\tau_{31}}{\tau_{31} + \tau_{32}} W_{13} \tag{70}$$

which takes into account the loss of pump efficiency due to decay from the pump band back to state 1. From Eq. (69) it is clear that the relevant parameter is not $\mathcal{N}_1$ or $\mathcal{N}_2$ but the density of population inversion $\mathcal{N}$ where

$$\mathcal{N} = \mathcal{N}_2 - (g_2/g_1)\mathcal{N}_1. \tag{71}$$

The Eq. (69) then becomes

$$\frac{\partial \mathcal{N}}{\partial t} = -\left(1 + \frac{g_2}{g_1}\right)\mathcal{N}\phi\sigma c - \frac{\mathcal{N} + \mathcal{N}_{tot}(g_2/g_1)}{\tau_{21}} + W_p(\mathcal{N}_{tot} - \mathcal{N})$$

$$\frac{\partial \phi}{\partial t} = c\phi\sigma\mathcal{N} - \frac{\phi}{\tau_c} + S. \tag{72}$$

These laser rate equations are used to determine general laser output features such as average and peak power, pulse envelope shapes, threshold conditions, etc. Detailed spatial, spectral, and temporal structure determinations must rely on other techniques. Except for a full two or three dimensional finite difference calculation (or its equivalent) these other techniques sacrifice the determination of general features to determine the specific details.

Some approximations are made by using Eqs. (72). Nonuniformities along the longitudinal axis are neglected, with the assumption that the gain and loss mechanisms are uniformly distributed between the reflectors. Furthermore, longitudinal and radial variations of the radiation are ignored so the ϕ and N must correspond to a single mode. Despite these approximations, there are many times when the equations adequately describe the laser system. The giant pulse of a Q-switched laser is one such example. When they can be used, the laser rate equations are particularly useful due to the ease with which numerical techniques may be used to obtain solutions.

In order to use a computer in solving the rate equations, ideally they should be rendered in a dimensionless form. The time variable and density of population inversion have a natural normalization

$$\tilde{\mathcal{N}} = \mathcal{N}/N_{\text{at threshold}}$$

$$\tilde{t} = t/t_R$$

$$t_R = \text{cavity round trip time.} \tag{73}$$

At threshold one wants $\partial\phi/\partial t \geqslant 0$ which from Eq. (72) gives

$$\mathcal{N}_{\text{threshold}} = \frac{1}{\sigma c \tau_c} . \tag{74}$$

The contribution of S has been ignored since its contribution to ϕ at or above threshold is small. Using this value for $N_{\text{threshold}}$ and expressing

$$\frac{1}{\tau_c} = \frac{\varepsilon}{t_R}$$

$$\varepsilon = \text{fractional round trip cavity losses} \tag{75}$$

we can define a more useful loss independent normalization

$$\tilde{\mathcal{N}} = \sigma c t_R \mathcal{N} = \varepsilon \mathcal{N}_{\text{threshold}}$$

$$\tilde{\phi} = \sigma c t_R \phi (1 + g_2/g_1)/2$$

$$\tilde{t} = t/t_R . \tag{76}$$

The normalization for ϕ has been selected to match that for N, with the factor $(1 + g_2/g_1)/2$ thrown in to make the final equations resemble the well known Statz and deMars equations for a single mode maser. The laser rate equations have the form

$$\frac{\partial\tilde{\mathcal{N}}}{\partial\tilde{t}} = -2\tilde{\mathcal{N}}\tilde{\phi} - \frac{\tilde{\mathcal{N}} + \tilde{\mathcal{N}}_{tot}(g_2/g_1)}{\tau_{21}/t_R} + W_p(\tilde{\mathcal{N}}_{tot} - \tilde{\mathcal{N}})t_R$$

cont'd

$$\frac{\partial\tilde{\phi}}{\partial\tilde{t}} = \tilde{\phi}\tilde{\mathcal{N}} - \tilde{\phi}\varepsilon + \frac{S}{\sigma c} . \tag{77}$$

For a giant pulse Q-switched laser, the pump and spontaneous emission may be ignored giving

$$\frac{\partial\tilde{\mathcal{N}}}{\partial\tilde{t}} = - 2\tilde{\mathcal{N}}\tilde{\phi}$$

$$\frac{\partial\tilde{\phi}}{\partial\tilde{t}} = \tilde{\phi}(\tilde{\mathcal{N}} - \varepsilon)$$

$$\tilde{\phi}_o \neq 0. \tag{78}$$

The last condition is an initial condition on $\tilde{\phi}$. $\tilde{\phi}_o$ is the flux present in the cavity at threshold. Retaining the noise term $S/\sigma c$ generates this flux automatically. Though the $S/\sigma c$ term is important below threshold to determine the seed pulse or noise that starts the lasing action, once lasing starts it has little affect on laser dynamics. Thus, the approximation of Eq. (78) where the small $S/\sigma c$ term is replaced by an initial condition on ϕ works well. An error in specifying ϕ_o results only in a shift in origin as long as ϕ_o is chosen small compared to the maximum value of ϕ. The actual value of ϕ_o will be specified when we solve Eq. (78). We shall return to Eq. (78) in Chapter III where we deal with the effects of an inducible loss in the laser cavity.

The laser rate equations , do not, as mentioned earlier, explain the spatial variation of the radiation field in the laser cavity. This variation is known as laser mode structure and can take two forms. Longitudinal modes have the same field distribution in a plane perpen-

dicular to the direction of propagation and differ from one another only in their oscillation frequency. Transverse modes differ from one another in field distribution with or without a difference in oscillation frequency. Thus, for each transverse mode there corresponds a number of longitudinal modes with the same field distribution. (See Fig. 12 for some typical mode patterns.) If the laser is being used as a light source where power emitted is the primary concern (such as for pumping) then an effort is made to maximize the number of transverse modes that lase, as this makes for maximal use of the population inversion. On the other hand, when the laser is being used in studies where it is important to know the laser dynamics of where the output radiation field distribution plays an important role, then the effort is made to allow only one transverse mode to lase thereby maximizing the knowledge of the laser characteristics and minimizing the error introduced by the laser source. Usually a TE_{oo} mode (see Fig. 12) is chosen since this mode has the smallest beam divergence, the highest power density and can be focused to a diffraction limited spot of maximum power per unit area. Selection of a single longitudinal mode is less critical, but again single mode operation is best. When it is desired to use the laser rate Eq. (78), then single mode operation becomes even more important.

Standard mode selecting procedure calls for a pinhole to be inserted into the laser cavity on axis. Only the TE_{oo} mode with its energy concentrated near the axis will survive. Proper mode selection requires a pinhole size small enough to discriminate against the next higher order mode yet large enough to permit lasing in the TE_{oo} mode. Often this results in lasing action solely in a TE_{oo} mode but at the

cost of an increased thresold for lasing. The actual choice of pinhole size will be discussed below after the discussion on cavity losses.

Longitudinal mode selection can be achieved in a variety of ways. For a saturable absorber Q-switched ruby laser though, the selection is automatic.[18] Since such a laser was used for our experiments, the discussion will be limited to this case. The case of most solid state lasers Q-switched by saturable absorber is similar. The principle underlying the mode selection is one of natural selection. When properly Q-switched, the laser output (for saturable absorber) occurs at the end of the pump pulse. Since the pump pulse is very long compared to the cavity round trip time, this assures a large build up time from noise to eventual threshold. This large build up time allows many cavity round trips during the process. Any difference in gain for the various longitudinal modes will be greatly amplified during these trips leading to a selection of one dominant mode when thresold is reached. The power in the dominant mode is compared to that of adjacent modes in Fig. 13. It is clear from this figure that the gain difference between the dominant and adjacent modes need not be large. However, at least some difference must be present. For most lasers the gain difference between adjacent modes directly attributable to the active material is insufficient to play a significant role in the selection process. Usually, a resonant reflector is used for the purpose. To insure single mode operation, the spectral width of the reflector resonance must be small enough to insure sufficient gain differentiation between the different modes. The gain differentiation needed is much less than the CW case would require where no amplication is possible. The output etalon used to select lasing transition in a ruby laser is usually suf-

ficient.

Assuming that the laser is successfully operated in a single TE_{oo} mode, the radiation field distribution will then have the form[18]

$$\mathcal{E}(r) = \mathcal{E}_o e^{-(r^2/w^2)} . \tag{79}$$

This is, of course, a Gaussian. Propagation of a beam with such a Gaussian profile is well understood.[29,30] A typical Gaussian beam is shown in Fig. 14 with the important parameters labelled. The beam can be described by the Gaussian beam parameter q(z)

$$\frac{1}{q(z)} = \frac{1}{R(z)} - i \frac{\lambda}{\pi n w^2(z)} \tag{80}$$

where λ is the wavelength of the radiation field and n is the index of refraction of the medium. In terms of this parameter q, the effects of some lens-like media can be specified. Ths subscript i refers to initial, f to final.

$$\text{straight propagation:} \quad q_f(z + \Delta z) = q_i(z) + \Delta z$$

$$\text{lens of focal length } \ell: \quad \frac{1}{q_f} = \frac{1}{q_i} - \frac{1}{f}$$

$$\text{mirror of radius R:} \quad \frac{1}{q_f} = \frac{1}{q_i} - \frac{2}{R} . \tag{81}$$

When many optical elements are present it is convenient to use a matrix representation of the transformation

$$q_2 = \begin{bmatrix} A_1 & B_1 \\ C_1 & D_1 \end{bmatrix}(q_1) = \frac{A_1 q_1 + B_1}{C_1 q_1 + D_1} \ . \tag{82}$$

Then for multiple elements

$$q_3 = \begin{bmatrix} A_2 & B_2 \\ C_2 & D_2 \end{bmatrix}(q_2) = \frac{A_2 \begin{bmatrix} A_1 & B_1 \\ C_1 & D_1 \end{bmatrix}(q_1) + B_2}{C_2 \begin{bmatrix} A_1 & B_1 \\ C_1 & D_1 \end{bmatrix}(q_1) + D_2}$$

$$= \frac{(A_2 A_1 + B_2 C_1) q_1 + (A_2 B_1 + B_2 D_1)}{(C_2 A_1 + D_2 C_1) q_1 + (C_2 B_1 + D_2 C_1)}$$

$$= \begin{bmatrix} A_2 & B_2 \\ C_2 & D_2 \end{bmatrix} \begin{bmatrix} A_1 & B_1 \\ C_1 & D_1 \end{bmatrix}(q_1) \tag{83}$$

which points out the utility of this representation, allowing one to use simple matrix multiplication to handle a series of optical elements. The matrix equivalent of Eq. (81) are

$$\begin{array}{rl} \text{straight propagation through distance d}: & \begin{bmatrix} 1 & d \\ 0 & 1 \end{bmatrix} \\ \text{interface } n_1 \to n_2: & \begin{bmatrix} 1 & 0 \\ 0 & n_1/n_2 \end{bmatrix} \\ \text{lens of focal length f}: & \begin{bmatrix} 1 & 0 \\ -1/f & 1 \end{bmatrix} \\ \text{mirror of radius R}: & \begin{bmatrix} 1 & 0 \\ -2/R & 1 \end{bmatrix} . \end{array} \tag{84}$$

As indicated in Fig. 14, Gaussian beams diverge at a full angle $\theta = 2\lambda/\pi w_o$. This Gaussian beam diffraction usually constitutes the primary cavity loss mechanism after loss from the mirrors.

There are three main sources of loss in a laser cavity: loss through the mirrors, diffraction losses, and losses due to elements inserted into the cavity. The first two loss sources have been extensively studied for resonators in general. This theory will be presented below. The third loss term, being experiment specific, will be presented in Sections III and IV.

With no inversion population density, the differential Eq. (78) for $\tilde{\phi}$ is

$$\frac{d}{d\tilde{t}}\tilde{\phi} = \tilde{\phi}\varepsilon \; ; \; \tilde{t} = t/t_R$$

$$\tilde{\phi} = \tilde{\phi}_o e^{-\varepsilon t/t_R} \tag{85}$$

with the indicated solution. Since in one round trip the mirrors induce a factor $(1 - T_1)(1 - T_2)$ to $\tilde{\phi}$, the value for ε due to the mirrors is [T_i is transmissivity of mirror i]

$$\varepsilon_M = - \ln(1 - T_1)(1 - T_2) = \ln[(1 - T_1)(1 - T_2)]^{-1}. \tag{86}$$

For most laser cavity one of the reflectivities, R_2 by convention, is very close to 1. Then

$$\varepsilon_M = - \ln(1 - T_2) - \ln(1 - T_1) \cong T_2 + \ln\left(\frac{1}{1 - T_1}\right) . \tag{87}$$

The case of diffraction loss is more complicated. Consider first the empty resonator cavity. Diffraction losses are specified by three parameters $(1 - L/R_1)$, $(1 - L/R_2)$ and N, where L is the resonator length,

R_i is radius of curvature of mirror i, and N is the resonator Fresnel number defined below (Eq. (88)). Passive laser resonators can be divided into two classes — stable or unstable — based on the parameters $(1 - L/R_1)$ and $(1 - L/R_2)$. The division between stable and unstable resonators is shown in Fig. 15 with several common resonators indicated. This discussion will be restricted to stable resonators, which have wider utility than the unstable resonators.

For a stable resonator, a cavity mode must have the same spatial profile and wavefront after completing a cavity round trip as it had at the start. This condition together with the parameters $(1 - L/R_1)$ and $(1 - L/R_2)$ uniquely determine the size of the cavity mode and the wavefront at any point in the cavity. Diffraction loss occurs whenever a cavity element is insufficient to pass the entire spatial extent of the mode. For example, the finite size of the mirrors results in spillage and an aperature in the cavity will block some of the cavity fields. For an empty cavity of length L and with mirrors of radius R the Fresnel number

$$N = \frac{a^2}{\lambda L} \tag{88}$$

characterizes the basic "lossiness" of the cavity due to this diffraction loss. Physically, N can be thought of as the ratio of the acceptance angle of one mirror (a/L) to the diffraction angle of a beam with a waist located at the second mirror (λ/a). For a cavity with $R_1 = R_2$, the diffraction loss is plotted as a function of N and $(1 - L/R_1)$ in Fig. 16.

Clearly, the theory must be extended to include elements in the

resonator such as active material, mode selection aperature, and whatever else is needed. One feature is particularly valuable in dealing with the mode selecting aperature. The parameters $(1 - L/R_1)$, $(1 - R_2)$, N fully describes the diffraction loss.[18] This means two resonators with identical values for those parameters will show the same loss. This holds even if the mirrors are not limiting aperature. For a resonator with a limiting aperature, Eq. (88) still holds but with "a" being the radius of the aperature rather than the radius of the mirrors. Given N determined this way, Fig. 16 remains valid.[18] An assymmetric cavity with a limiting aperature is easily transformed into two symmetric cavities for the purposes of calculating diffraction losses. The procedure is shown in Fig. 17. Since the size of the aperature is always much smaller than the size of the non mode-selected radiation field distribution, it is a good approximation to assume that a beam waist occurs at the pinhole as seen in Fig. 17a. The plane wavefront at the aperature allows the cavity to be viewed as two independent cavities each with a plane mirror the size of the aperature replacing the actual aperature, as shown in Fig. 17b. Reflection symmetry about this plane mirror implies that the diffraction loss for each of the sections in Fig. 17b is just ½ the diffraction loss for the symmetric cavity consisting of the section in question together with its reflection. The symmetric cavity is shown in Fig. 17c for the left section of 17b.

Any elements inserted into the cavity usually can be replaced by equivalent optical elements for the purpose of calculating diffraction loss or radiation field distributions. The laser active material usually is replaced by a thin lens. It turns out that a thin lens or an aperature is a good approximation for many of the commonly inserted in-

tracavity elements. The effect of an aperature bigger than the mode selecting aperature will have no effect and any smaller ones can be treated via the technique given above. The addition of a thin lens that does not change the limiting aperature leaves the Fresnel number N unchanged. The radiation field distribution is changed though, which affects the $(1 - L/R_i)$ parameters. Physically, $1 - L/R_i$ is the amount a beam with radius of curvature R_i at mirror i will expand or shrink by the time it reaches the opposite mirror in limit of infinitely large beam size. For the empty resonator we have, using Eqs. (80), (82), (84),

$$\frac{1}{q_1} = -\frac{1}{R_1} - \frac{i\lambda}{\pi w_1^2} \quad \text{[converging wavefront]}$$

$$q_2 = \begin{bmatrix} 1 & L \\ 0 & 1 \end{bmatrix} (q_1)$$

$$= q_1 + L$$

$$\frac{1}{q_2} = \frac{1/q_1}{1 + L/q_1} = \left\{1 - \frac{L}{R_1} - \frac{iL\lambda}{\pi w_1^2}\right\}^{-1} \left(-\frac{1}{R_1} - \frac{i\lambda}{\pi w_1^2}\right)$$

$$\frac{\lambda}{\pi w_2^2} = \frac{\lambda}{\pi w_1^2} \left\{\left(1 - \frac{L}{R_1}\right)^2 + \frac{L^2\lambda^2}{\pi^2 w_1^4}\right\}^{-1}$$

$$\lim_{w_1 \to \infty} \frac{w_2}{w_1} = \left(1 - \frac{L}{R_1}\right) \tag{89}$$

where the reasoning for each step is immediate. The generalization to the addition of a thin lens is now apparent. The matrix $\begin{bmatrix} 1 & L \\ 0 & 1 \end{bmatrix}$ describing the empty cavity should be replaced by the product of matrices representing the actual cavity. For the cavity shown in Fig. 18, one

would replace

$$\begin{bmatrix} 1 & L \\ 0 & 1 \end{bmatrix} \rightarrow \begin{bmatrix} 1 & L_2 \\ 0 & 1 \end{bmatrix} \begin{bmatrix} 1 & 0 \\ -1/f & 1 \end{bmatrix} \begin{bmatrix} 1 & L_1 \\ 0 & 1 \end{bmatrix}$$

$$= \begin{bmatrix} 1-L_2/f & L_o \\ -1/f & 1-L_1/f \end{bmatrix}$$

$$L_o = L_1 + L_2 - L_1 L_2/f. \tag{90}$$

Using the replacement Eq. (90) in the derivation Eq. (89) gives

$$q_2 = \frac{(1 - L_2/f)q_1 + L_o}{-1/f\ q_1 + (1 - L_1/f)}$$

$$\frac{1}{q_2} = \frac{-1/f + (1 - L_1/f)/q_1}{(1 - L_2/f) + L_o/q_1}$$

$$\frac{\lambda}{\pi w_2^2} = \frac{\lambda}{\pi w_1^2}\left\{\left(1 - \frac{L_2}{f} - \frac{L_o}{R_1}\right)^2 + \frac{\lambda^2 L_0^2}{\pi^2 w_1^4}\right\}^{-1}$$

$$\lim_{w_1 \to \infty} \frac{w_2}{w_1} = \left(1 - \frac{L_2}{f} - \frac{L_o}{R_1}\right). \tag{91}$$

From Eq. (91), it is clear that the parameters $(1 - L/R_1)$, $(1 - L/R_2)$ should be replaced by the parameters $(1 - L_2/f - L_o/R_1)$, $(1 - L_1/f - L_o/R_2)$. With this replacement the theory should hold as before for the empty resonator. The extension to more than one lens is obvious.

We finally address the topic of choosing the proper mode selection aperature size. The discussion above shows how the diffraction losses for the TE_{oo} mode can be determined. A similar technique could be used to determine the loss for the TE_{1o} mode, which is the next higher order mode. This becomes unnecessary since the ratios of losses for the TE_{1o}

and TE_{oo} losses has been calculated as a function of N and $(1 - L/R_1)$ for an empty symmetric cavity. The results are displayed in Fig. 19. Using Figs. 16 and 19, the trade off of increased threshold (large TE_{oo} mode loss) versus good discrimination (large TE_{1o} mode loss) can be evaluated for the particular setup and an aperature size selection can be made.

F. Conclusions

In Section II, we have presented the theory for topics that are necessary to the understanding of later sections. An effort has been made to retain generality in this presentation. Specific numbers and details will be added as needed in the subsequent discussions.

Figure Captions

Table 1. Chart of MBBA relaxation times at various sample temperatures.

Fig. 1. Molecular structure of MBBA. Dipole moment forms as indicated by (+) and (-).

Fig. 2. Free energy versus order parameter for a liquid crystal when the cubic term is small (from Priestly[4]).

Fig. 3. Free energy versus order parameter for a liquid crystal when the cubic term is large (from Priestly[4]).

Fig. 4. Relaxation time for MBBA as a function of sample temperature.

Fig. 5. Sketch of minimum output beam radius from an MBBA cell as a function of cell length.

Fig. 6. Sketch showing transient self focusing in a Kerr liquid. Different parts (a-f) of the pulse focus and defocus along different ray paths. The pulse first gets deformed into a horn shape and then propagates on without much further change (from Shen[3]).

Fig. 7. Plot of limiting beam radius versus pulse power for MBBA. Numbers are from Wong.[5] The assymtotic value is determined by competing nonlinear processes. $P_{critical}$ is 0.12 KW.

Fig. 8. Beam radius verus time for quasitransient self focusing at output of sample cell. Cell length is longer than the minimum required to reach the horn shape.

Fig. 9. An exaggerated sketch of how the wavefront for a plane wave input distorts due to mild self focusing.

Fig. 10. Optical path lengths corresponding to the distorted wavefront of Fig. 9.

Fig. 11. Diagram of the three level ruby laser energy levels. W_{13} is pump energy. τ_{ij} is the spontaneous lifetime for decay from state i to state j. E_i, g_i, N_i are the energy, degeneracy, and population density for the state i.

Fig. 12. Examples of (a) cylindrical and (b) rectangular transverse mode patterns. For cylindrical modes, the first subscript indicates the number of dark rings, whereas the second subscript indicates the number of dark bars across the pattern. A starred second subscript indicates a superposition of two unstarred modes rotated 90° from one another. For rectangular patterns, the two subscripts give the number of dark bars in the x and y directions (from Koechner[18]).

Fig. 13. Mode selection during the build-up of the pulse. The parameter R_n/R_m expresses the differences of the reflectivity which these two modes (n and m) experience at the mode selector during one round trip. Power ratio of the dominant mode to adjacent modes is plotted versus number of round trips involved in pulse build-up. Two values of the reflectivity ratio R_n/R_m are shown (from Koechner[18]).

Fig. 14. Side view of a Gaussian beam with the important parameters labelled. This figure provides the definition of w(z) and R(z).

Fig. 15. Stability diagram for the passive laser resonator.

Fig. 16. Diffraction loss per round trip for the TE_{oo} mode of various symmetric and stable resonators (from Koechner[18]).

Fig. 17. Reduction of an assymetric resonator with an aperature to an equivalent pair of symmetric resonators for calculating dif-

fraction losses.

Fig. 18. Passive resonator with one thin lens inserted.

Fig. 19. Ratio of the round trip losses of the two lowest-order modes for the symmetric geometry. The dotted lines are contours of constant loss for the TE_{oo} mode (from Koechner[18]).

Table 1	
Temperature	Relaxation Time
45° C	185 nsec
50° C	65 nsec
55° C	35 nsec
50° C	22 nsec
65° C	15 nsec
70° C	11 nsec

Figure 1

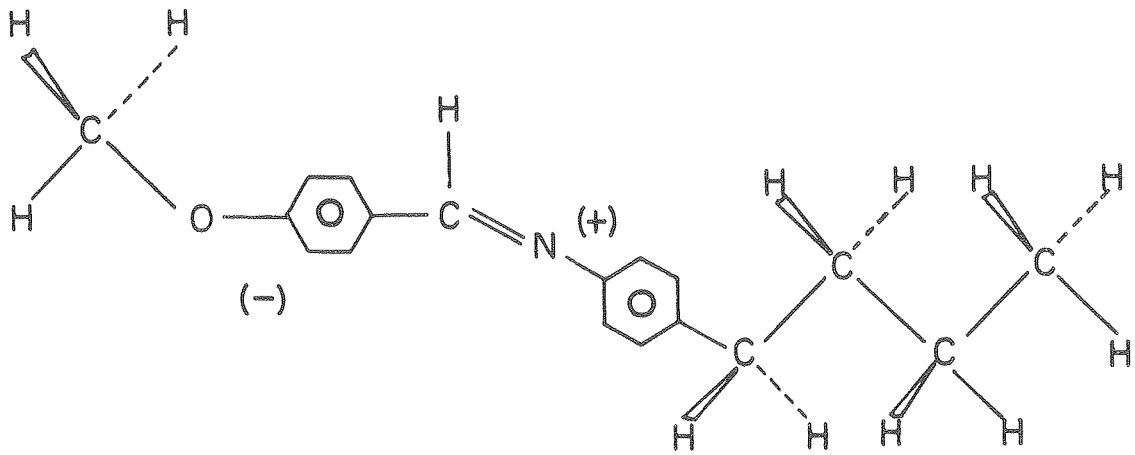

XBL 809-5792

Figure 2

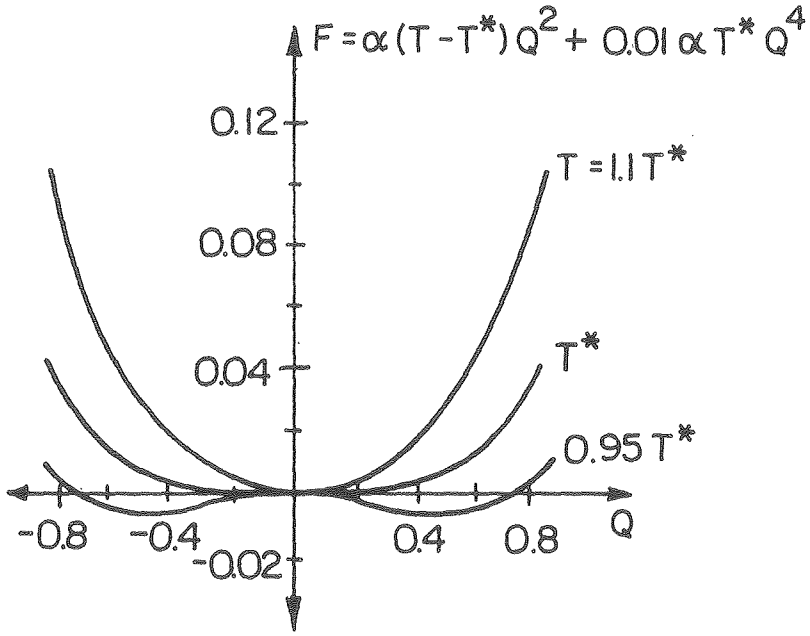

XBL 809-5793

Figure 3

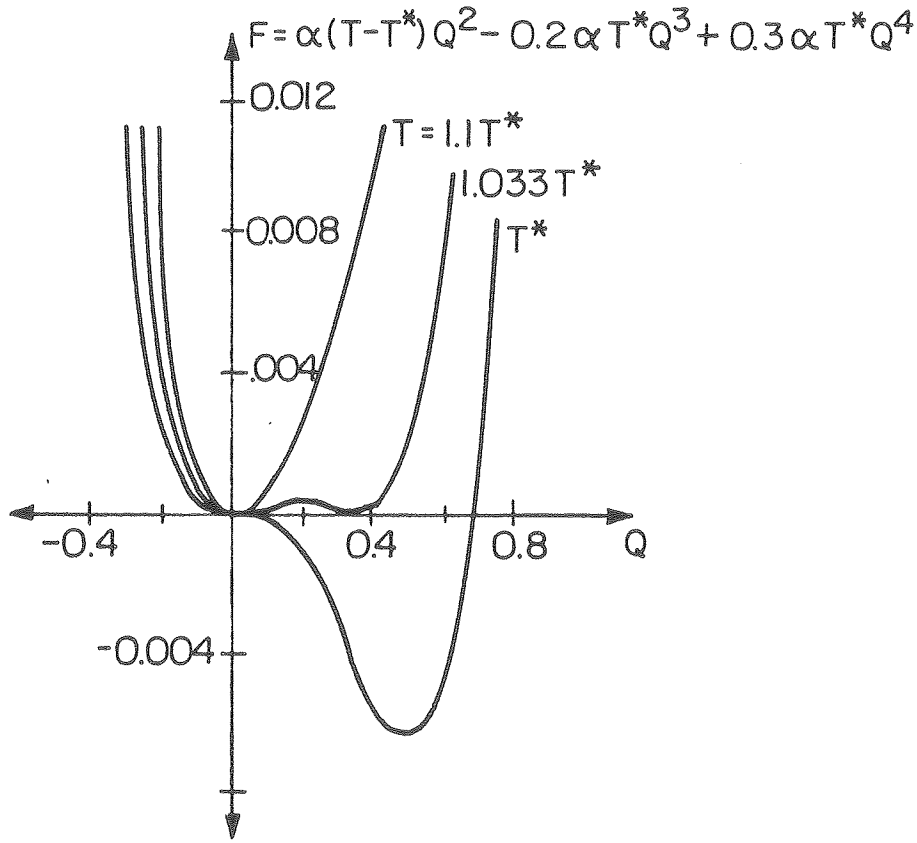

XBL809-5794

Figure 4

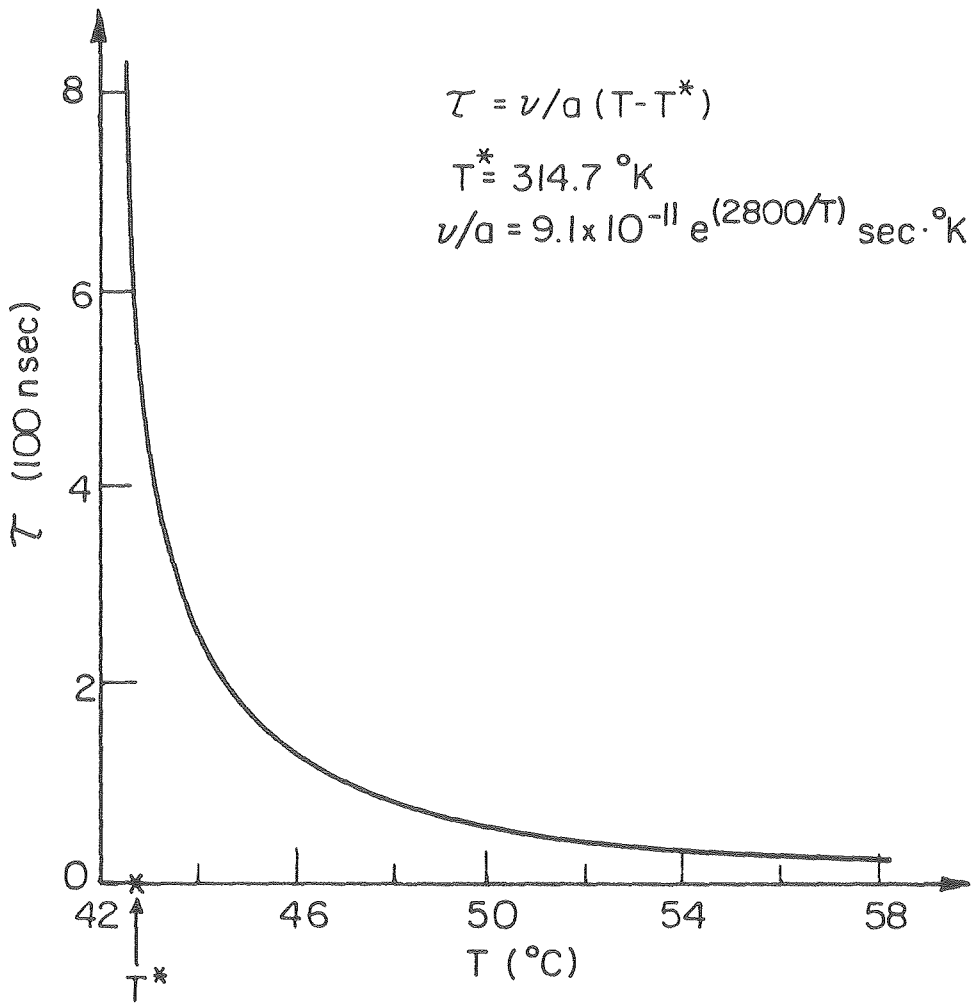

XBL 809-5795

Figure 5

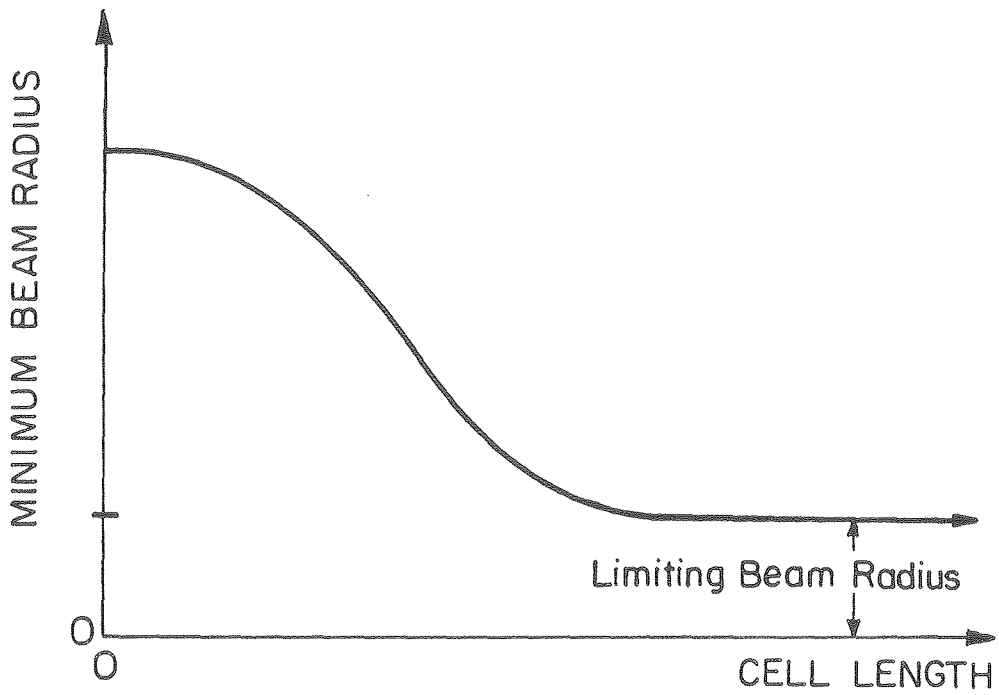

XBL 809-5796

Figure 6

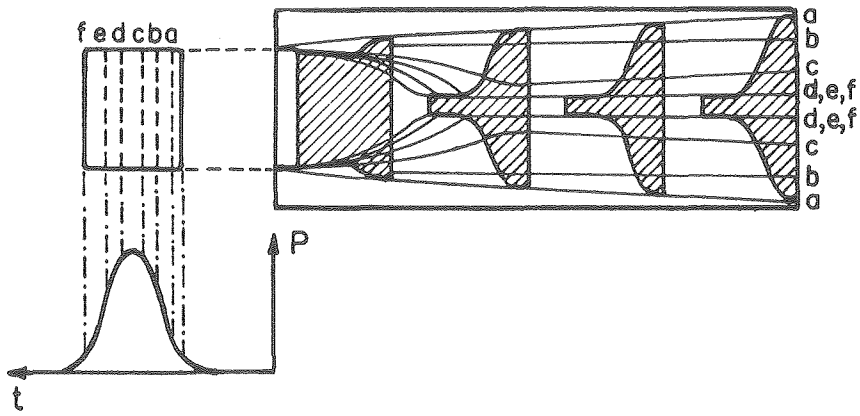

XBL809-5797

Figure 7

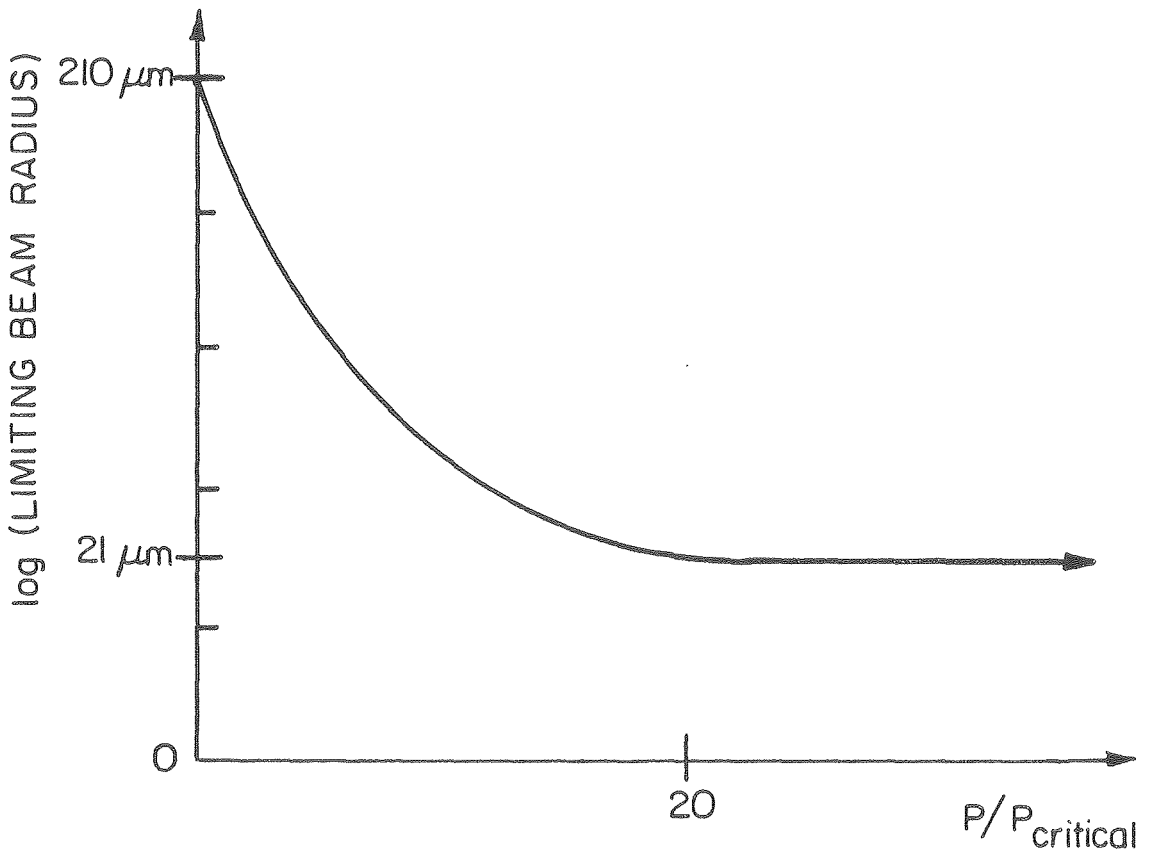

XBL809-5798

Figure 8

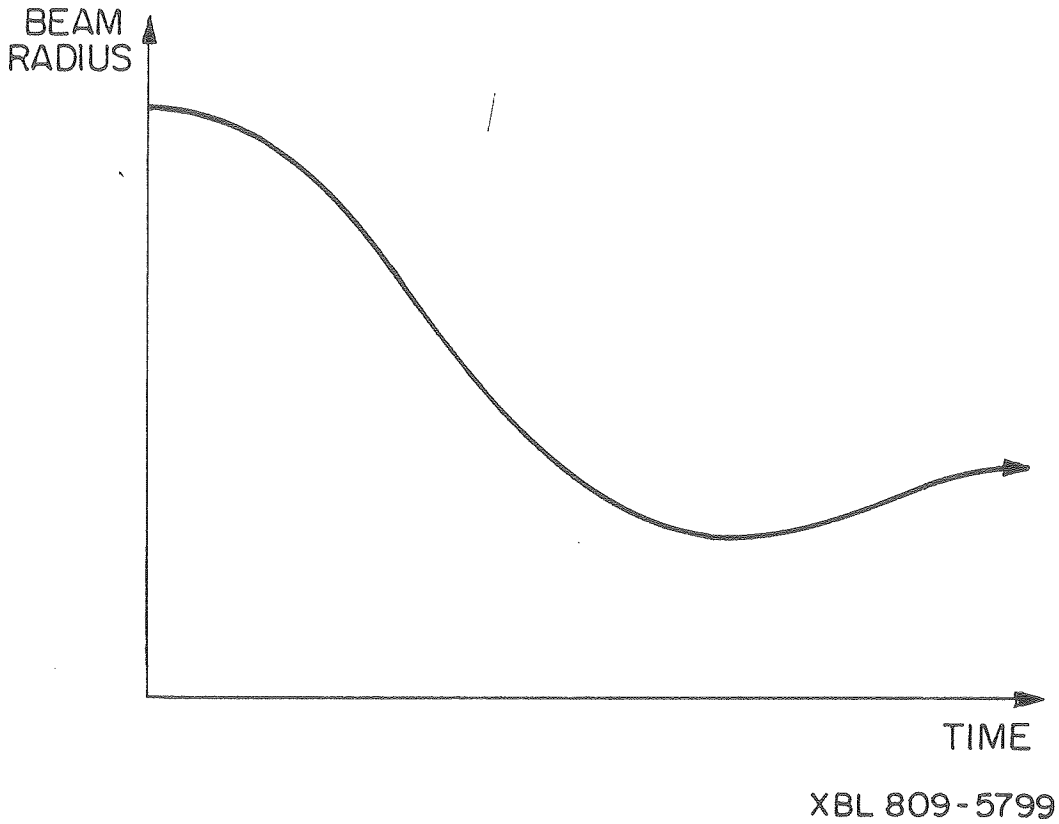

Figure 9

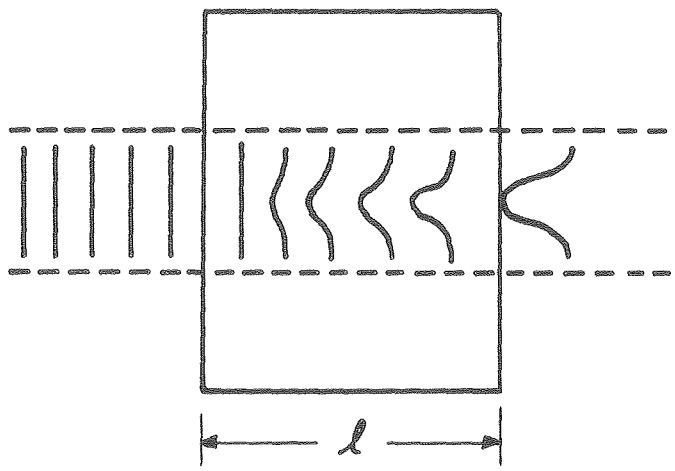

XBL809-5800

Figure 10

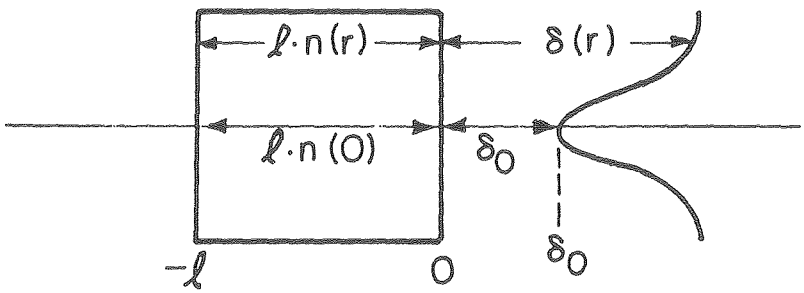

XBL809-5801

Figure 11

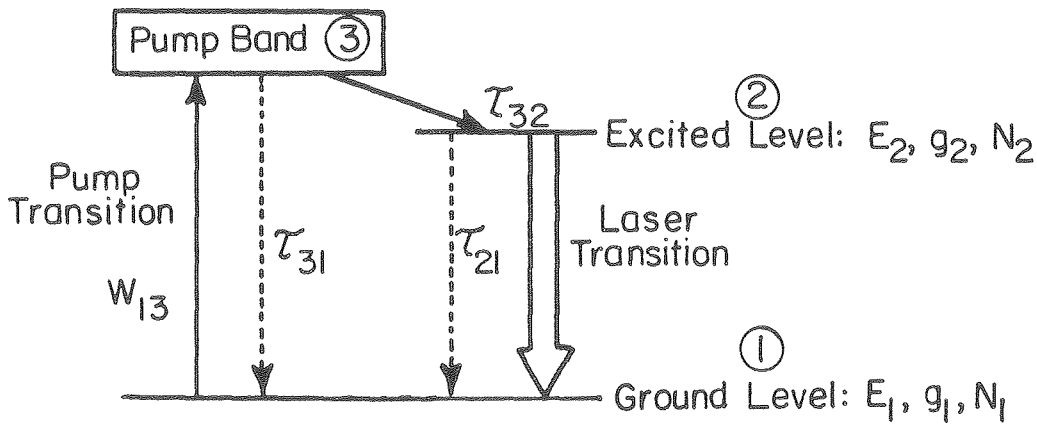

XBL 809-5802

Figure 12

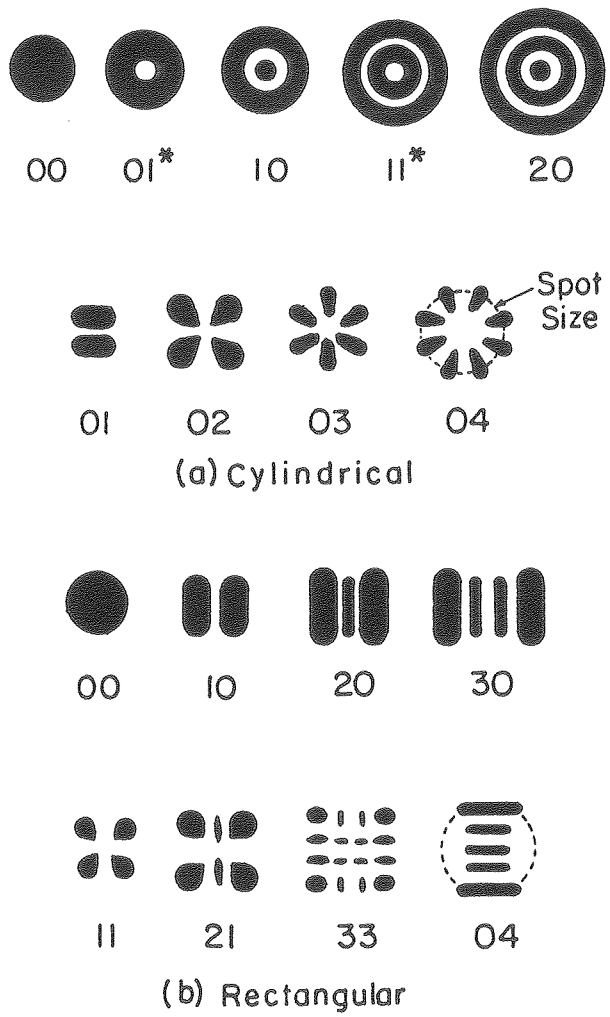

XBL809-5803

Figure 13

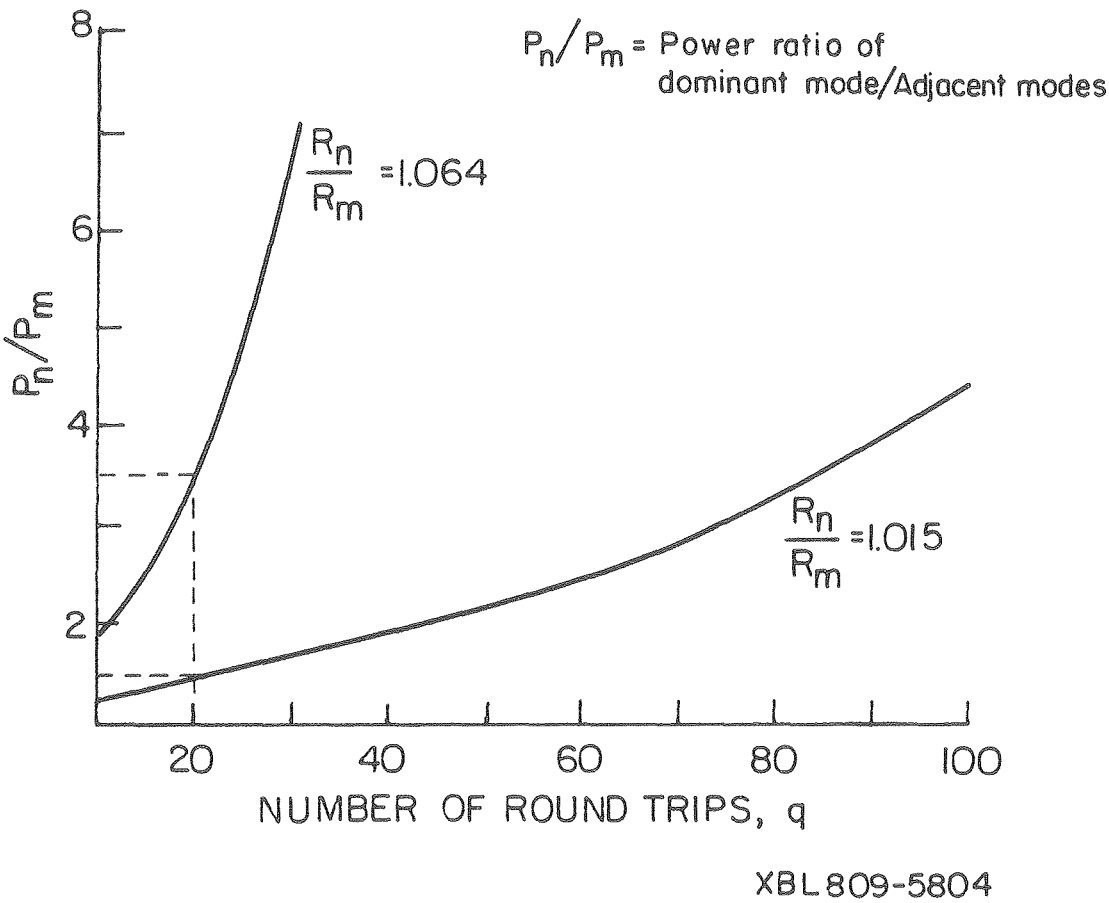

XBL809-5804

Figure 14

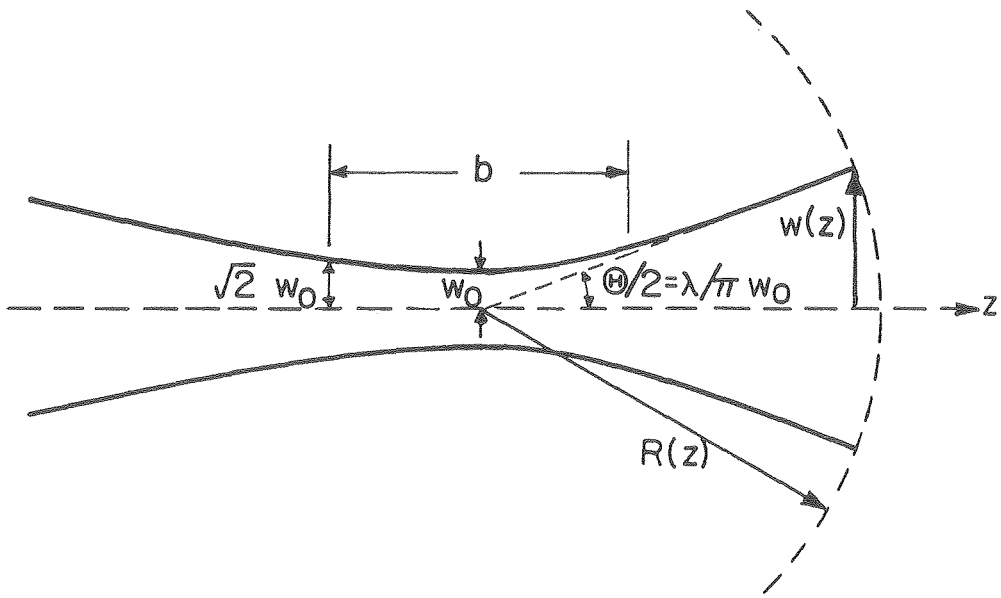

XBL809-5805

Figure 15

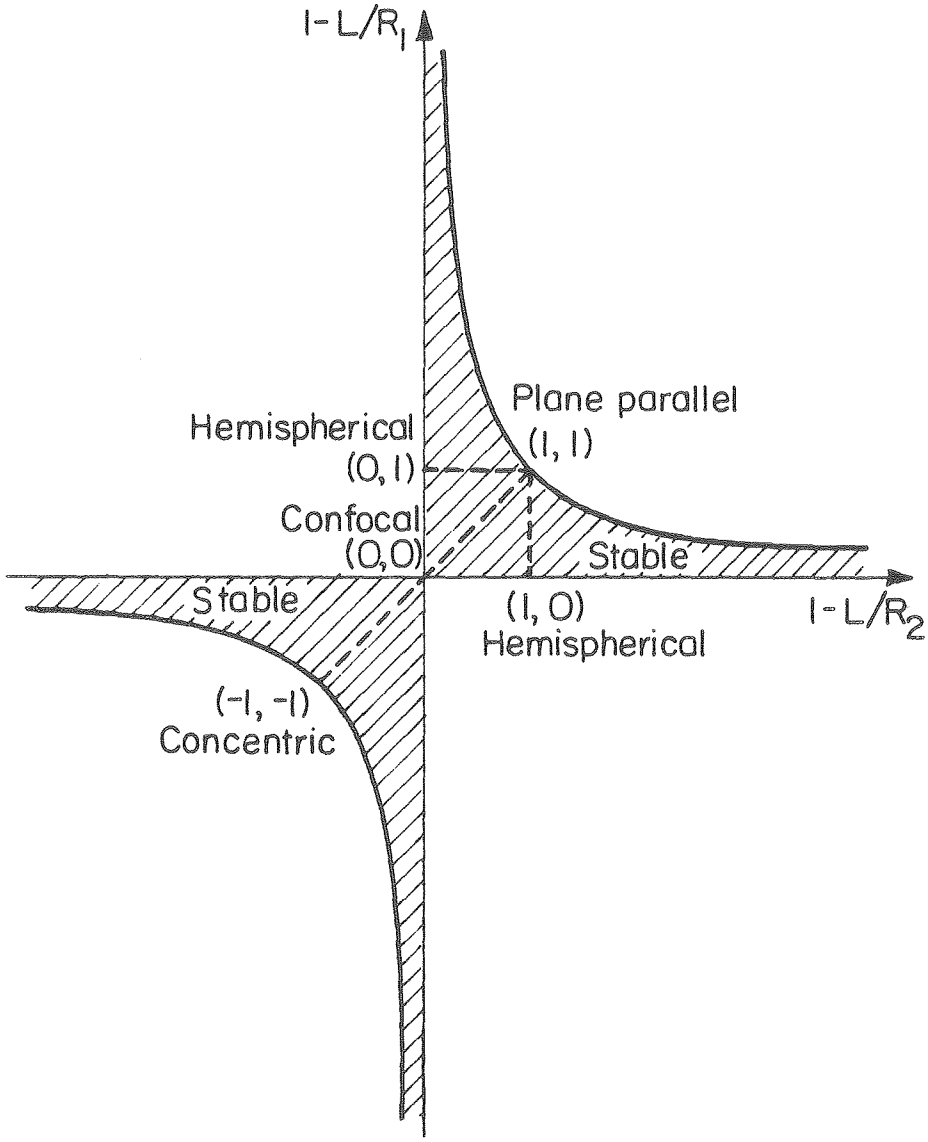

XBL809-5806

Figure 16

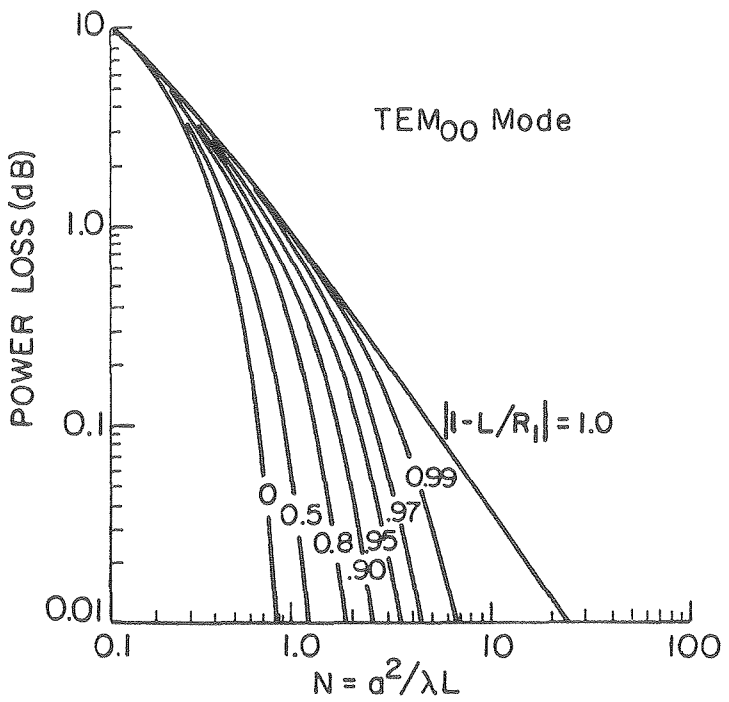

XBL809-5807

Figure 17

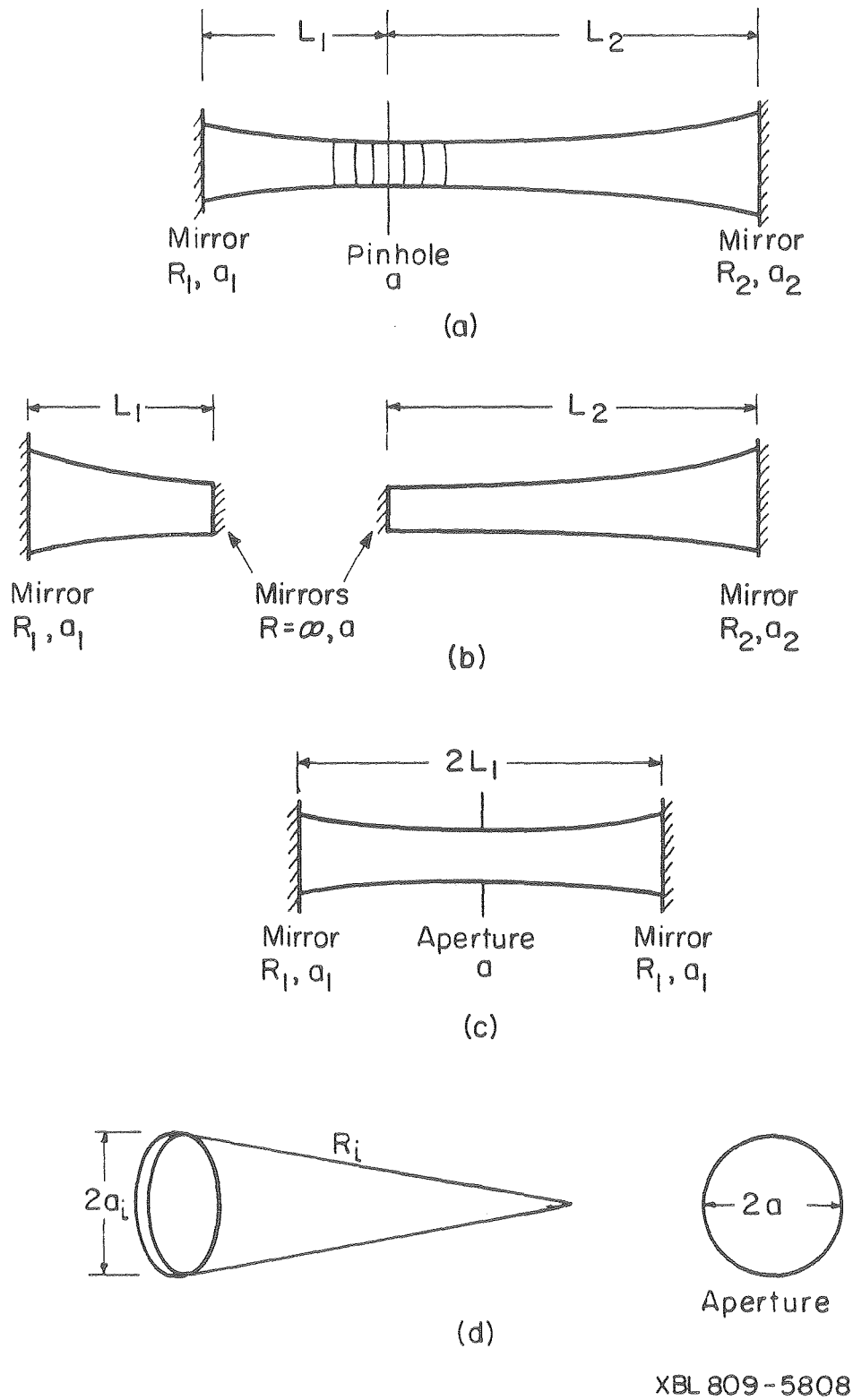

XBL 809-5808

Figure 18

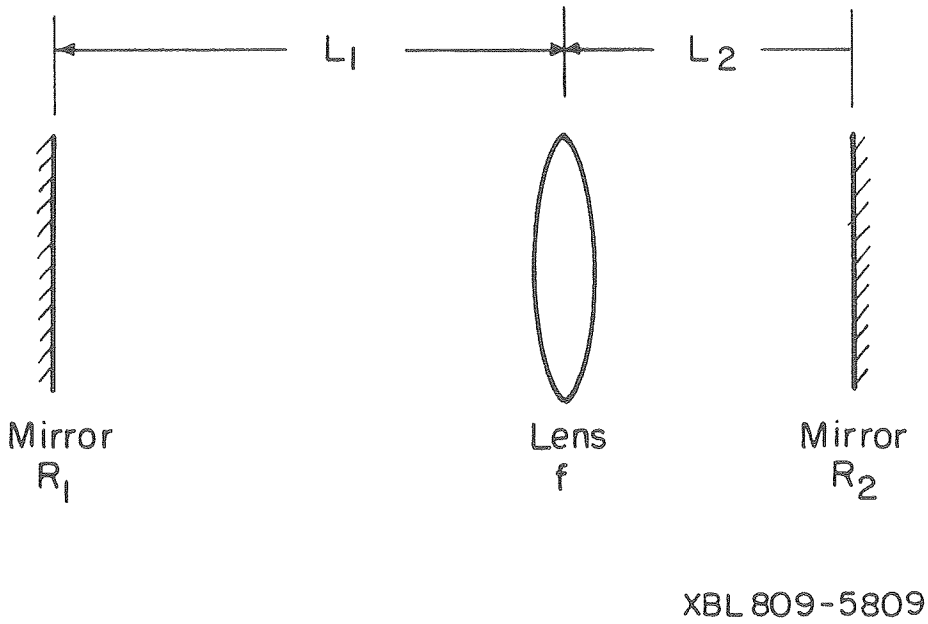

Figure 19

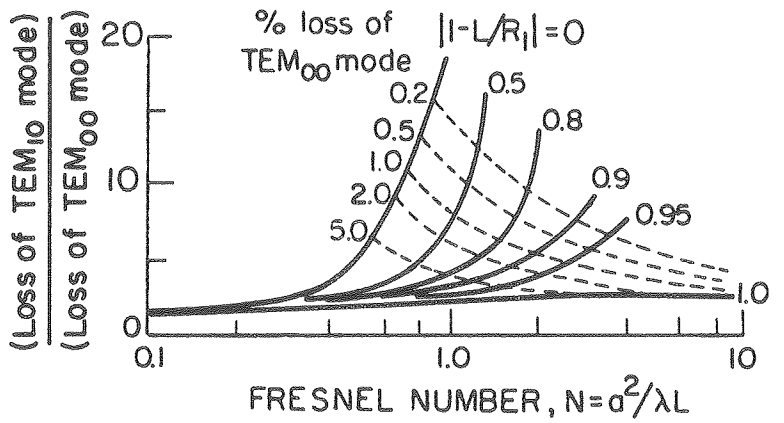

XBL 809-5810

III. ELLIPSE ROTATION INDUCIBLE LOSS

A. Introduction

This section investigates the potential for using self induced ellipse rotation (SIER) as an inducible loss in conjunction with a saturable absorber Q-switch. As SIER in liquid crystals shows particular promise for this application, any model must include the transient nature of liquid crystal response. A computer model doing so was developed and used to study the phenomena. The results as applied to liquid crystals are verified via experiment.

The development of the explicit computer model is lengthy and quite complicated. We summarize here the steps involved to give an overall view of the derivation. The basic equations of the computer model are given in Eq. (78). The ε term, which represents the cavity round trip loss, contains the physics of the model. There are four dominant contributions to ε: SIER induced loss, diffraction loss, transmission through the mirrors, and loss due to the Q-switch dye. The transmission through the mirrors has been discussed previously (Eq. (87)). Determination of the remaining contributions to ε, and the process of converting from physical fields and parameters to the normalized flux and inversion population densities used in the laser rate equations are covered in Sections IIIB-IIID. The highlights of these sections can be seen in the outline below:

IIIB. SIER contribution to ε

1) Use of Jones matrices to determine ellipse rotation
2) Averaging over the spatial variations in ellipse rotation to determine round trip loss due to SIER elements

3) Recommendations on optimal choice of settings for the SIER elements

IIIC. Calculation of cavity diffraction loss

IIID. Loose ends

1) Calculation of cavity loss due to Q-switch dye

2) Expressing physical fields and parameters in terms of the laser rate equations

Finally, Section IIIE presents the finite difference equivalent for the equations developed in IIIB-IIID. Proper values for unspecified initial conditions are determined and the equations are programmed into one computer for analysis.

B. Cavity Loss from SIER

SIER losses are polarization dependent. To handle the mathematics involved, it is convenient to use the technique of Jones matrices. In this technique the polarization is

$$\vec{P} = \begin{pmatrix} P_x \\ P_y \end{pmatrix} \tag{92}$$

where the z axis is along the direction of propagation. Each optical element is represented by a matrix such that

$$(\vec{P}_{out}) = \begin{bmatrix} \text{Jones} \\ \text{matrix} \end{bmatrix} (\vec{P}_{in}). \tag{93}$$

These matrices can be multiplied together to get a cumulative effect for several elements.[30]

A typical experimental setup for SIER induced cavity loss is shown

in Fig. 20. The details of the setup will be provided in the experimental Section IIIF. All that is important here is the sequence of elements a photon would pass through in a round trip. The SIER dependent loss arises from the elements between the pinhole and the 100% 10 m mirror. These elements are traversed in the sequence:

1) GT - Glan prism, passing horizontal polarization
2) FR1 - Fresnel rhomb, angle ϕ_1 between fast axis and horizontal
3) MBBA - MBBA cell, SIER angle $\theta_1 + \theta_2$
4) FR2 - Fresnel rhomb, angle ϕ_2 between fast axis and horizontal
5) MR - 100% mirror, radius of curvature 10 m
6) $\overline{\text{FR2}}$ - See above (4), but angle $-\phi_2$
7) $\overline{\text{MBBA}}$ - See above (3)
8) $\overline{\text{FR1}}$ - See above (2), but angle $-\phi_1$
9) GT - See above (1).

All elements are antireflection-coated except the MBBA cell and the inside surfaces of the Glan prism. The MBBA cell introduces a 4% loss at each face and the Glan prism a 9.4% loss for a single pass. Total round trip loss is $(1 - 90.6 \times 90.6 \times 96 \times 96 \times 96 \times 96) = 30\%$ for the horizontal polarization with no SIER. Of course, all the vertical polarization is reflected by the Glan prism so there is a 100% loss for that polarization. We can calculate the loss with SIER present. The Jones matrix for each element above will be referenced by the abreviations given above (GT, FR1, etc.). The $\hat{x}$ axis is assumed to be on the horizontal. Overall phase factors are ignored.

Some of the Jones matrices are immediate:

$$[GT] = \begin{pmatrix} \alpha_1 & 0 \\ 0 & 0 \end{pmatrix} \qquad \alpha_1 = \sqrt{.906}$$

cont'd

$$[M] = \begin{pmatrix} 1 & 0 \\ 0 & -1 \end{pmatrix} \tag{94}$$

When the fast axis of the Fresnel rhomb lies along $\hat{x}$ then

$$[FR1]' = \begin{pmatrix} 1 & 0 \\ 0 & i \end{pmatrix} = [RET]. \tag{95}$$

The case for the fast axis rotated by ϕ_1 from the horizontal can be obtained from Eq. (95) by a simple coordinant rotation:

$$[FR1] = [-\phi_1]\begin{pmatrix} 1 & 0 \\ 0 & i \end{pmatrix}[\phi_1] \tag{96}$$

where $[\phi]$ is the coordinant rotation matrix for a rotation of angle ϕ.

$$[\phi] = \begin{pmatrix} \cos\phi & \sin\phi \\ -\sin\phi & \cos\phi \end{pmatrix}. \tag{97}$$

By analogy

$$[FR2] = [-\phi_2]\begin{pmatrix} 1 & 0 \\ 0 & i \end{pmatrix}[\phi_2]$$

$$[\overline{FR1}] = [\phi_1]\begin{pmatrix} 1 & 0 \\ 0 & i \end{pmatrix}[-\phi_1]$$

$$[\overline{FR2}] = [\phi_2]\begin{pmatrix} 1 & 0 \\ 0 & i \end{pmatrix}[-\phi_2]. \tag{98}$$

The MBBA cell will rotate the polarization state of incident elliptically polarized light. The size of this rotation depends on both the ellipticity and the intensity of this incident field. While the ellipticity does not change, the intensity does (because of diffraction) be-

tween the first and second passages through the MBBA cell. As a result θ_1, induced by the forward travelling field is usually > θ_2, induced by the backwards travelling field. Forward and backward here refer to before and after reflection by the 100% mirror. Rotation of the polarization by an angle θ is equivalent to a coordinant rotation of $-\theta$. Including the loss at the windows we have

$$[\mathrm{MBBA}] = [\overline{\mathrm{MBBA}}] = [-(\theta_1 + \theta_2)]\alpha_2 \ , \ \alpha_2 = \sqrt{.96} \times \sqrt{.96} = .96. \qquad (99)$$

The α_1, α_2 are transmission factors due to reflection loss. α_1 refers to the Glan prism and α_2 to the MBBA cell. Multiplying the various Jones matrices together, the transmitted SIER fields are given by

$$(\vec{T}) = [\mathrm{GT}][\overline{\mathrm{FR1}}][\overline{\mathrm{MBBA}}][\overline{\mathrm{FR2}}][\mathrm{MR}][\mathrm{FR2}][\mathrm{MBBA}][\mathrm{FR1}[[\mathrm{GT}](\vec{P}_{in}). \qquad (100)$$

The relative magnitude of the output to input fields is given by $|\vec{T}|$ and the polarization of the output field by $\vec{T}/|\vec{T}|$. The equation for the reflected SIER fields $\vec{R}$, is identical to Eq. (100) with the first [GT] replaced by

$$[\mathrm{GT}]' = \begin{pmatrix} \alpha_3 & 0 \\ 0 & 1 \end{pmatrix} \quad \alpha_3 = \sqrt{.094} \qquad (101)$$

where α_3 is the reflection factor for the $\hat{x}$ polarization at the Glan prism. (The $\hat{y}$ polarization is totally reflected.) $|\vec{R}|$ and $\vec{R}/|\vec{R}|$ give the relative magnitude and polarization of these reflected fields. Using [RET] defined in Eq. (95), we expand Eq. (100) as

$$(\vec{T}) = \alpha_2^2[FT][\phi_1][RET][-\phi_1][-(\theta_1 + \theta_2)][\phi_2][RET][-\phi_2][MR]$$

$$\otimes\ [-\phi_2][RET][\phi_2][-(\theta_1 + \theta_2)][-\phi_1][RET][\phi_1][GT](\vec{P}_{in})$$

$$= \alpha_2^2[GT][\phi_1][RET][2(\phi_2 - \phi_1 - \theta_1 - \theta_2)][RET][\phi_1][GT](\vec{P}_{in})$$

$$= [GT]\begin{pmatrix} \cos\chi - i\ \sin 2\phi_1 \sin\chi & i\cos 2\phi_1 \sin\chi \\ -i\ \cos 2\phi_1 \sin\chi & -\cos\chi - i\ \sin 2\phi_1 \sin\chi \end{pmatrix}\begin{pmatrix} \alpha_1\alpha_2^2 Px \\ 0 \end{pmatrix}$$

$$\chi = 2(\phi_2 - \phi_1 - \theta_1 - \theta_2). \tag{102}$$

The setup for our experiment used $\phi_1 = \phi_2 = \phi$ and a brewster cut ruby rod. (Px = 1, therefore.) Equation (102) then becomes

$$(\vec{T}) = [GT]\begin{pmatrix} \cos 2(\theta_1 + \theta_2) + i\ \sin 2\phi\ \sin 2(\theta_1 + \theta_2) \\ i\ \cos 2\phi\ \sin 2(\theta_1 + \theta_2) \end{pmatrix}\alpha_1\alpha_2^2$$

$$= \alpha_1^2\alpha_2^2[\cos 2(\theta_1 + \theta_2) + i\ \sin 2\phi\ \sin 2(\theta_1 + \theta_2)]\hat{x} \tag{103}$$

$$(\vec{R}) = [GT]'\begin{pmatrix} \cos 2(\theta_1 + \theta_2) + i\ \sin 2\phi\ \sin 2(\theta_1 + \theta_2) \\ i\ \cos 2\phi\ \sin 2(\theta_1 + \theta_2) \end{pmatrix}\alpha_1\alpha_2^2$$

$$= \alpha_1\alpha_2^2\alpha_3[\cos 2(\theta_1 + \theta_2) + i\ \sin 2\phi\ \sin 2(\theta_1 + \theta_2)]\hat{x}$$

$$+ \alpha_1\alpha_2^2[i\ \cos 2\phi\ \sin 2(\theta_1 + \theta_2)]\hat{y}. \tag{104}$$

The final [GT] term was retained until the final step to allow $\vec{R}$ to be obtained easily.

Unfortunately, both $\vec{T}$ and $\vec{R}$ are a function of the incident field intensities. The incident field in our case is a TE_{oo} cavity mode, with

the envelope

$$\mathcal{E}(x,y,t) = \mathcal{E}_o(t)e^{-r^2/w^2} \qquad r = \sqrt{x^2 + y^2} \tag{105}$$

where w is the halfwidth of the Gaussian spatial field distribution and the cavity axis is assumed to lie on $\hat{z}$. This means that a unique SIER angle θ cannot be defined. Thus, the net SIER caused transmission or reflection must be an average over the Gaussian profile. Recall from the last chapter Eqs. (49), (52)-(54) with a cell length ℓ.

$$\theta = \frac{\omega\ell\pi\beta}{2cn\tau_M}\left(|E_+|^2 - |E_-|^2\right)e^{-2r^2/w^2}\int_{-\infty}^{t}|\mathcal{E}_o(t')|^2 e^{-(t-t')/\tau_M}\,dt'. \tag{106}$$

The factor $|E_+|^2 - |E_-|^2$ can now be evaluated. After the first passage through FR1, the polarization state is given by

$$\begin{aligned}(\vec{P}) &= [-\phi][RET][\phi]\begin{pmatrix}1\\0\end{pmatrix}\\ &= \begin{pmatrix}\cos^2\phi + i\sin^2\phi\\ \sin\phi\cos\phi(1-i)\end{pmatrix}\\ |E_+|^2 - |E_-|^2 &= \left[\frac{1}{\sqrt{2}}(\hat{x} + i\hat{y})\cdot\vec{P}\right]^2 - \left[\frac{1}{\sqrt{2}}(\hat{x} - i\hat{y})\cdot\vec{P}\right]^2\\ &= \sin 2\phi.\end{aligned} \tag{107}$$

The proper averaging is, of course, done for $|\vec{T}|^2$ and $|\vec{R}|^2$.

$$\langle|T|^2\rangle = \int_0^\infty 2\pi r dr\; e^{-2r^2/w^2}|\vec{T}(r)|^2 \Big/ \int_0^\infty 2\pi r dr\; e^{-2r^2/w^2} \tag{108}$$

$$<|\vec{R}|^2> = \int_0^\infty 2\pi r dr\ e^{-2r^2/w^2} |\vec{R}(r)|^2 \Big/ \int_0^\infty 2\pi r dr\ e^{-2r^2/w^2}. \tag{109}$$

The integration of Eqs. (108) and (109) is straightforward using the substitution

$$r' = e^{-2r^2/w^2} \tag{110}$$

$$\theta_i = \frac{\omega \ell \pi \beta \sin 2\phi}{2cn\tau_M} \int_{-\infty}^{t} |\mathcal{E}_o(t')|^2 e^{-(t-t')/\tau_M} dt' e^{-2r^2/w^2}$$

$$= \theta_i(r = 0) r' \qquad i = 1,2. \tag{111}$$

Using Eqs. (110) and (111), we get immediately

$$<|\vec{T}|^2> = \int_0^1 dr'\ \alpha_1^4 \alpha_2^4 \Big\{ \cos^2(2[\theta_1(r = 0) + \theta_2(r = 0)]r'$$

$$+ \sin^2(2\phi) \sin^2(2[\theta_1(r = 0) + \theta_2(r = 0)]r') \Big\}$$

$$= \alpha_1^4 \alpha_2^4 \left\{ \tfrac{1}{2} + \frac{\sin^2(2\phi)}{2} + \frac{\cos^2(2\phi)}{2} \frac{\sin(4[\theta_1(r = 0) + \theta_2(r = 0)])}{4[\theta_1(r = 0) + \theta_2(r = 0)]} \right\} \tag{112}$$

$$<|\vec{R}|^2> = \alpha_1^2 \alpha_2^4 \alpha_3^2 \left\{ \tfrac{1}{2} + \frac{\sin^2(2\phi)}{2} + \frac{\cos^2(2\phi)}{2} \frac{\sin(4[\theta_1(r = 0) + \theta_2(r = 0)])}{4[\theta_1(r = 0) + \theta_2(r = 0)]} \right\} \hat{x}$$

$$+ \alpha_1^2 \alpha_2^4 \frac{\cos^2(2\phi)}{2} \left\{ 1 - \frac{\sin(4[\theta_1(r = 0) + \theta_2(r = 0)])}{4[\theta_1(r = 0) + \theta_2(r = 0)]} \right\} \hat{y}. \tag{113}$$

The $\alpha_1, \alpha_2, \alpha_3$ are as defined previously. At this point, using experimentally determined data for the Gaussian width w for each passage through the MBBA cell, we can relate $\theta_1(r = 0)$ and $\theta_2(r = 0)$. If we call w_1 and w_2 the halfwidths for the Gaussian spatial distribution at the MBBA

cell, we have for the forward travelling field, just prior to entering the MBBA cell

$$\mathcal{E}(x,y,t) = \mathcal{E}_o^{(1)}(t)e^{-r^2/w_1^2}$$

while the backward travelling field, again just prior to entering the MBBA cell, is given by

$$\mathcal{E}(x,y,t) = \mathcal{E}_o^{(2)}(t)e^{-r^2/w_2^2}.$$

Conservation of energy requires

$$\int_o^\infty 2\pi r dr\ e^{-r^2/w_2^2}|\mathcal{E}_o^{(2)}(t)|^2 = \alpha_2^2 \int_o^\infty 2\pi r dr\ e^{-r^2/w_1^2}|\mathcal{E}_o^{(1)}(t)|^2 \qquad (114)$$

where the α_2^2 factor accounts for reflection loss at the MBBA cell windows. Solving Eq. (114) gives

$$|\mathcal{E}_o^{(2)}(t)|^2 = \alpha_2^2 \frac{w_1^2}{w_2^2} |\mathcal{E}_o^{(1)}(t)|^2.$$

Since $\theta_i(r = 0) \propto |\mathcal{E}_o^{(i)}(t)|^2$, we have

$$\theta_2(r = 0) = \frac{w_1^2}{w_2^2} \alpha_2^2\theta_1(r = 0)$$

$$= .53\theta_1(r = 0) \qquad (115)$$

where we use the experimentally determined values w_1 = .65 mm and w_2 = .86 mm. We can now write

$$\theta_1(r = 0) + \theta_2(r = 0) = 1.53\theta(t)$$

$$\theta(t) = \theta_1(r = 0)$$

$$= \frac{\omega \ell \pi \beta \sin 2\phi}{2cn\tau_M} \int_{-\infty}^{t} |\mathcal{E}_o^{(1)}(t')|^2 e^{-(t-t')/\tau_M} dt'. \tag{116}$$

We cannot study the transient limit until the computer model is fully developed. It is possible to look at the quasi-steady state limit to gain insight into the proper choice of Fresnel rhomb angle ϕ. The values for $<|T|^2>$ and $|T(r = 0)|^2$ are plotted in Fig. 21 as a function of peak intensity I_o incident on the sample for the steady state limit

$$I_o = \frac{c}{8\pi} |\mathcal{E}_o|^2. \tag{117}$$

We display $|T(r = 0)|^2$ primarily for comparison purposes. Previous work on SIER induced cavity loss has used $|T(r = 0)|^2$ instead of the proper $<|T|^2>$,[16] and it is informative to see what effect this had on their calculations.

Careful examination of Fig. 21 shows the important role played by the Fresnel rhomb setting angle ϕ. The setting $\phi = \pi/8$ radians induces the maximum SIER loss for low field intensities. (In low ϕ limit, $\sin\theta \approx \theta$, so loss $\sim \cos 2\phi \sin 2\phi$ which has max at $\phi = \pi/8$.) Despite this fast initial growth in loss as the power increases, the limiting value of $<|T|^2>$ is a relatively high 70-75% (25-30% loss). In contrast, a small angle $\phi = \pi/64$ radians, results in a slower increase in loss as the power increases, but a much higher limiting value (60% loss). Thus, for low cavity intensities it is natural to choose $\phi = \pi/8$ to take ad-

vantage of the rapid initial growth in loss. For higher intensities, it becomes beneficial to reduce ϕ and utilize the greater maximum losses attainable.

The plot of $<|T|^2>$ in Fig. 21a shows an initial region where the SIER induced loss increases monotonically with intensity, an intermediate region where the SIER induced loss ossillates as intensity increases, and a final region where the SIER induced loss remains fairly constant as the intensity increases. To simplify the discussion, we will refer to the first region as the increasing loss regime, to the second region as the oscillating loss regime, and to the third region as the constant loss regime. If the SIER induced cavity loss is to be used for pulse shaping, it is desirable to operate in the increasing loss regime. The reason should be clear. Operating in the oscillating loss regime will introduce temporal structure to (as opposed to smoothly stretching) the pulse. Operating in the constant loss regime not only requires passing through the oscillating loss regime but also defeats the purpose of using an inducible loss. No further increases in loss occur regardless of intensity increases once the constant loss regime is entered.

To insure operation in the increasing loss regime, it is important that an adequately low value of Fresnel rhomb angle ϕ be used. If too large a value is used, then the maximum loss may be insufficient to overcome the gain resulting in increases in intensity sufficient to reach the oscillating or constant gain regimes. If the proper value is chosen, the induced loss will be large enough to neutralize the gain while cavity intensity is still in the increasing loss regime. Since cavity intensity increases when gain > loss, but decreases when gain <

loss, this insures operation only in the increasing loss regime. Now, referring to Fig. 21a once again, we see that sensitivity, that is the loss induced at low cavity intensities, is much greater for $\phi = \pi/8$ radians than that of Fig. 21b where $\phi = \pi/64$ radians. Since the sensitivity is a measure of the effectiveness of the SIER induced losses, it is thus best to chose a Fresnel rhomb angle ϕ small enough to insure operation in the increasing loss regime, but no smaller. The actual choice of ϕ should be experimentally varied until this criterion is met.

Previous work with SIER induced cavity loss (by Murphy and Chang[16]) used a rotating prism Q-switch, with prism rotation so slow that the pulses were nearly free running. The low cavity intensities arising with such a Q-switch technique can only induce relatively small SIER induced cavity losses. Because of the low cavity intensities, two errors made by the authors turned out to be relatively insignificant. The authors assumed that $\phi = \pi/8$ radians was the optimal Fresnel rhomb setting. We have seen that this is true only in the case of low cavity intensities. More important, the authors neglected to spatially average the SIER transmission, using $|T|^2$ on axis as the transmission instead of the correct $\langle|T|^2\rangle$. As seen in Fig. 21a, for low cavity intensities, the difference between $|T|^2$ and $\langle|T|^2\rangle$ is primarily one of absolute values. The qualitative behavior at these low intensities does not differ greatly. Thus, the authors did not detect their errors. For saturable absorber Q-switching, high cavity intensities are common (at least if proper Q-switch dye concentration is used). For this case it is important not to repeat Murphy and Chang's errors (because of the high cavity intensities) and we incorporated into our model both proper spatial averaging ($\langle|T|^2\rangle$) and the necessity of properly choosing the

the Fresnel rhomb angle ϕ.

Using Eqs. (112) and (116), we can specify the fractional round trip SIER loss needed for the laser rate equations

$$\varepsilon_{SIER} = -\ \ell n[<|T|^2>]$$

$$= -\ \ell n\left\{\alpha_1^4\alpha_2^4\left[\tfrac{1}{2} + \frac{\sin^2(2\phi)}{2} + \frac{\cos^2(2\phi)}{2}\,\frac{\sin(6.12\theta)}{6.12\theta}\right]\right\}$$

$$= .36 - \ell n\left[\tfrac{1}{2} + \frac{\sin^2(2\phi)}{2} + \frac{\cos^2(2\phi)}{2}\,\frac{\sin(6.12\theta)}{6.12\theta}\right]$$

$$\theta = \frac{\omega\ell\pi\beta\ \sin 2\phi}{2cn\tau_M}\int_{-\infty}^{t}|\mathcal{E}_o(t')|^2 e^{-(t-t')/\tau_M}dt'. \qquad (118)$$

Equation (118) will be used in Section IIID where the laser rate equations are explicitly modeled.

C. Diffraction Loss

Having specified the experimental setup (see Fig. 20 and Section IIIF for details), it is straightforward to use the procedure outlined in Section IIE along with Figs. 16-19 to evaluate explicitly the cavity diffraction losses. This chapter examines the limit when self focusing may be neglected. In the limit where self focusing becomes noticeable, the substantial changes in the cavity radiation fields must be given consideration. This is done in Chapters IV-VI. In the absence of self-focusing, most of the elements contribute to diffraction loss only via a change in effective cavity length. From Figs. 22 and 23, the change in effective cavity length due to each Fresnel rhomb is (n = 1.51 glass)

$$\delta L = \frac{2(.5\ \text{cm})}{n \tan 35.4^\circ} + \frac{(\sin 54.6^\circ)(1\ \text{cm})}{n \sin 35.4^\circ} - \frac{2(.5\ \text{cm})}{\tan 35.4^\circ}$$

$$- \frac{(\sin 19.2^\circ)(\sin 54.6^\circ)(1\ \text{cm})}{\sin 35.4^\circ}$$

$$= (1\ \text{cm})(\tan 54.6^\circ)\left[\frac{2}{1.51} - 1 - \sin 19.2^\circ\right]$$

$$= -\ 0.01\ \text{cm} \tag{119}$$

which can be ignored when compared to the 1 m cavity length. The MBBA cell, Glan prism, and Q-switch cell each have (Fig. 23)

$$\delta L = \text{cell length}/n$$

$$(\delta L)_{\text{Q-switch}} = 1\ \text{cm}/1.33 - 1\ \text{cm} = -\ .25\ \text{cm} \qquad (n = 1.33\ \text{methanol})$$

$$(\delta L)_{\text{Glan prism}} = 1\ \text{cm}/1.66 - 1\ \text{cm} = -\ .40\ \text{cm} \qquad (n = 1.66\ \text{calcite})$$

$$(\delta L)_{\text{MBBA}} = \ell/1.59 - \ell\ \text{cm} = (\ell)(-\ .37) \qquad (n = 1.59\ \text{MBBA})^{31}$$

$$(\delta L)_{\text{Window}} = .5\ \text{cm}/1.51 - .5\ \text{cm} = -\ .17\ \text{cm} \qquad (n = 1.51\ \text{glass}). \tag{120}$$

Again, these corrections are all small compared to the cavity length, and within the accuracy needs of the calculation can be safely ignored. Likewise, the effect of the ruby rod on effective cavity length will be negligible for reasons similar to those leading to the small δL for the Fresnel rhomb (Eq. 119).

Thus, the only component that should affect the diffraction loss

is the lensing effect of the ruby rod. It has been found that the ruby rod can be approximated by a thin lens when dealing with spatial characteristics of the cavity radiation fields.[18] Thermal effects due to absorption of the pump energy and the cooling water flow induce the lensing. Following the procedure outlined in Fig. 17 and Section IIE, the cavity can be viewed as the two symmetric cavities shown in Fig. 24. Of course, for the two lens cavity of Fig. 24b, the propagation matrix (see Eqs. (80)-84), (89)) is given by

$$\begin{bmatrix} 1 & L \\ 0 & 1 \end{bmatrix} \rightarrow \begin{bmatrix} 1 & L_1 \\ 0 & 1 \end{bmatrix} \begin{bmatrix} 1 & 0 \\ -1/f & 1 \end{bmatrix} \begin{bmatrix} 1 & 2L_2 \\ 0 & 1 \end{bmatrix} \begin{bmatrix} 1 & 0 \\ -1/f & 1 \end{bmatrix} \begin{bmatrix} 1 & L_1 \\ 0 & 1 \end{bmatrix}$$

$$= \begin{bmatrix} 1 - (2L_1 + 2L_2)/f + 2L_1L_2/f^2 & (2L_1 + 2L_2 - 2L_1L_2/f)(1 - L_1/f) \\ -2/f + L_2/f & 1 - (2L_1 + 2L_2)/f + 2L_1L_2/f^2 \end{bmatrix}$$

$$\frac{1}{q^2} = \frac{-2/f + L_2/f + (1 - (2L_1 + 2L_2)/f + 2L_1L_1/f^2)/q_1}{1 - (2L_1 + 2L_2)/f + 2L_1L_2/f^2 + (2L_1 + 2L_2 - 2L_1L_1/f)(1 - L_1/f)/q_1} ,$$

$$\frac{1}{q_1} = \frac{i\lambda}{\pi w_1^2}$$

$$\frac{\lambda}{\pi w_2^2} = \frac{\lambda}{\pi w_1^2} \{1 - (2L_1 + 2L_2)/f + 2L_1L_2/f^2\}^{-2}$$

$$\lim_{w_1 \to \infty} \frac{w_2}{w_1} = 1 - (2L_1 + 2L_2 - 2L_1L_2/f)/f. \tag{121}$$

The numerical values for the resonator parameters necessary to specify diffraction loss are shown on Fig. 24 as well. The experimental setup of Fig. 20 has been used to provide the numerical parameters and the experimentally determined focal length for the ruby rod is used. The diffraction loss can now be determined using Figs. 16 and 18, bearing

in mind the relationship

actual cavity loss = ½ loss of cavity in 24a + ½ loss of cavity in 24b. (122)

The table for various values of pinhole radius a are displayed in Table 2. The fractional round trip cavity loss ε is as before

$$\varepsilon_{DIFF} = - \ln[\text{single pass transmission after diffraction}]. \quad (123)$$

From Table 2, once the aperature size is selected, the diffraction loss ε_{DIFF} can be determined. The experimental setup uses an aperature 1.75 mm in diameter, so

$$\varepsilon_{DIFF} = .06. \quad (124)$$

The choice of pinhole size will be discussed in the experimental Section IIIF.

D. Laser Rate Equations - Computer Model

The necessary equations for establishing a computer model were presented in Section IIE (Eq. (78)). Only the ε needs to be specified. So far, the contribution of the SIER cavity elements and cavity diffraction to ε have been derived. To complete the specification of ε, we need to determine ε for the Q-switch cell.

On the time scale of a Q-switch laser pulse ($\sim$ 10 nsec for our experimental setup), the response time of the saturable absorber Q-switch cell is very small. Because of this, it is customary to treat the loss

as the reciprocal of a step function t = 0.[32] We choose to refine the treatment and use an exponential decay with a time constant equaling the saturable absorber relaxation time.

$$\left(\frac{\text{TRANS}}{\text{PASS}}\right)_{\text{Q-SWITCH}} = \begin{cases} \alpha_2^4 \alpha_4^2 & t < 0 \\ \alpha_2^4 \left(1 - \left(1 - \alpha_4^2\right) e^{-t/\tau_{SA}}\right) & t \geqslant 0 \end{cases} \tag{125}$$

where τ_{SA} = relaxation time for the saturable absorber, α_2 = transmission through an uncoated glass window = .96 (same as α_2 for MBBA cell), and α_4 = transmission through the Q-switch cell due to saturable loss at time lasing beings. In Eq. (125), $1 - \alpha_4^2$ is the saturable loss, which is assumed to decay exponentially. α_4 is not equivalent to the presaturation transmission. Since lasing typically does begin until partial bleaching occurs, α_4 is typically greater than the presaturation transmission. Thus, α_4 will have to be determined experimentally. Using Eq. (125) the fractional round trip loss due to Q-switching is

$$\begin{aligned} \varepsilon_{\text{Q-SWITCH}} &= -\ln\left[\frac{\text{TRANS}}{\text{PASS}}\right]_{\text{Q-SWITCH}} \\ &= \begin{cases} .16 - \ln\left[\alpha_4^2\right] & t < 0 \\ .16 - \ln\left[1 - \left(1 - \alpha_4^2\right) e^{-t/\tau_{SA}}\right] & t \geqslant 0 \ . \end{cases} \end{aligned} \tag{126}$$

With ε specified, we now relate the field strengths $|\mathcal{E}_o(t)|^2$ to the normalized photon density $\tilde{\phi}$. As before, it is important to average over the Gaussian field distribtution to evaluate the average photon density to be used in the laser rate equation

$$\tilde{\phi}(t) = \frac{\sigma c t_R (1 + g_2/g_1)}{2} \phi(t)$$

cont'd

$$= \frac{\sigma c t_R (1 + g_2/g_1)}{2} \left(\frac{<|E|^2>}{8\pi\hbar\omega} \right)$$

$$= \frac{\frac{\sigma c t_R (1 + g_2/g_1)}{2} \frac{1}{8\pi\hbar\omega} \int_0^\infty 2\pi r dr \; e^{-2r^2/w^2} \; 2|\mathcal{E}_o(t)|^2 \; e^{-2r^2/w^2}}{\int_0^\infty 2\pi r dr \; e^{-2r^2/w^2}}$$

$$= \frac{\sigma c t_R (1 + g_2/g_1)}{2} \frac{2|\mathcal{E}_o(t)|^2}{8\pi\hbar\omega} \left(\tfrac{1}{2}\right) \tag{127}$$

where we have used the conversion

$$\frac{1}{8\pi} <|E|^2> = \hbar\omega\phi(t) \;, \quad |E|^2 = 2|\mathcal{E}_o(t)|^2 e^{-2r^2/w^2} . \tag{128}$$

It is now possible to begin evaluating some of the equations developed and casting them into a form that can be used in a computer model. From Eqs. (38), (76), and (118)

$$\theta(t) = \frac{\omega \ell \pi \beta \sin 2\phi}{2cn\tau_M} \frac{16\pi\hbar\omega}{\sigma c t_T (1 + g_2/g_1)} \int_{-\infty}^{t} \tilde{\phi}(t') e^{-(t-t')/\tau_M} dt'$$

$$\theta(\tilde{t}) = \frac{8\pi^2 \hbar\omega^2 \beta \ell \sin 2\phi}{nc^2 \sigma \tau_M (1 + g_2/g_1)} \int_{-\infty}^{\tilde{t}} \tilde{\phi}(\tilde{t}') e^{-(\tilde{t}-\tilde{t}')(t_R/\tau_M)} d\tilde{t}'$$

$$= 8.5 \times 10^{-15} \frac{\ell \sin 2\phi}{\sigma \; e^{2800/T}} \int_{-\infty}^{\tilde{t}} \tilde{\phi}(\tilde{t}') e^{-(\tilde{t}-\tilde{t}')(t_R/\tau_M)} d\tilde{t}' . \tag{129}$$

t_R is, as defined before, the cavity round trip time. From Eqs. (85), (87), (118), (124) and (126), we have

$$\varepsilon = \varepsilon_M + \varepsilon_{SIER} + \varepsilon_{DIFF} + \varepsilon_{Q\text{-}SWITCH}$$

$$= .69 + .36 + .06 + .16 - \left\{ \begin{matrix} \ln \alpha_4^2 \\ \ln \left[1 - \left(1 - \alpha_4^2\right) e^{-\tilde{t}(t_R/\tau_{SA})} \right] \end{matrix} \right\}$$

cont'd

$$- \ln\left[\tfrac{1}{2} + \frac{\sin^2(2\phi)}{2} + \frac{\cos^2(2\phi)}{2}\,\frac{\sin(6.12\theta(\tilde{t}))}{6.12\theta(\tilde{t})}\right] \tag{130}$$

where $\left\{\begin{matrix} t < 0 \\ t \geqslant 0 \end{matrix}\right\}$ is implied by the use of brackets. We convert the behavior at $t = 0$ into an initial condition on $\tilde{n}(\tilde{t})$, $\varepsilon(t)$

$$n_o = \tilde{n}(\tilde{t} = 0) = 1.27 - \ln\left(\alpha_4^2\right) - \ln\left[\tfrac{1}{2} + \frac{\sin^2(2\phi)}{2} + \frac{\cos^2(2\phi)}{2}\,\frac{\sin(6.12\theta(0))}{6.12\theta(0)}\right]$$

$$\varepsilon_o = \varepsilon(\tilde{t} = 0) = n_o. \tag{131}$$

For convenience we present here the laser rate Eq. (78)

$$\frac{d\tilde{n}(\tilde{t})}{d\tilde{t}} = -\,2\tilde{n}(\tilde{t})\tilde{\phi}(\tilde{t})$$

$$\frac{d\tilde{\phi}(\tilde{t})}{d\tilde{t}} = \tilde{\phi}(\tilde{t})(\tilde{n}(\tilde{t}) - \varepsilon(\tilde{t})) \tag{132}$$

with θ and ε given by Eqs. (129) (130), using the initial conditions in Eq. (131) and a small seed $\tilde{\phi}(\tilde{t} = 0) = \phi_o$ to represent spontaneous emission.

Equations (129)-(132) represent the proposed model for calculating the dynamic effects of SIER induced loss in a laser cavity. The numerical solution of this model is the topic for the next section.

E. Computer Results

To be used in a computer calculation, the model from the last section must be cast as finite difference equations. We define a subscript i to refer to $\tilde{t} = i\Delta t$ where Δt is the step size for the finite differ-

ence calculation. The conversion of the differential and integral equations is straightforward.

$$\tilde{n}_i = (1 - 2\tilde{\phi}_{i-1}\Delta t)\tilde{n}_{i-1}$$

$$\tilde{\phi}_i = [1 + (\tilde{n}_{i-1} - \varepsilon_{i-1})\Delta t]\tilde{\phi}_{i-1}$$

$$\varepsilon_i = 1.27 - \ln\left[1 - \left(1 - \alpha_4^2\right)\exp\left(- i\Delta t \frac{t_R}{\tau_{SA}}\right)\right] - \ln\left[.5 + \frac{\sin^2(2\phi)}{2} + \frac{\cos^2(2\phi)}{2} \times \frac{\sin(6.12\theta_i)}{6.12\theta_i}\right]$$

$$\theta_i = \left[\theta_{i-1} + 8.5 \times 10^{-15} \frac{\ell\sin(2\phi)}{\sigma\exp(2800/T)} \tilde{\phi}_{i-1}\Delta t\right]\exp\left(- \Delta t \frac{t_R}{\tau_M}\right)$$

$$\theta_o = 8.5 \times 10^{-15} \frac{\ell\sin(2\phi)}{\sigma\exp(2800/T)} \frac{\tau_M}{t_R} \phi_o$$

$$\mathcal{E}_o = 1.27 - \ln\left(\alpha_4^2\right) - \ln\left[.5 + \frac{\sin^2(2\phi)}{2} + \frac{\cos^2(2\phi)}{2} \frac{\sin(6.12\theta_o)}{6.12\theta_o}\right]$$

$$\tilde{n}_o = \mathcal{E}_o$$

$$\phi_o = \text{Small Seed Value.} \tag{133}$$

The parameter α_4^2 can be determined by measuring the increased pump energy necessary for lasing. This increase will give the inversion population density when lasing begins as compared with the inversion population for free running threshold (methanol only in the Q-switch cell), and thus determines α_4^2. For our setup, we found $\alpha_4^2 = .61$. The only parameter still unknown is the stimulated emission cross section σ.

Previous work has shown the laser rate equations work extremely well in predicting the dynamic behavior of a Q-switch laser pulse with no inducible loss.[18] Thus, we choose σ to be the value that allows the computer predicted cavity intensity with $\ell = 0$ in Eq. (133) to agree with experimental observations. $\sigma = 2.83 \times 10^{-19}$ cm^2 was the value determined to give the correct cavity intensities. This value agrees with known values for σ. The pulse width predicted was 70 nsec, which agrees with experiment, confirming that the choice $\alpha_4^2 = .61$ was proper. We display the computer calculations in the absence of MBBA (sample length $\ell = 0$) in Fig. 25. The pattern used for Fig. 25 will be used to display the results for all the computer calculations in this section.

a) On axis cavity intensity; 2 MW/cm^2 per division.

b) Normalized inversion population density, $\tilde{n}$;

   Fractional cavity round trip loss, ε; .5 per division.

c) On axis SIER angle; $\pi/4$ radians per division.

d) On axis intensity for the horizontally and vertically polarized light reflected out of the cavity by the Glan prism .2 MW/cm^2 per division.

Horizontal scale: 50 nsec per division.

As expected, Fig. 25 shows no SIER induced loss and a cavity intensity of 16 MW/cm^2. The curves in Fig. 25d represent the fields that can be easily measured, and are presented for later comparison with experiment. With no SIER induced loss, there is no vertically polarized reflection from GLAN prism, and the horizontal reflection follows accurately the cavity intensities.

To properly study the effects of SIER inducible loss from MBBA, several parameters must be varied, and the effects studied. The key

parameters in our experiment were:

1) Sample length; 1 cm reference

2) Sample temperature; 60°C reference

3) Fresnel rhomb angle; 15° reference

4) Transmission through saturable loss element; .61 reference

5) Saturable absorber relaxation time; 4×10^{-11} sec reference.

We assume the reference values are used unless a different value is stated explicitly. Figures 26-28 show the effects of increasing sample length from 1 cm to 5 cm. With a one cm sample length, significant ellipse rotation is induced ($\theta \approx \pi/4$ - Fig. 26c). However, the induced loss peaks after most of the population inversion is depleted (Fig. 26b) resulting in only mild effects on the cavity intensity, which is 30% smaller, and slightly stretched in the trailing edge. In contrast, the ellipse rotation max ($\theta \approx 3\pi/8$ - Fig. 28c) for a 5 cm cell though not much larger, occurs when the population inversion is still substantial (Fig. 28b). For this case, the cavity intensity shows a 75% reduction in intensity and dramatic stretching of the pulse (Fig. 28a). The pulse itself shows an exponentially decaying tail after an initial rapidly damped oscillatory behavior. This oscillation is typical of transient response to a rapidly rising driving force. There is an initial overshoot followed by damped oscillations to the "proper" response. The damping rate depends on the viscosity, which for MBBA is quite high. The counterpart to cavity intensity can be seen in Fig. 28b where one sees that the loss also shows a rapidly damped oscillatory section leading to a steady state condition with the loss just slightly above the gain(normalized population inversion). Both the loss and gain decay slowly to the steady state (no inducible contribution) value of 1.27.

Figure 27 shows behavior intermediate between that of Figs. 26 and 28.

Comparing Figs. 25b and 28b, one sees that the final inversion population is much lower when sample length = 0 than when sample length = 5 cm. In fact, since relative population inversion density change measures how much total energy is released, the cavity with 5 cm of MBBA will only emit less energy than a cavity with no MBBA would emit. The remaining energy is dissipated as heat in the laser active material. Figure 28b shows clearly that for long MBBA sample length the final normalized population inversion density

$$\tilde{n}_f \to \bar{\varepsilon} \tag{134}$$

where $\bar{\varepsilon}$ is the fractional round trip cavity loss after the Q-switch dye bleaches and excluding any SIER induced loss. We can determine analytically the ratio of energy released for case of Eq. (134) and the case with no liquid crystal present. Using Eq. (132) (dividing bottom equation by top equation) we have

$$\frac{d\tilde{\phi}}{d\tilde{n}} = \tfrac{1}{2}\left(\frac{\varepsilon}{\tilde{n}} - 1\right) \tag{135}$$

with no MBBA present, ε can be replaced by the constant $\bar{\varepsilon}$ to give

$$\tilde{\phi} - \tilde{\phi}_o = \tfrac{1}{2}\left[\bar{\varepsilon}\ \ell n \frac{\tilde{n}}{\tilde{n}_o} - (\tilde{n} - \tilde{n}_o)\right]. \tag{136}$$

Since $\tilde{\phi}_o$ is very small, we have for large time

$$\tilde{\phi} = \tfrac{1}{2}\left[\bar{\varepsilon}\ \ell n \frac{\tilde{n}}{\tilde{n}_o} - (\tilde{n} - \tilde{n}_o)\right] \to 0$$

cont'd

$$\frac{\tilde{n}_f}{\tilde{n}_o} = e^{\tilde{n}_f - \tilde{n}_o/\bar{\varepsilon}} . \tag{137}$$

Then, knowing $\tilde{n}_o/\bar{\varepsilon}$ we can solve for $\tilde{n}_f$. The ratio of energy released is then

$$\frac{E_{output(MBBA)}}{E_{output(No\ MBBA)}} \rightarrow \frac{\tilde{n}_o - \bar{\varepsilon}}{\tilde{n}_o - \tilde{n}_f} \tag{138}$$

in limit of long MBBA sample where $\tilde{n}_f$ is given by Eq. (134). For our experimental setup, we have $\bar{\varepsilon} \approx 1.27$, $\tilde{n}_o \approx 1.7$, which gives $\tilde{n}_f \approx .92$. Thus, the limit (Eq. (138)), for our case is $\approx .55$. In conclusion, we summarize the effects of increasing MBBA sample length:

1) Energy output decreases asymtotically to a limiting value for long cell lengths. This energy decrease is given by Eqs. (137) and (138).
2) Trailing edge first stretches, then shows oscillations, then shows damped oscillations followed by slow exponential decay.
3) Max ellipse rotation rapidly reaches value of $\pi/4$ then slowly increases to $3\pi/8$.
4) Cavity intensity drops so total energy in pulse follows 1) above.

Next, we consider the effects of varying sample temperature. As temperature is varied, two competing effects occur, to a large extent offsetting one another. Recall from Chapter II that both the relaxation time and the nonlinear constants diverge as $T \rightarrow T^*$. The divergence of the nonlinear constants leads to a larger steady state ellipse rotation while the divergence in relaxation time leads to a slower response to the laser pulse. In the transient case, these effects tend to cancel.

In Eq. (129), for example, the critically divergent parts of β and τ_M cancel, leaving terms that are much less sensitive to temperature changes. The behavior outside the cavity where the induced ellipse rotation does not affect the input field can be seen in Fig. 29. Both the steady state and transient response are shown. A Gaussian input with half width of 35 nsec is assumed for Fig. 29, and the values shown for the transient response are from Eq. (129) at $\tilde{t} = 0$. Though the behavior inside the cavity may vary slightly from Fig. 29, it is best to use the behavior of a known case to extrapolate to the unfamiliar. In this case, we see that the transient conditions change the critically divergent behavior as $T \to T^*$ to a behavior showing only mild increases in nonlinear response at $T \to T^*$. We expect similar behavior inside the cavity, with peak ellipse rotation being mildly greater at T = 50° than at T = 70°.

The computer calculations are shown in Figs. 30-33 and support the expectations. Comparing Figs. 30 and 31, we see that the induced SIER angle is slightly greater at T = 50°C than at 70°C. Yet, we also see that the smaller induced cavity loss at T = 70°C has the larger effect on cavity intensity. The cause behind this can be seen in Figs. 30b and 31b. At 50°C, the cavity loss remains high until the population inversion has been depleted. The large loss causes a steep trailing edge, much like the effect seen in cavity dumping. At 70°C, the shorter relaxation time allows the induced cavity loss to decay more quickly. The population inversion is still present as the loss is decreasing, with the result that the cavity fields do not decay as quickly leading to the stretching of the trailing edge. The actual release of energy from the laser active material is slowed by SIER induced loss. A mea-

sure of this slowing is the peak cavity intensities. For 50°C and 70°C the peak intensities are comparable, as expected, since the nonlinear responses are comparable. The energy remaining in the laser active material after the peak cavity intensity is reached is therefore not greatly different at T = 50°C and T = 70°C. The release of this remaining energy depends strongly on the relaxation time of the MBBA. For long relaxation times (T = 50°C), the induced loss stays high long enough so that the cavity intensities decay completely, leaving the remaining energy in the laser active material. For short relaxation times (T = 70°C), the induced loss decays quickly enough so that the cavity fields remaining when the loss drops are sufficient to extract the stored energy via stimulated emission, which appears in the form of a stretched trailing edge.

The situation for a 2.5 cm sample length is similar but magnified, as seen in Figs. 32 and 33. Again, the release of energy is slowed by the SIER induced loss. The greater loss for 2.5 cm of MBBA leads to smaller peak intensities. As for the 1 cm sample, the basic nonlinear response as measured by this peak intensity reduction does not differ much between T = 50°C and T = 70°C. The release of the energy left in the active medium after the peak intensity is reached determines the shape of the trailing edge. For T = 70°C, as before, the short relaxation time leads to a release of this energy as the cavity intensities fall, leading to a stretching of the trailing edge (Fig. 33a). For 50° C, the long relaxation time prevents any release of this energy until after the cavity intensities have decayed. With a 2.5 cm sample, unlike the 1 cm sample, enough energy remains in the active material to generate a second pulse once this induced loss does decay (Fig. 32a).

We summarize here the effects of temperature variation:

1) The basic nonlinear response as measured by reduced peak intensity or energy left in the laser active material at peak intensity depends only weakly on sample temperature.

2) The release of the stored energy remaining after the peak depends strongly on temperature. This dependence is purely due to the change in response time of the MBBA.

3) For short relaxation times, the energy will be released as the cavity intensities fall leading to a broadened pulse.

4) For long relaxation times, the energy will be released as a second pulse delayed by $\sim \tau_M$ from the first.

5) Intermediate relaxation time will show a mixture of 3) and 4).

Next, we turn to the third parameter-Fresnel rhomb setting. Much of the discussion on effects of the Fresnel rhomb setting have been discussed previously in Section IIIB, where the implications of round trip transmission through the SIER elements was considered (Fig. 21 and discussion thereof). Observations made in that section are fully supported by the computer calculations. The behavior for strong response (i.e., long sample length) can be seen in Figs. 35 and 35. At a 15° Fresnel rhomb setting, the inducible loss varies monotonically with cavity intensities. The maximum inducible loss is sufficient to insure that the loss remains in this monotonic regime. As a result, the loss quickly reaches a steady state condition with a value just slightly larger than the gain (Fig. 34b). The cavity intensity shows a small peak quickly settling into a long exponential tail, reflecting the slow release of energy stored in the laser active material. The small limiting peak intensity and long pulse length are an indication of effective use of

SIER for pulse shaping. In contrast, at a 22.5° Fresnel rhomb setting, the maximum loss is insufficiently large to limit cavity intensity to the regime where the inducible loss varies monotonically with cavity intensity. Instead, the loss rapidly enters the oscillatory regime (Figs. 21 and 35b), greatly reducing the effectiveness of the inducible loss in pulse shaping. This can be seen clearly in Fig. 35a, where the peak height is larger and the pulse length much smaller than that seen for a 15° Fresnel rhomb setting (Fig. 34a).

The behavior for weak response (i.e., short sample length) can be seen in Figs. 36 and 37. Here we find that even for a 22.5° Fresnel rhomb setting, the loss is weak enough so that the attainable cavity intensity is insufficient to drive the loss past the regime where the inducible loss varies monotonically with cavity intensity. Both the 22.5° setting and 7.5° setting result in operation in the monotonic regime. Since both settings allow operation in the same regime, one expects the larger effect for a Fresnel rhomb setting of 22.5°, where the induced loss grows more quickly with increasing cavity intensity than any other Fresnel rhomb setting. (Figure 21, Eqs. (111) and (112) - for weak response, $\theta \approx \sin\theta$ so loss $\sim \sin 2\phi \cos 2\phi$ which has max at $\phi = 22.5°$.) This is verified by the computer calculation where the peak height is lower and the pulse longer for a Fresnel rhomb setting of 22.5° (Fig. 37a) than for a Fresnel rhomb setting of 7.5° (Fig. 36a).

We summarize the effects of Fresnel rhomb setting angle:

1) For weak response, a 22.5° Fresnel rhomb setting is optimal, taking full advantage of the larger initial inducible losses.
2) As response becomes stronger, it is necessary to decrease the Fresnel rhomb setting and use the larger maximum losses thus

available to restrict operation to the regime where induced losses vary monotonically with cavity intensity. Failure to do this severely reduces the effectiveness of SIER inducible loss pulse shaping.

3) Further reduction in Fresnel rhomb setting beyond what is needed for 2) merely reduces the induced loss and thus the effectiveness of SIER inducible loss pulse shaping. This reduction is smooth, and is thus a convenient method of changing the amount of pulse stretching from no stretching at a setting of 0° to same maximum stretching at the setting determined by 2) above.

We now deal with the fourth parameter-transmission through the saturable loss element, as lasing starts. Varying this parameter is effectively varying the inversion population density at the onset of lasing action. (Gain is determined by population inversion and equals loss at the instant lasing action starts.) Physically, this parameter (α_4^2 in Eq. (133)) is varied by changing the concentration of the saturable dye Q-switch solution. The more concentrated the dye solution, the greater the intensities needed for bleaching, thus allowing more population inversion to build up before lasing starts. Analysis for this section is complicated by the fact that changes in α_4^2 affect both the laser behavior with MBBA present and the laser behavior with no MBBA present. Therefore, it is the difference in laser performance with and without MBBA present that has significance. The computer calculations when MBBA is absent from the cavity are seen in Figs. 38 and 40. The corresponding calculations when MBBA is present are seen in Figs. 39 and 41. Figures 38 and 39 represent a Q-switch concentration weaker than the

actual experimental concentration, while Figs. 40 and 41 represent stronger than actual experimental Q-switch concentration.

Comparing Figs. 38 and 39, one finds that the presence of MBBA limits cavity intensity to half that seen in its absence. The pulse length is longer, as well. The stretching seen here is quite similar to that seen in Fig. 33 for a 70°C sample. Relatively mild SIER angles occur ($\pi/4$ maximum). Comparing Figs. 40 and 41, one finds that the presence of MBBA limits cavity intensity to one-third that seen in its absence. The pulse dynamics show behavior that is quite similar to that seen in Fig. 32 for a 50°C sample. In Fig. 41, the second pulse has not fully developed, but the tendency towards formation of a second pulse is seen quite clearly. Large SIER angles occur ($\pi/2$ maximum), indicating substantial SIER losses. The results of our examination of Figs. 38-41 are summarized below:

1) In the absence of MBBA, increasing the Q-switch concentration results in greater peak intensities and shorter pulse lengths.
2) The effects that changing the Q-switch concentration has on laser behavior with MBBA present, are largely due to 1) above.
3) For higher Q-switch concentrations the higher cavity intensities lead to greater SIER induced losses, delaying the release of energy from the laser active material much as increased cell length would. This increases the relative pulse stretching though the absolute pulse length is not any greater (due to the shorter initial pulse length).
4) The energy stored due to 3) above for higher Q-switch concentrations, is released in a fashion that is similar to the case where the MBBA was at 50°C. In this case, the shorter initial

pulse length due to higher Q-switch concentration is equivalent to the longer response time due to lowering the temperature.

5) For lower Q-switch concentration, the opposite of 3) and 4) above occurs.

The final parameter to be studied is the saturable absorber relaxation time. The computer calculations for a 400 nsec relaxation time can be seen in Figs. 42 and 43. The analysis is quite simple once we observe that though the pulse is delayed somewhat, its shape is almost identical to that observed in Figs. 38 and 39. The obvious conclusion, of course, is that effects of increased Q-switch response time are equivalent to the effects of decreased Q-switch concentration.

The computer model for SIER induced pulse shaping using MBBA has been thoroughly analyzed at this point. We will present experimental data supporting these calculations in the following section. Before concluding this section though, we wish to make use of the formalism developed for MBBA and transient response to evaluate a hypothetical quasi-steady state SIER inducible loss. This hypothetical material will simply be MBBA with $\tau_M \rightarrow 0$ replacing the true τ_M. The model developed in this section can then be used directly to calculate the expected behavior.

The results for a 2.5 cm sample length and a 10 cm sample length are shown in Figs. 45 and 46. Figure 44 shows the previously calculated behavior for a 2.5 cm sample length with the actual τ_M (Fig. 27) redrawn with a different time scale for easier comparison. In performing the calculations, the previously described reference values were used for all other parameters. Figures 44 and 45 can be compared to determine the difference between a transient and a steady state SIER induc-

ible loss. The steady state case is basically the same as the transient case, except that the initial peak and subsequent oscillations disappear. Instead, the cavity intensity peaks at a lower value progressing immediately to an exponential like decay. Physically, the steady state and transient cases can be viewed as overdamped and underdamped regimes of the same basic loss mechanism.

As we increase the sample length to 10 cm, we notice a very pleasant phenomena (Fig. 45). The maximum SIER angle only increases slightly with the result that cavity intensity is limited to a value that is one fourth the value observed for a 2.5 cm sample length. The pulse length stretches by a comparable amount. This is exactly the behavior desired for pulse shaping. The basic shape of the pulse remains the same as cell length changes. The energy released in a pulse also remains fairly constant. Under such conditions, the pulse length can be changed substantially through changes in the limiting peak cavity intensity, while the pulse shape after such changes remaining completely predictable. In order to determine the best way to set the peak cavity intensity, the relevant calculations done above for the transient limit have been repeated for the steady state limit. The results are essentially the same as found before, with any changes attributable to the damping of the transient oscillations. (Just like Fig. 45 is essentially the same as Fig. 44 with the initial oscillations damped.) Thus the conclusions drawn about how each of the important parameters affects cavity intensity remain valid and may be applied to the steady state limit.

F. Experimental Results

Figure 20 depicts the experimental setup. A brewster cut ruby rod

(¼" × 4") oriented to lase in the horizontal polarization, was used for the laser active material. Two linear flashlamps provided pumping. These flashlamps were located at the two outer foci of a double ellipse reflector, with their output focused onto the ruby rod located at the center focus. Water jackets about the flashlamps and the rod allowed flowing water cooling. We used crypto cyanine as the saturable dye for Q-switching the laser. Different pinholes were tried, to determine the largest aperature size which could be used, that would consistently result in the fundamental (TE_{oo}) cavity mode. We found that a 1.75 mm diameter pinhole worked best. The laser resonator was formed using a 100% mirror with a 10 m radius of curvature (which we will often refer to as the "back" mirror) and a 50% resonant reflector (which we may refer to as the "front" mirror). Naturally, the resonant reflector is flat. Transmission through the resonant reflector provides the normal means of extracting laser energy. References to laser output are references to the fields leaving the resonator via this route. These fields are monitored using a fast photodiode (200 psec rise time) with a Tektronic 519 oscilloscope (300 psec rise time).

The elements between the pinhole and the back (100%) mirror comprise the SIER elements. From left to right in Fig. 20 we have an air spaced Glan prism, a Fresnel rhomb, the MBBA sample, and a second Fresnel rhomb. The Glan prism serves the dual purpose of defining a definite polarization state and rejecting the polarization component induced through ellipse rotation. The Glan prism was oriented to pass horizontally polarized light, to match the output from the laser active material. We chose to use a Glan prism over other polarizers because high optical quality and resistance to damage were well suited for use inside

a laser cavity. The outside faces of the prism were anti-reflection coated to minimize insertion losses. The requirement of high damage threshold required the use of the airspace configuration to avoid the need for cements. Though this caused higher insertion losses (due to the internal air-prism interfaces), the presence of the horizontal polarization as well as the vertical polarization in the rejected beam from the Glan prism was useful in that we could better determine the actual cavity intensities. As shown in Fig. 20, the vertically and horizontally polarized fields leave the Glan prism spatially separated, allowing us to easily monitor both polarizations simultaneously. Both polarizations were detected using fast photodiodes (200 psec rise time) with matched detector surfaces to simplify comparisons. For the horizontally polarized beam, the photodiode output was measured with a Tektronix 519 scope (300 psec rise time). For the vertically polarized beam, the photodiode output was measured with a Tektronix 7904 scope (1 nsec rise time). Though the 7904 was a slower scope, the variations in maximum vertically polarized intensity required the use of an adjustable scope.

As determined in Section IIC, the induced ellipse rotation depends on the ellipticity of the incident fields (Eqs. (51)-(53)). Basically, any retarder following the Glan prism will provide the required elliptical polarization. The most readily available of the high quality retarders is the Fresnel rhomb, which is what we use. Varying degrees of ellipticity can be obtained by rotating the fast axis around the direction of propagation. The entrance and exit faces are antireflection coated to minimize insertion losses.

The second Fresnel rhomb serves to neutralize the effects of the

first Fresnel rhomb. The desired setting for this rhomb is such that with no ellipse rotation the SIER elements leave the fields horizontally polarized. Using Eq. (102), we see that this condition requires that

$$\sin[(\phi_2 - \phi_1)2] = 0 \tag{139}$$

which is satisfied by the choice

$$\phi_2 = \phi_1 \pm k\frac{\pi}{2} \quad , \quad k = 0, 1, 2, \ldots . \tag{140}$$

Conventional SIER setups use k = 1. However, for our purposes, the choice k = 0 proves more useful. This choice allows us to use the second Fresnel rhomb to compensate for the beam displacement due to the first Fresnel rhomb (see Fig. 20). This way, we can vary the Fresnel rhomb settings without the need to reposition optical elements.

Our MBBA sample was placed in a glass cell which was then sealed under a nitrogen atmosphere. Samples prepared in this fashion showed no change in the isotropic nematic transition temperature over a period of many months. This stability indicates that little if any deterioration of the MBBA occurs over that time period. Sample temperature was maintained by use of a copper oven. Heating was controlled by a Yellow Springs temperature controller via ohmic heating. Temperature stability was maintained to .1°C. Sample length changes were achieved by changing cells. Cell orientation was carefully maintained so that the cell windows were perpendicular to the direction of propagation so as to introduce as little pertrubation as possible to the wavefront entering the sample.

Our laser operated reliably in a single TE_{oo} transverse mode. Longitudinal mode selection was not as reliable, with occasional instances of lasing in two adjacent modes. Such instances produced a very distinctive beating pattern in the laser output and were very easily rejected during analysis. With no liquid crystal present, 2.2 mj were emitted in a 70 nsec pulse. This corresponds to a saturable dye concentration such that round trip transmission through the Q-switch cell due to saturable absorber is 61% at the instant lasing starts. (This can be measured via the increased pump energy needed to compensate for insertion of the cell.) The choice of concentrations was severely limited by large insertion losses that accompany introduction of the SIER elements into the laser cavity. This raised the lasing threshold sufficiently to require a reduction Q-switch dye concentration from its normally higher value. As seen in the previous section, this choice of α_4^2 is actually better for our purposes than the standard choice. Further reductions in concentration were undesirable as they led to double pulsing which complicated the analysis.

The output of PD3 (see Fig. 20) was used to monitor laser performance. The output of PD1 and PD2 were recorded on polaroid film for permanent records. These photographs can be compared with the computer predictions (part d of Figs. 25-28, 30-46) to determine how well the experimental results support the theoretical calculations.

Most of the parameters discussed in the previous theoretical section remain important for experimental work. However, not all these parameters are freely variable. The decision to work with MBBA, the restrictions on Q-switch dye concentration (discussed above), and other laser constraints limit us to three free parameters: sample length, sam-

ple temperature and Fresnel rhomb setting. Experimental data revealed that the Fresnel rhomb angle ϕ_1 was a somewhat redundant parameter. Small angles were equivalent to small sample lengths. Large angles could not be used because the maximum value of induced loss was insufficiently large to insure operation in regions where inducible loss increased monotonically with intensity. Thus it was decided to treat ϕ as a set up parameter, that is, we would determine the best value of ϕ for our system and use that value to gather the remainder of the data. ϕ for our laser system was optimal at $\phi = 15°$.

The remaining parameters, sample length and temperature were varied systematically over reasonable values ($0 <$ sample length < 5 cm; $45° < T < 70°C$). The fields rejected by the Glan prism were recorded for each set of values. In Fig. 47 can be seen some of this data. We chose to display only the data for which we have shown matching theoretical predictions. The sequence 47a, 47c, and 47d shows the effects of changing sample length as temperature is held constant. The sequence 47b, 47c, and 47e shows the complimentary effects of changing temperature while holding sample length constant. These figures (47a-e) should be compared to their theoretical counterparts (25d, 32d, 27d, 28d, 33d respectively). The excellent qualitative agreement should be noted. This agreement gives us confidence that the model developed can be used to predict qualitative behavior.

With good qualitative agreement, there is always the temptation to draw quantitative conclusions. We wish to caution the reader against this here for the following reasons:

1) The computer theory blatantly ignores the discrete location of cavity elements and for the large part, spatial dependence of

the cavity fields. Though certain spatial features had to be accounted for to give reasonable results (such as spatially averaging the SIER transmission), the underlying laser rate equations still assume infinite plane waves. Our modifications have greatly improved the utility of the laser rate equations when applied to SIER induced loss but cannot totally eliminate inaccuracies due to the basic assumptions of the laser rate equations themselves.

2) Self focusing has been totally neglected. As will be seen in Chapters IV-VI, self focusing is important for sample lengths $\gtrsim$ 1 cm when the sample is in the laser cavity.

In regards to 2) above, we point out that self focusing made it impossible for us to determine an absolute intensity for Figs. 47b-e. Instead, it was necessary to normalize the experimental peak intensity to the calculated value — all the more reason not to make quantitative comparisons. Of course, the intensity scale for Fig. 47a is exact since there was no MBBA present to complicate matters.

G. Conclusions

In this chapter we have developed a computer model to describe SIER inducible loss in a laser cavity. In the model, we attempted to correct for the omissions found in previous models such as transient response and proper averaging of the SIER transmission. The results of the model show excellent qualitative agreement with experiment. Quantitative agreement was not possible due to complications caused by self focusing. A combined self focusing, SIER theory would have required several orders of magnitude larger computing facilities and much too

much programming development to be practical for this piece of work.

Despite the lack of quantitative comparisons, the excellent qualitative agreement shows that the model is useful as a tool to predict what materials and what values each of the experimental parameters should take to provide the optimal effects. The most important conclusions are summarized below:

1 a) In MBBA, changes in temperature have little effect on pulse stretching.

b) Steady state Kerr liquids provide much more effective stretching for the same $\chi^{(3)}$. This coupled with a) means that steady state materials should be used.

2) Fresnel rhomb settings must be experimentally optimized for the particular setup chosen. Particular care must be taken not to use too large a setting.

3) Q-switch liquid concentration must be chosen to match the results desired. Varying Q-switch concentration can be a means to vary pulse stretching.

The final point to be mentioned is the use of both a saturable absorber and an inducible absorber to "clamp" the output intensity. The calculations show that a prohibitively long cell length is needed to generate inducible losses from SIER at intensities near those necessary to bleach cryptocyanine. It is possible that other laser systems using higher bleaching intensity saturable absorbers could show this effect. In particular, the dyes used for Nd lasers meet this criteria. It would be an interesting experiment to combine such a saturable dye with CS_2, for example, inside a SIER setup. The reader is warned that a much more sophisticated Q-switch model than used in this chapter would be needed.

Figure Captions

Table 2. Chart of various diffraction losses for our experimental set-up at different aperature sizes.

Fig. 20. Experimental setup for the ellipse rotation inducible loss experiment.

Fig. 21. Round trip transmission through the SIER cavity elements in the steady state limit. Both the unaveraged and the averaged values are shown. ϕ is the Fresnel rhomb angle, T is the temperature, T^* is the isotropic to nematic transition temperature, and L is the sample length. The sample is MBBA.

Fig. 22. Parameters for calculating the change in optical path length due to the presence of a Fresnel rhomb.

Fig. 23. Replacement of a medium of index of refraction n_2 by an equivalent medium of index of refraction n_1, showing how the n_2 material shortens the effective cavity length ($n_2 > n_1$).

Fig. 24. Equivalent symmetric cavity for the experimental area of Fig. 20. The relevant resonator parameters are calculated.

Fig. 25. Computer calculations, no MBBA.

Fig. 26. Computer calculations, MBBA sample length = 1 cm.

Fig. 27. Computer calculations, MBBA sample length = 2.5 cm.

Fig. 28. Computer calculations, MBBA sample length = 5 cm.

Fig. 29. Comparison of steady state and transient response of MBBA as a function of sample temperature. Curves are normalized to the response at 80°C and show the absence of critical divergence in the transient case.

Fig. 30. Computer calculations, MBBA sample length = 1 cm, sample temperature = 50°C.

Fig. 31. Computer calculations, MBBA sample length = 1 cm, sample temperature = 70°C.

Fig. 32. Computer calculations, MBBA sample length = 2.5 cm, sample temperature = 50°C.

Fig. 33. Computer calculations, MBBA sample length = 2.5 cm, sample temperature = 70°C.

Fig. 34. Computer calculations, MBBA sample length = 10 cm, Fresnel rhomb setting = 15°.

Fig. 35. Computer calculations, MBBA sample length = 10 cm, Fresnel rhomb setting = 22.5°.

Fig. 36. Computer calculations, MBBA sample length = 1 cm, Fresnel rhomb setting = 7.5°.

Fig. 37. Computer calculations, MBBA sample length = 1 cm, Fresnel rhomb setting = 22.5°.

Fig. 38. Computer calculations, no MBBA, $\alpha_4^2 = .75$.

Fig. 39. Computer calculations, MBBA sample length = 2.5 cm, $\alpha_4^2 = .75$.

Fig. 40. Computer calculations, no MBBA, $\alpha_4^2 = .50$.

Fig. 41. Computer calculations, MBBA sample length = 2.5 cm, $\alpha_4^2 = .50$.

Fig. 42. Computer calculations, no MBBA, $\tau_{SA} = 4 \times 10^{-7}$ sec.

Fig. 43. Computer calculations, MBBA sample length = 2.5 cm, $\tau_{SA} = 4 \times 10^{-7}$ sec.

Fig. 44. Computer calculations, MBBA sample length = 2.5 cm, actual τ_M. This is Fig. 27 redrawn with a different time scale.

Fig. 45. Computer calculations, MBBA sample length = 2.5 cm, steady state limit ($\tau_M \to 0$).

Fig. 46. Computer calculations, MBBA sample length = 10 cm, steady state limit ($\tau_M \to 0$).

Fig. 47. Experimental data for various values of temperature (T) and sample length (ℓ). The intensities as seen at photodiodes 1 and 2 are plotted versus time.

Pinhole Size Radius (mm)	Fresnel Number N		TE_{oo} Mode Power Loss/Power (%)		TE_{1o} Mode Power Loss / TE_{oo} Mode Power Loss		TE_{1o} Mode Power Loss/Pass (%)		Actual Cavity TE_{oo} Mode Power Loss/Pass (%)	ε_{DIFF}
	a	b	a	b	a	b	a	b		
.25 mm	.10	.09	68%	75%	1.3	1.2	88%	90%	71%	1.24
.375 mm	.22	.19	44%	53%	1.6	1.4	70%	74%	48%	.65
.50 mm	.39	.33	28%	35%	2.0	1.7	56%	60%	31%	.37
.625 mm	.61	.52	15%	20%	2.4	2.0	36%	40%	17%	.19
.75 mm	.88	.75	9%	12%	2.9	2.3	26%	28%	10%	.11
.875 mm	1.20	1.02	4%	8%	3.5	2.6	14%	21%	6%	.06
1.00 mm	1.56	1.33	3%	6%	4.1	3.0	12%	18%	4%	.04

Table 2. Diffraction loss for various aperature sizes.

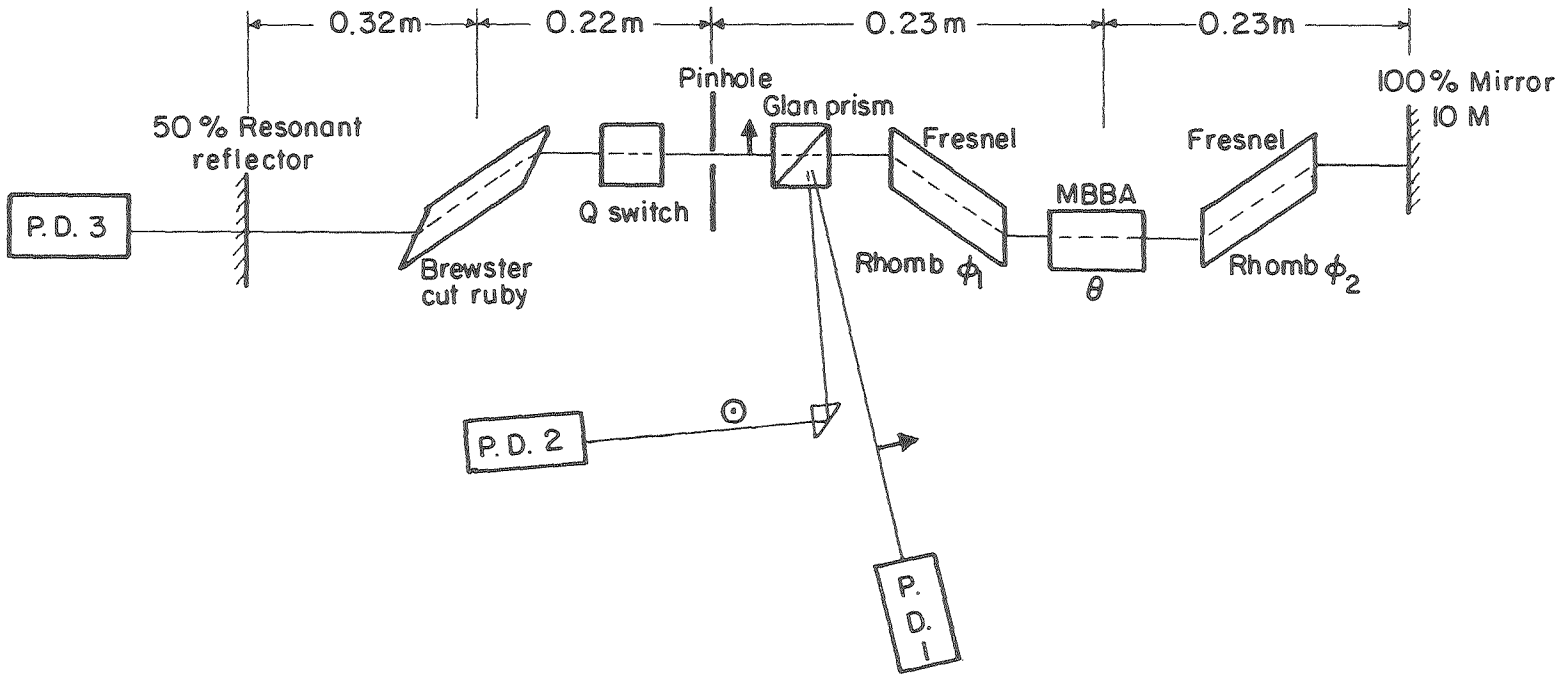

XBL 809-5811

Figure 20

Figure 21

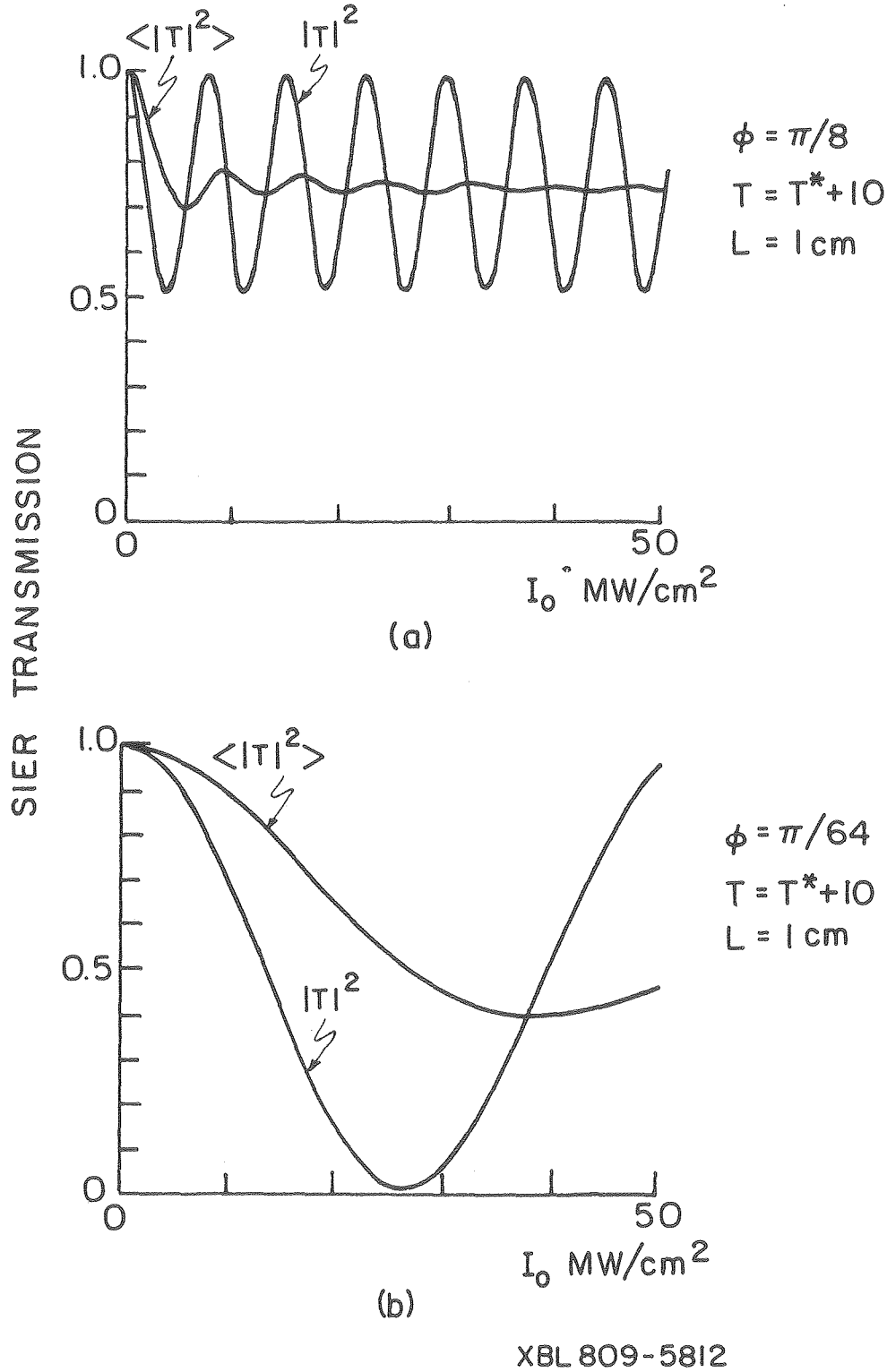

XBL 809-5812

Figure 22

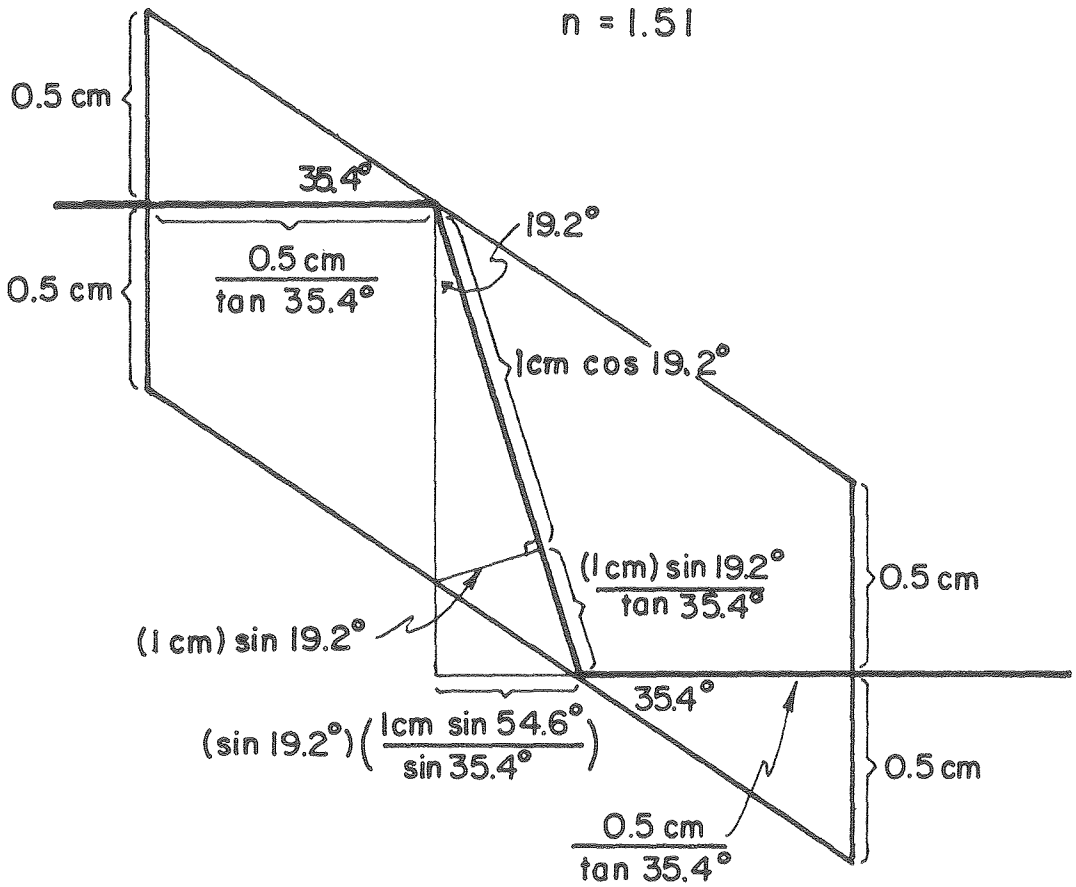

XBL809-5813

Figure 23

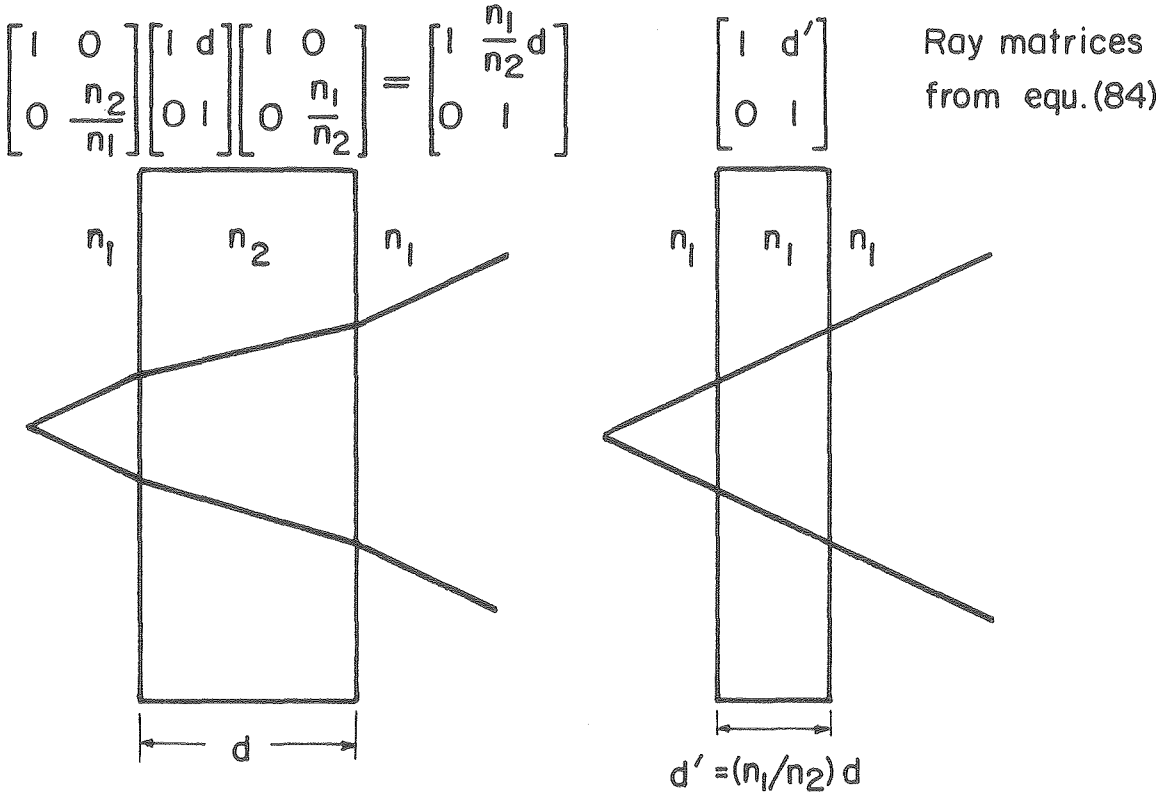

XBL 809-5814

Figure 24

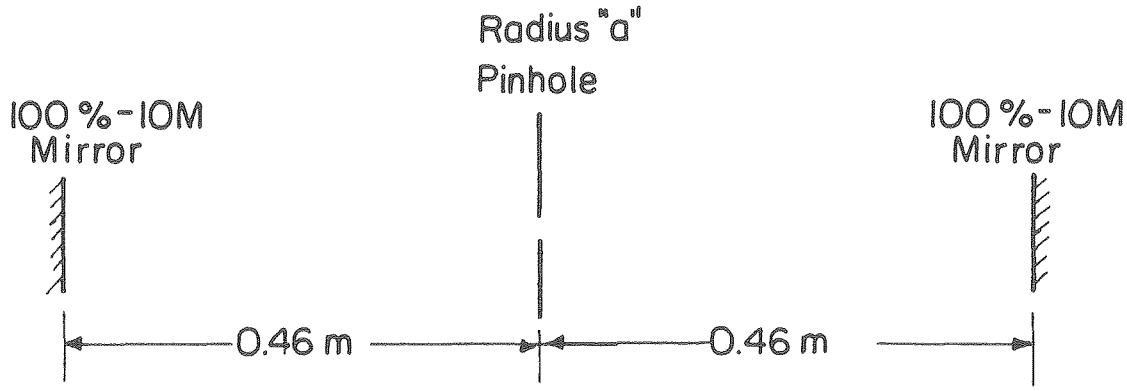

$1 - L/R_i = 0.91$ $\qquad$ $N = a^2/\lambda L = \dfrac{a^2(\text{cm})}{6.39 \times 10^{-3}}$

(a)

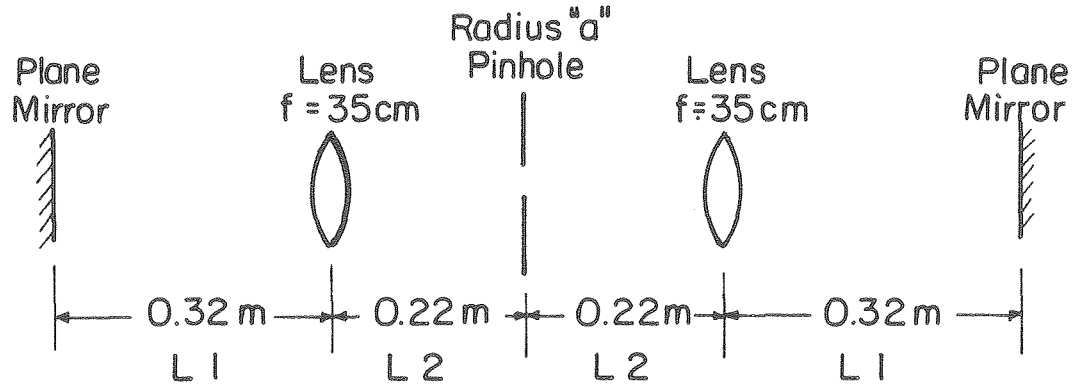

$1 - L/R_i \rightarrow 1 - \dfrac{2L_1 + 2L_2 - 2L_1L_2/f}{f} = -0.94$; $\quad N = a^2/\lambda L = \dfrac{a^2(\text{cm})}{7.50 \times 10^{-3}}$

(b)

XBL 809 - 5815

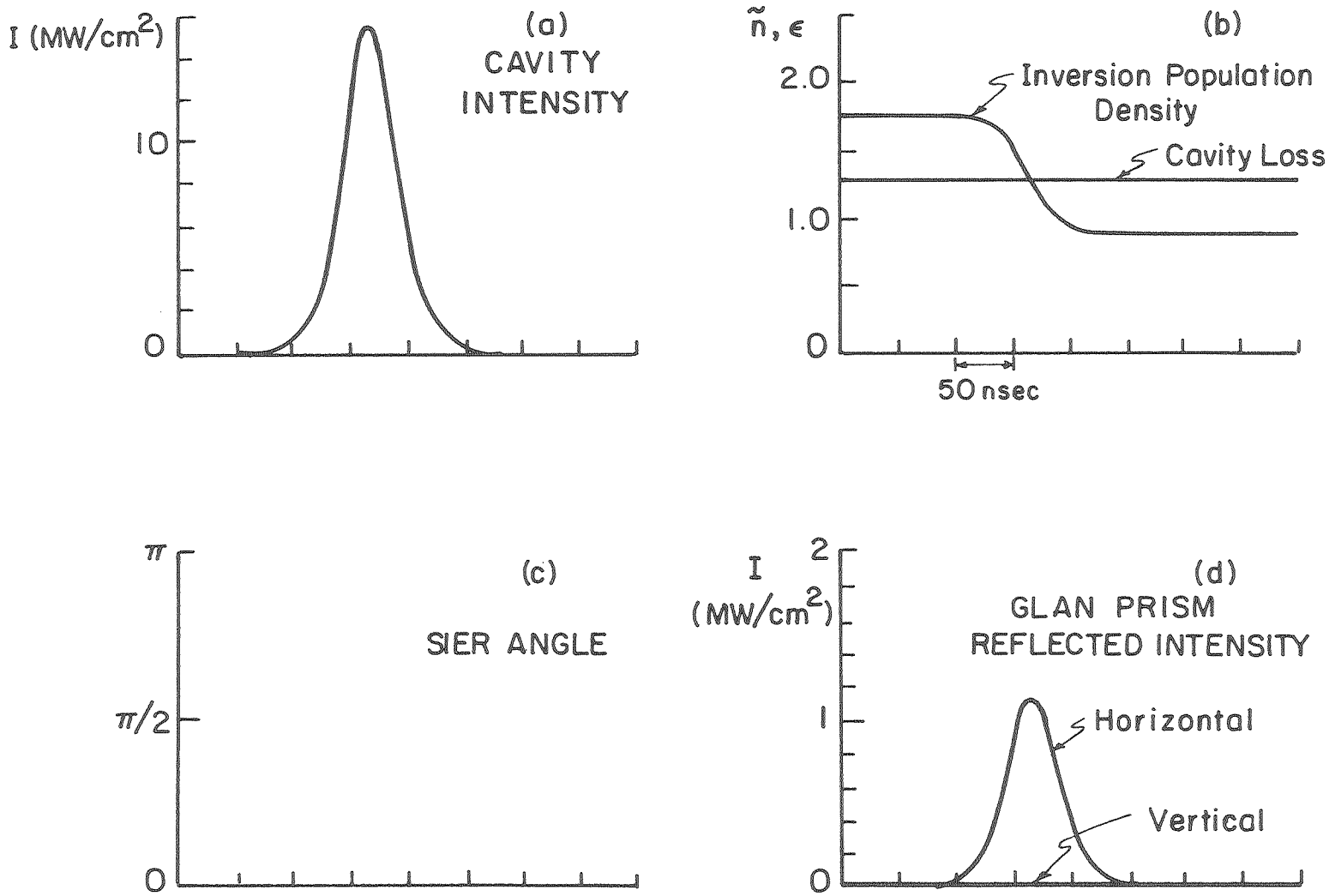

XBL 809-5816

Figure 25

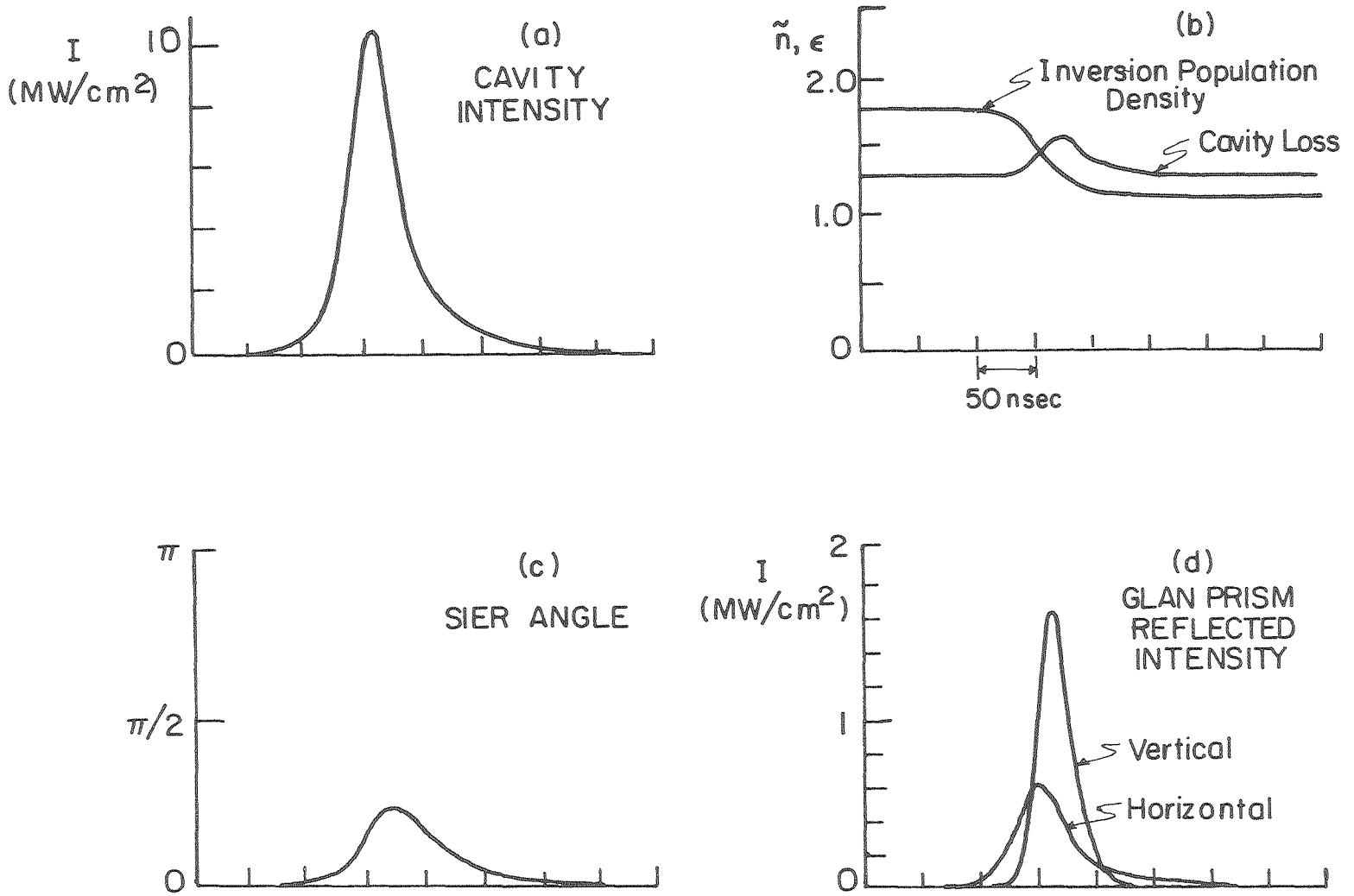

XBL 809-5817

Figure 26

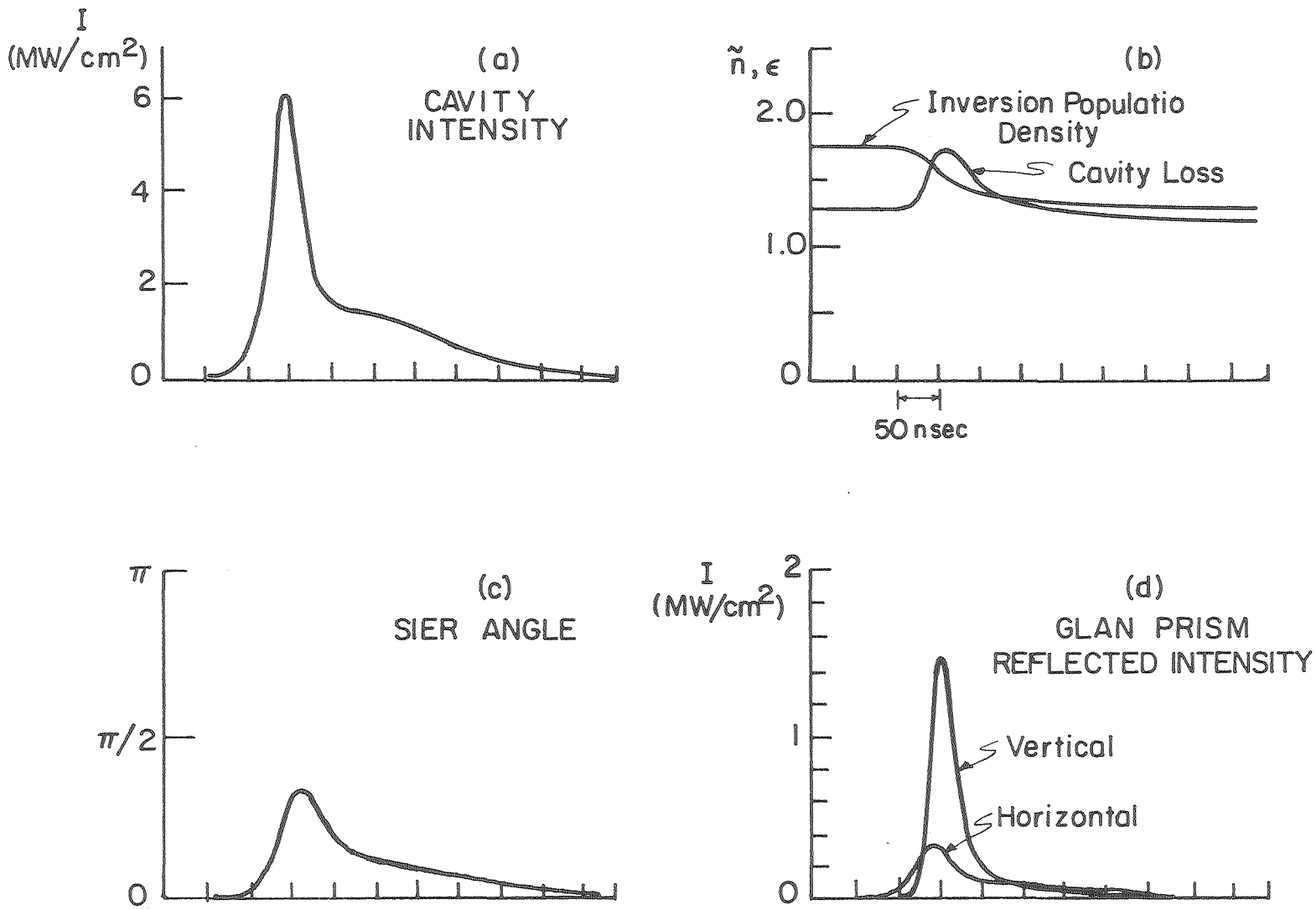

XBL 809-5818

Figure 27

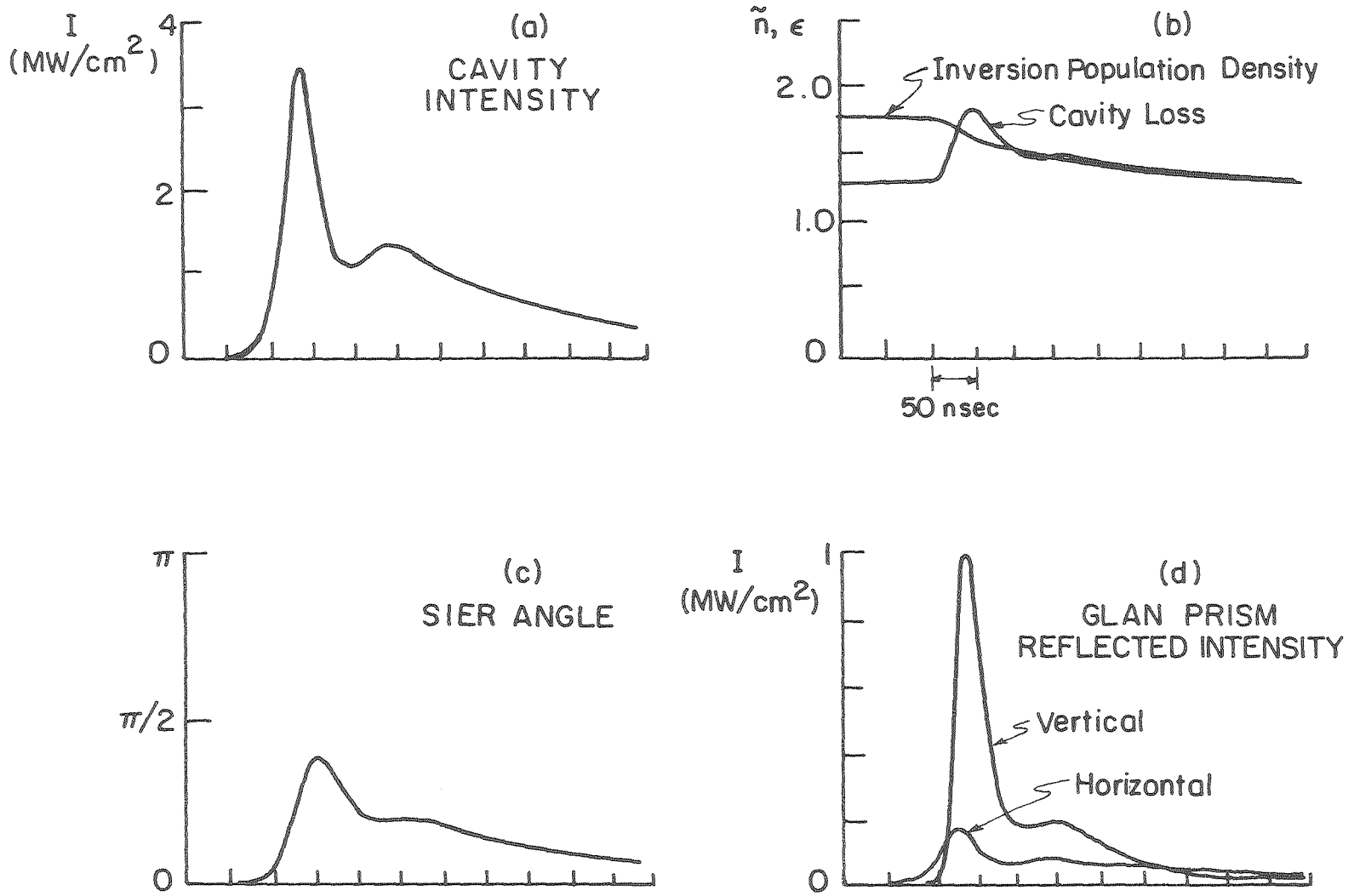

XBL 809-5819

Figure 28

Figure 29

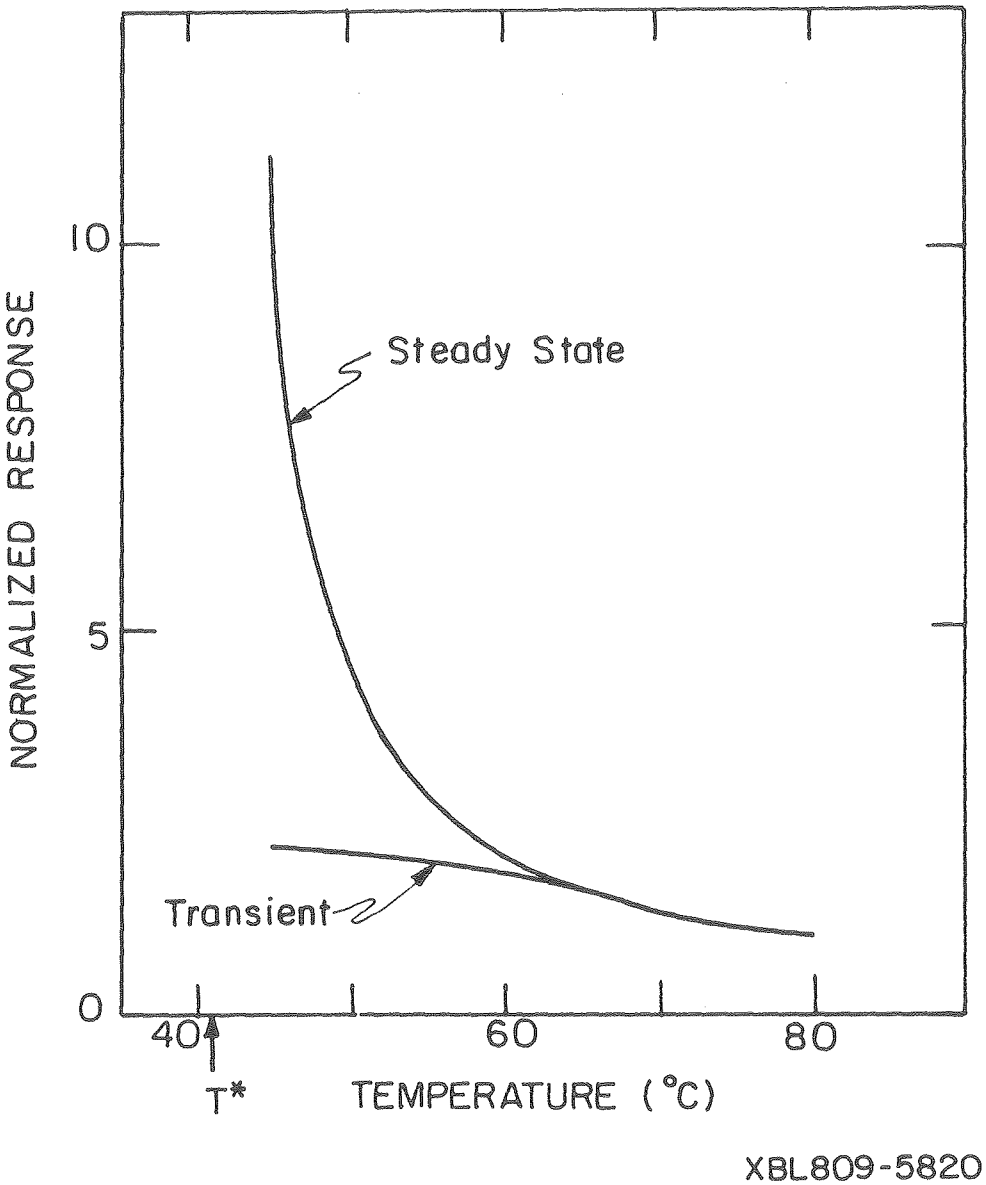
NORMALIZED RESPONSE
10
5
0
Steady State
Transient
40
60
80
T*
TEMPERATURE (°C)
XBL809-5820

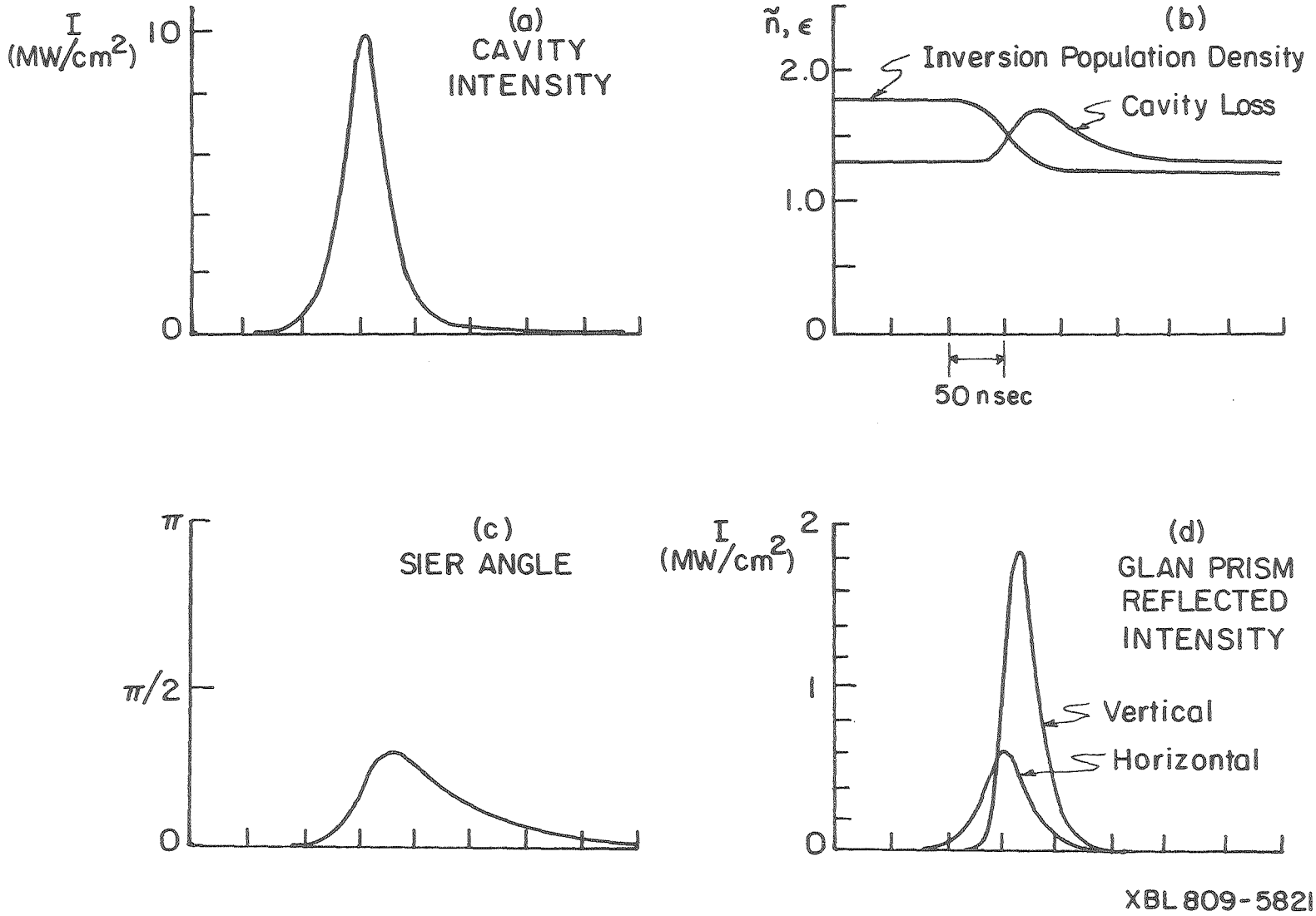
I
(MW/cm²)
10
0
(a)
CAVITY
INTENSITY
ñ, ε
2.0
1.0
0
(b)
Inversion Population Density
Cavity Loss
50 nsec
π
π/2
0
(c)
SIER ANGLE
I
(MW/cm²)
2
1
0
(d)
GLAN PRISM
REFLECTED
INTENSITY
Vertical
Horizontal
XBL 809-5821

Figure 30

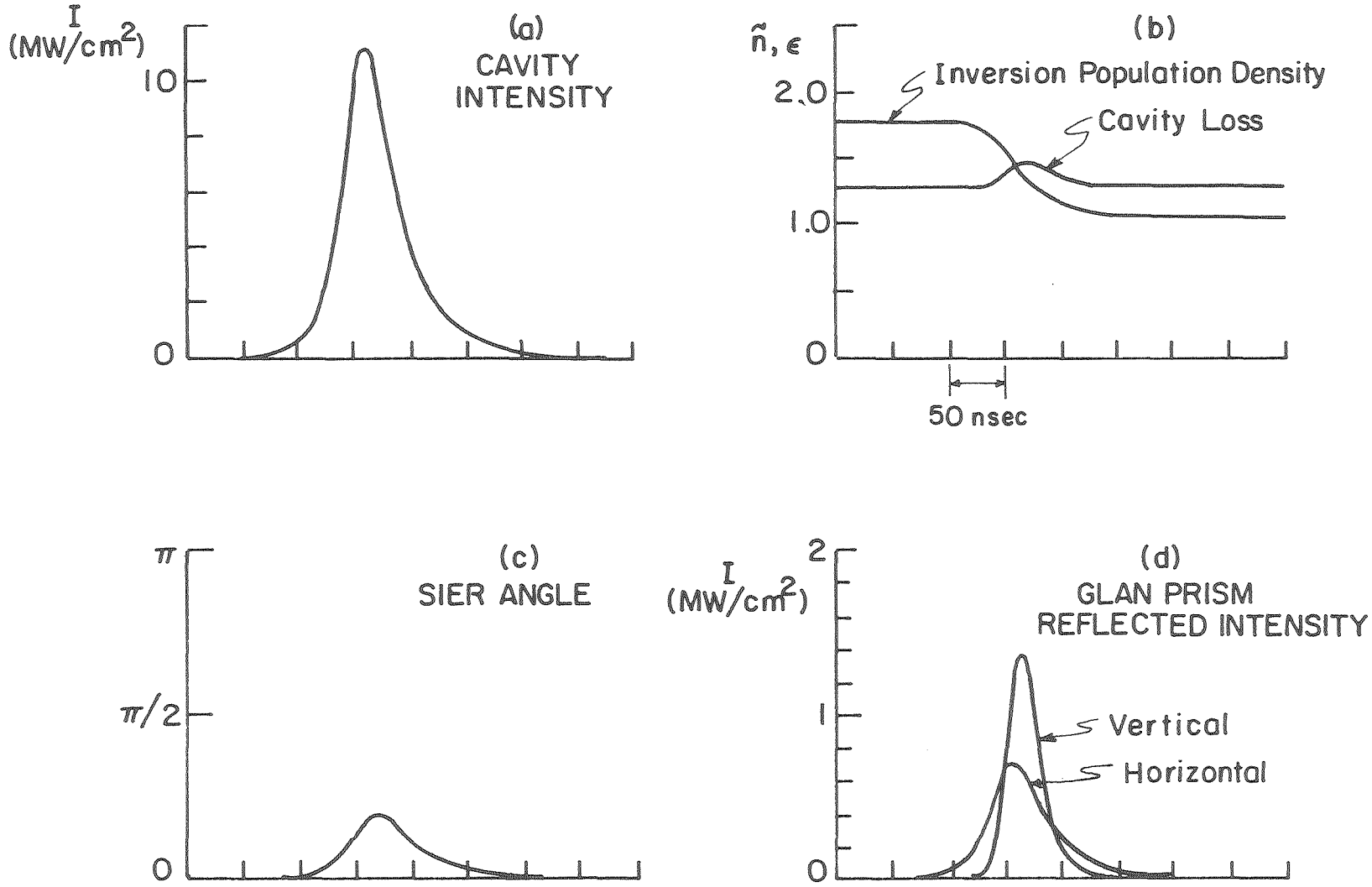

XBL809-5822

Figure 31

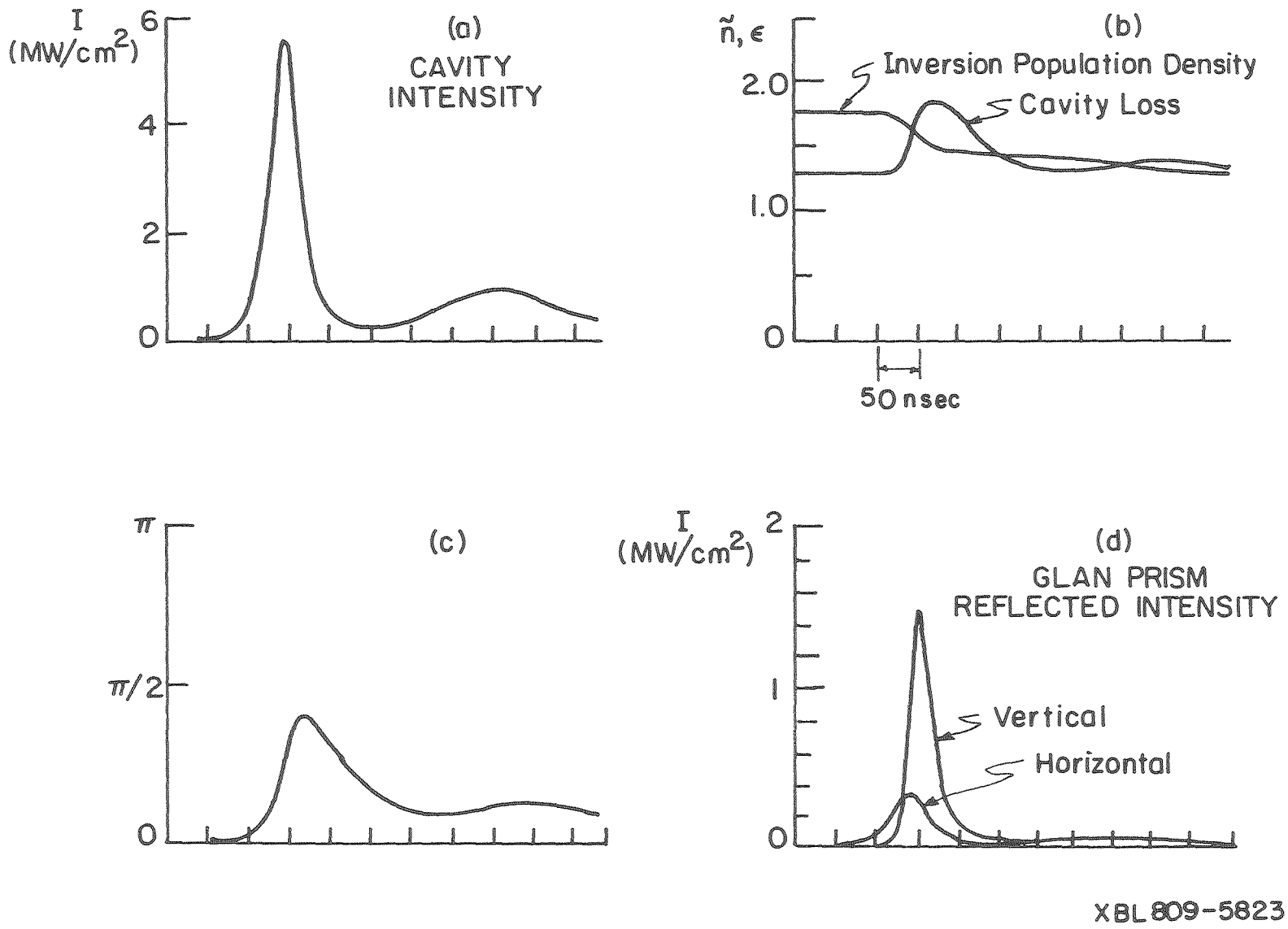
I
(MW/cm²)
6
4
2
0
(a)
CAVITY
INTENSITY
ñ, ε
2.0
1.0
0
(b)
Inversion Population Density
Cavity Loss
50 nsec
π
π/2
0
(c)
I
(MW/cm²)
2
1
0
(d)
GLAN PRISM
REFLECTED INTENSITY
Vertical
Horizontal
XBL 809-5823

Figure 32

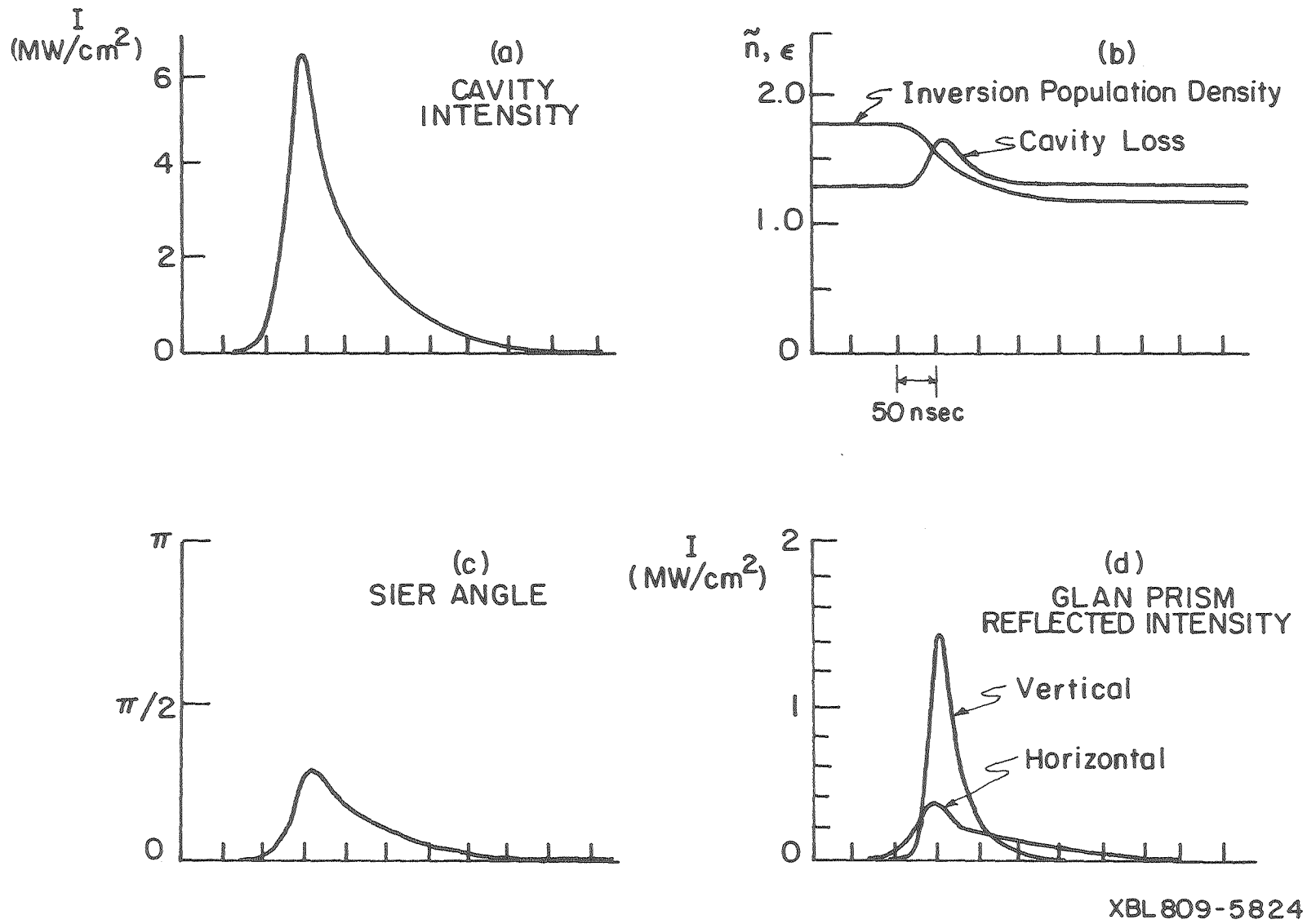
I
(MW/cm²)
6
4
2
0
(a)
CAVITY
INTENSITY
ñ, ε
2.0
1.0
0
(b)
Inversion Population Density
Cavity Loss
50 nsec
π
π/2
0
(c)
SIER ANGLE
I
(MW/cm²)
2
1
0
(d)
GLAN PRISM
REFLECTED INTENSITY
Vertical
Horizontal
XBL809-5824

Figure 33

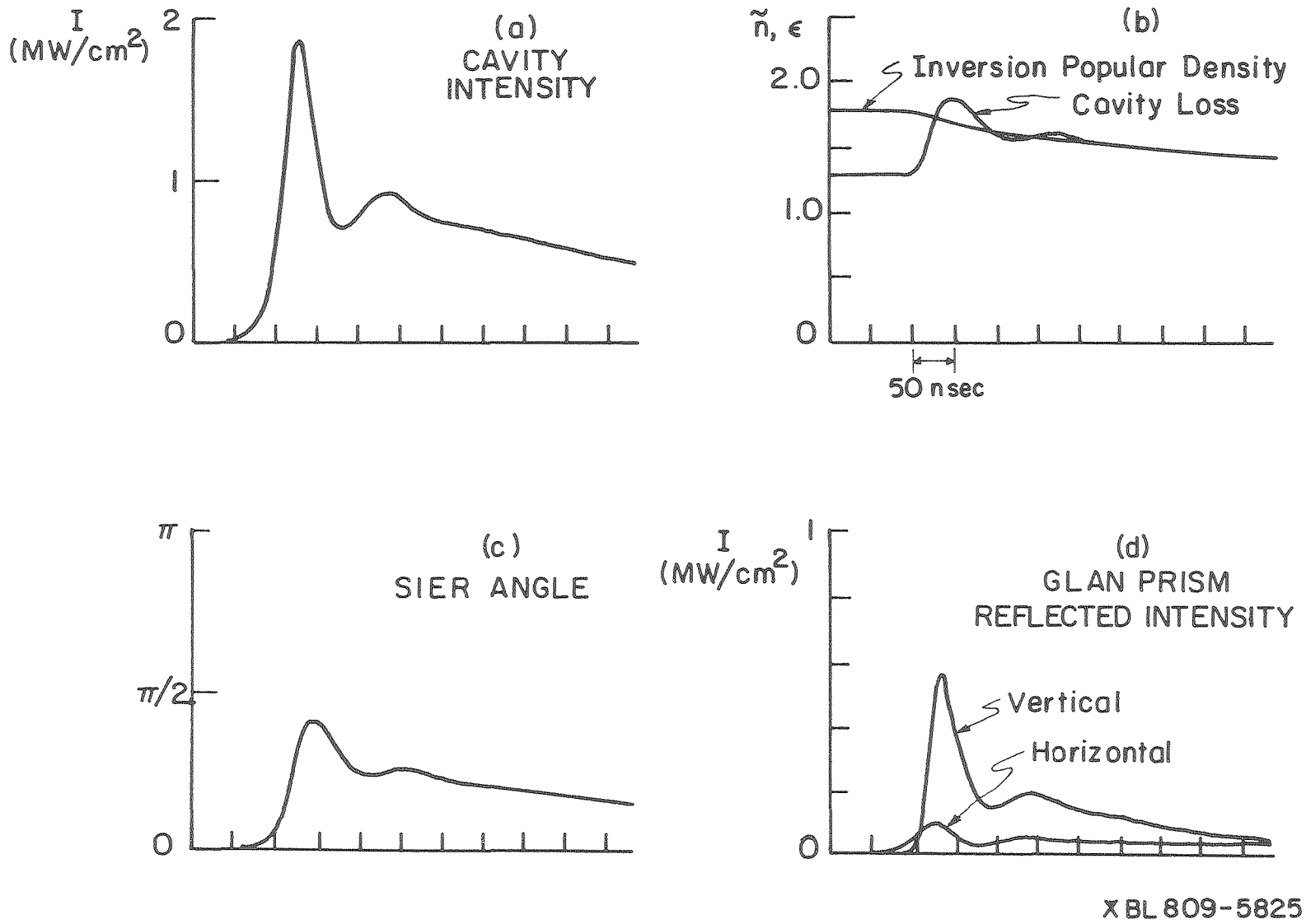
I
(MW/cm²)
2
1
0
(a)
CAVITY
INTENSITY
ñ, ε
2.0
1.0
0
(b)
Inversion Popular Density
Cavity Loss
50 nsec
π
π/2
0
(c)
SIER ANGLE
I
(MW/cm²)
1
0
(d)
GLAN PRISM
REFLECTED INTENSITY
Vertical
Horizontal
XBL 809-5825

Figure 34

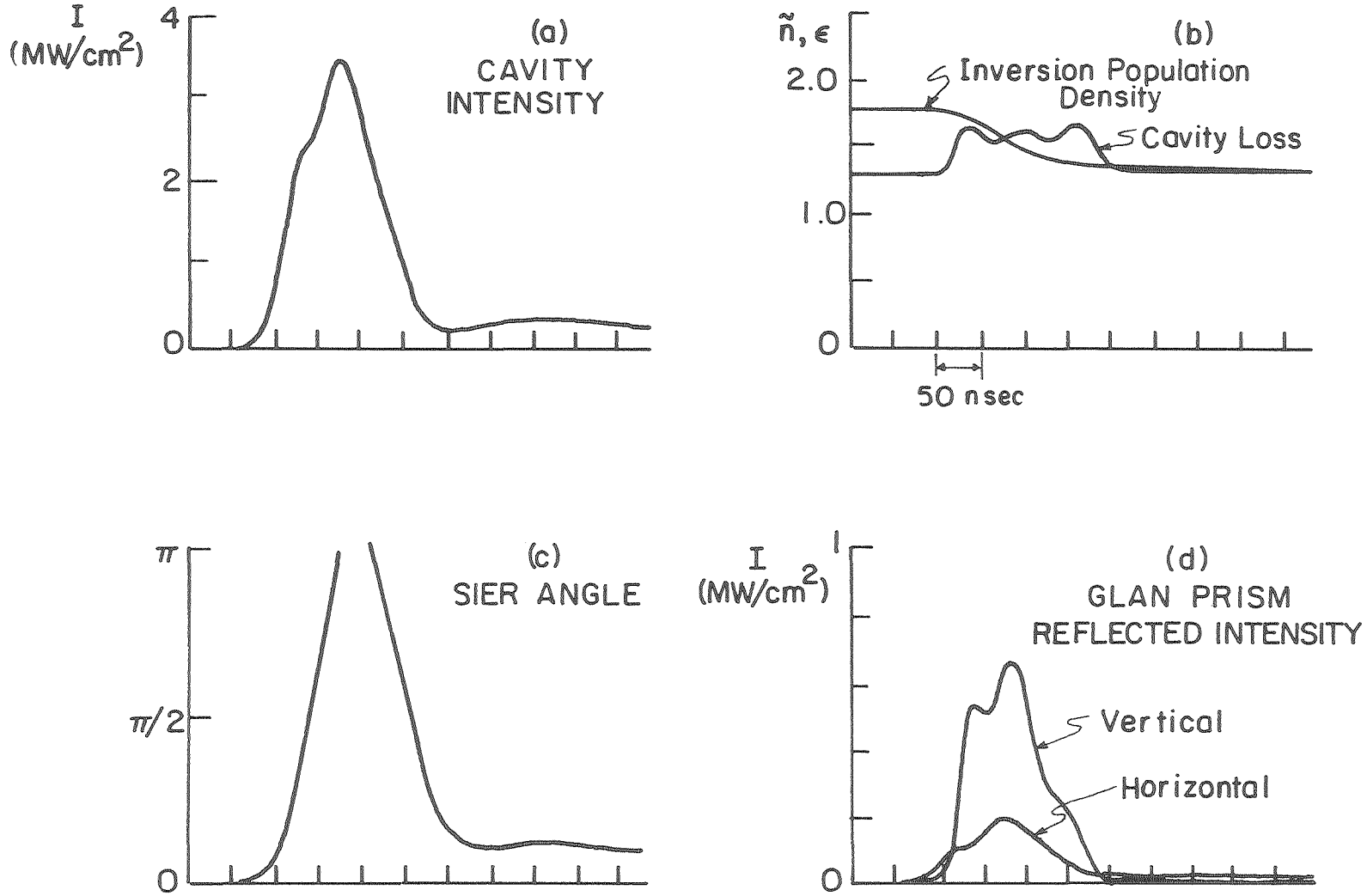

XBL 809-5826

Figure 35

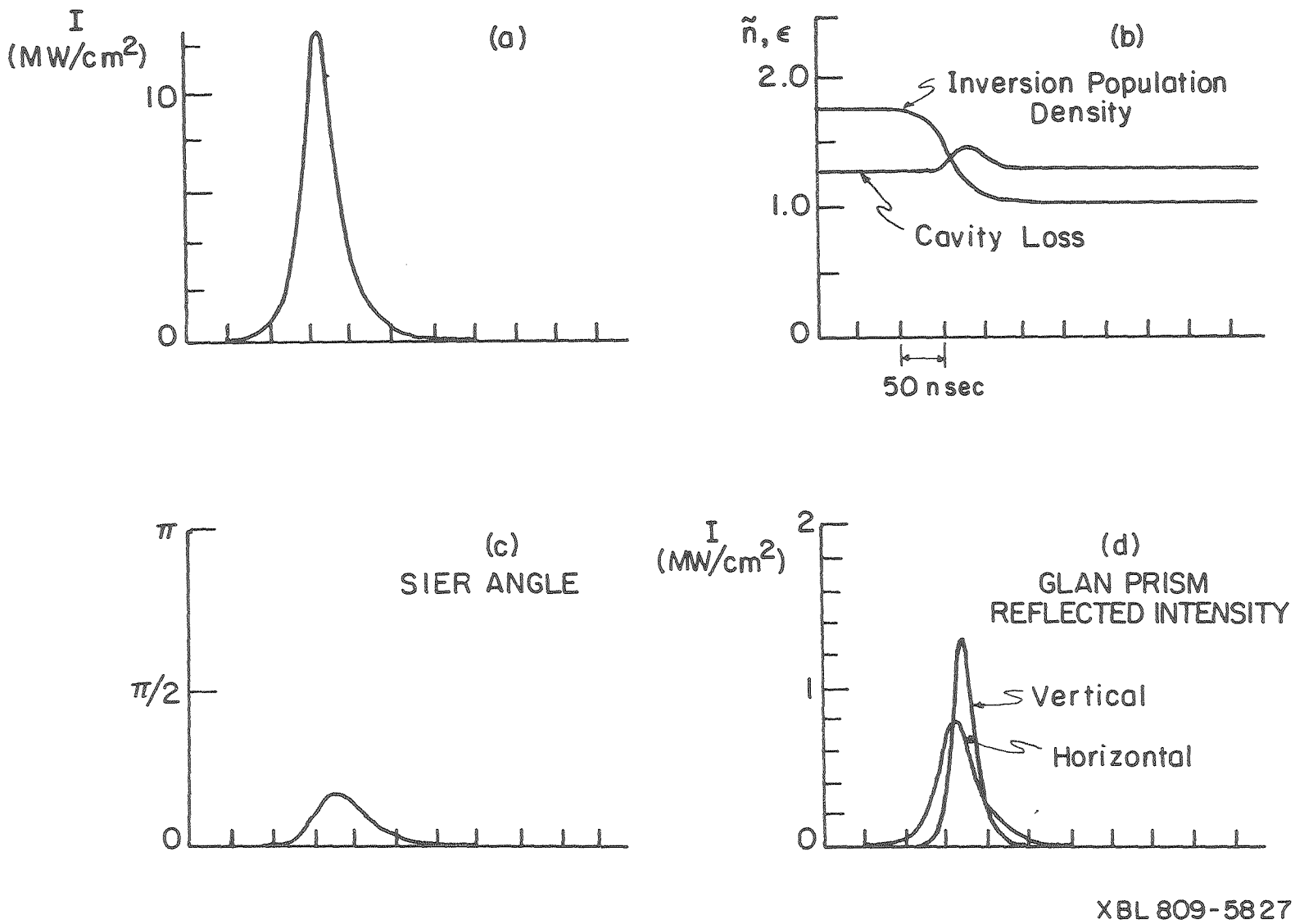
I
(MW/cm2)
10
0
(a)
ñ, ε
2.0
1.0
0
(b)
Inversion Population
Density
Cavity Loss
50 nsec
π
π/2
0
(c)
SIER ANGLE
I
(MW/cm2)
2
1
0
(d)
GLAN PRISM
REFLECTED INTENSITY
Vertical
Horizontal
XBL 809-5827

Figure 36

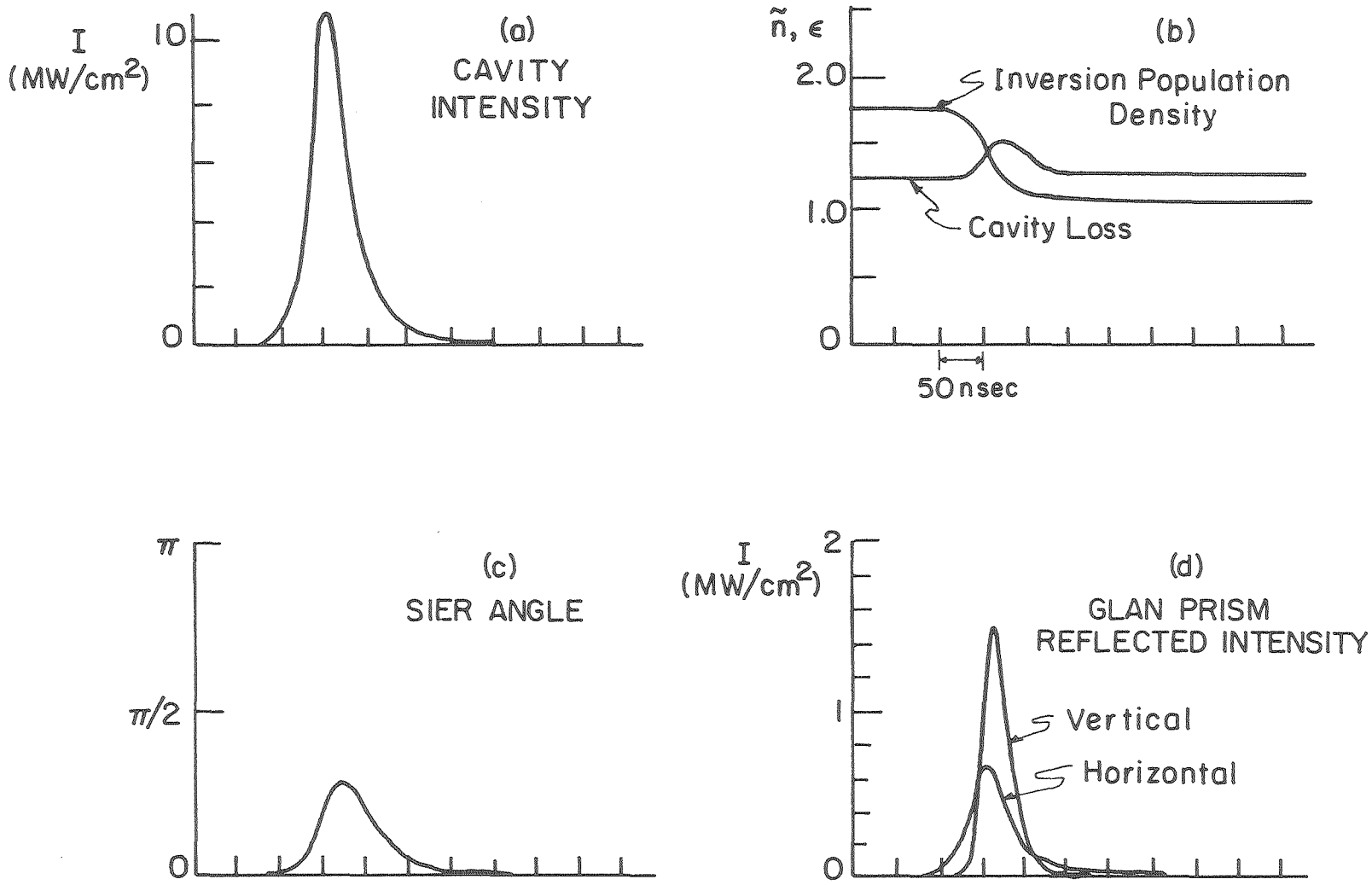

XBL 809-5828

Figure 37

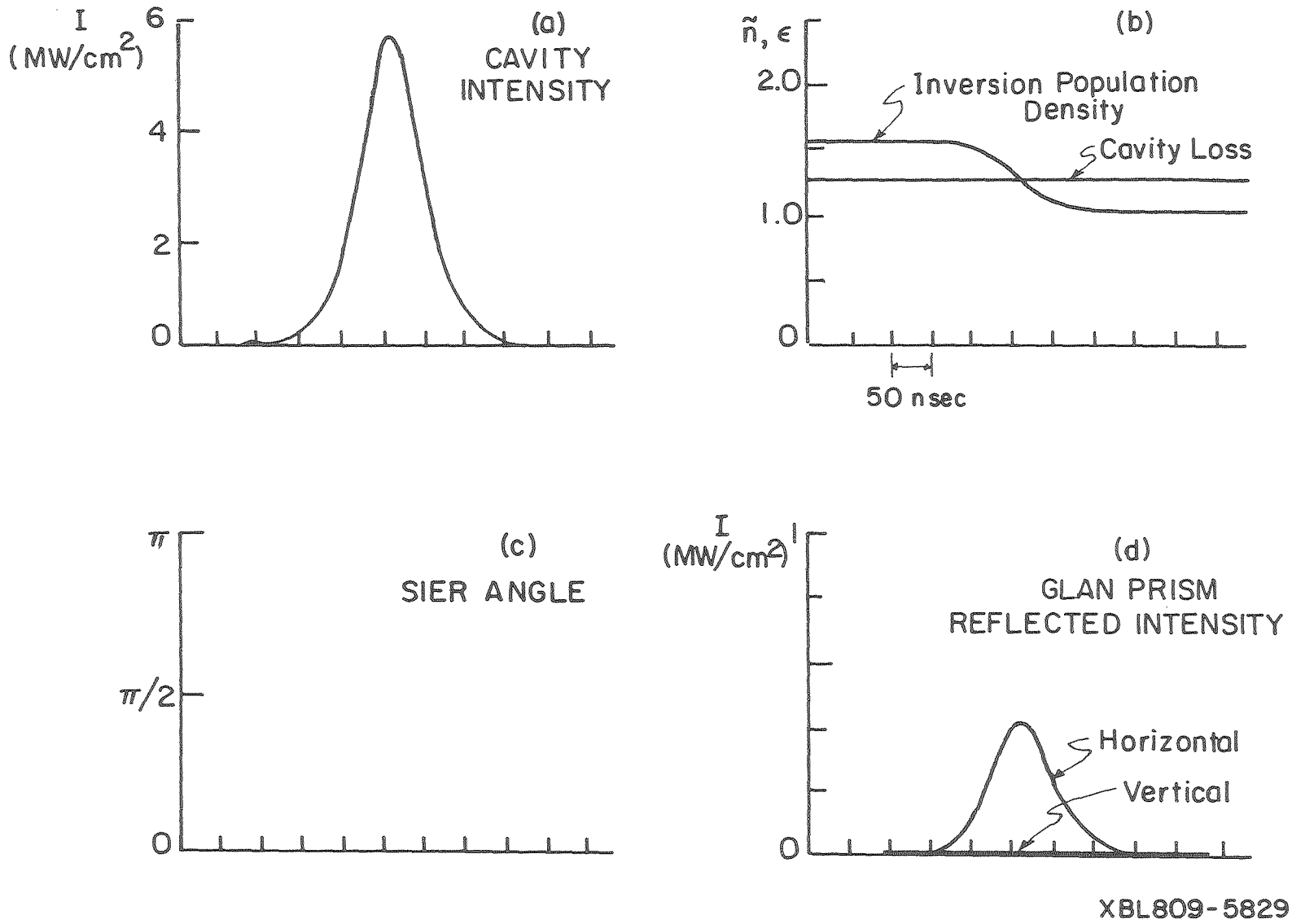
I
(MW/cm²)
6
4
2
0
(a)
CAVITY
INTENSITY
ñ, ε
2.0
1.0
0
(b)
Inversion Population
Density
Cavity Loss
50 nsec
π
π/2
0
(c)
SIER ANGLE
I
(MW/cm²)
1
0
(d)
GLAN PRISM
REFLECTED INTENSITY
Horizontal
Vertical
XBL809-5829

Figure 38

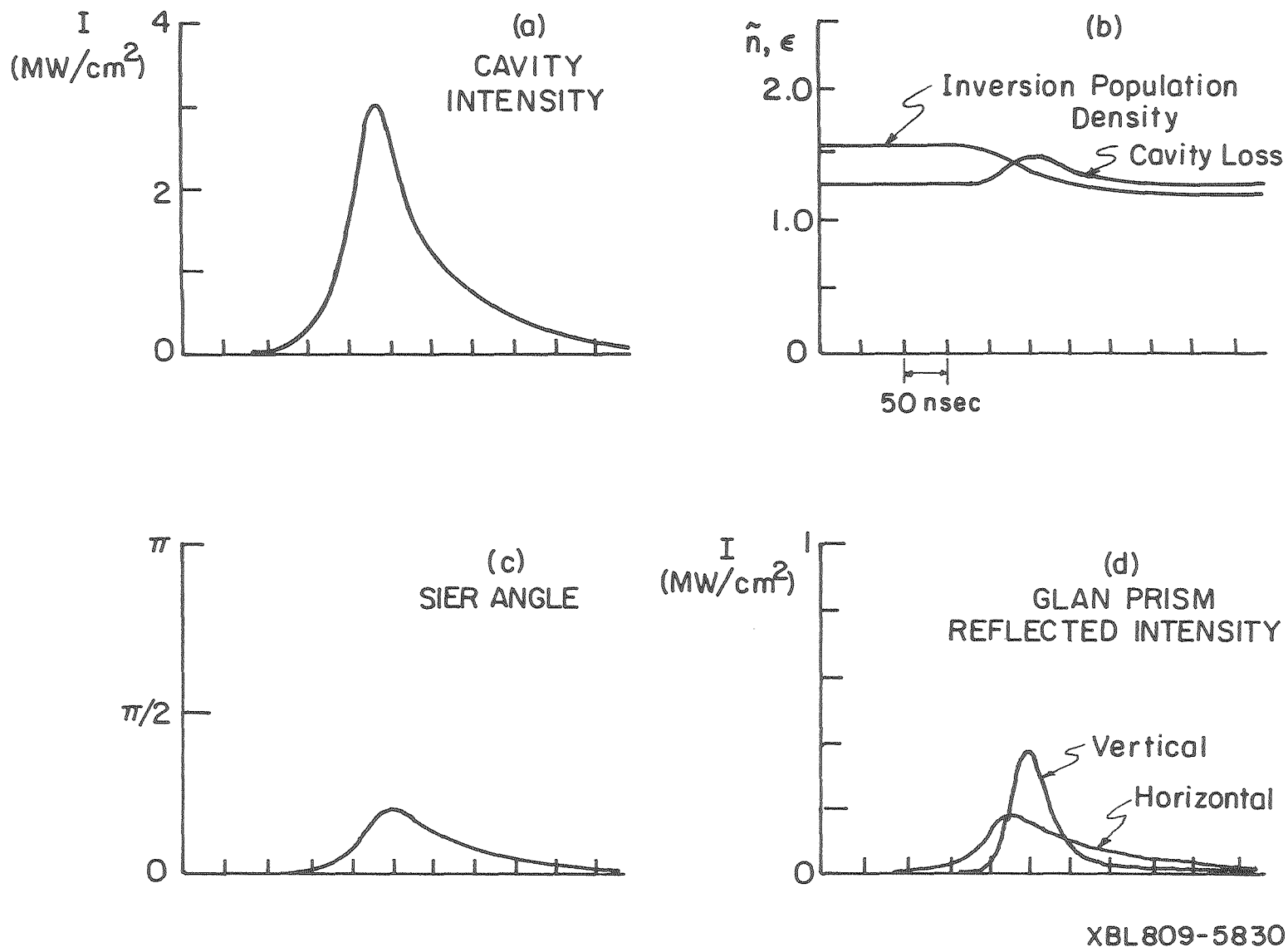
I
(MW/cm²)
4
2
0
(a)
CAVITY
INTENSITY
ñ, ε
2.0
1.0
0
(b)
Inversion Population
Density
Cavity Loss
50 nsec
π
π/2
0
(c)
SIER ANGLE
I
(MW/cm²)
1
0
(d)
GLAN PRISM
REFLECTED INTENSITY
Vertical
Horizontal
XBL809-5830

Figure 39

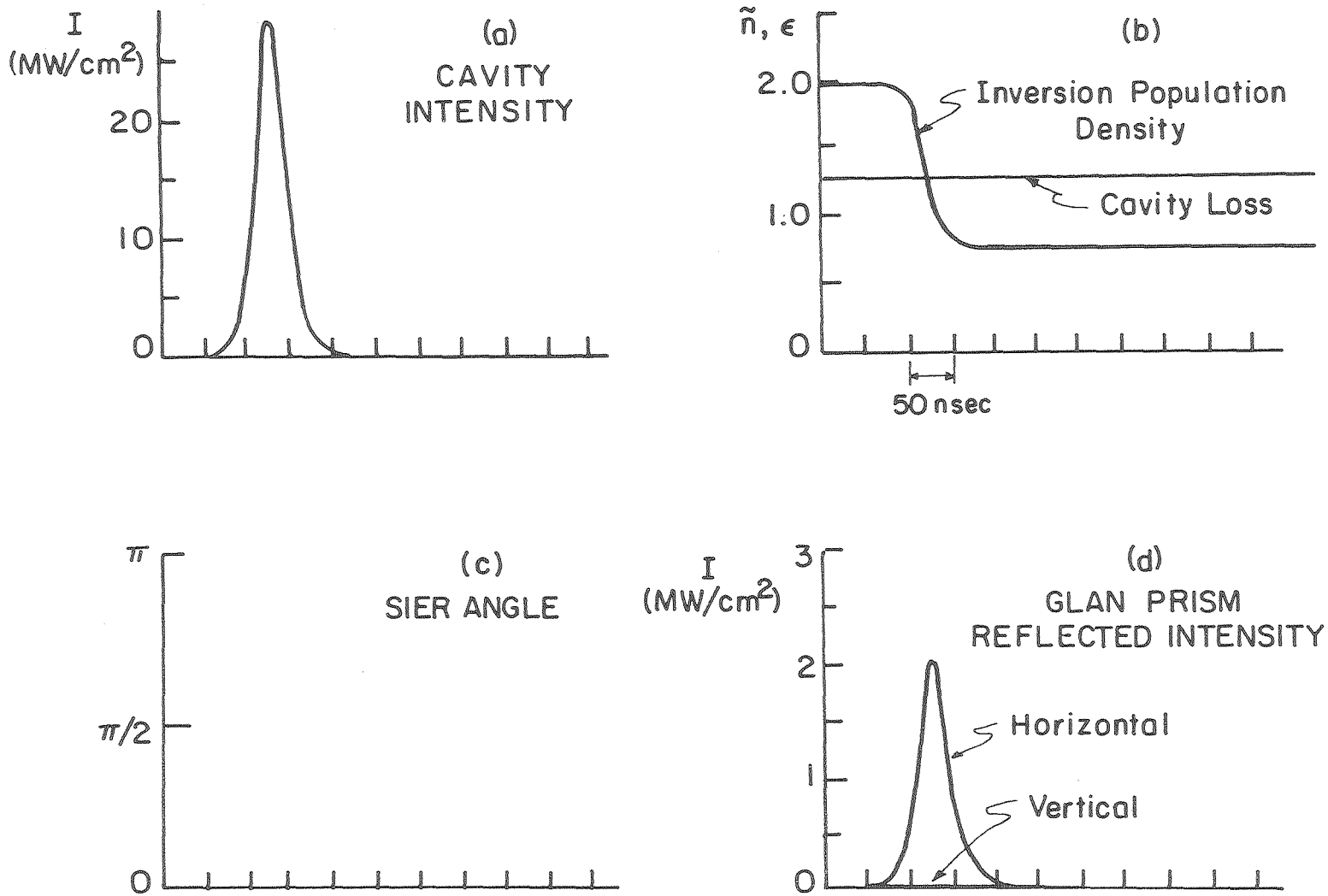

XBL809-5831

Figure 40

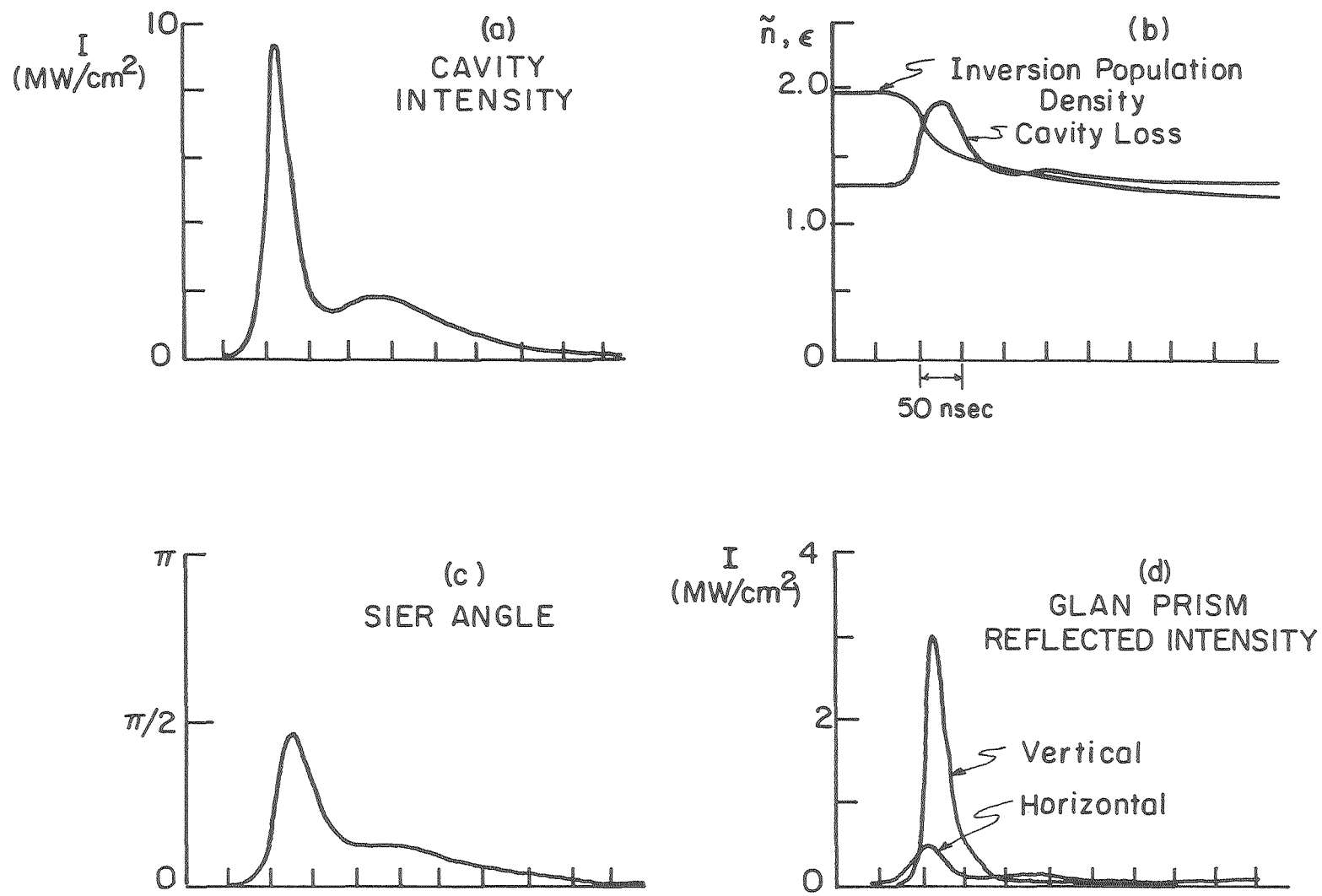

XBL 809-5832

Figure 41

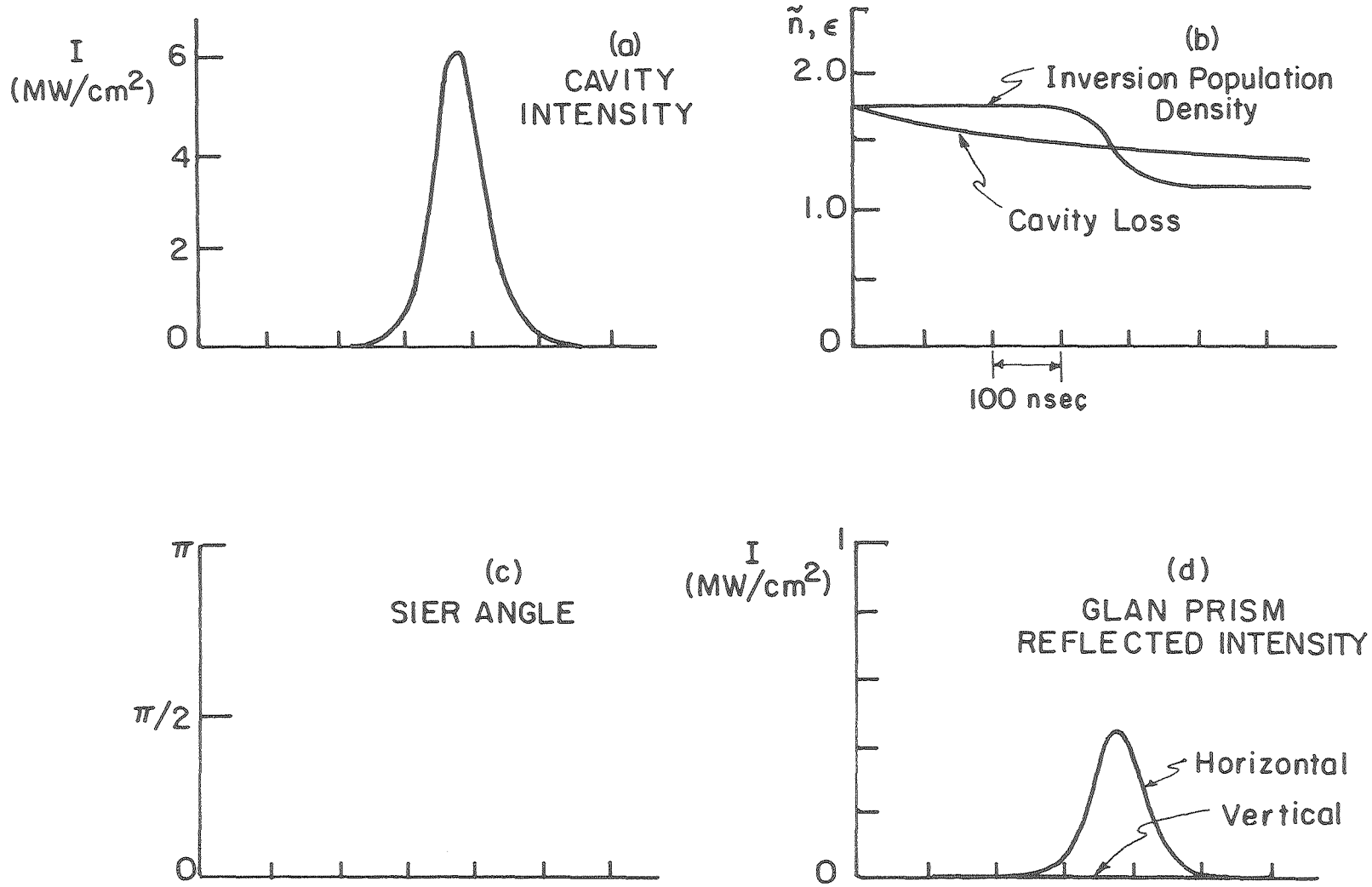

XBL809-5833

Figure 42

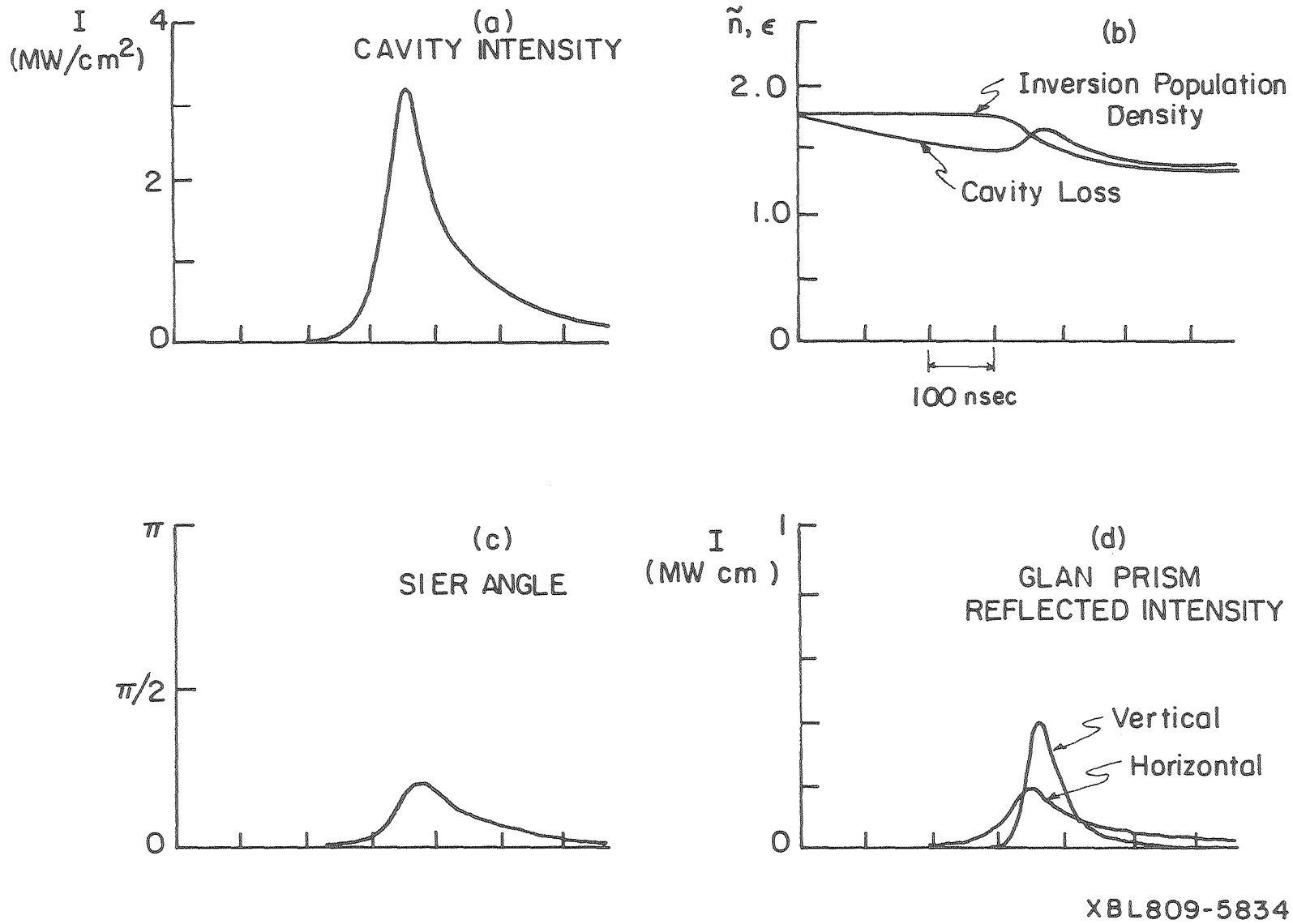
I
(MW/cm2)
4
2
0
(a)
CAVITY INTENSITY
ñ, ε
2.0
1.0
0
(b)
Inversion Population
Density
Cavity Loss
100 nsec
π
π/2
0
(c)
SIER ANGLE
I
(MW cm)
1
0
(d)
GLAN PRISM
REFLECTED INTENSITY
Vertical
Horizontal
XBL809-5834

Figure 43

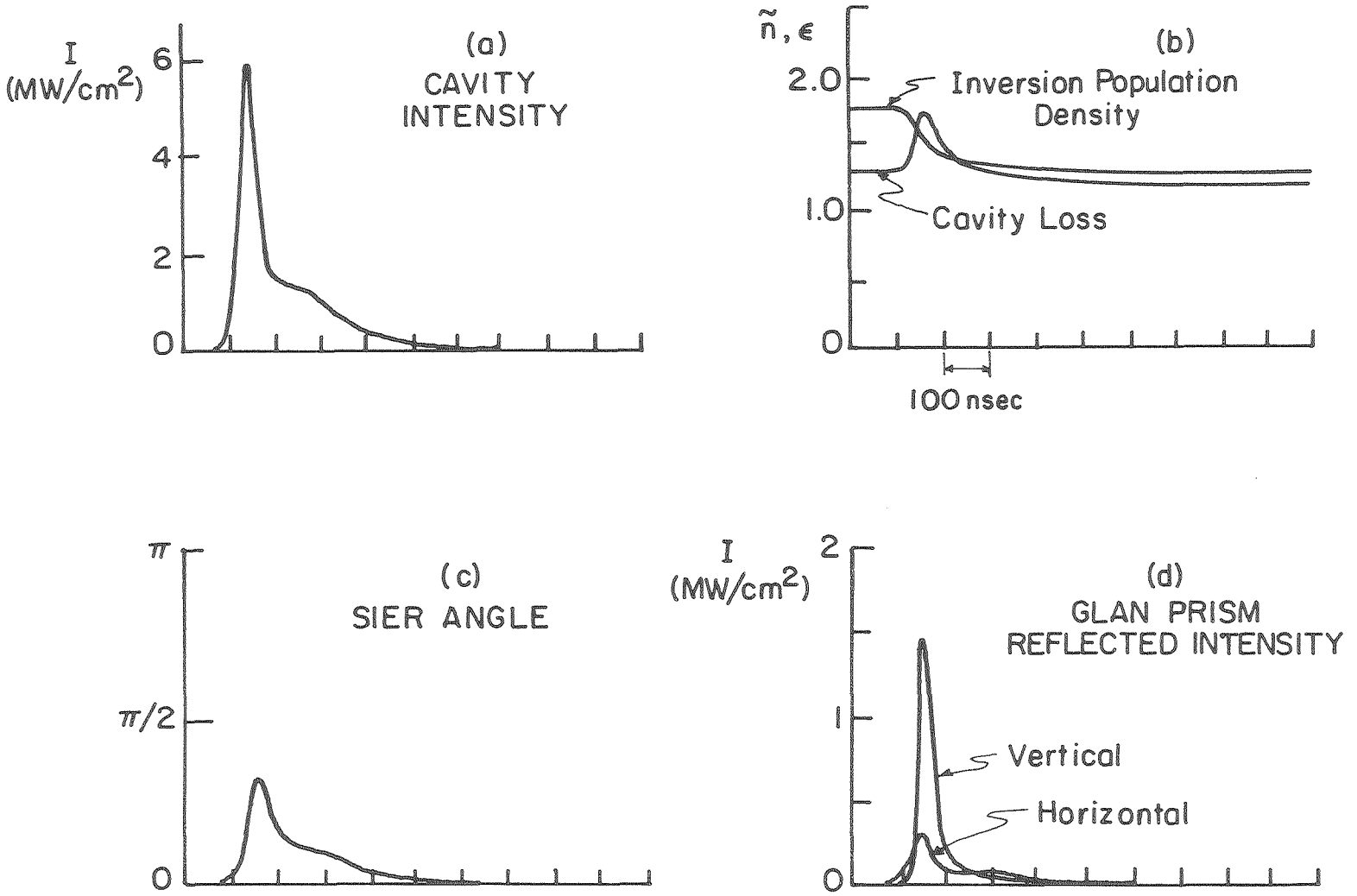

XBL 809-5835

Figure 44

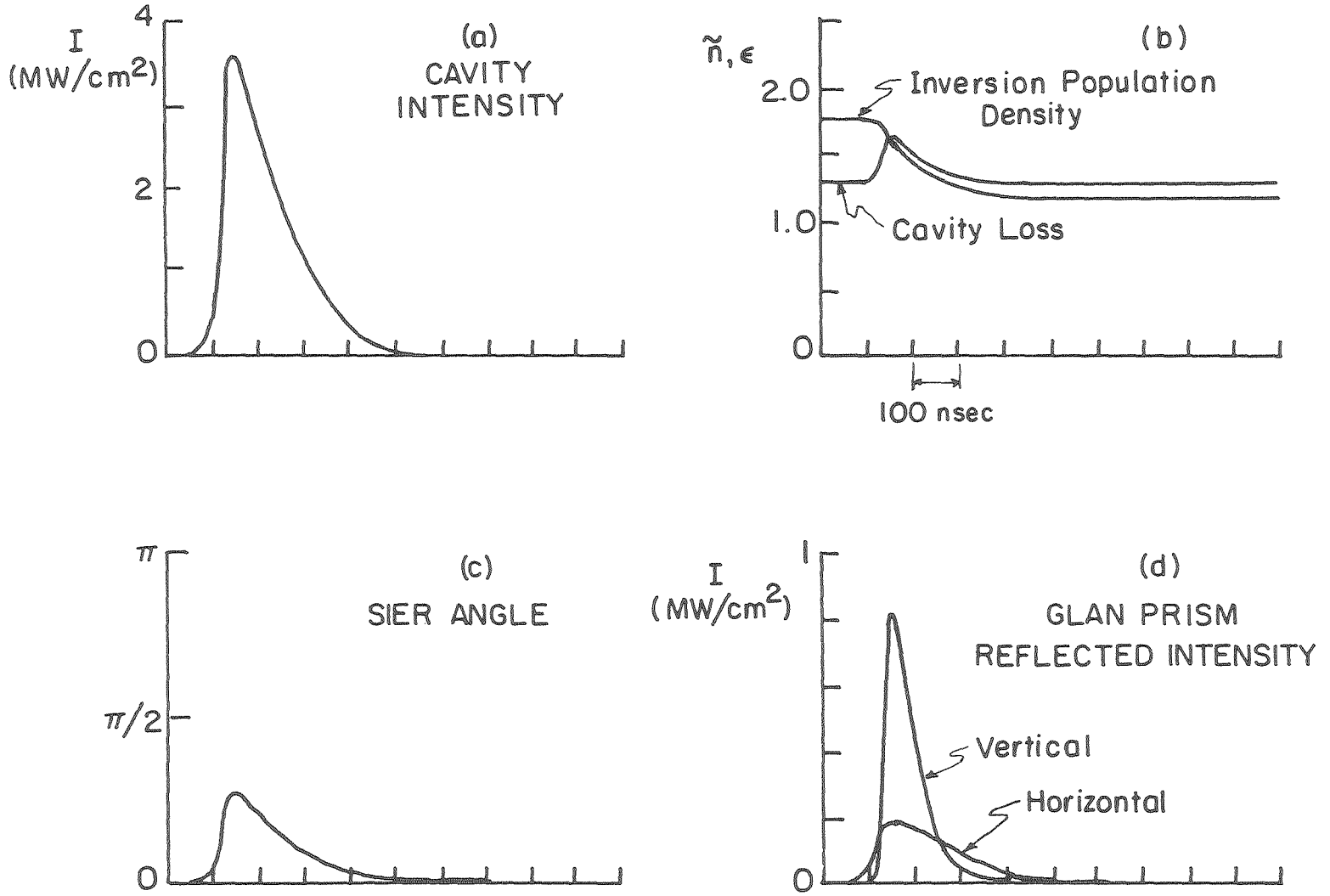

XBL 809-5836

Figure 45

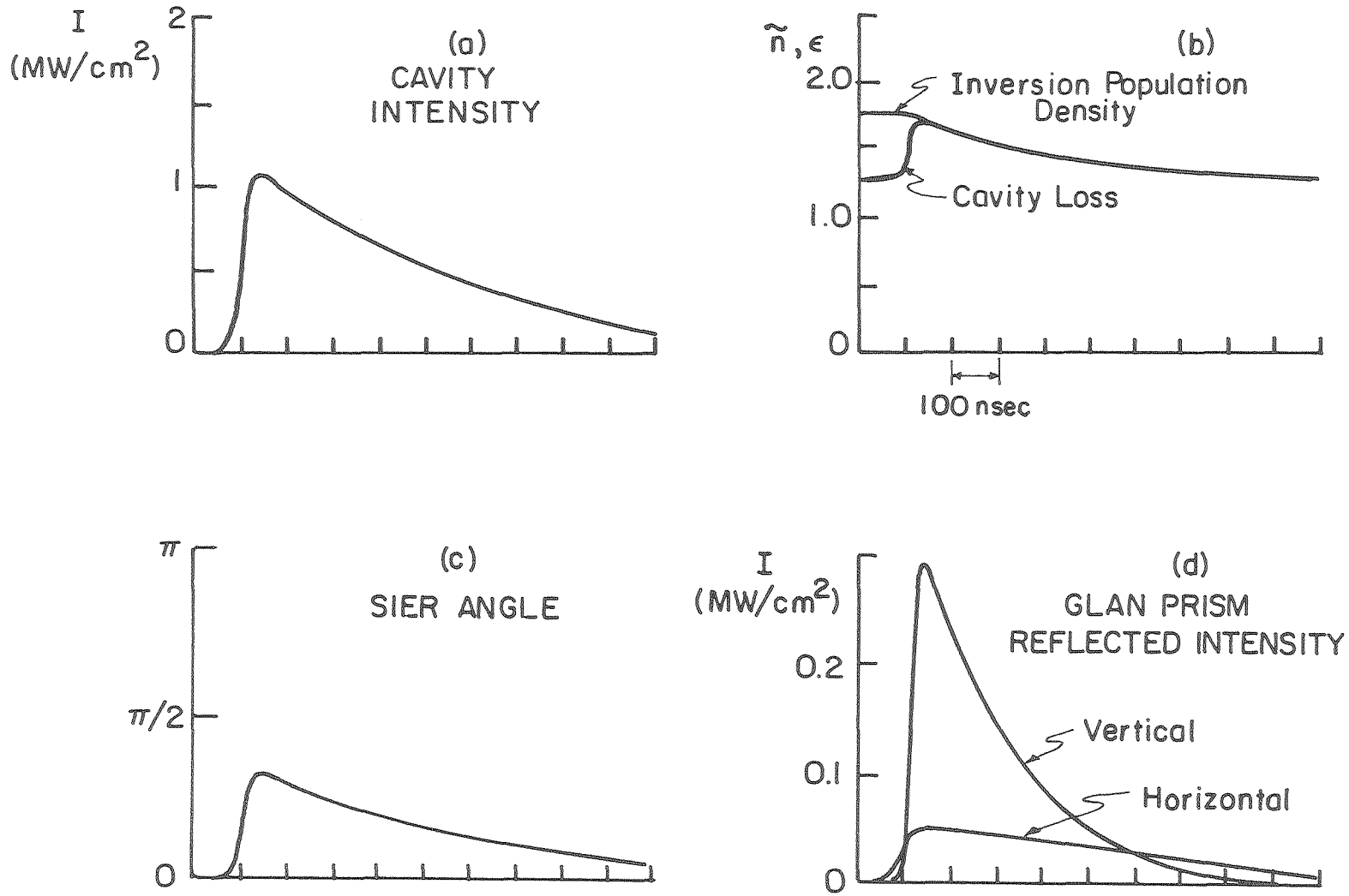

XBL 809-5837

Figure 46

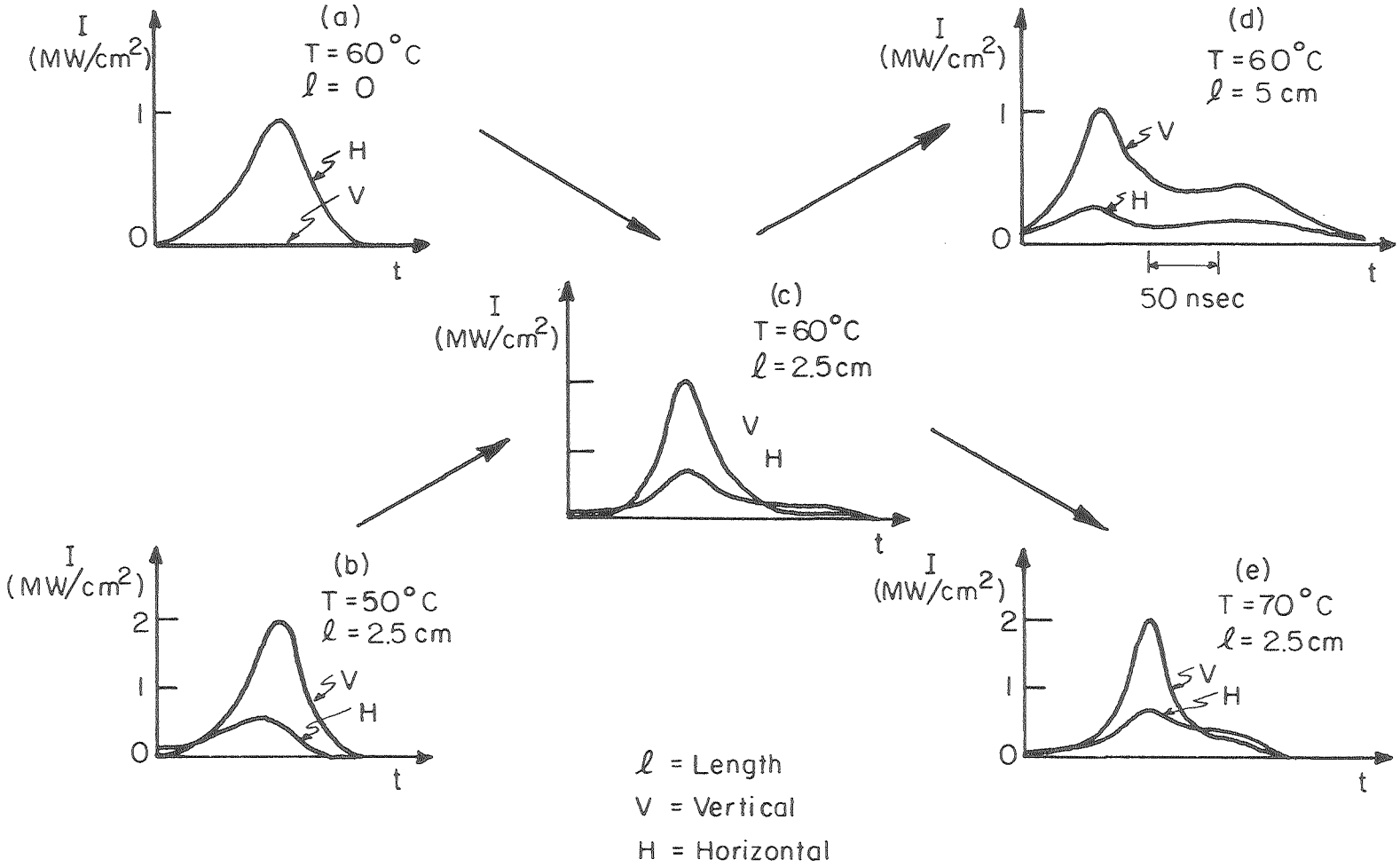

XBL809-5838

Figure 47

IV. SELF FOCUSING IN A LASER CAVITY-MODEL

A. Introduction

As pointed out in the preceeding chapter, self focusing plays a major role in determining laser output characteristics when MBBA is present in a ruby laser cavity. In this chapter, we present a model to describe this role. The model presented is fully general and may be applied to any material exhibiting intensity dependent self focusing when placed in a laser cavity. Because of the impracticality of developing the spatially dependent laser rate equations needed to analyze the self focusing, an adequate computer model describing the dynamic features of the laser output was unavailable. Consequently, the work on self focusing places a stronger emphasis on experimental results than does the SIER inducible loss study. The large amount of experimental data and the complicated analysis needed to analyze it are presented most logically as separate chapters (Chapters V and VI).

B. Self Focusing Model

Both the laser cavity and the self focusing process have been discussed separately (Chapter II). Here, we seek to combine the two theories. The interaction of the self focusing and laser cavity feedback can be classified into four regimes, depending on the relative degree of self focusing that occurs. When the self focusing acts to reduce the diffraction loss of the cavity, we have the energy limiter regime. When the self focusing acts to increase the diffraction loss (but not lasing threshold), we have the inducible loss regime. Intermediate between these two regimes, we have a transition regime. And when the self

focusing causes a change in the lasing threshold, we have the variable threshold regime. We can change the operating regime most easily by changing the sample length. These names are descriptive and their significance will become clear when we discuss each regime in detail. As implied by the above, self focusing interacts with the laser cavity via changes in spatial characteristics of the cavity field, especially changes in diffraction of these fields. This being the case, it is convenient to treat the cavity fields in terms of its two travelling wave components. In this approach, one follows one of these components as it makes a round trip passage through the cavity elements. Any reference to spatial size or spatial distribution of the cavity fields should be viewed as a reference to the spatial size or spatial distribution of the appropriate travelling wave component. The advantage with this approach is the ease in dealing with expansion due to diffraction, or focusing and beam shrinkage due to self focusing. These are most easily pictured as travelling wave phenomena. Any use of the word beam inside the cavity will be an explicit reference to one of the travelling wave components.

The energy limiter regime is characterized by smaller cavity mode size, improved cavity mode structure and smaller output beam divergence, as compared to that seen for normal operation. We use the term normal operation to refer to laser operation with no intensity dependent self focusing material present in the laser cavity. Consistent output characteristics require transverse mode stability. Use of a sufficiently small aperature insures this stability by allowing only the TE_{oo} cavity mode to lase. The size of the aperature, together with resonator geometry determines cavity diffraction loss. Physically, this loss arises

because the aperature is smaller than the cavity mode size, thus preventing part of the cavity fields from returning through the aperature. Diffraction loss from normal operation can be seen in Fig. 48a. The corresponding loss for the energy limiter regime can be seen in Fig. 48b. The fields shown in Fig. 48 are only an example, not actually observed fields. The effects are exaggerated for clearer viewing. The reduction in diffraction loss seen in Fig. 48b should be noted. (Since the fields do not expand as much, more gets back through the aperature.)

We define the energy limiter regime to be laser operation where the self focusing material acts to decrease diffraction loss, such as the case shown in Fig. 48b. Aside from unusual configurations (such as immersing the entire cavity in the self focusing material), operation in the energy limiter regime requires weak self focusing. The rather ambiguous quantifier "weak" in this case indicates self focusing where little if any shrinkage of the cavity fields occurs during a single passage through the self focusing material. For this limit, the effects of the self focusing material can be approximated by an intensity dependent lens (see Section IID). Operation in the energy limiter regime requires in addition that the induced lens be of sufficiently long focal length so diffraction after the focus is not worse than the original diffraction without the lens. In Chapter II, an expression for the effective focal length of the induced lens (with MBBA) was determined (Eqs. (61)-(67)) as a function of time and cavity intensity in the limit of weak self focusing. Since the required values of cavity intensity will not be determined until Chapter VI, a numerical analysis must wail until then. Here we present a qualitative picture that should clarify the physics of the process and give an understanding for the experimental

motivation and interpretation.

Initially, as the cavity fields are building up from noise, the intensity is low enough so no self focusing effects are observable. Thus, threshold conditions and the initial build up of cavity fields are unchanged from normal operation. As the intensity of the cavity fields increases, self focusing manifests itself as an induced lens whose focal length decreases as the intensity increases. This induced lens counteracts diffraction of the cavity fields, becoming more effective as the focal length decreases (Fig. 48). As a result, feedback to the center of the laser active material increases while feedback to the outer regions decreases. (All comparisons are comparisons to normal operation.) By center, we refer to the axis of the laser rod and by outer regions, we refer to the portion of the laser rod far off axis. When feedback to these outer regions decreases sufficiently, lasing will no longer occur in these regions, reducing the active lasing volume. Further intensity increases will cause continued reduction of lasing volume as long as these intensity increases act to reduce diffraction (via induced self focusing).

The energy stored in the laser rod for release depends primarily upon the pumping process and absorption of this pump prior to the start of the laser pulse. Once lasing starts, the population inversion is depleted so rapidly that any effects of the pump can be ignored. This means that the maximum energy available for lasing is independent of the actual pulse dynamics. How much of this energy gets released, however, depends strongly on these dynamics. Since the stored energy is localized, only the energy stored in the portion of the rod that lases can be emitted as laser output. Thus, any reduction in active lasing volume will

be accompanied by a proportional reduction in output energy. This is why we choose to call this the energy limiter regime. As the cavity intensity increases, the amount of energy emitted does not increase as rapidly and thus the energy output is limited. For a longer sample of self focusing material, the reduction of lasing volume should occur more quickly. Thus, less energy will be emitted for a given cavity intensity. Again, this is consistent with the name "energy limiter regime."

We next consider behavior of the on axis cavity intenstiy for this regime. Diffraction loss on axis comprises only a small fraction of the total on axis loss for our experimental set up (Eqs. (124) and (130)). We can use the experimental set up of Chapter III, since the set ups used for Chapters V and VI do not differ substantially and we seek here only a qualitative picture. The energy released from a small volume element on axis is proportional to $\tilde{n}_o - \tilde{n}_f$, the difference in initial and final normalized inversion population densities. The cavity loss enters in via the determination of $\tilde{n}_f$ (Eq. (137)). Because the diffraction loss is such a small fraction of the total loss, we expect the final inversion population density to change only inconsequentially from what it would be for normal operation. Thus, the total energy released from this small volume element on axis should be roughly the same as the total energy released with normal operation. (Self focusing in this regime serves to reduce diffraction loss but does not affect the remainder of the loss.)

Though the energy released from the center portion of the rod does not change much, the dynamics of the pulse do. The extra feedback to the center of the laser rod is amplified by the laser gain, so it has a large effect. The result is a quicker release of energy stored in the

center sections of the rod. This means dynamically, that the on axis cavity intensity will rise faster, and have a greater peak value than for normal operation, while the energy released from the center portion of the rod is approximately unchanged.

The utility of this technique lies in the inducible nature of the lens. We look at the cavity in a slightly different light to understand this utility. Using the ABCD matrices (see Chapter II), we can describe the combination of an induced positive lens with focal length f and a concave mirror with radius of curvature R, separated by a distance d as

$$\begin{bmatrix} 1 & 0 \\ -1/f & 1 \end{bmatrix}\begin{bmatrix} 1 & d \\ 0 & 1 \end{bmatrix}\begin{bmatrix} 1 & 0 \\ -2/R & 1 \end{bmatrix}\begin{bmatrix} 1 & d \\ 0 & 1 \end{bmatrix}\begin{bmatrix} 1 & 0 \\ -1/f & 1 \end{bmatrix}$$

$$= \begin{bmatrix} 1 - \frac{2d}{R} - \frac{2d}{f} + \frac{2d^2}{fR} & 2d - \frac{2d^2}{R} \\ -\left(1 - \frac{d}{f}\right)\left(\frac{2}{f} + \frac{2}{R} - \frac{2d}{Rf}\right) & 1 - \frac{2d}{R} - \frac{2d}{f} + \frac{2d^2}{fR} \end{bmatrix}$$

$$= \begin{bmatrix} 1 - \frac{2d}{\left(1 - \frac{d}{f}\right)}\left(1 - \frac{d}{f}\right)\left[\frac{1}{f} + \frac{1}{R} - \frac{d}{fR}\right] & , \frac{2d}{\left(1 - \frac{d}{f}\right)}\left[1 - \frac{d}{\left(1 - \frac{d}{f}\right)}\left(1 - \frac{d}{f}\right)\left[\frac{1}{f} + \frac{1}{R} - \frac{d}{fR}\right]\right] \\ -2\left(1 - \frac{d}{f}\right)\left[\frac{1}{f} + \frac{1}{R} - \frac{d}{fR}\right] & , 1 - \frac{2d}{\left(1 - \frac{d}{f}\right)}\left(1 - \frac{d}{f}\right)\left[\frac{1}{f} + \frac{1}{R} + \frac{d}{fR}\right] \end{bmatrix}$$

$$= \begin{bmatrix} 1 & \frac{d}{1 - \frac{d}{f}} \\ 0 & 1 \end{bmatrix}\begin{bmatrix} 1 & 0 \\ -2\left(1 - \frac{d}{f}\right)\left[\frac{1}{f} + \frac{1}{R} - \frac{d}{fR}\right] & 1 \end{bmatrix}\begin{bmatrix} 1 & \frac{d}{1 - \frac{d}{f}} \\ 0 & 1 \end{bmatrix} \tag{141}$$

which means we can replace the lens and mirror by a mirror with a radius of curvature R'

$$\frac{1}{R'} = \left(1 - \frac{d}{f}\right)\left[\frac{1}{f} + \frac{1}{R} - \frac{d}{fR}\right] \tag{142}$$

located at a distance

$$d' = \frac{d}{\left(1 - \frac{d}{f}\right)} \tag{143}$$

from the location of the induced lens. It is informative to plot 1 - L'/R' for the equivalent cavity versus 1/f. This is done in Fig. 49. L' is, of course, the length of the equivalent cavity

$$L' = L - d + d' = L + \frac{\frac{d^2}{f}}{\left(1 - \frac{d}{f}\right)} . \tag{144}$$

We use the values given in Fig. 20 for d and L. Four values of R are shown. For the moment, attention should be directed at the graph labelled "actual (R = 10 m)." We see that the equivalent cavity starts out nearly plane parallel ($f = \infty$) and as f decreases changes towards a confocal cavity ($1 - L'/R' = 0$). Graphically, the energy limiter regime is the region from $f = \infty$ to whatever f gives $1 - L'/R' = 0$ (confocal cavity). The reason for this should be clear; minimum beam size and diffraction loss occur for a confocal cavity (see Fig. 16). Thus any smaller f will result in increased diffraction loss.

Traditionally, the advantage of using a plane parallel cavity is the ability to easily select the TE_{oo} cavity mode with an aperature. The advantage of a confocal cavity lies in the smaller beam size and smaller output divergence angle. Operation in the energy limiter regime offers the advantage of both. Near threshold, where mode selection occurs, self focusing effects are negligible. So starting with a nearly plane parallel cavity gives good mode selection. As cavity intensities increase, the induced lens changes the effective cavity towards a confocal cavity. If the self focusing material parameters have been properly

selected, the peak of cavity intensity will occur when the effective cavity configuration is confocal, thus allowing most of the energy to be released near confocal conditions with an accompanying minimal output beam divergence.

Looking at the self focusing process as one of changing effective cavity configurations underscores the importance of the starting cavity configuration. We show the effects of an induced lens for different starting cavities in Fig. 49. From Fig. 49, several conclusions can be drawn. Since the self focusing for the energy limiter regime acts to move the cavity from a plane parallel configuration towards a confocal one, the closer to confocal the original cavity is, the less effect the self focusing will have. The intensity range over which the laser will continue to operate in the energy limiter regime is largest for a plane parallel cavity and decreases until it becomes nonexistent for a confocal cavity. If the cavity starts out with minimum possible diffraction loss (confocal cavity), any induced lens can only act to increase the loss. Thus, operation in the energy limiter regime will most likely favor a starting configuration close to plane parallel. This is what we use. A concentric cavity is also a possibility assuming the initial small increase in diffraction loss can be overcome. This choice is less desireable because of the weaker (i.e. slower) decrease in diffraction loss than for the plane parallel cavity.

So far, the discussion has been totally general and applies to any self focusing material. We now consider the actual material we use (MBBA) and features particular to its use. The immediate consideration is the response time of MBBA which with our laser system indicates a transient response. Since we are dealing with weak self focusing, the

transient case and the quasi-steady state case qualitatively do not differ greatly. In both cases, the self focusing has the effect of a thin lens. The precise behavior is described by the ABCD matrix given in Eq. (67). The primary qualitative difference is the temporal behavior of the induced δn. While the quasi-steady state induced δn will follow closely the cavity intensities, as the material response time becomes comparable to or exceeds the pulse width, the peak in induced δn will occur after the peak in cavity intensity. This delay will be longer for larger material response times. The decay of the induced δn from its peak value will depend primarily on the material response time. The latter causes the most noticeable effect on laser output. For very long material response times, the peak δn induced will decay very slowly (much slower than the cavity intensity will drop) so the trailing edge of the laser pulse will experience the peak δn. In terms of cavity configurations, this means that if the cavity is confocal at the peak, it will remain confocal for the remainder of the pulse. For shorter material response times, on the order of the pulse lengths, the induced δn will decay substantially during the trailing edge of the laser pulse. This means that if the cavity configuration was confocal at the peak δn, the trailing edge will see a cavity that is between confocal and plane parallel. Since cavity mode size grows as the cavity departs from confocal, the areas of the laser rod which were inhibited from lasing will again receive feedback. Since these sections have not yet released most of their energy, this return of feedback can induce a second laser pulse. The size of this second pulse should get larger as the material response time decreases from very much larger than the pulse width to a size comparable to the pulse width. (Less delay before feedback to the previous-

ly inhibited laser volume starts.)

A second feature that MBBA possesses is its critically divergent nonlinear response and relaxation time. We found in Chapter III, for the SIER induced loss, that the divergent behavior in both the relaxation time and the nonlinear response offset one another, leaving an effective nonlinear response which was only weakly dependent on temperature (Fig. 29). We expect to find a similar effect here, with the size of the induced δn only weakly dependent on temperature. Just as for the SIER induced loss, we expect that the greatest effect on the process attributable to temperature will be the modification of the dynamics of the process via the change in relaxation time. A description of how different relaxation times should affect the laser output was given in the preceeding paragraph. Using Table 1 or Fig. 4 to determine the relaxation time of the MBBA and assuming a pulse half width of 15-20 nsec, we see that at 50°C we expect a very small, if any, second pulse. The second pulse should become noticeable around 60°C, since the relaxation time is nearing pulse half width in length. This second pulse should be quite noticeable at 70°C where the relaxation time is less than the laser pulse half width.

For higher cavity intensities, longer sample lengths, larger nonlinear constants or any combination, the laser operation moves out of the energy limiter regime to a transition regime. Experimentally, we utilized longer sample to shift to this regime. Referring to Fig. 49, the transition regime is specified as operation with the induced cavity configuration between confocal and concentric ($-1 < 1 - L'/R' < 0$). Qualitatively, this regime is quite similar to the energy limiter regime. Though the exact behavior of the laser output will depend on the initial

configuration, its analysis does not change greatly. Thus, we will limit our discussion to the actual experimental set up (labelled actual on Fig. 49). From Fig. 16, we see that cavity diffraction loss is strongly dependent on cavity configuration near the plane parallel configuration, and only weakly dependent near the confocal configuration. Since the cavity configuration in the transition regime stays close to confocal, we expect only mild changes in laser output. These changes should be similar in nature to the second pulse seen in the energy limiter regime. For both cases, increased diffraction loss with an accompanying increase in feedback to the outer portions of the laser rod is responsible for this second pulse. One important qualitative difference exists. For the energy limiter regime, the second pulse occurs as the cavity intensity decreases, while for the transient regime this pulse occurs at peak cavity intensity. We expect, therefore, that the second pulse will be larger and take less time to reach its peak intensity in the transition regime. (Larger cavity intensity when feedback to the outer sections of the ruby rod starts.)

For still larger cavity intensities or longer cell lengths, laser operation takes place in the inducible loss regime. Laser behavior in this regime is quite similar to that seen for SIER inducible loss. As cavity intensity increases, the diffraction loss increases, thereby limiting the cavity intensity. The inducible loss regime is characterized by moderate self focusing. By moderate self focusing, we refer to sufficiently strong focusing so that the cavity fields leaving the sample will focus at or before the 100% rear mirror. This focusing can occur with or without an accompanying shrinkage of the cavity fields during a single pass through the sample. The induced diffraction loss increases mono-

tonically with cavity intensity once the inducible loss regime is reached, leading to pulse stretching. As with SIER induced loss, this pulse stretching is due to the "capping" of cavity intensity due to the induced loss. As sample length is increased, this limiting intensity will decrease. Using MBBA as a sample, we expect to see an overshoot of this limiting intensity followed by damping to an equilibrium behavior as typical of transient response.

An absolute limit for the sample length is given by the decrease of the limiting intensity to a value below laser threshold intensity. As the sample length approaches this limit, the self focusing will be sufficiently strong near laser threshold intensities to affect the threshold conditions. This regime is the variable threshold regime. It is characterized by substantial changes in the amount of pumping needed to start the lasing process. We mention this regime simply for completeness; in general it is to be avoided as it provides no useful properties and substantially increases pump energy requirements.

C. Conclusions

In this chapter, we have given a qualitative picture for self focusing in a laser cavity. This picture will guide us in the choice of experiments needed to more fully understand the phenomenon. These experiments will allow a self consistent quantitative model to be determined. In the following chapter, various experiments will be described and the data presented. This data will be analyzed in Chapter VI. From the experimental results, we have seen that significant SIER induced loss can occur for sample lengths on the order of 1-2 cm. At these lengths, the self focusing induced effects are those of the energy limiter and trans-

ient regimes. Thus, longer sample lengths are needed to operate in the self focusing inducible loss regime than for SIER inducible loss. This together with the complications of a changing cavity configuration means that SIER inducible loss is the preferred means of obtaining an inducible loss. Because of this, our experimental work will concentrate primarily on the energy limiter regime. This regime offers the greatest promise in terms of utility.

Figure Captions

Fig. 48. Comparison of cavity diffraction under normal operation (a) with cavity diffraction in the energy limiter regime (b). Both (a) and (b) have been exaggerated for viewing clarity.

Fig. 49. $1 - L'/R'$ of a cavity with an induced lens replacing the MBBA cell. We plot $1 - L'/R'$ versus the inverse of the focal length of the induced lens for various starting cavity configurations. Cavity parameters are as indicated.

Figure 48

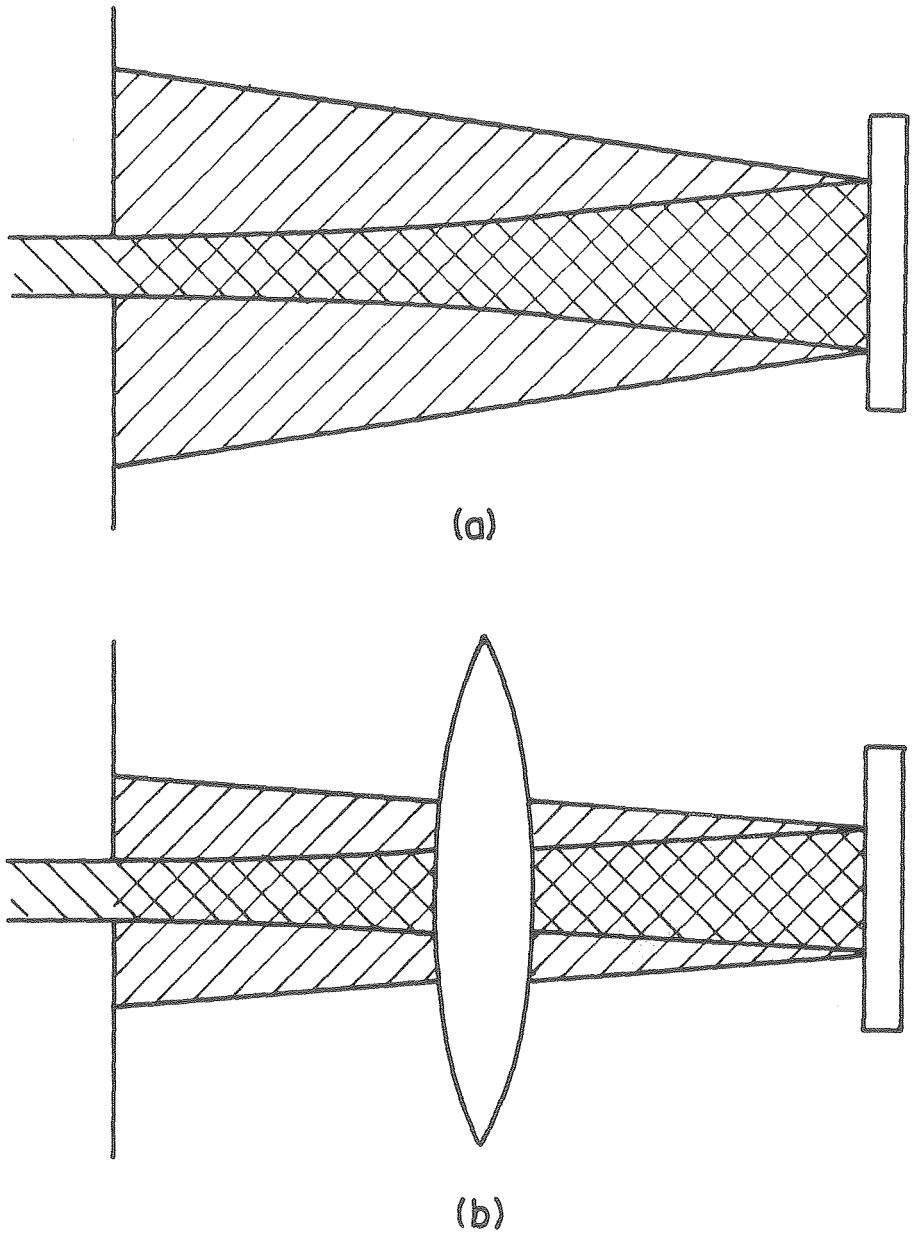

XBL 8010-6162

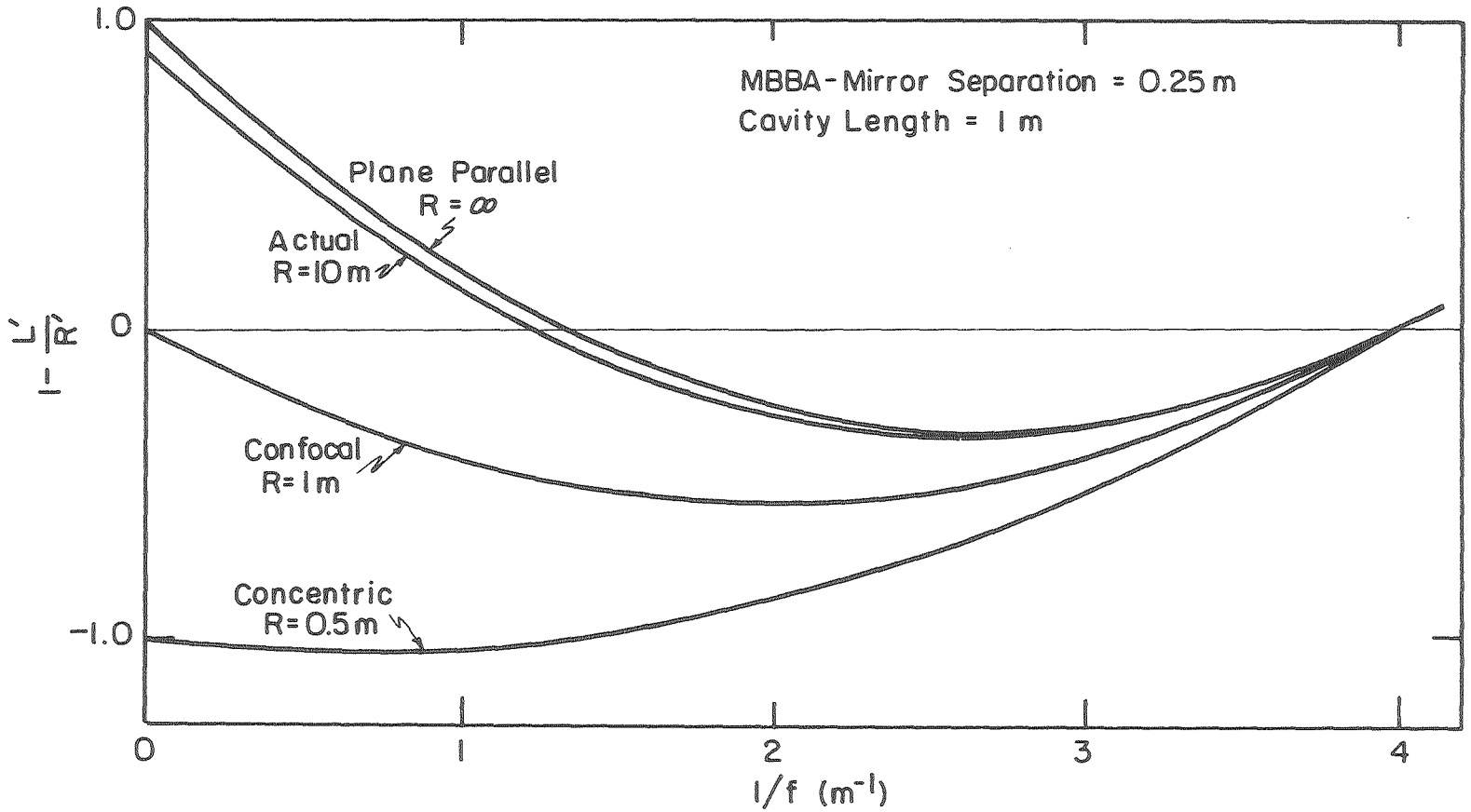

XBL8010-6163

Figure 49

V. SELF FOCUSING EXPERIMENTAL SET UPS AND DATA

A. Introduction

In this chapter, we describe various experiments we have done to better understand intracavity self focusing. For each experiment we give the motivation for the experiment, the set up used, the data taken and the techniques used to reduce the data. The experiments can be grouped as follows:

Section B - Mode size vs. sample length

C - Time dependence of total output power for different sample lengths

D - Temperature dependence for a fixed sample length

E - Mode fluctuation

F - Origin of secondary peak

G - Cavity fluence at different cavity locations.

Actual analysis of the data will be done in Chapter VI.

The basic experimental set up is shown in Fig. 50. The laser source is a ruby laser Q-switched by a saturable absorber, cryptocyanine. The laser rod was brewster cut with a 50% resonant reflector as the output coupler. This resonant reflector provided longitudinal mode selection. The second mirror had a 10 m radius of curvature with a 100% reflecting dielectric coating. Spatial mode selection was provided by the use of a 1.7 mm pinhole. The unperturbed laser output was 2.7 mj into a 45 nsec pulse. The He-Ne laser was used for alignment, the photodiode for recording output power and the camera/pellicle pair for recording the spatial distribution of the cavity fields.

Photodiode output was monitored on a Textronix 519 oscilloscope and

recorded on high speed polaroid film. A vacuum photodiode with an S1 surface was used, providing a 200 picosecond response time. Together with the scope response time of 300 picoseconds, we have an overall time resolution of 0.5 nanoseconds. This was more than sufficient to observe the 20-40 nanosecond ruby laser pulses. From its position at the laser cavity output, the photodiode provided spatially integrated, time resolved profiles of laser output power, to compliment the data obtained by the 35 mm camera/pellicle combination.

Using a pellicle enabled us to couple out a fraction of the cavity fields, while perturbing these same fields to the smallest degree possible. The light reflected by the pellicle passed through a 5 cm lens, located 16.5 cm from the film plane of our 35 mm camera. This provided a small magnification ($\sim 2.3\times$). Kodak panatomic-X film was chosen for its good resolution (~ 5 μm) and large latitude or range of linear response (~ 10 f-stops or 3 orders of magnitude). Care was taken to develop related rolls of film together, and to keep developing times and conditions as similar as possible for different batches. We scanned the negatives using a PDS microdensitometer at 50 μm resoltuion. A full two-dimensional scan was performed, and the data transmitted to a computer for processing. This computer processing recreated the spatial profile of the cavity fluence.

The process described above to determine cavity fluences was tedious and time consuming. In those instances when only a rough indication of the cavity mode size was needed, we used a much cruder but quicker method. This method used the size of the burn spot on a piece of exposed polaroid film as a measure of cavity mode size. The burn spot is generated by placing the exposed film directly in the path of the laser out-

put. In addition to giving a rough measure of cavity mode size, the burn pattern also served as a monitor for the spatial mode composition of the cavity fields. For our experiments, the burn patterns were taken a point immediately in front of the He-Ne laser, thus allowing the signal to reach the fast photodiode simultaneously.

Temperature control for the MBBA cell was provided by a Yellow Springs temperature controller together with an oven surrounding the cell. This enabled us to maintain the temperature to 0.1°C. The oven and cell were made of stainless steel to avoid MBBA reaction with the cell walls. Windows were 3/8 inch fused silica anti-reflection coated to minimize insertion losses. Large variations in cell length were achieved by switching cells while small changes were achieved by tilting the cell.

B. Mode Size vs. Sample Length

One essential requirement is to establish that the sample, MBBA in our case, indeed is responsible for the effects seen. A simple method of verification is to change the length of the MBBA cell while monitoring any induced changes in laser output. Using the basic set up shown in Fig. 50 and described in part A of this chapter, we measure the cavity mode size as the cell length is varied. The simpler technique which measures the size of the burn spot on polaroid film was used to determine this mode size. As explained in Chapter IV, this mode size will vary over the duration of the pulse. However, most of the energy will be released in a mode whose size corresponds to the peak of laser output. This makes it easy to pick out this mode size when examining the burn spots. The cavity mode sizes as measured using burn spots one meter from

the cavity are shown in Fig. 51. Clearly there is a strong dependence on MBBA sample length.

C. Time Dependence of Output Power for Different Cell Lengths

Simultaneously with the data taken for part B, the output power as measured at the photodiode (see Fig. 50) was monitored. The time dependence of this output power for three different sample lengths (1 cm, 1.75 cm, 5 cm) can be seen in Fig. 52 together with the data when no MBBA is present at all. Here again, a definite change is seen as sample length varies. The spatial mode structure as determined by the shape of the burn pattern of part B above indicated excellent spatial mode selection. The data of Figs. 51 and 52 will be used to verify the qualitative aspects of the proposed model in Chapter VI.

D. Temperature Dependence at Fixed Cell Length

To understand how the self focusing action in the sample changes laser output, it is best to study the simplest of the regimes. This, of course, is the energy limiter regime. From Fig. 51, it appears that a sample length of 1 cm should be ideal for this purpose. (Recall from Chapter IV that mode size should be smallest at the sample length giving the optimal energy limiter operation.) Having selected a cell length, we are interested in seeing how changes in sample temperature will affect laser operation. This information is of value because of the strong temperature dependence of the MBBA material properties. It is important to know how this temperature dependence will manifest itself.

As in parts B and C of this chapter, we use the basic set up of Fig. 50. The output power was monitored at the photodiode while cavity mode

structure and mode size was monitored by examining the burn spot on a sheet of polaroid film placed directly in front of the He-Ne laser. (This also helps protect the He-Ne tube from the high intensity ruby laser output.) The results are shown in Fig. 53. In parts a-g, we have plotted the output power of the laser as a function of time. In part h, we have shown the size of the burn spot for various sample temperatures. The lower set of points for Fig. 53h represents the mode size when laser output power is at its peak, while the upper set of data points represents the total size of the burn spot. As will be seen in later analysis, both sets of points provide support for the proposed model.

E. Mode Fluctuations

Three major sources of fluctuation affect the shot to shot stability of the laser system and hence the reproducibility of any results seen. It clearly is desirable to eliminate these fluctuations, but this frequently can prove to be exceedingly difficult and time consuming. A more easily attained goal and one nearly as effective is to identify the effects of these fluctuations and thereby learn how to screen out the fluctuations before any analysis is done. The sources of fluctuation can be divided into intensity fluctuations, spatial mode fluctuations, and longitudinal mode fluctuations. We will consider each source in turn and discuss how it was handled.

Under the classification of intensity fluctuation, we include any change in laser output which cannot be associated with mode fluctuations. Typical causes are varying pump absorption, temperature fluctuation in the active medium or misalignment of the laser. This source of fluctuation was difficult, but not impossible, to eliminate. Careful attention

to alignment, flashlamp condition, flashlamp placement, the orientation and positioning of intracavity elements, the time interval between pulses, and the power delivered to the flashlamps was sufficient to substantially reduce intensity fluctuations to < 1% over the short term (5-10 minutes) and < 10% over the long term (1-2 days). This reduction lowered errors induced by intensity fluctuations to a level much below than that generated from the mode fluctuations. What little fluctuation remained could easily be normalized.

Spatial mode fluctuations encompass both the change in the transverse distribution of energy in a laser cavity and power fluctuations resulting from these changes. Use of a pinhole properly centered and careful alignment of the laser produced a relatively pure TE_{oo} mode. Mode quality could be easily monitored by examination of the burn spot on a piece of exposed polaroid film. Because of this relatively pure TE_{oo} mode structure output power fluctuations due to transverse mode fluctuation were very small. Occasionally, a pulse with a large admixture of a higher morder mode occured. When this happened, the reduction in lasing volume due to self focusing was inhibited, which could clearly be seen in the burn pattern on the polaroid film. The result was a dramatically increased output power. This effect allowed us to easily discriminate against such pulses, retaining only the relatively pure TE_{oo} pulses for analysis. Though we were able to effectively eliminate spatial mode fluctuation, substantial errors remained manifesting themselves as deviation from cylindrical symmetry expected for TE_{oo} modes, local hot spots in the energy distribution and small changes in overall mode size. These problems can be traced to imperfections in the ruby rod, dust particles in the cavity, defects in the surface of the pellicle and damage

to the windows or coatings of the various intracavity elements. As such, the errors cannot easily be removed and cannot easily be corrected for. The best that can be done is to average over the flaws seeking to recreate the energy distribution which would have been seen, given a perfect cavity. This was done and the errors could be greatly reduced, in effect, but not eliminated.

Longitudinal mode fluctuation represents the presence of two or more longitudinal modes in the cavity rather than a single mode. The output etalon serves as the primary mode selector. The combination of this resonant reflector with the natural lineshape of the ruby line is sufficient to achieve single mode operation (see Chapter IIE). However, it is necessary to take proper precautions, among which are operation in a single transverse mode and not pumping the laser too hard. By this latter statement, we mean that the laser is to be operating above threshold but not excessively so. This is usually sufficient to limit lasing to one or two modes. Unfortunately, the reflection peaks of the etalon shift with temperature. This means that because our set up did not stabilize the temperature of the resonant reflector, it was impossible to guarantee a single mode — there always being the possibility that two adjacent modes will lase symmetrically about the etalon peak. However, with only two modes, it is easy to detect the presence of the second mode. When both modes lase, they will beat together modulating the output at the beat frequency, which is clearly seen. Thus, it is simple to reject the data which corresponds to multiple modes, leaving only the single mode data for analysis. By this means, we successfully neutralize any errors due to longitudinal mode fluctuation.

F. Origin of Second Peak

Looking again at Fig. 53, we see the very prominent second peak that develops at the higher temperatures. This peak is predicted by the theory and it would be useful to determine experimentally the origin of this peak. Ideally, we would use a gate which would admit only a selected portion of the pulse. Shifting the gate would then allow us to generate a motion picture of the spatial evolution of the laser pulse. These measurements could also be made for the cavity fields, giving a clear picture of the progression for cavity fields as well. Unfortunately, using a saturable absorber Q-switch introduces a jitter in the start time of the pulse, which is greater than the length of the pulse. It was therefore impossible to synch the gate to any external electronics. Combined trigger delay and Pockel cell response time was sufficiently long so that we could not use the laser output itself to trigger the Pockel cell either. Because of this impossibility of synchronizing the gate, we were unable to implement this more favorable technique of determining the data. It should be pointed out that this technique could have been implemented in a system utilizing a Pockel cell Q-switching technique. For the purposes of this experiment, it was considered impractical to switch over to such a system. The method of Q-switching plays a major role in any intracavity studies and this experiment was the last data obtained. (Chronologically, this experiment followed that of section G.) The large quantities of data already accumulated using a saturable absorber Q-switch rendered any change in Q-switch technique an unreasonable waste of the data collected and unfeasible in terms of time needed to redo the entirety of the experiments. Thus, we use a less precise technique to obtain our motion picture, leaving the better technique to be

implemented in some future experiment.

The technique we used measured the light transmitted through a pinhole, whose size was lesser than the spatial extent of the beam. By translating the pinhole, it is possible to measure the cavity power versus time for the different spatial elements of the beam cross section. The set up used can be seen in Fig. 54. The orientation of the pellicle is such that the travelling wave component of the cavity propagating from the 100% mirror towards the laser rod was measured. The pinhole size and lens focal length were chosen to give a reasonably large signal at the photodiode when the pinhole is positioned near the edge of the beam. This resulted in a pinhole size roughly 10% of the spatial extent of the beam when it arrives at the pinhole. Translation of the lens shifted the beam across the pinhole. Data were taken for three positions of the pinhole with respect to the beam, as shown in Fig. 55. The data corresponding to these positions can be seen in Fig. 56. The positions a, b, c in Fig. 55 correspond to parts a-c in Fig. 56. The ordinant for Fig. 56d is output power of the laser and is shown for comparison purposes. Figures 56a-c, on the other hand, plot cavity power (power at photodiode corrected for pellicle reflection and loss at lens/air or prism/air interfaces). Once again, a burn spot on polaroid film was used to monitor cavity spatial mode structure. Care was taken to use pulses exhibiting identical burn patterns and total output power for the comparisons in Fig. 56a-d.

G. Cavity Fluence at Different Cavity Positions

We have saved until the last the most important of the data taken — the detailed determination of the spatial distribution of the laser

cavity fields, both in the presence and absence of MBBA. It is this data that will enable us to make semi-quantitative comparisons in Chapter VI. The analysis is quite complicated and we will include the portion of the analysis having to do with optical propagation of Gaussian beams and other data reduction here, to avoid confusion in Chapter VI. This section will first present the data with an explanation of how it was obtained. This will be followed by an outline of the analysis. Finally, we will present the detailed analysis.

The spatial distribution of the cavity fields was measured by reflecting a small fraction of the fields (2-3%) out of the cavity with a pellicle and projecting these fields onto photographic film, as shown in Fig. 50. With the pellicle oriented as shown in Fig. 50, the travelling wave component travelling away from the 100% mirror and towards the ruby rod is recorded. With a 90° rotation in pellicle orientation, we record instead the travelling wave component travelling away from the ruby rod and towards the 100% mirror. Both orientations of the pellicle were utilized at the six positions labelled 1-6 in Fig. 57. Insertion losses for the pellicle make it undesirable to use more than one pellicle, so the data was obtained using separate pulses, moving the pellicle after data acquisition was completed for each position.

Each photograph taken records the energy/unit area incident on the film. Thus, by analyzing the film, we can determine the cavity fluence $\mathscr{F}(r,\theta)$ through a plane perpendicular to the cavity axis and passing through the pellicle position. The cavity fluence is related to the cavity intensity by

$$\mathscr{F}(r,\theta) = \int_{-\infty}^{+\infty} I(r,\theta,t)dt \tag{145}$$

where r,θ are polar coordinants in the plane described above and $I(r,\theta,t)$ is the intensity of the cavity field. Of course, both $\mathscr{F}(r,\theta)$ and $I(r,\theta,t)$ refer to the travelling wave component being recorded. We choose $r = 0$ to be the intersection of the plane and the cavity axis. Due to the predominance of the TE_{oo} mode, the fluence is maximal for $r = 0$ and to a large extent cylindrically symmetric. We show a computer recreation of two of the photographs in Figs. 58 and 59. These photographs were taken with the pellicle in position 1 oriented as shown in Fig. 50. Figure 58 was taken with no MBBA present, while Fig. 59 was taken with it present. The expected reduction of the lasing volume can apparently be seen in Fig. 59, where there clearly is a bright central spot or region surrounded by a much weaker "halo." This implies that lasing action has been restricted in some fashion by the MBBA, particularly since the "halo" has much the same size as the spatial cross section of Fig. 58 and thus is likely to have resulted from lasing action before self focusing became effective. The area represented is roughly 4 mm in diameter on the film and the density of print corresponds roughly to the density of the film negative.

Each of the photographic negatives was analyzed using a PDS scanning microdensitometer. A 50 μm square window was used in conjunction with a 50 μm step size to give complete coverage of the image. We scanned a 7.5 mm × 7.5 mm square containing the 4 mm image with a two-dimensional scan pattern, recording the density at each of the 22,500 scan points onto magnetic computer tape. Figures 58 and 59 were constructed using two of the data files so generated. The data taken by the PDS microdensitometer (i.e. the data values on computer tape) will be considered the starting point for our analysis.

In the analysis that follows, we will follow a systematic procedure whose end goal is a determination of the Gaussian mode size inside the cavity. The steps involved are as follows:

1) Convert densitometer output units to actual physical units. Correct for any errors introduced by the photographic film.
2) Determine mode size at the film.
3) Use results of 2), apply standard equations for propagation of Gaussian beam to determine mode size in the cavity.

A typical film response curve for Kodak Pan-X film can be seen in Fig. 60, where we plot the density of the photographic negative as a function of the log of the energy fluence falling on the negative. The coordinants r', θ' refer to polar coordinants on the negative, with $r' = 0$ on the negative corresponding to $r = 0$ in the cavity. $\mathscr{F}'_o$ is the threshold fluence for which the film first starts responding to the incident light and $\mathscr{F}'_m$ is the fluence for which the film response saturates. There is roughly a three order of magnitude range of fluence between $\mathscr{F}'_o$ and $\mathscr{F}'_m$, for which the negative density varies linearly with the log of the incident fluence. Peak incident fluences were between $\mathscr{F}'_o$ and $\mathscr{F}'_m$ in value. This means that a correction factor for the toe of the film response curve will be required, but that one for the shoulder will not be.

The densitometer reads the film densities and generates a numerical output in nonphysical "densitometer units." These "densitometer units" $D_o(r',\theta')$ vary linearly with the actual film density.

$$D_o(r',\theta') = \alpha' D(r',\theta') + \beta'. \tag{146}$$

If we replace the film response curve (Fig. 60) with the linear approxi-

mation

$$D(r',\theta') \cong \begin{cases} \alpha'' \log(\mathscr{F}'(r',\theta')/\mathscr{F}'_o) + \beta'' & \mathscr{F}'(r',\theta') \geqslant \mathscr{F}'_o \\ \beta'' & \mathscr{F}'(r',\theta') < \mathscr{F}'_o \end{cases} \tag{147}$$

we have for the densitometer output

$$D_o(r',\theta') = \begin{cases} \alpha \log(\mathscr{F}'(r',\theta')/\mathscr{F}'_o) + \beta & \mathscr{F}'(r',\theta') \geqslant \mathscr{F}'_o \\ \beta & \mathscr{F}'(r',\theta') < \mathscr{F}'_o \end{cases}$$

$$\alpha = \alpha'\alpha''$$

$$\beta = \alpha'\beta'' + \beta'. \tag{148}$$

The problem of converting $D_o(r',\theta')$ to physical units is thus seen to be one of finding α, β, and $\mathscr{F}'_o$.

The determination of α, β, and $\mathscr{F}'_o$ depends on relating $D_o(r',\theta')$ to some physical quantity whose size can be determined. The only quantity which can be easily measured is the total output energy present in the pulse. (The quantity must be a time integrated quantity, such as energy rather than power, because the film density measures fluence, also a time integrated quantity.) The energy related to the fluence by

$$E = \int_o^{2\pi}\int_o^{\infty} \mathscr{F}(r,\theta) r dr d\theta \gamma$$

$$= \gamma C \mathscr{F}(r = 0) \tag{149}$$

where we have defined a quantity C, which is the spatial integral over the cavity fluence profile:

$$C = \int_0^{2\pi}\int_0^{\infty} \frac{\mathscr{F}(r,\theta)}{\mathscr{F}(r = 0)}\, r dr d\theta \tag{150}$$

and γ is the ratio of output energy to cavity energy. It is important to distinguish between the unprimed $\mathscr{F}$'s, which refer to cavity fluences, and the primed $\mathscr{F}$''s, which refer to film plane fluences. The cavity fluence is related to that of the film plane by

$$C'\mathscr{F}'(r' = 0) = \mathscr{T} C \mathscr{F}(r = 0) \tag{151}$$

where $\mathscr{T}$ is the energy transport from the cavity to the film (i.e. fraction of cavity energy reaching the film). C' is equivalent to C, but defined at the film plane. It is now possible to relate the densitometer output to the energy E.

$$D_o(r' = 0) = \alpha \log(\mathscr{F}'(r' = 0)/\mathscr{F}'_o) + \beta$$

$$= \alpha \log(E/1 \text{ mJ}) + \alpha \log(1 \text{ mJ} \cdot \mathscr{T}/\gamma C'\mathscr{F}'_o) + \beta. \tag{152}$$

By plotting $D_o(r' = 0)$ vs. the corresponding E's, we can do a least square fit to Eq. (152) to determine α. The unavoidable long term intensity fluctuations can be put to good use here, providing the range in energy content needed for a good fit. (Recall from section VE that we eliminated short term fluctuations.) The data taken for the various pellicle positions shows this spread of energies and is used for the purpose. Unfortunately, the presence of the C' in the expression of Eq. (152) requires the use of data for which C' varies only weakly, or not at all.

After examination of the data, it was determined that the bright central region containing most of the energy and seen with MBBA in the cavity, would fit this criterion. The presence of the MBBA is sufficient to substantially reduce diffraction in the cavity and thus reduce the change in C' between data taken for the different pellicle positions. Looking at the data, we see that the spatial profiles may be grouped as follows:

$\left\{\begin{matrix}① \\ ② \\ ③\end{matrix}\right\}$ $\left\{\begin{matrix}④ \\ ⑤ \\ ⑥\end{matrix}\right\}$ component travelling towards mirror

$\left\{\begin{matrix}\boxed{1} \\ \boxed{2} \\ \boxed{3}\end{matrix}\right\}$ $\left\{\begin{matrix}\boxed{4} \\ \boxed{5} \\ \boxed{6}\end{matrix}\right\}$ component travelling towards rod.

The numbers refer to pellicle position. These groupings are empirical and within each grouping the C''s do not seem to vary significantly. However, the C''s do seem to change between the groups. Thus, we must do a fit for each group separately. Since the C' appears only in the constant term of Eq. (152) and not in the log(E/1 mJ) term, we expect the same α for all the groups. In Fig. 61, we plot the various $D_o(r' = 0)$ as a function of log(E/1 mJ). We do a linear least squares fit for each of the four groups above, requiring the same slope α for all four groups, but possibly different intercepts. The resulting fit is seen superimposed on the data points in Fig. 61. The final value determined for α is

$$\alpha = 115.4 \text{ densitometer units.} \tag{153}$$

The intercepts at log (E/1 mJ) = 0 also have significance and this will be discussed at the end of the chapter.

Having determined α, it is now possible to convert $D_o(r',\theta')$ to log $(\mathscr{F}'(r',\theta')/\mathscr{F}'_o)$ for all our photographs by using Eq. (148). β being the background, can be easily determined by averaging over the film density where no signal is present. As mentioned in section VE, there is a shot to shot departure from perfect cylindrical symmetry. This deviation is small and appears random (as opposed to systematic). Therefore, we cylindrically averaged the data. Two examples of the averaged and converted data are seen in Figs. 62 and 63. These correspond to the raw data of Figs. 58 and 59.

Consider once again Fig. 60. Near the toe region, our approximation in Eq. (147) is not accurate, predicting much too sharp a threshold. Instead the slope α' goes smoothly to 0 near $\mathscr{F}'_o$. Because of the gradual threshold, information is contained in the toe region which can be extracted if one knows qualitatively how much weaker the response in the toe region is compared to the response in the linear region. The procedure for determining the toe response is to expose the film to a known spatial pattern and compare the measured film densities to the known intensities. The equivalent technique for our experiment is to use the photographs taken with no MBBA in the cavity to determine the toe response. According to well known theory,[18,29] the spatial distribution of fields in the cavity for a TE_{oo} mode should follow a Gaussian shape. Thus, the fluence $\mathscr{F}'(r',\theta')$ falling on the film with no MBBA present should also follow a Gaussian shape. We expect

$$\mathscr{F}'(r',\theta') = \mathscr{F}'(r' = 0)e^{-2r'^2/w^2}$$

$$D_o(r',\theta') = \alpha \log(\mathscr{F}'(r' = 0)/\mathscr{F}'_o) - 2\alpha r'^2/w^2 + \beta. \qquad (154)$$

Thus, the density on the film should follow a quadratic behavior with r'.

It is now a simple matter to fit the densities from the linear response region of the film curve to a parabola, extrapolate the parabola into the toe region, and then compare the fluences calculated using the observed densities to those calculated using the extrapolated densities. This generates a correction factor δ where

$$\delta = \log\left(\frac{\langle\mathscr{F}'(r',\theta')\rangle_{\theta'} \text{ calculated using observed densities}}{\langle\mathscr{F}'(r',\theta')\rangle_{\theta'} \text{ calculated using extrapolated densities}}\right)$$

$$= \log\left(\frac{\langle\mathscr{F}'(r',\theta')\rangle_{\theta'}}{\mathscr{F}'_o}\right)_{\text{observed}} - \log\left(\frac{\langle\mathscr{F}'(r',\theta')\rangle_{\theta'}}{\mathscr{F}'_o}\right)_{\text{actual}}. \qquad (155)$$

Only those photographs for which the densities in the linear regime were clearly parabolic were used; this insures that the extrapolation is reasonable. Also, only those photographs taken with no MBBA in the cavity could be used; the MBBA introduces changes in the cavity field distribution. The various δ's determined by the photographs satisfying these criteria are plotted in Fig. 64 as a function of observed $\log(\langle\mathscr{F}'(r',\theta')\rangle_{\theta'}/\mathscr{F}'_o)$. A hand-drawn average is shown as well. This average correction factor can then be used with Eq. (155) to determine actual film plane fluences from the observed fluences for all of the photographs. Note that the average δ is still a function of the observed fluences, the averaging being only over the various photographs used to determine the δ's.

We now have accomplished the first of the three tasks planned for this section. Knowing the actual fluences at the film plane, we must analyze these fluences to determine mode sizes at the film plane. This procedure for data taken with no MBBA in the cavity is straightforward. Since the mode structure is predominantly TE_{oo}, we expect a Gaussian shape for the fluence (Eq. (154)). This is indeed what we find. The width of this Gaussian distribution can be seen in Fig. 65 as a function of pellicle position. Error bars indicate a relatively poorer fit to a Gaussian so that the width could not be as accurately determined. In displaying Fig. 65, we arranged the pellicle positions to correspond to what an observer on a photon would see as the photon travelled from the pinhole to the 100% mirror and back to the pinhole. Essentially, we have unfolded the cavity for display purposes.

The data when MBBA is present in the cavity is slightly more complicated. The bright central region can be fitted quite well by a Gaussian shape. Likewise, the outer edge of the recorded data can be fitted by a Gaussian, though one with a different width than for the central region. The data between these areas does not appear to fit any simple function. These different regions are portrayed schematically in Fig. 66. Figure 67 corresponds to Fig. 65 and displays the widths for the two Gaussian components as a function of pellicle position.

The last task for this section is the determination of cavity mode size from the measured film plane mode sizes (Figs. 65 and 67). The propagation of Gaussian modes was discussed in Chapter IIE (Fig. 14 and Eqs. (80)-(84)). We will use the theory presented there to calculate how a Gaussian beam with a Gaussian beam parameter

$$\frac{1}{q_c} = \frac{1}{R_c} - i\,\frac{\lambda}{\pi n w_c^2} \tag{155}$$

in the cavity will change by the time it reaches the film plane. The subscript c refers to the laser cavity, λ refers to the wavelength of the light, n refers to the index of refraction of the propagation medium, and R_c and w_c refer to the beam radius of curvature and beam size, as defined in Fig. 14. After leaving the cavity (reflected out by the pellicle), the beam propagates through α_1 cm till it reaches a lens of focal length f cm, passes through the lens and propagates a distance d_2 cm until it impinges on the film. The ABCD matrices for these steps are given in Eq. (84). Applying these matrices to the Gaussian beam parameter q_c in the cavity, we obtain the Gaussian beam parameter q_f at the film.

$$\begin{aligned} q_f &= \begin{bmatrix} 1 & d_2 \\ 0 & 1 \end{bmatrix} \begin{bmatrix} 1 & 0 \\ -\frac{1}{f} & 1 \end{bmatrix} \begin{bmatrix} 1 & d_1 \\ 0 & 1 \end{bmatrix} (q_c) \\ &= \begin{bmatrix} 1 - \frac{d_2}{f} & d_1 + d_2 - \frac{d_1 d_2}{f} \\ -\frac{1}{f} & 1 - \frac{d_1}{f} \end{bmatrix} (q_c). \end{aligned} \tag{156}$$

At this point, if we knew both w_f and R_f, the beam size and beam radius of curvature at the film plane, we could invert Eq. (156) and solve for q_c. Unfortunately, the film only measures w_f. We need more information to uniquely determine the q_c.

This information can come from the relationship between the q_c at various points in the cavity. Since we are measuring the travelling wave component, the q_c must obey the equations for propagation of a Gaussian beam inside the cavity. We establish the notation

$$q_c(z) = q_c \text{ at position } z$$

$$q_c(z + \Delta z) = q_c \text{ at position } z + \Delta z$$

$$q_f(z) = q_f \text{ corresponding to } q_c(z)$$

$$q_f(z + \Delta z) = q_f \text{ corresponding to } q_c(z + \Delta z). \tag{157}$$

The $q_c(z)$ and $q_c(z + \Delta z)$ must be related by

$$q_c(z + \Delta z) = \begin{bmatrix} 1 & \Delta z \\ 0 & 1 \end{bmatrix} (q_c(z)). \tag{158}$$

We can combine Eqs. (156)-(158) to get

$$\begin{aligned} q_f(z + \Delta z) &= \begin{bmatrix} 1 - \frac{d_2}{f} & d_1 + d_2 - \frac{d_1 d_2}{f} \\ -\frac{1}{f} & 1 - \frac{d_1}{f} \end{bmatrix} \begin{bmatrix} 1 & \Delta z \\ 0 & 1 \end{bmatrix} (q_c(z)) \\ &= \begin{bmatrix} 1 - \frac{d_2}{f} & D(\Delta z) \\ -\frac{1}{f} & 1 - \frac{(d_1 + \Delta z)}{f} \end{bmatrix} (q_c(z)) \end{aligned} \tag{159}$$

where

$$D(\Delta z) = d_1 + d_2 + \Delta z - \frac{(d_1 + \Delta z) d_2)}{f} . \tag{160}$$

We have expressed q_f in terms of q_c, rather than the inverse, because the real part of $1/q_f = 1/R_f$ is not known. However, we can use Eq. (159) to solve for $w_f(z + \Delta z)$ in terms of $w_c(z)$ and $R_c(z)$ for various values of Δz. This enables us to iterate over possible values for $w_c(z)$ and $R_c(z)$

to obtain the best least squares fit of Eq. (159) to the measured $w_f(z + \Delta z)$, and thereby determine the $w_c(z)$ and $R_c(z)$. Using Eqs. (156) and (159) we have:

$$
\begin{aligned}
w_f(z + \Delta z) &= \left[- \frac{\pi n}{\lambda} \operatorname{Im} \frac{1}{q_f(z + \Delta z)} \right]^{-\frac{1}{2}} \\
&= \left[- \frac{\pi n}{\lambda} \operatorname{Im} \left\{ \frac{- q_c(z)/f + 1 - (d_1 + \Delta z)/f}{q_c(z)(1 - d_2/f) + D(\Delta z)} \right\} \right]^{-\frac{1}{2}} \\
&= \left[\frac{\pi n}{\lambda f} \operatorname{Im} \left\{ \frac{1 - (f - d_1 - \Delta z)/q_c(z)}{(1 - d_2/f) + D(\Delta z)/q_c(z)} \right\} \right]^{-\frac{1}{2}} \\
&= w_c(z) \left\{ [(1 - d_2/f) + D(\Delta z)/R_c(z)]^2 + \lambda^2 D^2(\Delta z)/\pi^2 n^2 w_c^4(z) \right\}^{\frac{1}{2}}.
\end{aligned}
\tag{161}
$$

In doing the least squares fit of Eq. (161) to the measured $w_f(z + \Delta z)$, it is useful to have a starting value for $w_c(z)$ and $R_c(z)$. We obtain such a starting value by inverting Eq. (161) and solving the resulting equation for two of the measured $w_f(z + \Delta z)$. The procedure involved is straightforward and algebraically tedious. Since no new information or knowledge is gainged in doing the calculation, we skip the intermediate steps and present directly the solutions.

$$
\begin{aligned}
w_c(z_1) = \frac{1}{(1 - d_2/f)^2 (z_2 - z_1)} \Bigg\{ & D^2(0) w_f^2(z_2) + D^2(z_2 - z_1) w_f^2(z_1) \pm 2D(0) \\
& \times D(z_2 - z_1) \sqrt{w_f^2(z_1) w_f^2(z_2) - \frac{\lambda^2 (1 - d_2/f)^4 (z_2 - z_1)^2}{\pi^2 n^2}} \Bigg\}^{\frac{1}{2}}
\end{aligned}
$$

$$
\begin{aligned}
R_c(z_1) = - (1 - d_2/f)^3 (z_2 - z_1)^2 w_c^2(z_1) / \Bigg\{ & D(0) w_f^2(z_2) + D(z_2 - z_1) w_f^2(z_1) \\
& \pm (D(0) + D(z_2 - z_1)) \sqrt{w_f^2(z_1) w_f^2(z_2) - \frac{\lambda^2 (1 - d_2/f)^4 (z_2 - z_1)^2}{\pi^2 n^2}} \Bigg\}
\end{aligned}
$$

z_1, z_2 are the cavity positions corresponding to the measured w_f's.

(162)

Of course, when we do the fitting, we use the physical values for d_1, d_2, f:

$$d_1 = 18 \text{ cm}$$

$$d_2 = 16.5 \text{ cm}$$

$$f = 5 \text{ cm}. \tag{163}$$

The results for w_c and R_c can be seen in Figs. 68 and 69. We use the same organization of the data as in Figs. 65 and 67, that is to day, the abscissa represents the different pellicle positions and the ordinant represents either w_c or R_c. The theoretical values of $w_f(z)$ calculated using these values of w_c and R_c and Eq. (161) is shown as a solid line on Fig. 65. In our solution for w_c and R_c, we imposed the restriction

$$w_c^{(+)}(\text{mirror}) = w_c^{(-)}(\text{mirror})$$

$$\frac{1}{R_c}^{(+)}(\text{mirror}) = \frac{1}{R_c}^{(-)}(\text{mirror}) - \frac{2}{10}\text{ m} \tag{164}$$

which accounts for the action of a mirror on the Gaussian mode. The superscript (-) refers to parameters just before reflection from the mirror, while the superscript (+) refers to parameters just after reflection. The mirror had a radius of curvature of 10 m.

The data for the cavity with MBBA present (Fig. 67) is treated in

the same manner as when no MBBA is present. Each of the two components shown in Fig. 67 are treated independently. The procedure described is applied to both of these Gaussians, to determine their size in the cavity rather than at the film plane. In addition to Eq. (164), we also impose the restriction that the MBBA cell must produce the same effect regardless of the travelling wave component being fitted. (The MBBA cell effects are determined by the total field present, not just one of the travelling wave components.) Aside from this, the fitting procedure is exactly like that described above and the results for w_c and R_c can be seen in Figs. 68-70. The theoretical values for $w_f(z)$ calculated with these values of w_c and R_c and Eq. (161) is shown as a solid line on Fig. 67. It should be explained that the fitted values of w_c and R_c for the larger of the two Gaussian compoents present when MBBA is present turned out to be identical to those values of w_c and R_c for the single Gaussian component present when no MBBA was in the cavity.

Having determined the cavity mode size, we return to the final piece of data reduction that remains. This consists of analyzing the intercepts for Fig. 61 as alluded to earlier. Originally, when we performed the experiment, only passing attention was given to the exact pellicle orientation. Since we planned to fit the photographic densities to a Gaussian mode, the exact reflectivity of the pellicle was not of major importance. This moderate attention given to pellicle orientation was enough to insure constant orientation for each of the sets {①, ②, ③}, {④, ⑤, ⑥}, {$\boxed{1}$, $\boxed{2}$, $\boxed{3}$}, and {$\boxed{4}$, $\boxed{5}$, $\boxed{6}$}, where the numbers refer to possible pellicle positions, the circles to one of the pellicle orientations, the squares to the other orientation. The effort, however, was insufficient to insure constant orientation between sets. The pur-

pose of this last piece of data analysis is to determine the pellicle reflectivities for each of these sets.

Using Eq. (152), we can solve for $\mathscr{T}$ the energy transport from the camera to the film

$$\mathscr{T} = \frac{\gamma C' \mathscr{F}'_o}{1 \text{ mJ}} \exp\left(\frac{D_{int} - \beta}{\alpha}\right) \tag{165}$$

where D_{int} is the on axis densitometer reading for E = 1 mJ and other values are as defined in Eq. (152). We used the previously determined values for α (115.4 densitomer units) and β (3 densitometer units). Using the Fresnel equations for reflection from a pellicle with n = 1.5 and assuming that there is no loss at the lens, we have:

$$\mathscr{T} = 2\left(\frac{n^2\cos\theta - \sqrt{n^2 - \sin^2\theta}}{n^2\cos\theta + \sqrt{n^2 - \sin^2\theta}}\right) \tag{166}$$

where θ is the pellicle orientation with respect to the cavity axis. Now, if we assume that the maximal fluctuation of this angle θ is symmetrical about $\theta = 45°$, the nominal value, we have

$$\mathscr{F}'_o = 0.2 \text{ mJ/cm}^2 \tag{167}$$

and values for $\mathscr{T}$ and θ as indicated in Table 3. In deriving Table 3, we have used the value for C' (Eq. (151))

$$C' = \int_0^{2\pi} \int_0^{\infty} \frac{\mathscr{F}'(r,\theta)}{\mathscr{F}'(r = 0)} \, r dr d\theta$$

$$= \int_0^{2\pi} \int_0^{\infty} e^{-2r^2/w^2} \, r dr d\theta$$

cont'd

$$= \frac{\pi w^2}{2}$$

where w is the beam radius at the film plane.

H. Conclusion

This is the end of the data chapter. We have described the data taken and the procedure used to obtain this data. Wherever there was any analysis distinct from the mechanics of the self focusing effect, we have carried out such analysis here to simplify and clarify the analysis chpater, which follows. Besides, that type of data reduction properly belongs in the data chapter. In the following chapter (VI), the data presented here will be analyzed, and we will discuss how this data supports our proposed model, both qualitatively and quantitatively.

Figure Captions

Table 3. Pellicale reflectivities and orientation.

Fig. 50. Basic experimental set up.

Fig. 51. Cavity mode size vs. MBBA cell length as measured by a burn spot on polaroid film.

Fig. 52. Time dependence of laser output power for various MBBA sample lengths.

Fig. 53. (a)-(g) show time dependence of laser output power for various MBBA temperatures. (h) shows cavity mode size as measured by a burn spot on polaroid film for these temperatures.

Fig. 54. Blow-up of the experimental area from Fig. 50, used for measuring cavity power vs. time for different regions of the beam cross section.

Fig. 55. Relative pinhole positions with respect to the total beam size for set up of Fig. 54.

Fig. 56. Cavity power vs. time for different elements of the beam cross section. MBBA temperature = 50°C.

Fig. 57. Blow-up of the experimental area from Fig. 50, used for measuring the spatial distribution of cavity fields.

Fig. 58. Computer recreation of the density profile on a picture taken of cavity fields. (No MBBA)

Fig. 59. Computer recreation of the density profile on a picture taken of cavity fields. (MBBA temperature = 50°C)

Fig. 60. Typical film response curve for Kodak Pan-X film.

Fig. 61. Least squares fit to determine conversion constants for converting densitometer readings to fluences.

Fig. 62. Film plane fluence as a function of position on the fim (cor-

responds to data of Fig. 58). No MBBA is present.

Fig. 63. Film plane fluence as a function of position on the film (corresponds to data of Fig. 59). MBBA temperature = 50°C.

Fig. 64. Determination of the correction factor δ for the toe of the film response curve.

Fig. 65. Gaussian widths of the film plane fluences as a function of pellicle position. No MBBA.

Fig. 66. Origin of the two Gaussian widths seen with MBBA present in the cavity.

Fig. 67. Guassian widths of film plane fluences as a function of pellicle position. MBBA temperature = 50°C.

Fig. 68. Gaussian widths of cavity modes as a function of cavity position. Both the case with MBBA and the case with no MBBA are shown.

Fig. 69. Wavefront radius of curvature for the cavity mode as a function of cavity position. Results apply to both the case with no MBBA in the cavity and to the larger component present with MBBA in the cacity.

Fig. 70. Wavefront radius of curvature for the cavity mode as a function of cavity position. Results apply to the smaller component present with MBBA in the cavity.

Set	$\mathscr{T}$	θ
{① , ② , ③}	.8%	49°
{④ , ⑤ , ⑥}	2.1%	43°
{$\boxed{1}$, $\boxed{2}$, $\boxed{3}$}	2.6%	41°
{$\boxed{4}$, $\boxed{5}$, $\boxed{6}$}	2.5%	42°

Table 3 - Pellicle reflectivities and orientation.

Figure 50

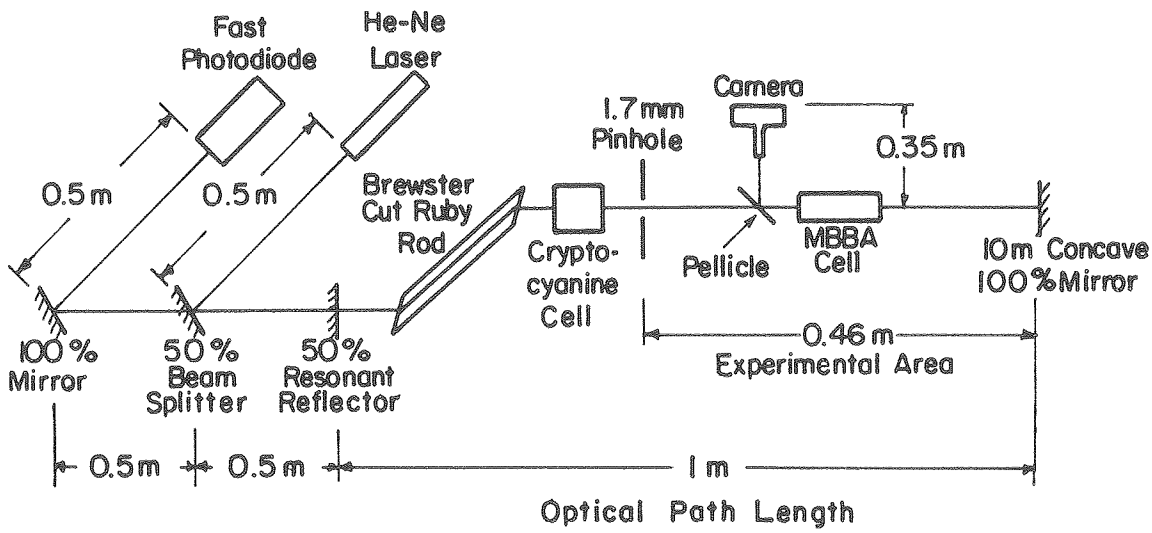

XBL 8010-6164

Figure 51

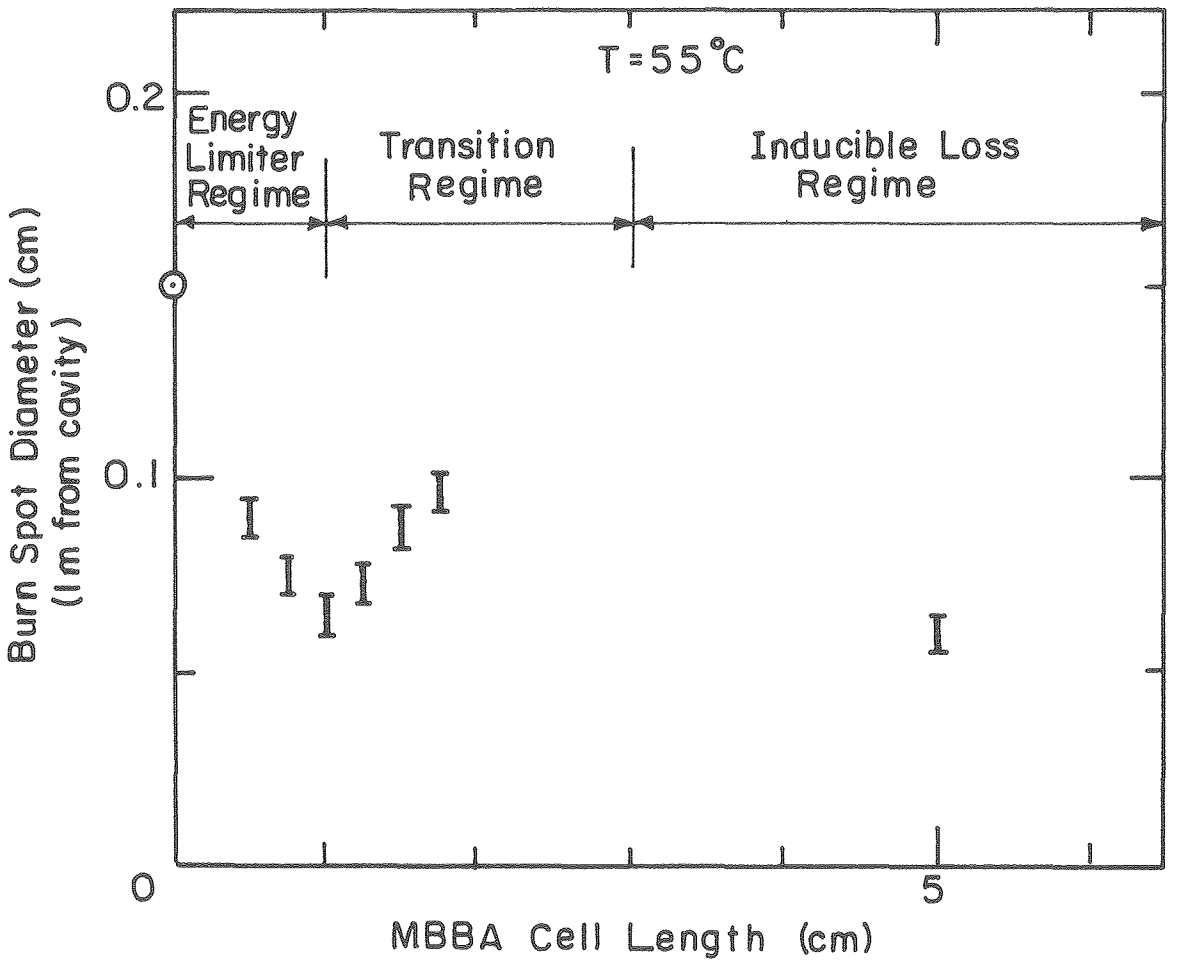

XBL 8010-6165

Figure 52

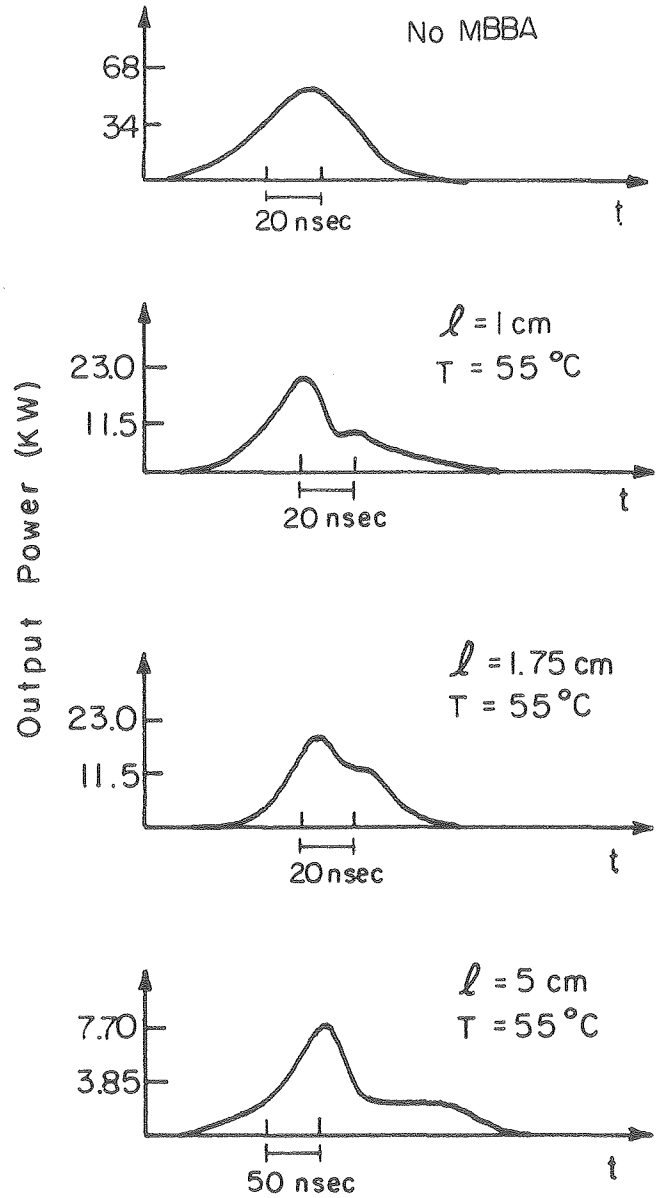

XBL8010-6166

Figure 53

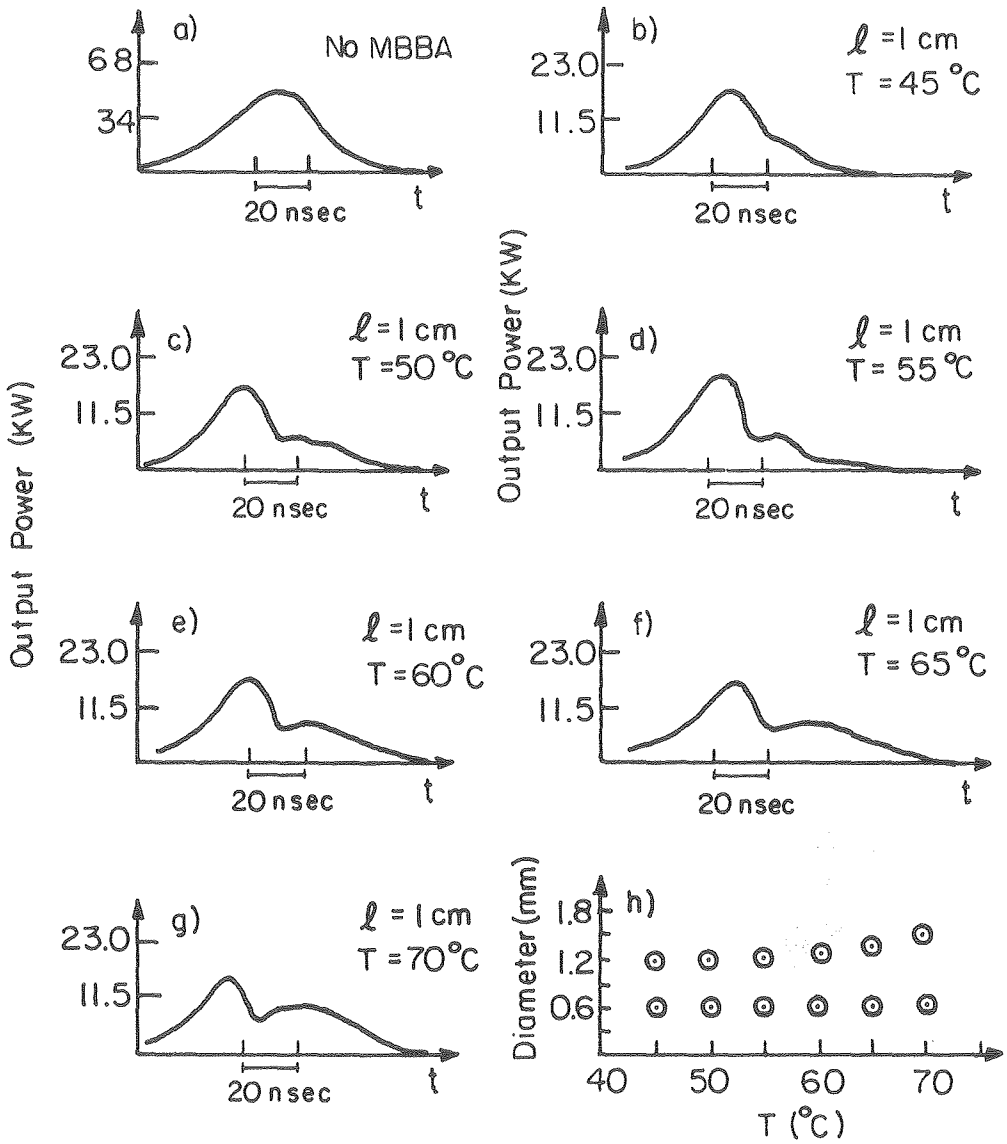

XBL 8010-6167

Figure 54

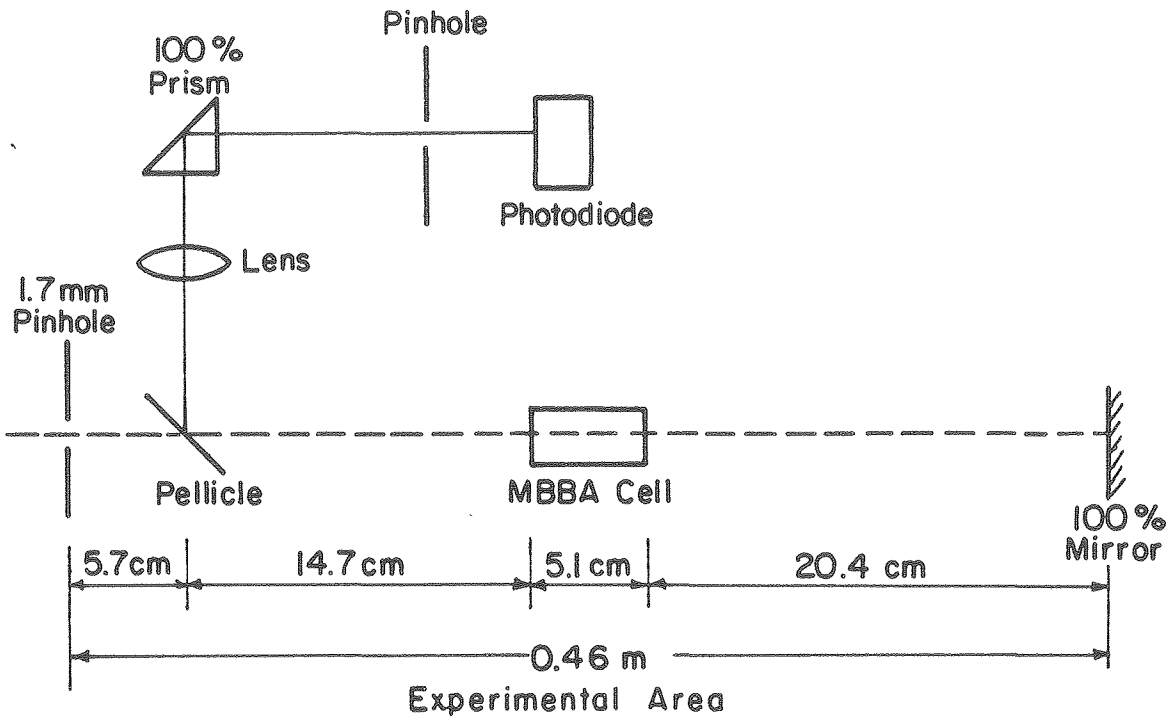

XBL 8010-6168

Figure 55

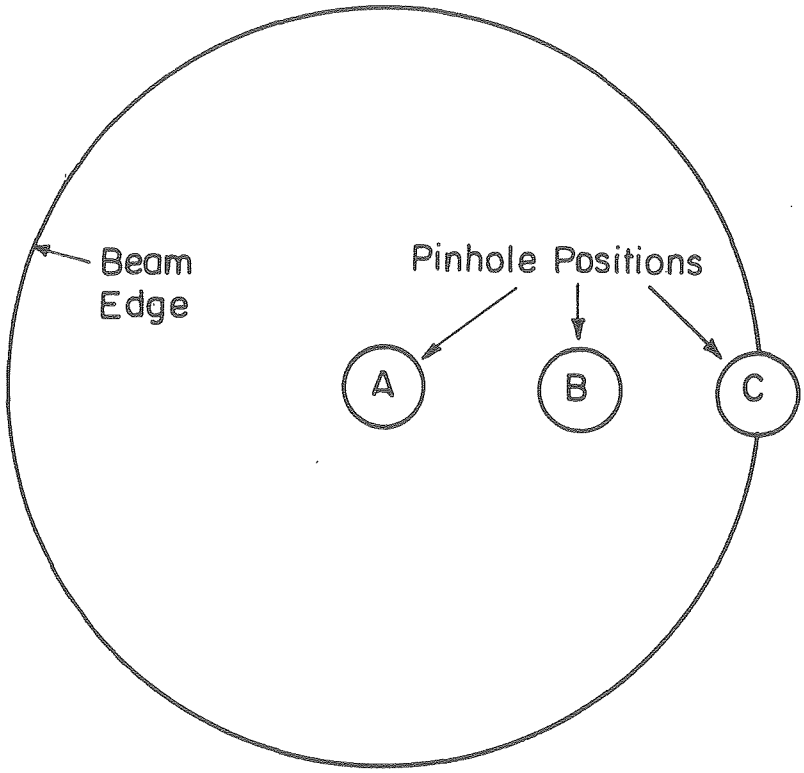

XBL8010-6169

Figure 56

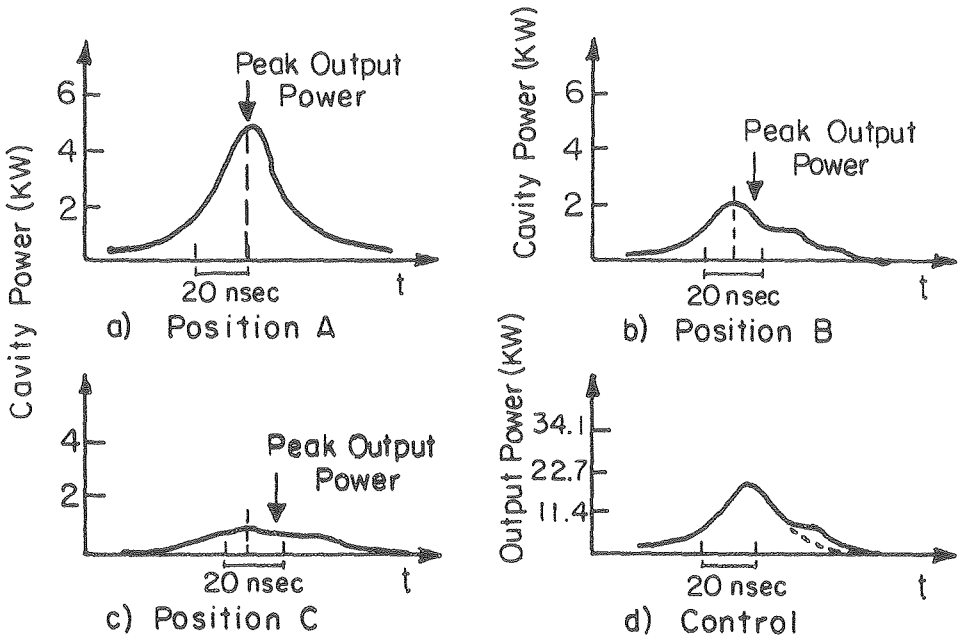

XBL 8010-6170

Figure 57

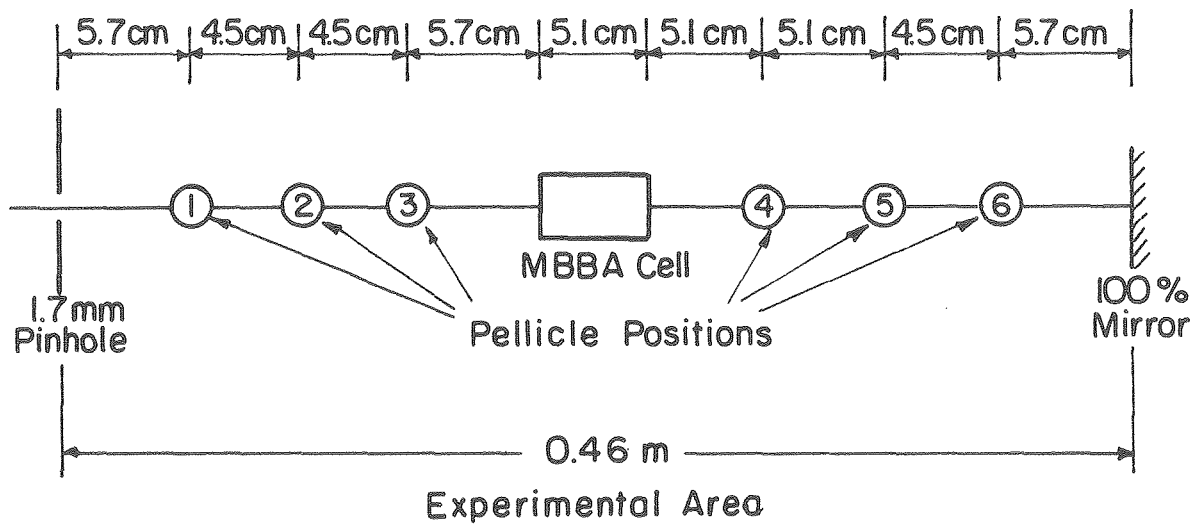

XBL 8010-6171

Figure 58

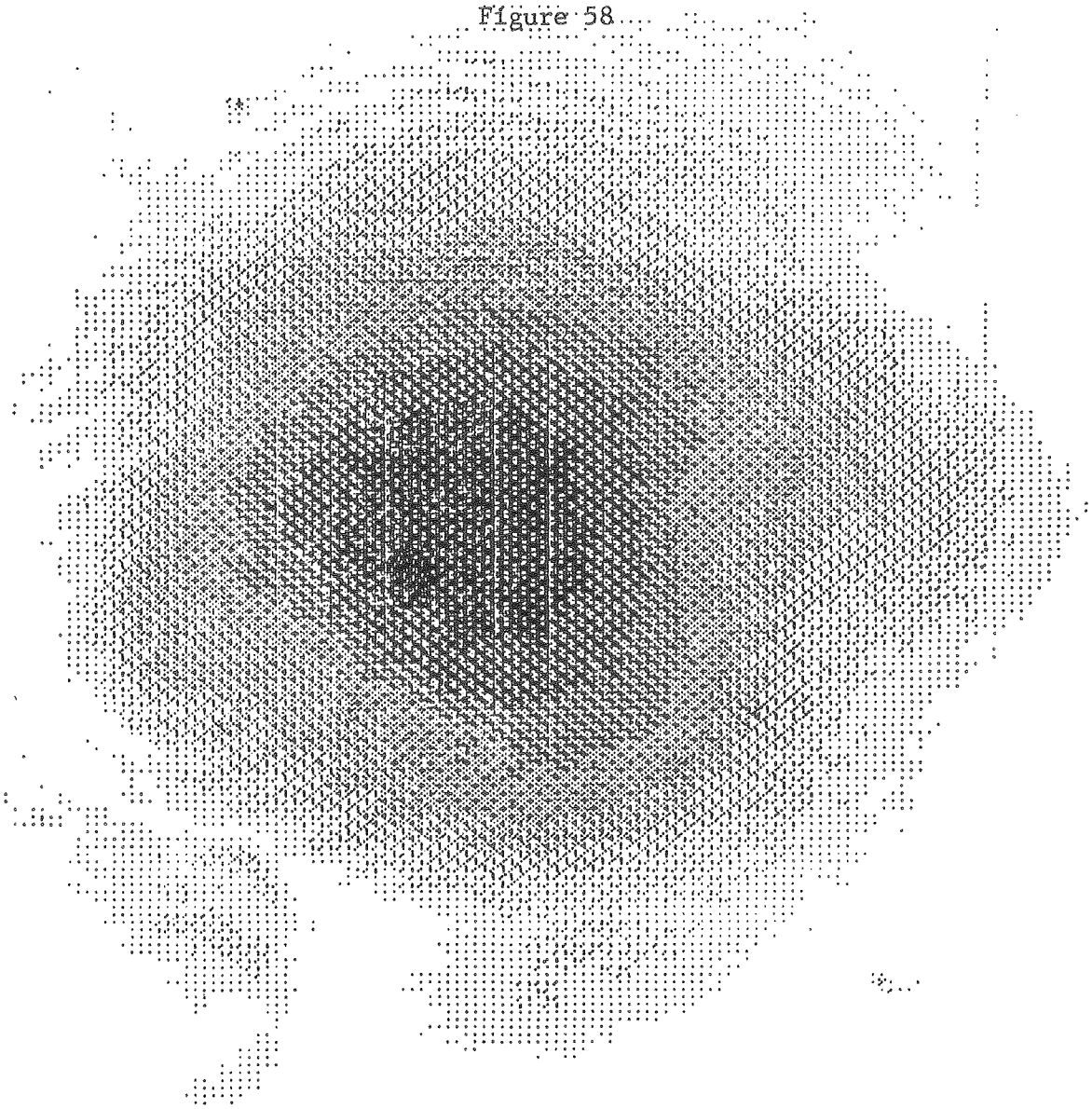

XBL 8010-6172

Figure 59

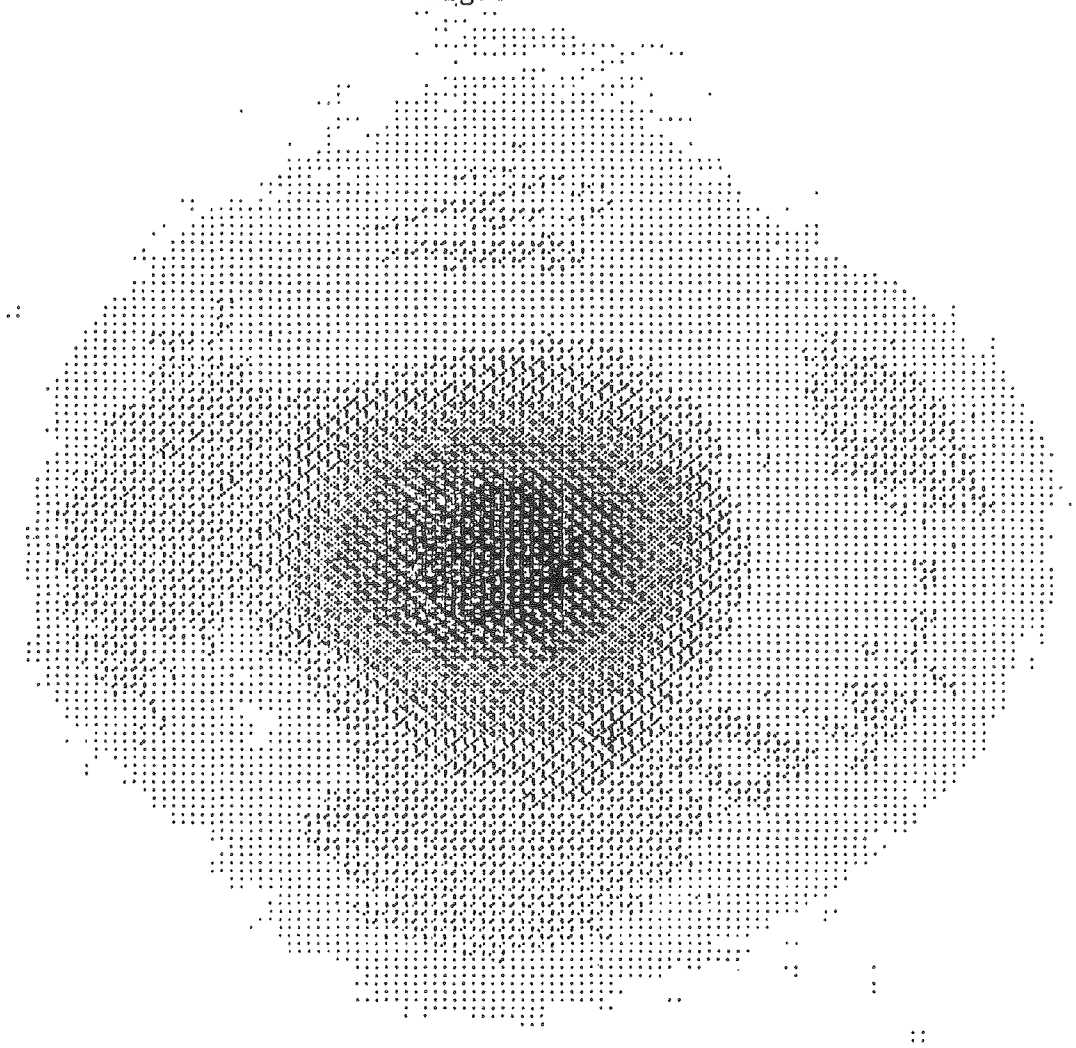

XBL 8010-6173

Figure 60

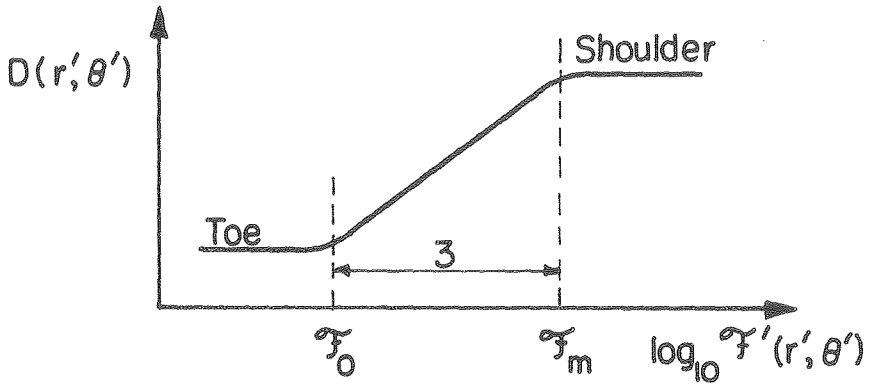

XBL 8010-6174

Figure 61

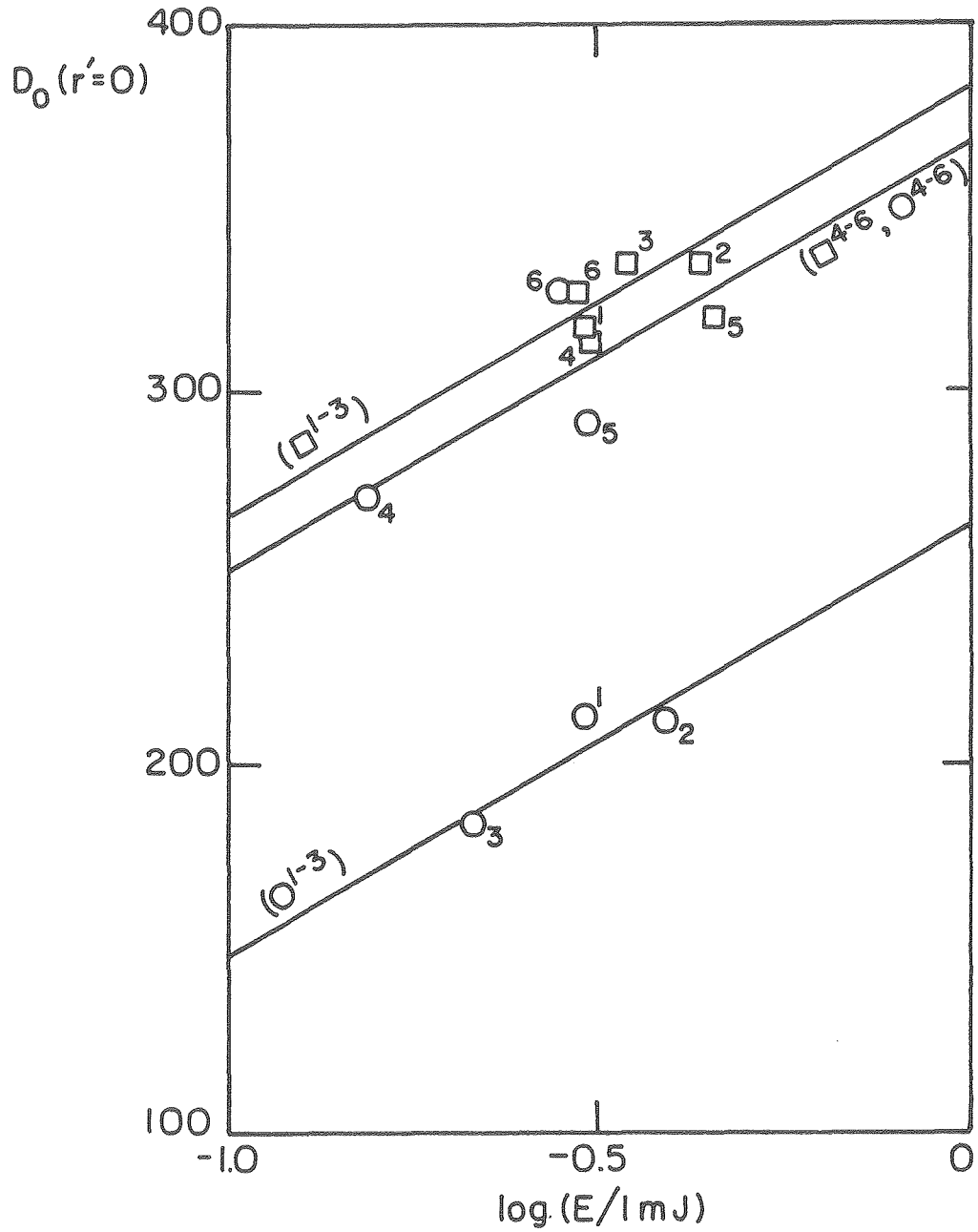

XBL 8010-6175

Figure 62

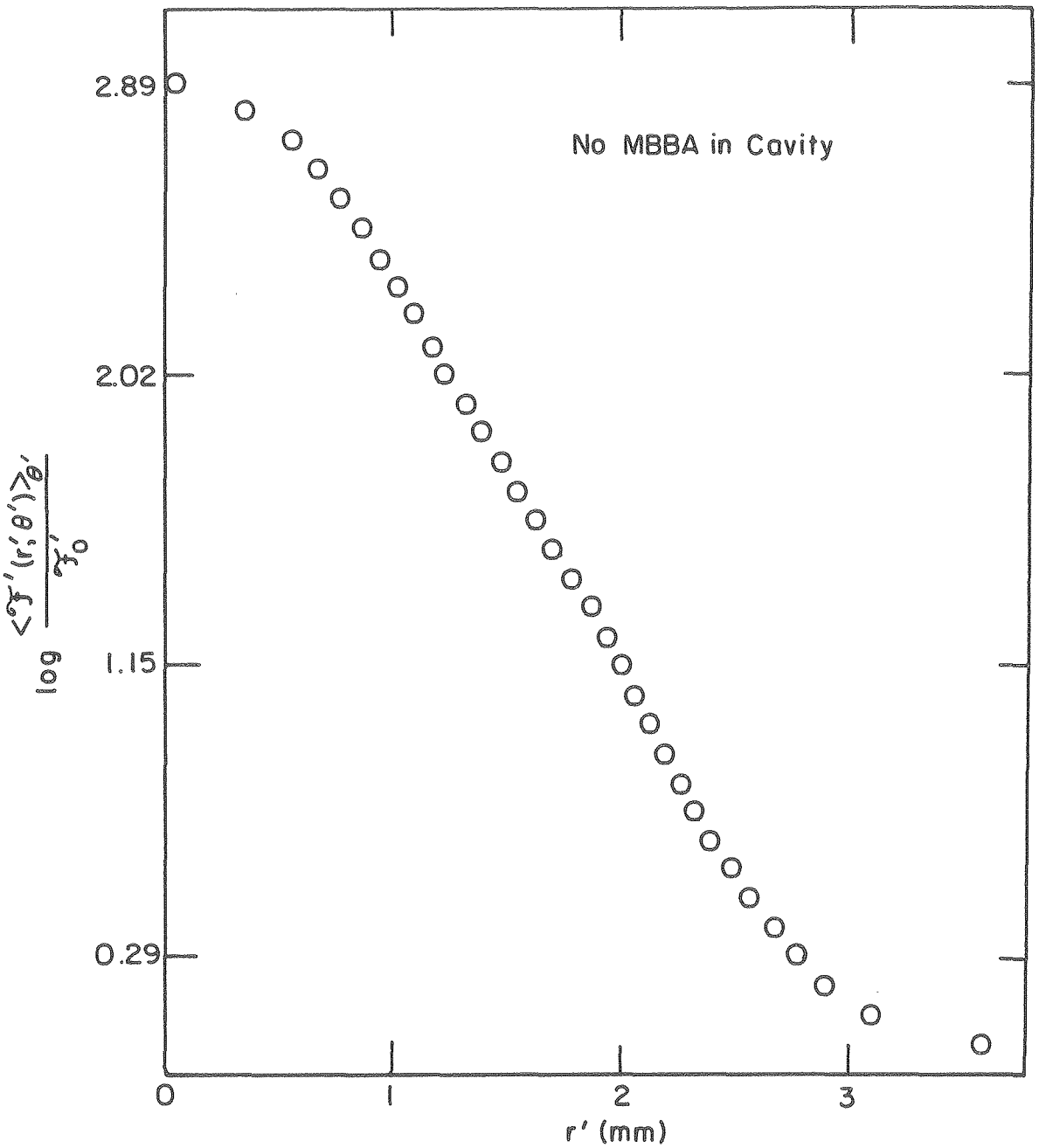

XBL 8010-6176

Figure 63

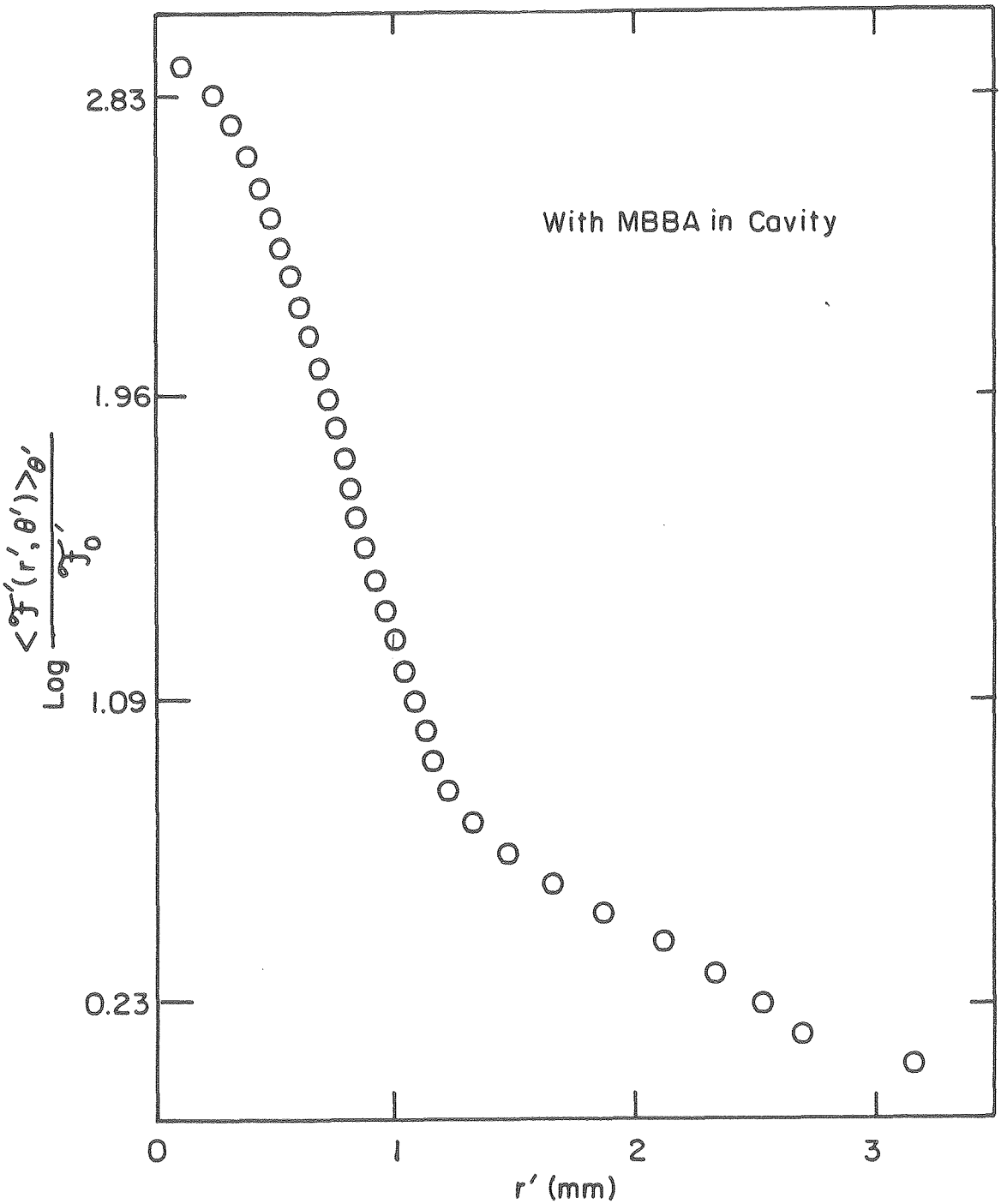

XBL8010-6187

Figure 64

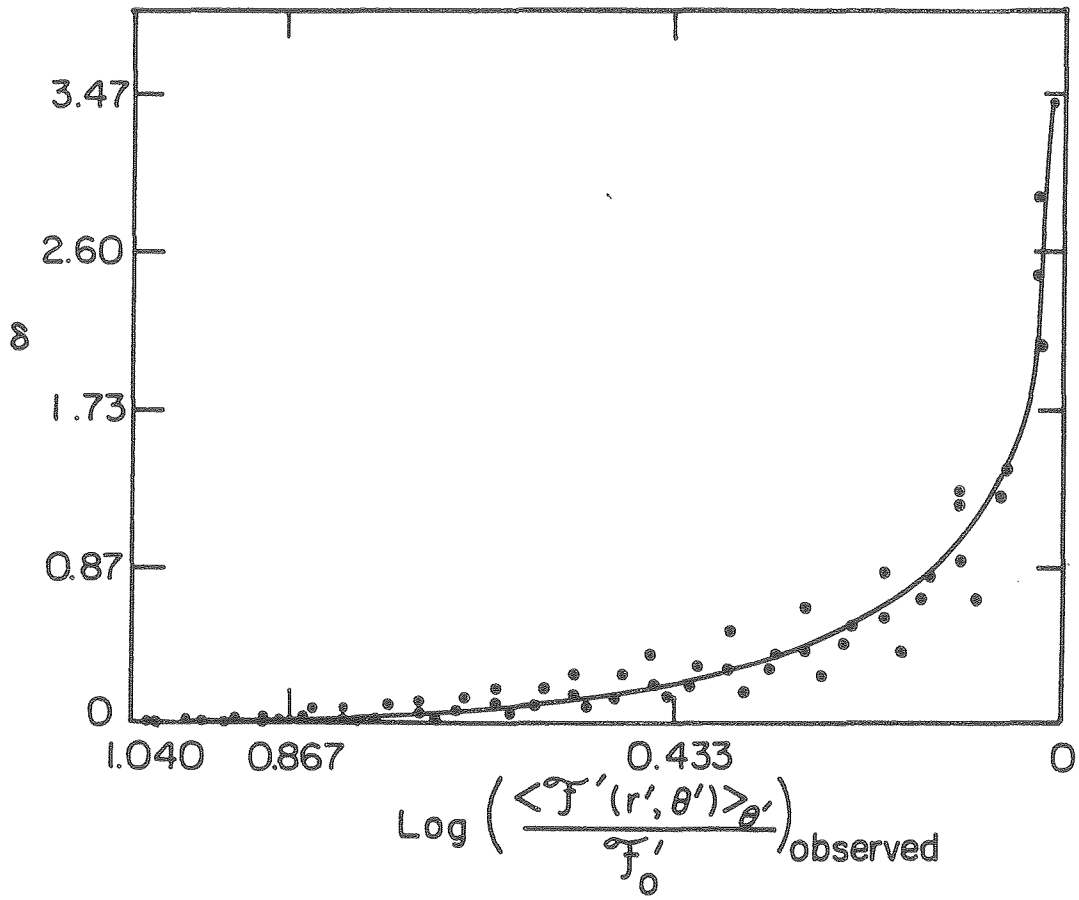

XBL 8010-6188

Figure 65

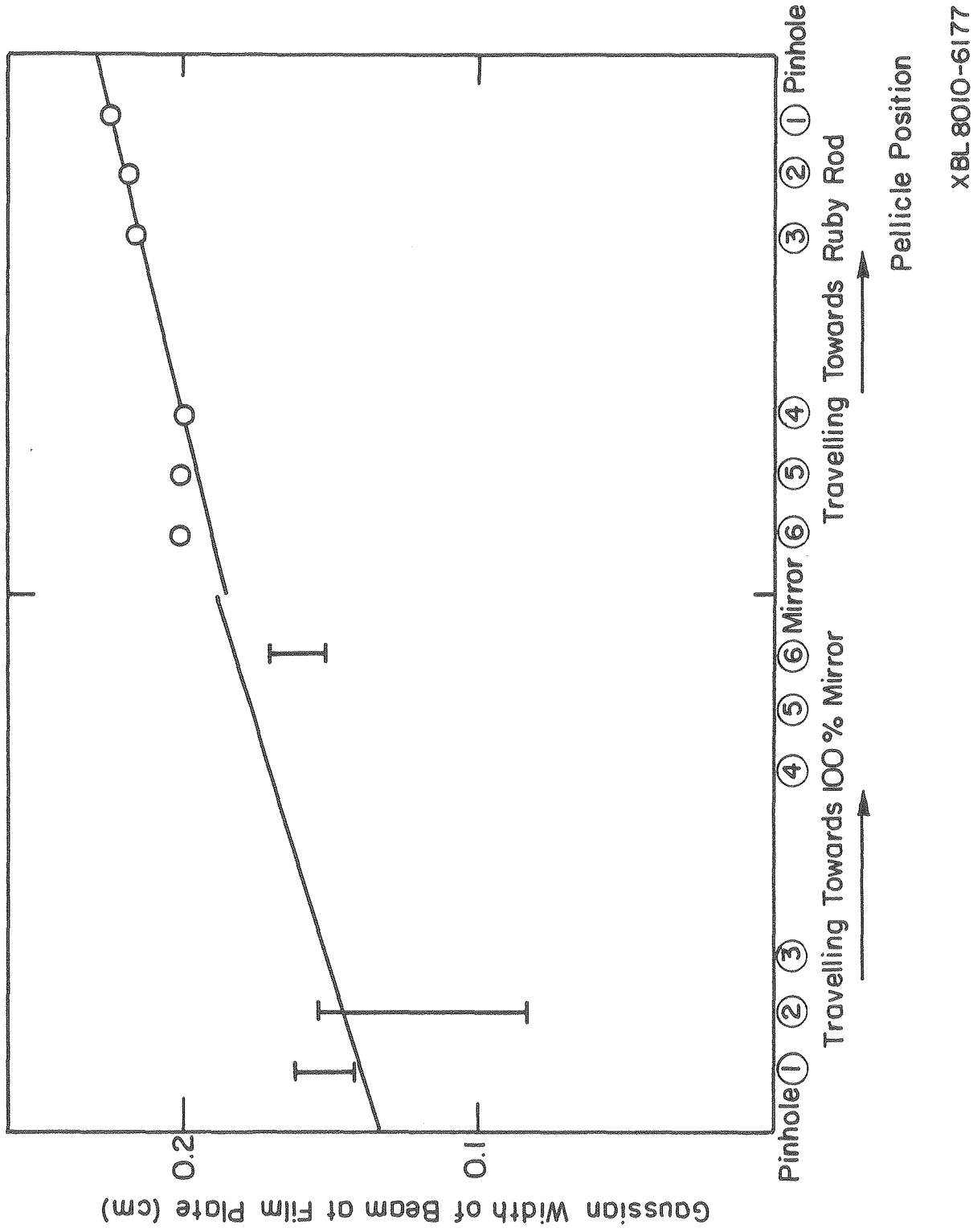
Gaussian Width of Beam at Film Plate (cm)
0.2
0.1
Pinhole ① ② ③ ④ ⑤ ⑥ Mirror ⑥ ⑤ ④ ③ ② ① Pinhole
Travelling Towards 100% Mirror
Travelling Towards Ruby Rod
Pellicle Position
XBL 8010-6177

Figure 66

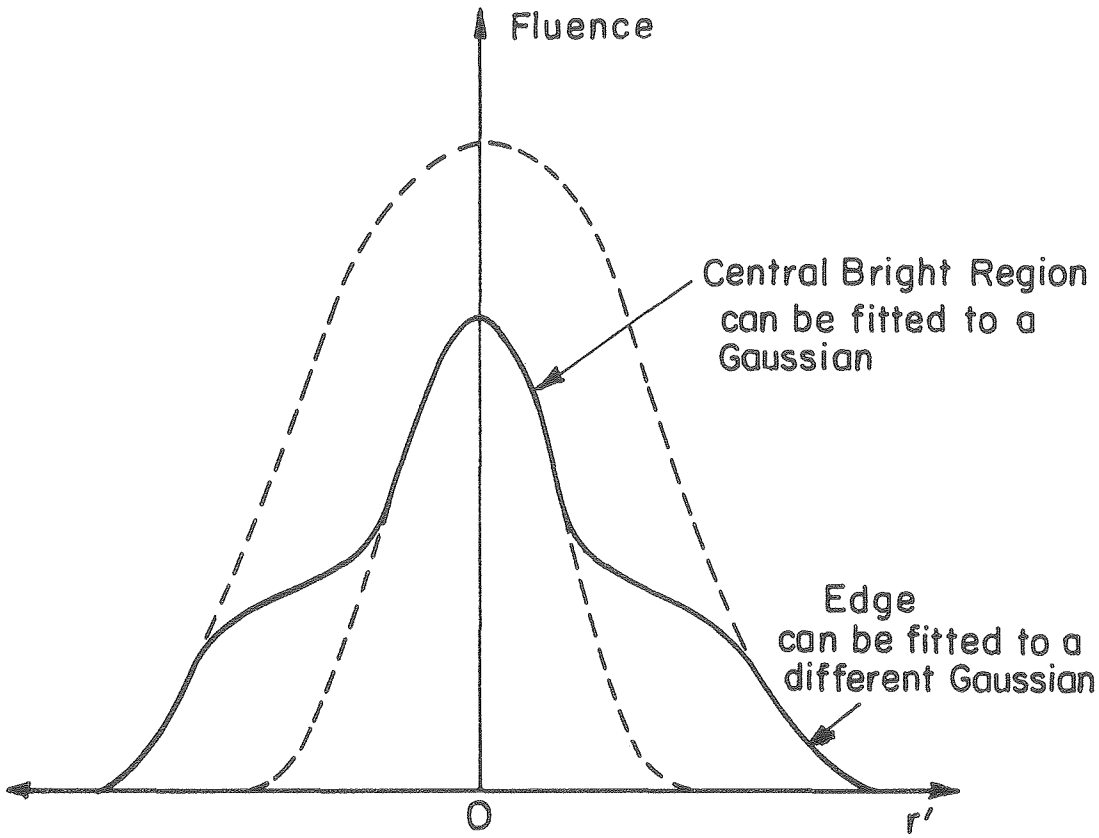

XBL8010-6178

Figure 67

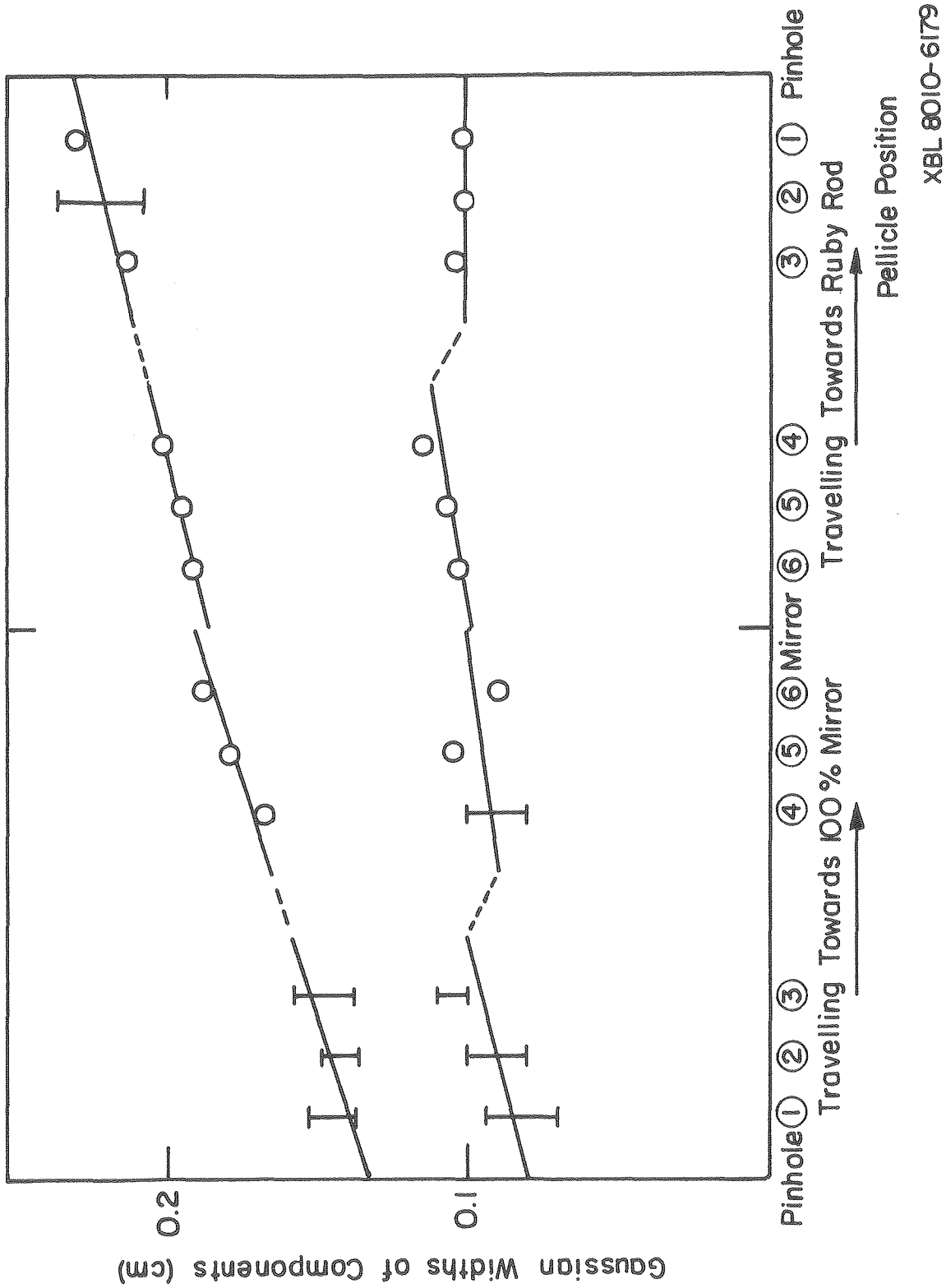
Gaussian Widths of Components (cm)
0.2
0.1
Pinhole ① ② ③ ④ ⑤ ⑥ Mirror
Travelling Towards 100% Mirror
⑥ ⑤ ④ ③ ② ① Pinhole
Travelling Towards Ruby Rod
Pellicle Position
XBL 8010-6179

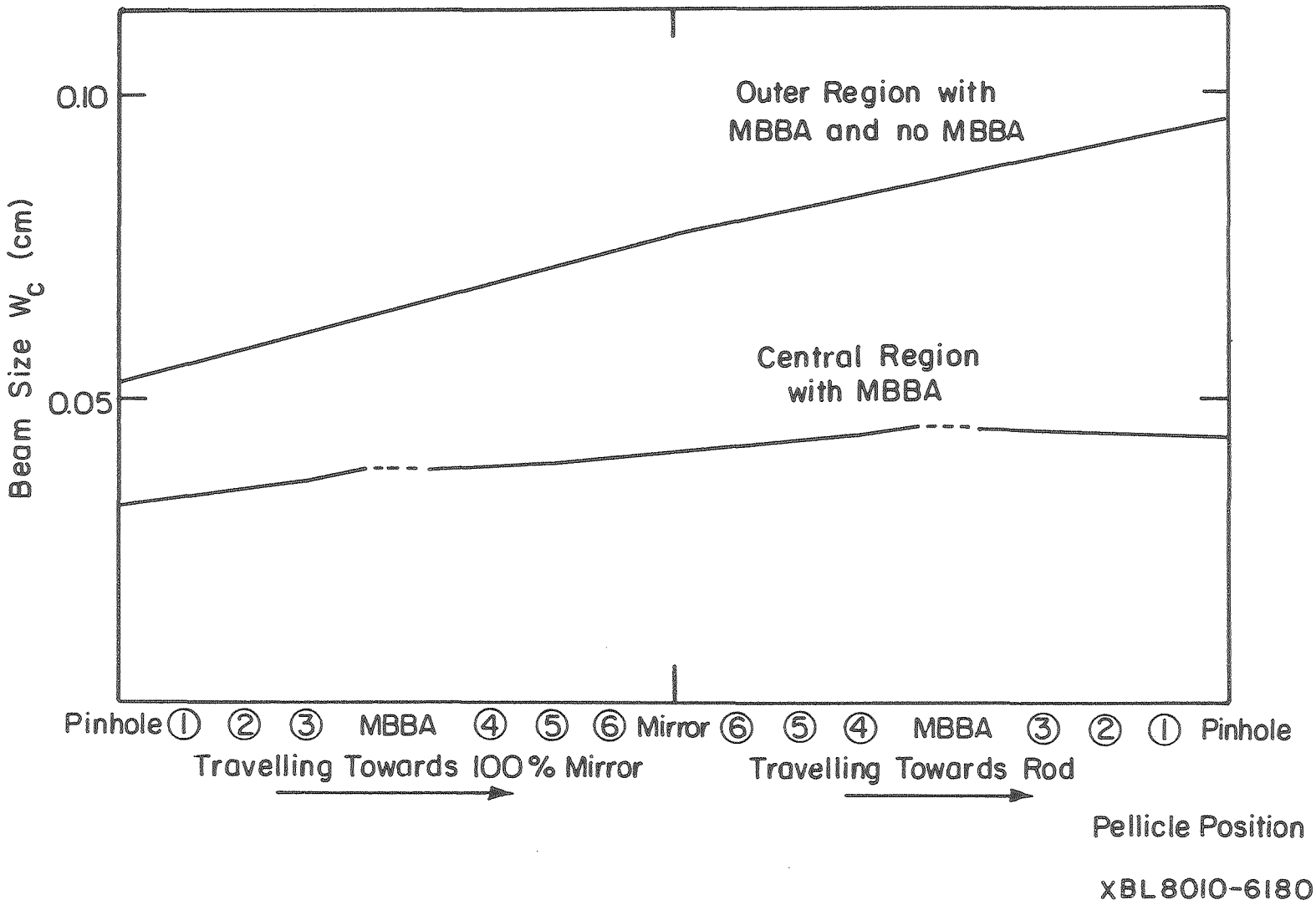
0.10
0.05
Beam Size W_c (cm)
Outer Region with
MBBA and no MBBA
Central Region
with MBBA
Pinhole ① ② ③ MBBA ④ ⑤ ⑥ Mirror ⑥ ⑤ ④ MBBA ③ ② ① Pinhole
Travelling Towards 100% Mirror
Travelling Towards Rod
Pellicle Position
XBL8010-6180

Figure 68

Figure 69

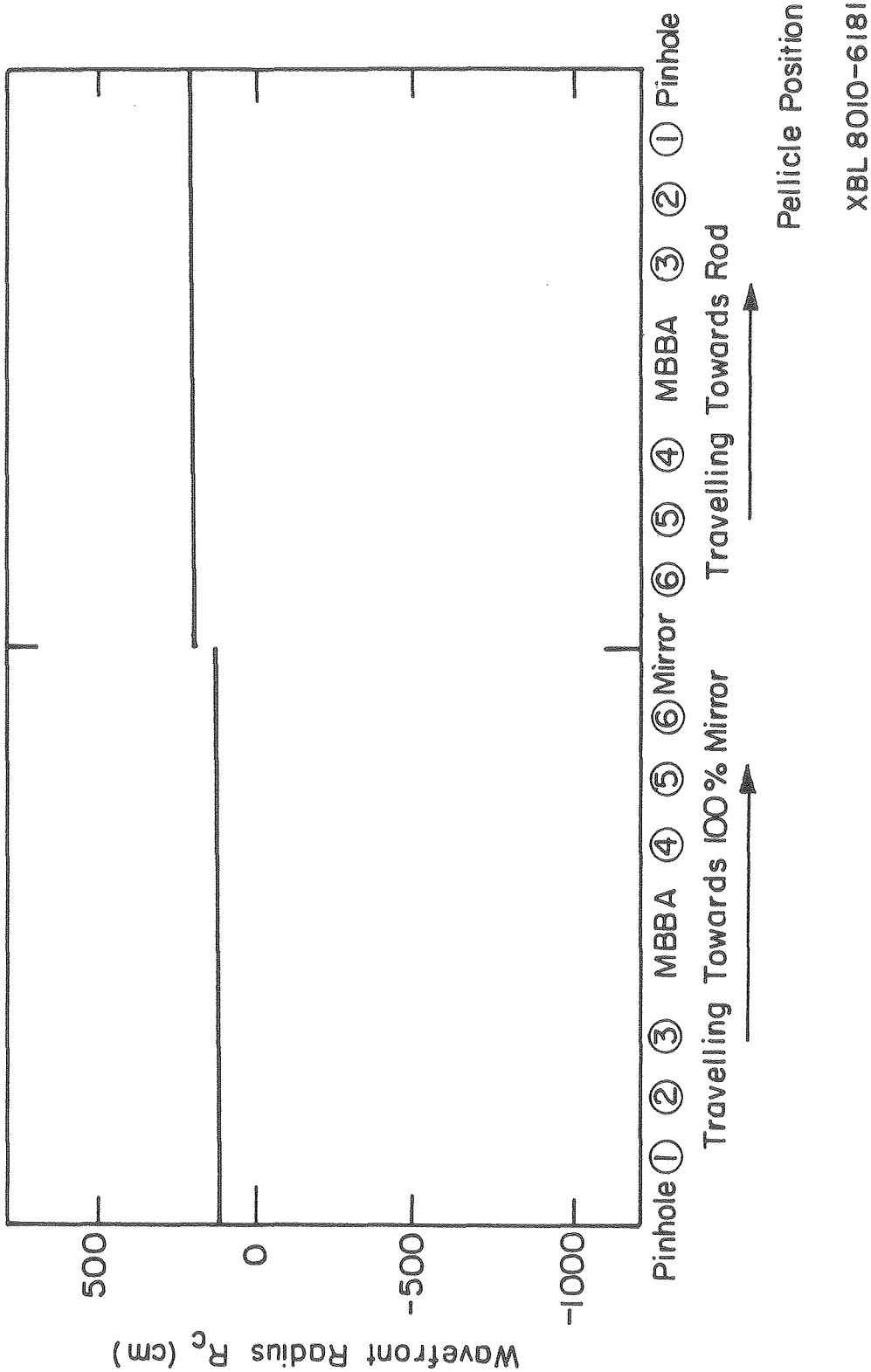
500
0
-500
-1000
Wavefront Radius R_c (cm)
Pinhole ① ② ③ MBBA ④ ⑤ ⑥ Mirror
Travelling Towards 100% Mirror
⑥ ⑤ ④ MBBA ③ ② ① Pinhole
Travelling Towards Rod
Pellicle Position
XBL 8010-6181

Figure 70

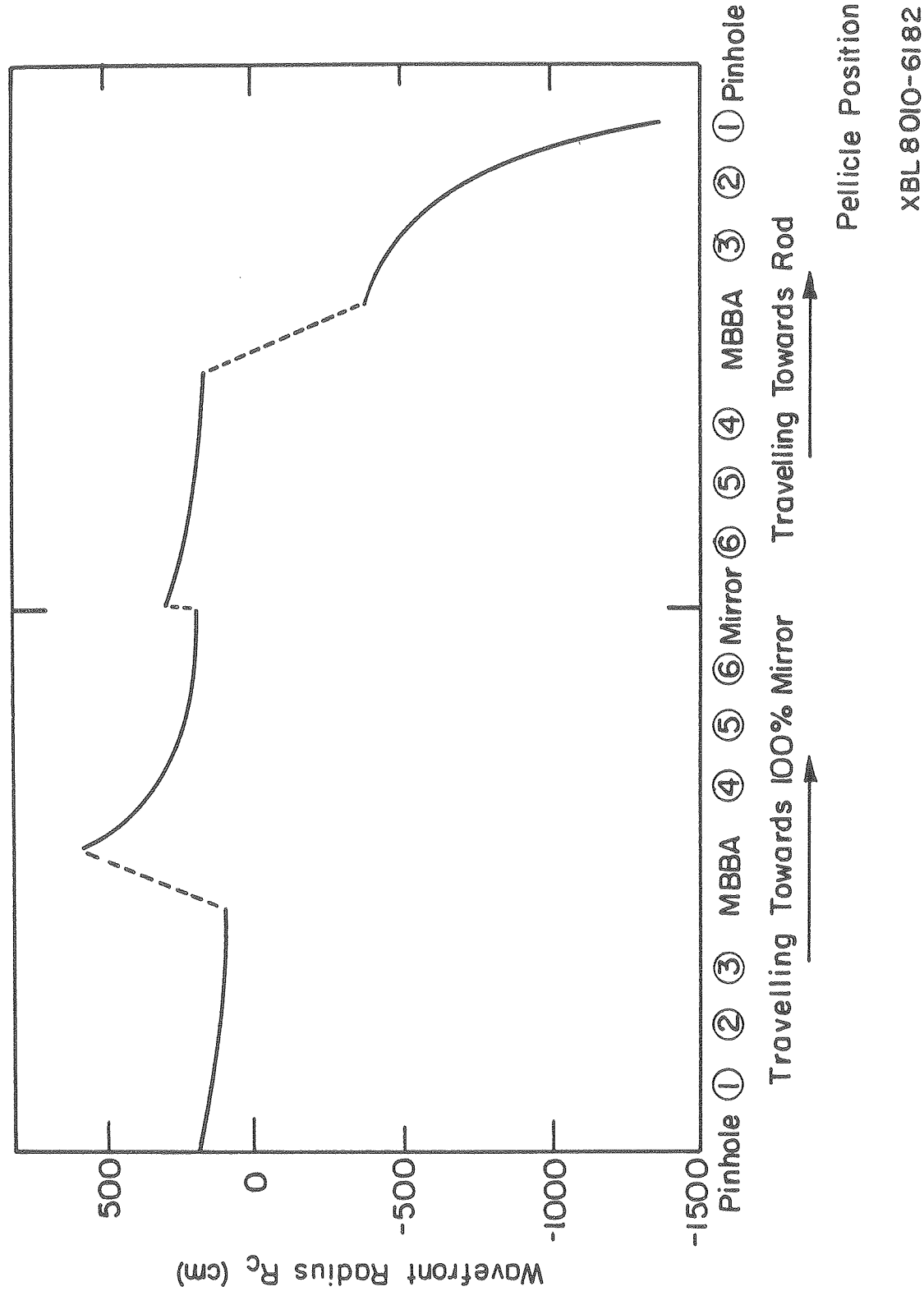
Wavefront Radius R_c (cm)
500
0
-500
-1000
-1500
Pinhole ① ② ③ MBBA ④ ⑤ ⑥ Mirror ⑥ ⑤ ④ MBBA ③ ② ① Pinhole
Travelling Towards 100% Mirror
Travelling Towards Rod
Pellicle Position
XBL 8010-6182

VI. SELF FOCUSING - COMPARISON OF DATA WITH PROPOSED MODEL

A. Qualitative Discussion

We start this chapter with some guidelines that must be followed in treating some of the data. Recall that as a crude measure of cavity mode size, we measured the size of the burn pattern on polaroid film, generated by placing exposed polaroid film in the beam path. This procedure measures the area of the beam for which the intensity exceeds the threshold for burning the film. There is no reason to expect that the size of this spot will have apriori any specific relationship to the mode size, only that changes in mode size will be seen as a similar (qualitatively) change in the size of the burn spot. Thus, we must use caution to use such data only for qualitative comparisons, not for quantitative ones. The other precaution that must be used it to keep in mind that the size of the burn spot also depends on incident intensity, as seen in Fig. 71, where we sketch how increasing intensity can increase the size of the burn spot even when the Gaussian beam waist is unchanged. Thus, care must be taken to distinguish between intensity induced and cavity mode size induced changes in the size of the burn spot.

The data seen in Fig. 51 is an example of data taken by measuring the size of the burn spot. The data can be qualitatively explained by our proposed model. As the MBBA sample length is increased from 0, the size of the spot shrinks. This shrinkage continues until a sample length of 1 cm is reached, whereupon the spot size begins to grow as the sample length continues to increase. Somewhere between a sample length of 2 cm and one of 5 cm, this trend again reverses, and the spot size shrinks. This behavior is consistent with our model if we assume the

various regimes to be as indicated on Fig. 51. For the energy limiter regime, the model predicts the cavity configuration will shift from near plane parallel to confocal as the sample length increases; since the cavity mode size is smallest for a confocal configuration, this is consistent with the data. For the transition regime, the model predicts a cavity configuration that shifts from confocal away from confocal and back to confocal as the sample length increases. This would cause an initial increase in mode size followed by a decrease to that seen for the confocal configuration. Again, this is consistent with the data, although not enough data exists to verify the eventual decrease. For the inducible loss regime, the model predicts both an increase cavity mode size (as cavity configuration shifts away from confocal) and a reduction in cavity intensities due to the inducible loss. The increase in mode size is limited, of course, by the presence of the pinhole, to the size seen when no MBBA is present. The reduction in cavity intensities causes a reduction in burn spot size. Eventually , since the mode size increase is limited, we expect this intensity caused reduction to predominate and the spot size to shrink. This is consistent with the one data point we have for this regime.

In Fig. 52, we have plotted the power as a function of time for each of the various regimes (no MBBA, energy limiter, transition, and inducible loss). Again, we see behavior as predicted by the model. For the energy limiter regime, there is a large reduction in total output power though the pulse length is shorter. This is consistent with a reduction in lasing volume (which accounts for the lower power) and an increase in cavity feedback to the volume which does lase (which accounts for the shorter pulse). A weak second pulse is seen, confirming that energy ex-

ists in the rod which can be released as the cavity configuration relaxes from confocal back towards plane parallel. This occurs as the cavity intensity is decreasing.

The transition regime (ℓ = 1.75 cm) shows a similar behavior. The primary peak shows very little change from the energy limiter regime. The secondary peak is considerably larger though, almost as large as the primary peak, while the separation between the primary and secondary peaks is smaller. From Fig. 49, we would expect just this behavior. The cavity configurations for the initial portions of the pulse are quite similar to both regimes discussed so far. Thus, we expect the similarity in the primary peaks. The difference occurs after the cavity configuration has reached the confocal configuration. For the transition regime, the configuration continues to evolve past confocal towards concentric, with an attendant increase in mode size. This occurs near the peak of cavity intensity. The increased feedback, provided by this increased mode size, to the volume of active material previously inhibited from lasing, thus also occurs near the peak of cavity intensity rather than after this intensity has fallen significantly, as is the case for the energy limiter regime. This leads to both a larger second peak (due to larger feedback) and one that occurs more quickly (since this feedback starts earlier in the pulse) than for the energy limiter regime.

For the inducible loss regime, we expect behavior similar to that studied in Chapter III for SIER inducible loss. The intensity should be reduced, and there should be an accompanying stretching of the pulse. This can quite clearly be seen in Fig. 52, where the peak power is substantially reduced, even from the depressed levels of the energy limiter and transition regimes, and the pulse length is noticeably longer (200

nsec vs. 40 nsec). For long enough cell lengths, we expect the inducible loss regime to change into the variable threshold regime where lasing action is expected to require substantially higher threshold energies if it is seen at all. We use a 10 cm MBBA sample and found no lasing action up to the pump energy limits imposed by our flashlamps.

The size of the induced nonlinear refractive index dn for our pulse lengths is expected to depend only weakly on temperature because of the transient nature of this response (Fig. 29 and Cahpter IV). The behavior of the first peak on Figs. 53b-g show that this is indeed true. The first peak on each of these figures depends on the dynamics of the cavity configuration change from plane parallel to confocal. The similarity in the shape of this peak for all the sample temperatures used, indicates that the induced nonlinear refractive indices must be similar for all the temperatures (and thus only weakly temperature dependent).

The relaxation time will depend strongly on temperature, and as explained in Chapter IV, this dependence will manifest itself, in Figs. 53b-g, as different behavior of the second peak at different temperatures. The relaxation time controls the relaxation of the cavity configuration from confocal back to plane parallel. This affects the feedback to the volume of active material previously inhibited from lasing and thereby affects the strength of the second peak. We expect a small second peak when the relaxation time is greater than the pulse length, and a large second peak when the relaxation time is less than the pulse length. For a pulse length of $\sim$ 30 nsec, using Fig. 4 or Table 1, we expect the dividing point to be at a temperature 55°C-60°C (22 nsec - 30 nsec response time). This behavior is clearly seen in Fig. 53b-g, where the second peak grows as temperature increases (and relaxation time decreases).

The second peak becomes noticeably larger for temperature above 60°C, as expected.

The data of Fig. 53h provides additional corroboration. In discussing this data, we will use the following terminology. When MBBA is present in the cavity, the burn spot exhibits a central region of high intensity surrounded by a region of much lower intensity. We will refer to the bright central area of the burn spot as the "central peak." This region corresponds to energy released near the first or primary peak of laser output. We will refer to the surrounding area as the "halo." This region corresponds to energy released before or after the primary peak and includes energy released in the secondary peak. When MBBA is absent from the cavity, the burn spot exhibits only one region, this region having the brightness of the "central peak" but the size of the "halo." This is consistent with the identification of the central peak with energy released near the the first peak, when the cavity configuration is near confocal and the cavity mode is considerably smaller than when no MBBA is present, and the cavity mode is near plane parallel.

The constant size of the central peak, as measured by the lower set of points in Fig. 53h, together with the temperature insensitivity of the primary peaks in Figs. 53b-g, indicates that the cavity mode size at the peak is also only weakly dependent on temperature. This reinforces the fact that temperature changes in the MBBA affect the laser output primarily via a change in relaxation time for the MBBA (which in turn affects primarily the second peak). The increasing spot size with increasing temperature for the upper set of points in Fig. 53h, is consistent with the increased energy in the secondary peak as temperature increases. It is impossible to evaluate how much of the increase in size of the

burn spot is due to the increased energy in the second spot, so no inferences regarding mode size for this secondary peak should be made. (Recall, that spot size depends on both mode size and incident intensity.)

Based on the data of Fig. 53, we decided to use a sample temperature of 50°C for the remainder of the data yet to be taken. It was felt that the analysis would be most fruitful when the complications posed by the presence of the second peak were minimized. The choice of 50°C is well above the transition point (41.6°C), which avoids the problem of increased scattering loss near the phase transition, and at this temperature (50°C) the secondary peak is present only weakly.

Confidence in our model, especially in the role that relaxation time plays, is strengthened by a clear-cut demonstration that the second peak indeed consists of energy released from the "halo" region. The data of Fig. 56 provides this demonstration. (Data is described in Section IVE.) As the pinhole is swept outward from the center (the progression 56a → 56b → 56c), the relative size of the second peak, for the fields transmitted through the pinhole, grows with respect to the primary peak. The relative importance of the second peak with respect to the entire output is seen in Fig. 56d. Comparing Figs. 56a and 56c to Fig. 56d shows that very little energy from the second peak gets through a pinhole on axis, while for a pinhole far off axis a large amount of the energy from the second peak passes. This supports the model which predicts that the second peak arises from energy released from the "halo" region.

The position of the peak in Fig. 56d is indicated by an arrow on Figs. 56a-56c. The first peak in Fig. 56a coincides with the peak in laser output. The first peak of Figs. 56b and 56c precede the peak in laser output by 8 nsec and 12 nsec respectively. This indicates initial-

ly increasing fields for positions b and c of Fig. 55, which peak and then decrease as a result of the evolution of the cavity configuration towards a confocal configuration. In the course of the evolution, the natural cavity mode size decreases, inhibiting portions of the laser medium. As the portion of the laser medium contributing to the energy passing through positions b and c stops lasing, we expect to see a corresponding decrease in the energy passing through a pinhole at these positions. This decrease should be seen first at the edges (position c) and work towards the center as the configuration evolves. Indeed, we see that the decrease in power starts for position c, 12 nsec before the peak in output power, while at position b this decrease starts only 8 nsec before this peak.

The decrease above should be greatest at the peak of laser output as that should correspond to the smallest mode size and thus greatest induced loss for the outer portions of the laser rod (the inhibited region). For short relaxation times, we expect the power at positions b and c to increase again as the cavity configuration relaxes back to plane parallel. For long relaxation times (as compared to pulse widths) we expect this relaxation to be much slower than the pulse duration so that the power at positions b anc c should remain relatively constant or decrease further as the cavity intensities drop. This latter behavior is what we expect for Fig. 56 as the response time of MBBA at 50°C is ~ 65 nsec which is considerably longer than the pulse duration. From Fig. 56b and 56c we see the behavior is as expected.

There were two modes discernible from the photographs taken of the cavity fields (Fig. 68). One mode, the smaller, contained energy emitted near the peak of laser output and was noticeably affected by the MBBA.

The other larger mode contained energy emitted near the edge of the lasing volume (far off axis). This larger mode is apparently unaffected by the presence of the MBBA. The behavior of the larger mode, as measured by beam radius w and curvature R, is identical to the behavior of the single mode present when no MBBA is in the cavity, though the energy in the mode is greatly reduced when compared to that case. Thus, the larger component must consist primarily of energy released before the MBBA can substantially change the cavity configuration, that is for the initial portion of the pulse when the intensities are still small and the MBBA has not yet started to respond. This accounts for both the low energy content and the similarity to the mode seen when no MBBA is in the cavity, as well as supporting our model. The behavior of the smaller component clearly shows the focusing nature of the MBBA (see Fig. 68). The precise nature of the focusing will be examined in the quantitative discussion of section VIb, which follows this section.

Using the data of Figs. 53 and 68, we can determine the on axis cavity intensity. We choose to evaluate this intensity at the pinhole.

$$P_{out}(t) = \frac{c}{8\pi}\gamma\left[\int_0^{2\pi}\int_0^{\infty} r\left|e^{-r^2/w_+^2}E_+(r=0) + e^{-r^2/w_-^2}E_-(r=0)\right|^2 drd\theta\right] \quad (165)$$

where $P_{out}(t)$ is the output power, $w_\pm$ is the cavity mode size at the pinhole for the two travelling components, $E_\pm(r = 0)$ is the on axis cavity field for these components, and γ is the ratio of output to cavity energy. We have explicitly used the fact that energy in the cavity must be in one of the two modes. Now, using the data shown in Table 3 for the pellicle orientation and assuming that the major loss between the (+) and (-) travelling wave components is due to the pellicle (scattering

loss in the MBBA is small, the MBBA cell windows are anti-reflection coated, and the 10 M mirror has 100% reflectivity), the travelling wave component travelling towards the mirror will have more energy than the returning component.

Energy in backwards component = .966 × energy in forward component. (169)

Using Eqs. (168) and (169), we can express the power in terms of either E_+ or E_-. We then obtain

$$|E_+|^2 = \frac{8\pi}{c}\frac{2P_{out}(t)}{\gamma\pi}\frac{w_+^2 + w_-^2}{w_+^2(w_+ - w_-)^2(1.966)}$$

$$|E_-|^2 = \frac{8\pi}{c}\frac{2P_{out}(t)}{\gamma\pi}\frac{w_+^2 + w_-^2}{w_-^2(w_+ + w_-)^2(2.035)} .$$

We can combine these expressions to obtain

$$I(r = 0) = \frac{c}{8\pi}\left|E_+(r = 0) + E_-(r = 0)\right|^2$$

$$\cong \frac{P_{out}(t)}{\gamma\pi}\left(\frac{1}{w_+^2} + \frac{1}{w_-^2}\right). \qquad (170)$$

Using the value for $w_\pm$ from Fig. 68, and $P_{out}(t)$ from Fig. 53, in Eq. (169) we obtain Fig. 72. Only the first peak is plotted as we have seen that the second peak does not contribute significantly to the on axis intensity.

Figure 72 clearly shows the higher axial intensity and shorter pulse that is expected when MBBA is in the cavity (as compared to the axial intensity and pulse length with no MBBA present). The larger feedback

to the axial volume of lasing material is responsible. With the larger feedback, this axial volume releases its stored energy more quickly, accounting for both the increased intensity and shorter pulse. Naturally, the on axis fluence (integrated intensity with respect to time) remains the same regardless of the presence of the MBBA. The fluence is determined by the total energy stored in the axial lasing volume, not by the dynamics of the energy release.

B. Quantitative Discussion

Our discussion for this section, though quantitative, follows a self consistent treatment. As mentioned earlier, it was unfeasible to perfom the fullblown computer calculation necessary to determine an absolute theoretical behavior. Instead we calculate the induced on axis change in refractive index $\delta n(0)$ by two different techniques, showing that the results are self consistent. First we use the observed spatial distribution of cavity fields together with observed output power to determine on axis cavity intensity. This was done in the previous section (Eq. (170)). From this, we can use the material properties of MBBA to obtain an expected $\delta n(0)$. We call this the theoretical value. Second, we can use the spatial distribution of the cavity fields together with Gaussian optics to calculate what $\delta n(0)$ is necessary to produce the observed change in spatial distribution after passage through the MBBA cell. This value of $\delta n(0)$ we call the experimental value. As we shall see, the theoretical value (9.1×10^{-6}) and the experimental value ($9.2 \pm 1.5 \times 10^{-6}$) agree quite well, showing that our model is quantitatively correct, at least at this self consistent level.

In Chapter II, we derived a theoretical expression for the induced

change in the index of refraction on axis of MBBA, $\delta n(0)$, as a function of cavity fields (Eqs. (55), (61), and (62)).

$$\delta n(0) = \frac{2\pi}{3n}\beta\frac{\sqrt{\pi}}{2}\frac{|\mathcal{E}_o|^2}{b\tau_M}e^{-t/\tau_M}e^{\frac{1}{4b^2\tau_M^2}}\left\{1 + \mathrm{erf}\left[bt - \frac{1}{2b\tau_M}\right]\right\} \tag{171}$$

where various terms are defined in Eqs. (38) and (54). We can use Eq. (170) in Eq. (171) to obtain directly the theoretical $\delta n(0)$ at the peak of laser output ($t = 0$)

$$\delta n(0) = 9.1 \times 10^{-6} \text{ (theoretical)}. \tag{172}$$

The maximal $\delta n(0)$ does not occur at $t = 0$ but at t where

$$\frac{d\delta n(0)}{dt} = 0$$

which occurs for

$$\frac{\sqrt{\pi}}{2b\tau_M}\left(1 + \mathrm{erf}\left[bt - \frac{1}{2b\tau_M}\right]\right) = \exp\left(-\left[bt - \frac{1}{2b\tau_M}\right]^2\right).$$

This must be solved numerically using the experimentally observed $b = (15 \text{ nsec})^{-1}$. With this value for b, the maximal value of $\delta n(0)$ is given by

$$\delta n(0)_{max} = \frac{2\pi}{3n_o}\beta|\mathcal{E}_o|^2 e^{-b^2\bar{t}^2}$$

$$\bar{t} = 16.5 \text{ nsec}. \tag{173}$$

Using the experimentally measured values for $w_{\pm}$ at the MBBA cell (Fig. 68), and P_{out} from Fig. 53, Eq. (173) can be evaluated using $|\mathcal{E}_o|^2 = (8\pi/c)I$ and Eq. (170) to give

$$\delta n(0)_{max} = 1.5 \times 10^{-5} \text{ (theoretical)}. \tag{174}$$

In Chapter II, we also obtained an expression for how the MBBA sample will affect the cavity fields. In the weak self focusing limit, we were able to express this as an [ABCD] matrix indicated in Eq. (67). This allows us to use Gaussian optics to evaluate from experimental data, what $\delta n(0)$ is needed to obtain this observed behavior. To simplify our notation, we define a parameter

$$\psi = \frac{2}{w}\sqrt{\frac{\delta n(0)}{n_o}} \tag{175}$$

where $n_o = \bar{n} + \delta n(0)$ and w is the size of the induced Gaussian $\delta n(r)$. Then Eq. (67) becomes:

$$[ABCD] = \begin{bmatrix} \cos\psi\ell & \frac{1}{\psi}\sin\psi\ell \\ -\psi\sin\psi\ell & \cos\psi\ell \end{bmatrix} \tag{176}$$

where ℓ is the sample length of MBBA. The area indicated as MBBA cell on Fig. 57 is actually as shown in Fig. 73. We define a "d" to indicate the optically equivalent length of air replacing the air + window as indicated on Fig. 73. Then for the region shown in Fig. 73, we have:

$$q_o = \begin{bmatrix} 1 & d \\ 0 & 1 \end{bmatrix} \begin{bmatrix} 1 & 0 \\ 0 & n_o \end{bmatrix} \begin{bmatrix} \cos\psi\ell & \frac{1}{\psi}\sin\psi\ell \\ -\psi\sin\psi\ell & \cos\psi\ell \end{bmatrix} \begin{bmatrix} 1 & 0 \\ 0 & 1/n_o \end{bmatrix} \begin{bmatrix} 1 & d \\ 0 & 1 \end{bmatrix} q_i \tag{177}$$

where i and o refer to the Gaussian beam parameter q entering or leaving this region. For weak $\psi \ll 1$ we expand the $\cos\psi\ell$ and $\sin\psi\ell$ keeping terms to ψ^2.

$$q_o = \begin{bmatrix} 1 - \frac{\psi^2\ell^2}{2} - dn_o\psi^2\ell & 2d\left(1 - \frac{\psi^2\ell^2}{2}\right) + \frac{1}{n_o}\left(\ell - \frac{\psi^2\ell^3}{6}\right) - d^2n_o\psi^2\ell \\ -\psi^2\ell n_o & 1 - \frac{\psi^2\ell^2}{2} - dn_o\psi^2\ell \end{bmatrix} q_i . \tag{178}$$

It is now merely a matter of algebra to solve for ψ^2 using the experimentally determined q_i and q_o (Figs. 68-70). We have

$$\frac{1}{q_o} = \frac{-\psi^2\ell n_o + \left(1 - \frac{\psi^2\ell^2}{2} - dn_o\psi^2\ell\right)1/q_i}{1 - \frac{\psi^2\ell^2}{2} - dn_o\psi^2\ell + \left[2d\left(1 - \frac{\psi^2\ell^2}{2}\right) + \frac{1}{n_o}\left(\ell - \frac{\psi^2\ell^3}{6}\right) - d^2n_o\psi^2\ell\right]1/q_i}$$

which gives for ψ^2: (179)

$$\psi^2 = \frac{\left(\frac{1}{R_o} - \frac{1}{R_i}\right) + \left(2d + \frac{\ell}{n_o}\right)\left(\frac{1}{R_o}\frac{1}{R_i} - \frac{\lambda^2}{\pi^2 w_i^2 w_o^2}\right)}{\left(\frac{\ell^2}{2} + dn_o\ell\right)\left(\frac{1}{R_o} - \frac{1}{R_i}\right) + \left(\frac{2d\ell^2}{2} + \frac{\ell^3}{6n_o} + d^2\ell n_o\right)\left(\frac{1}{R_o}\frac{1}{R_i} - \frac{\lambda^2}{\pi^2 w_i^2 w_o^2}\right) - \ell n_o} \tag{180}$$

where the $w_{i,o}$ and $R_{i,o}$ are related to the $q_{i,o}$ by Eq. (80). Using values from Fig. 68 and 70, we obtain:

$$\psi^2 = 5.9 \pm 0.2 \times 10^{-3}\ \mathrm{cm}^{-1} \tag{181}$$

where the error reflects the disagreement between values obtained for ψ using the two travelling wave components.

We can now use Eq. (175) to evaluate $\delta n(0)$ except for the fact that w in Eq. (175) changes during the pulse history. Early in the pulse the large component is prevalent so w is large, later in the pulse the small component is prevalent so w is small. In Eq. (175) we must be careful to use the properly averaged value of w. It is the determination of this average w that introduces the largest uncertainty into the calculation. We know from Fig. 56 that the large component is prevalent until

12 nsec before the peak. From Eq. (173) we know that the contribution from the large mode to $\delta n(0)$ will peak 16 nsec after the energy in the mode peaks. This means that the $\delta n(0)$ induced by the large mode will in fact probably dominate the total induced $\delta n(0)$ at the time $t = 0$ (peak of laser output).

We can estimate the contribution of the large mode to the total $\delta n(0)$ by using Eq. (171) at time $t' = 12$ nsec (laser peak occurs 12 nsec after large mode peak) and replacing

$$|\mathcal{E}_o|^2 \rightarrow |\mathcal{E}_o|^2 e^{-b^2 t'^2}$$

$$b = (15 \text{ nsec})^{-1}$$

$$t' = 12 \text{ nsec} \tag{182}$$

to account for the lower fields present 12 nsec before the peak. We obtain the result that the proper averaging of $1/w^2$ is given by

$$\left\langle \frac{1}{w^2} \right\rangle = .84 \left\langle \frac{1}{w^2} \right\rangle_{\text{large mode}} + .16 \left\langle \frac{1}{w^2} \right\rangle_{\text{small mode}} . \tag{183}$$

Using values for w indicated by Fig. 68 with Eqs. (175) and (181), we have $\delta n(0)$ at peak of laser output as:

$$\delta n(0) = 9.2 \pm 1.5 \times 10^{-6} \quad \text{experimental} \tag{184}$$

where the indicated error arises almost entirely from the uncertainties involved in the determination of $\langle 1/w^2 \rangle$. We have used an error of 50%

in the relative weight for the smaller mode in Eq. (183) as a measure of this uncertainty. This leads to the error used for Eq. (184). The actual error most likely is less than this, but without more detailed knowledge of how w changes at different times in the pulse, there is no justification to claim any smaller errors than provided by this worst case estimate.

The experimental value in Eq. (184) can be compared with the theoretical value calculated directly from Eq. (172). The close agreement between the theoretical and experimental values shows that the proposed model is quantitatively self-consistent.

In addition to calculating the induced δn, we can also calculate the expected divergence of the laser output. This was not measured quantitatively by experiment, but the results of the calculation clearly show the improved output characteristics with MBBA. As discussed in Chapter III, when calculating spatial behavior of the laser cavity fields, the laser rod is usually replaced by an equivalent thin lens. We will follow this procedure. The focal length of this equivalent lens will be called f, and the lens will be located at the center of the ruby rod ℓ_1 = 22 cm from the pinhole and ℓ_2 = 32 cm from the output etalon. We deal with only the smaller mode, predominant at peak of laser output, and thus can assume a single mode Gaussian in the cavity. Using the standard technique of [ABCD] matrices, we can write the Gaussian beam parameter q_f for the travelling wave component returning to the pinhole in terms of the beam parameter q_i for the travelling wave compoment just leaving the pinhole.

$$q_f = \begin{bmatrix} 1 & \ell_1 \\ 0 & 1 \end{bmatrix} \begin{bmatrix} 1 & 0 \\ -1/f & 1 \end{bmatrix} \begin{bmatrix} 1 & \ell_2 \\ 0 & 1 \end{bmatrix} \begin{bmatrix} 1 & 0 \\ -1/\infty & 1 \end{bmatrix} \begin{bmatrix} 1 & \ell_2 \\ 0 & 1 \end{bmatrix} \begin{bmatrix} 1 & 0 \\ -1/f & 1 \end{bmatrix} \begin{bmatrix} 1 & \ell_1 \\ 0 & 1 \end{bmatrix} q_i$$

$$= \begin{bmatrix} 1 - 2L/f & 2(1 - \ell_1/f)L \\ -(2/f)(1 - \ell_2/f) & 1 - 2L/f \end{bmatrix} q_i$$

$$L = \ell_1 + \ell_2 - \frac{\ell_1 \ell_2}{f} \; . \tag{185}$$

Using the definition for the Gaussian beam parameter (Eq. (80)), we can express Eq. (185) in terms of the measured $w_{i,f}$ and $R_{i,f}$ (Figs. 68-70):

$$\frac{1}{R_f} - \frac{i\lambda}{\pi w_f^2} =$$

$$\frac{(-2/f)(1-\ell_2/f)(1-2L/f) + [2(1-2L/f)^2 - 1]\frac{1}{R_i} + 2L(1-2L/f)(1-\ell_1/f)X - \frac{i\lambda}{\pi w_i^2}}{(1 - 2L/f)^2 + 4L(1 - 2L/f)(1 - \ell_1/f)\frac{1}{R_i} + 4L^2(1 - \ell_1/f)^2 X}$$

$$X = \frac{1}{R_i^2} + \frac{\lambda^2}{\pi^2 w_i^4} \; . \tag{186}$$

It is now easy to iterate over value of f to solve Eq. (186) for f given the measured values of $w_{i,f}$ and $R_{i,f}$. We obtain

$$f = 35 \text{ cm} \quad [\text{no MBBA}]$$

$$f = 64 \text{ cm} \quad [\text{with MBBA}]. \tag{187}$$

With f determined by Eq. (187), we write directly the Gaussian beam parameter q_o for laser output as a function of distance Δ from the cavity, and the beam parameter at the pinhole q_i:

$$q_o = \begin{bmatrix} 1 & \Delta \\ 0 & 1 \end{bmatrix} \begin{bmatrix} 1 & \ell_2 \\ 0 & 1 \end{bmatrix} \begin{bmatrix} 1 & 0 \\ -1/f & 1 \end{bmatrix} \begin{bmatrix} 1 & \ell_1 \\ 0 & 1 \end{bmatrix} q_i$$

$$= \begin{bmatrix} 1 - (\ell_2 + \Delta)/f & L' \\ -1/f & 1 \end{bmatrix} q_i$$

$$L' = \ell_1 + \ell_2 + \Delta - \frac{\ell_1(\ell_2 + \Delta)}{f} \quad . \tag{188}$$

Equation (188) can be solved for the physically relevant w_o and R_o:

$$\frac{1}{R_o} - \frac{i\lambda}{\pi w_o^2} = \frac{(-1/f)(1 - (\ell_2 + \Delta)/f) + (1 - 2L/f)\frac{1}{R_i} + (1 - \ell_1/f)LX - \frac{i\lambda}{\pi w_i^2}}{(1 - (\ell_2 + \Delta)/f)^2 + 2(1 - (\ell_2 + \Delta)/f)L\frac{1}{R_i} + L^2X}$$

$$X = \frac{1}{R_i^2} + \frac{\lambda^2}{\pi^2 w_i^4} \quad . \tag{189}$$

The solution to Eq. (189) can be seen in Fig. 74. The improvement in divergence of the output is quite clear, with a reduction from 1.6 mrad to only 0.9 mrad. The behavior predicted by Fig. 74 and Eq. (189) was verified qualitatively by experiment. This verification process consisted merely of placing polaroid film in the beam path, and then moving this film further from the cavity on successive shots. The behavior predicted by Fig. 74 was clearly seen both with and without MBBA.

Figure Captions

Fig. 71. Sketch of how increased fluence can increase size of burn spot on polaroid film even if there is no change in Gaussian mode size.

Fig. 72. On axis cavity intensity vs. time measured at the pinhole.

Fig. 73. Blow up of region on Fig. 57 labelled MBBA cell.

Fig. 74. Output divergence of laser with and without MBBA present. Beam mode size is plotted vs. distance from the laser.

Figure 71

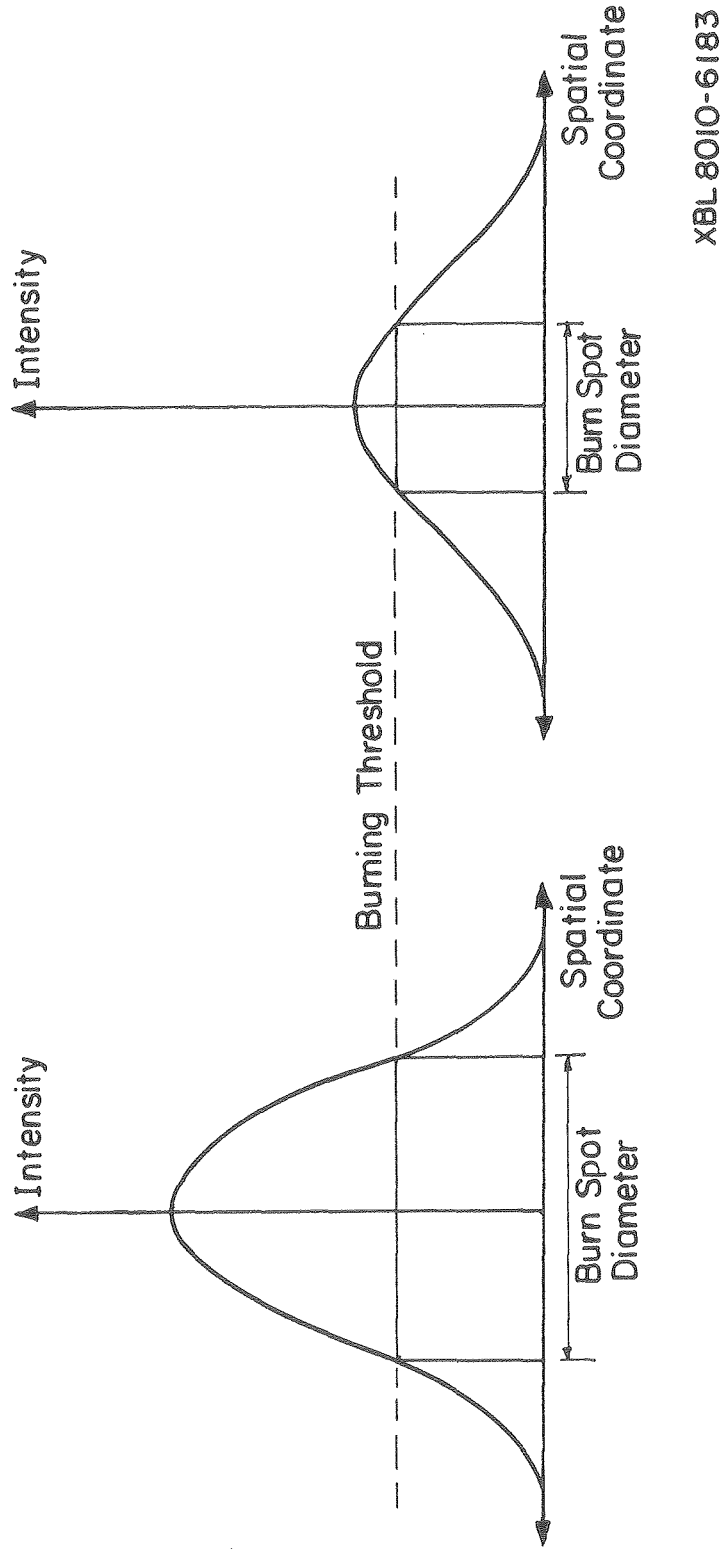
Intensity
Burn Spot Diameter
Spatial Coordinate
Burning Threshold
Intensity
Burn Spot Diameter
Spatial Coordinate
XBL 8010-6183

Figure 72

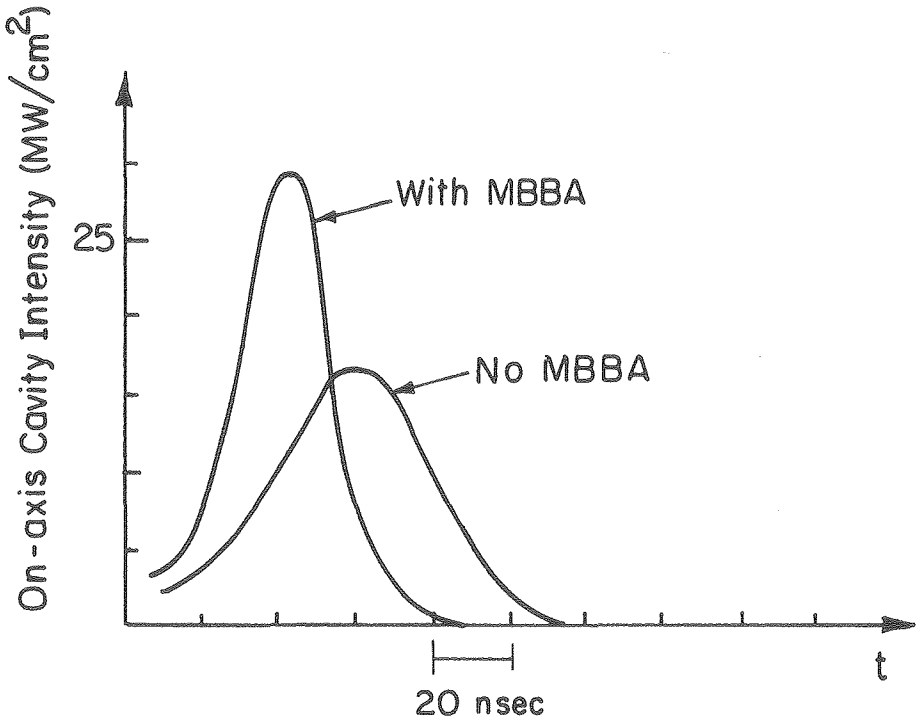

XBL8010-6184

Figure 73

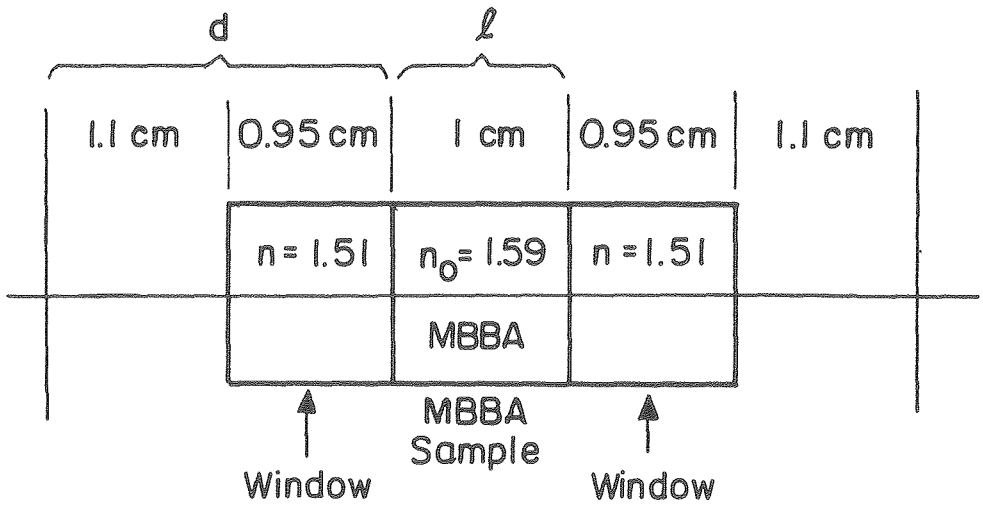

$$d = 1.1\,\text{cm} + \frac{0.95\,\text{cm}}{1.51} = 1.73\,\text{cm}$$

$$\ell = 1\,\text{cm}$$

XBL 8010-6185

Figure 74

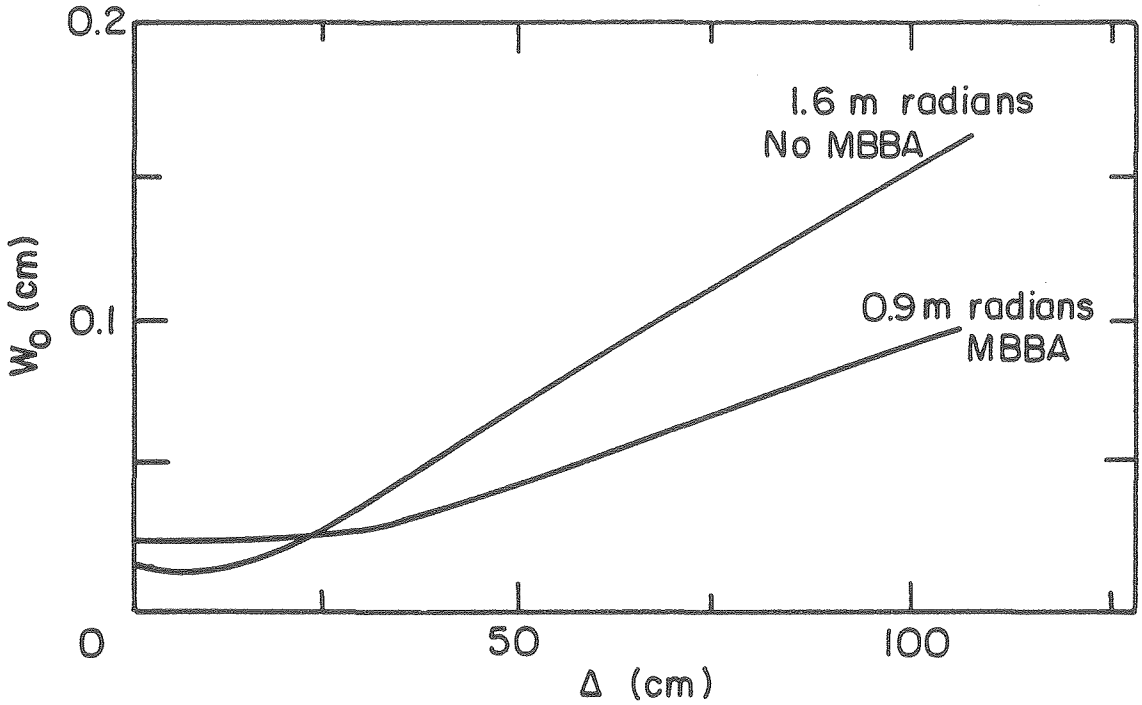

XBL 8010-6186

VII. CONCLUSIONS

We have presented a quantitative model for intracavity SIER induced losses. The theory remains valid for the entire range of material response time from quasi-steady state to fully transient. We explicitly incorporate the Gaussian spatial distribution of the cavity mode, thus improving on previous calculations which assume a plane wave cavity mode. The two treatments give substantially differing results for a saturable dye Q-switched laser, indicating the importance of properly treating the cavity mode. A thorough study was done both theoretically and experimentally for transient SIER inducible loss, with excellent agreement. We also examined theoretically, but not experimentally, the quasi-steady state SIER indicuble loss. The basic onclusions can be summarized:

1) SIER inducible loss can be used for pulse shaping.
2) Best pulse shaping occurs for the quasi-steady state limit.
3) Self focusing effects are non-negligible and should be carefully studied.

The details can be found in Chapter III. Though our studies indicate that the cleanest pulse shaping occurs at the quasi-steady state limit, the lack of experimental data makes it impossible to anticipate whether the self focusing effects will interfere with the SIER inducible loss process. Thus, the conclusion 2) is dependent on the self focusing in conclusion 3) being sufficiently small.

The self focusing properties of Kerr liquids in a laser cavity were also studied. As mentioned above, these effects play a significant role. Our study was primarily experimental, and dealt with transient intercavity self focusing. A self-consistent quantitative model was developed

(to account for the observed behavior). This theory could be extended to the quasi-steady state limit. Again, excellent agreement with experiment was seen. Again, the basic conclusions can be summarized:

1) The weak self focusing regime is most useful.
2) For the weak regime, good mode structure and small output divergence is observed.
3) Best results occur for the fully transient limit.

In contrast to SIER inducible loss, the transient response is preferable for this case. Mild self focusing acts to change the effective cavity configuration. This configuration change allows the good mode selection of a plane parallel cavity to be combined with the better output characteristics of a confocal cavity. The transient response slows the decay of the induced cavity configuration allowing maximal use of its beneficial effects.

There remains three questions or studies that should be pursued. The SIER inducible loss should be studied experimentally for the quasi-steady state limit. For the transient limit we know that the SIER process can be set so that the laser operates only in the mild self focusing regime of the MBBA, indicating that the SIER process dominates the self focusing process. Theoretically, this is true for the quasi-steady state limit as well, but needs to be verified experimentally. Second, the theories developed for both the processes need to be combined. The SIER inducible loss theory treats explicitly the laser dynamics, but treats only crudely the spatial features of cavity fields and cavity elements. Conversely, the self focusing theory treats explicitly these spatial features, but ignores the dynamics. It would be best if there could be developed a combined theory incorporating both the spatial fea-

tures and the dynamic features. This theory would then allow the treatment of SIER inducible loss and self focusing as a combined process, as it logically should be treated. Lastly, the experimental technique for measuring cavity fields should be refined. A technique to measure both time resolved and spatially resolved data simultaneously is needed. The best solution would likely be to sacrifice some spatial resolution and use some of the new high resolution, high sensitivity, low response time diode arrays in place of photographic film. This would serve the triple purpose of eliminating the tedious analysis required for film, providing direct input for computer analysis, allowing the real possibility of shot-to-shot averaging, and most important, providing temporal information at each diode element. The possibility of shot-to-shot averaging could, to a large extent, offset the loss of spatial resolution.

The techniques and models present in Chapters I-VI have both direct and indirect applications. As an indirect application, we see, for example, the continuation of intracavity self focusing studies as a scaled down examination of the self focusing problems in high power lasers. Direct study requires both the high power (as the self focusing is very weak) and picosecond pulses (because the self focusing process is both transient and fast). We avoid these problems by using liquid crystals (strong self focusing so moderate power lasers suitable, and long response time so nsec and longer pulse lengths can be used) with laser dye dissolved in the liquid crystal "host" to simulate the action of a Nd: Glass laser for example. One could hope to understand the process and thus learn how to best build the high power versions. Direct applications, of course, include the use of SIER inducible loss to control laser pulse length or self foucisng to improve laser output characteris-

tics where an external lens would be impractical. We can classify Kerr liquids into those having long or short relaxation times and we can classify them into those with large or small nonlinearities. Which Kerr liquids are best suited for which applications can be seen in Table 4. Mode shaping is used to refer to the use of intracavity self focusing to improve output characteristics. One entry on Table 4 needs explanation. Small δn requires a longer sample to achieve a desired effect than a large δn. The longer sample is much easier to deal with when determining optimal sample lengths. Since only weak self focusing is needed, these smaller δn's are sufficient and preferred. However, this is not to be carried to extremes — obviously $\delta n = 0$ would do no good at all. How small a δn is permissible is determined by the output power desired.

	large δn	small δn
long relaxation time	High power modelling 2nd choice for mode shaping 2nd choice for pulse stretching	1st choice for mode shaping
short relaxation time	1st choice for pulse stretching	Not suitable for any of the applications

Table 4. Table of possible applications of Kerr liquids in laser cavities based on response time and relative size of the induced nonlinear index of refraction.

References

1. For a more thorough discussion of ellipse rotation and the Kerr effect, see, for example, A. Owyoung, R. W. Helworth, and N. George, Phys. Rev. B 5, 628 (1972) and

2. G. Wong and Y. R. Shen, Phys. Rev. A 10, 1277 (1974).

3. For a more thorough discussion of self focusing, see Y. R. Shen, Progress in Quantum Electronics 5, 1 (1975).

4. For a discussion on the basic properties of liquid crystals, see, for example, Introduction to Liquid Crystals, E. B. Priestly, P. J. Wojtowicz, and P. Sheng, eds. (Plenum Press, New York, 1965).

5. G. Wong and Y. R. Shen, Phys. Rev. Lett. 32, 527 (1974).

6. E. G. Hansen, Y. R. Shen, and G. Wong, Appl. Phys. 14, 65 (1977); Opt. Commun. 20, 45 (1977).

7. Y. R. Shen, "Nonlinear Optical Study of Pretransitional Behavior in Liquid Crystalline Materials" in Nonlinear Spectroscopy, N. Bloembergen, ed. (Society Italiana de Fisica, Bologna, Italy, 1977) Course 64.

8. J. Comly, E. Garmire, J. P. Laussade, and A. Yariv, Appl. Phys. Lett. 13, 176 (1968).

9. J. P. Laussade and A. Yariv, Appl. Phys. Lett. 13, 65 (1968).

10. For general background on mode locking, see, for example. P. W. Smith, Proc. of the IEEE 58, 1342 (1970).

11. L. Dahlström, Opt. Commun. 4, 214 (1971).

12. For more details on cavity dumping, see R. G. Morton, M. E. Mack, I. Itzkan, Appl. Opt. 17, 3268 (1978).

13. L. Dahlström, Opt. Commun. 4, 289 (1971).

14. K. Sala, M. C. Richardson, N. R. Isenor, IEEE J. Quan. Elec. QE13, 915 (1977).

15. J. Schwartz, C. S. Naiman, and R. K. Chang, Appl. Phys. Lett. 11, 242 (1967).

16. D. V. Murphy and R. K. Chang, Opt. Commun. 23, 268 (1977).

17. D. Röss, Lasers, Light Amplifiers and Oscillators (Academic Press, New York, 1969).

18. W. Kochner, Solid State Laser Engineering (Springer-Verlag, New York, 1976).

19. J. M. Ralston and R. K. Chang, J. Opt.-Elec. 1, 182 (1969).

20. L. M. Lititsyn, JETP Lett. 9, 165 (1969).

21. J. Schwartz, W. Weiler, and R. K. Chang, IEEE J. Quan. Elec. QE6, 442 (1970).

22. G. K. L. Wong and Y. R. Shen, Phys. Rev. Lett. 30, 895 (1973).

23. E. G. Hansen, Y. R. Shen, and G. K. L. Wong, Phys. Rev. A 14, 1281 (1976).

24. P. G. de Gennes, Phys. Lett. A30, 454 (1969); Mol. Crys. Liq. Crys. 12, 193 (1971).

25. P. D. Maker and R. W. Terhune, Phys. Rev. 137, A801 (1965).

26. For a thorough discussion of third order susceptibilities, see R. W. Hellwarth, Progress in Quantum Electronics 5, 1 (1977).

27. P. N. Butcher, Nonlinear Optical Phenomena, Bulletin 200 (Engineering Experiment Station, Ohio State University, Columbus Ohio, 1965).

28. T. W. Stinson III and J. D. Litster, Phys. Rev. Lett. 25, 503 (1970).

29. A. Yariv, Quantum Electronics, 2nd ed. (John Wiley and Sons, Inc. New York, 1975).

30. R. M. A. Azzam and N. M. Bashara, Ellipsometry and Polarized Light (North Holland Publishing Co., New York, 1977).

31. M. Brunet-Germain and P. Chatelain, Comptes Rendue de L'Académie des Sciences 271, Série B, 1075 (1970).

32. W. G. Wagner and B. A. Lengyal, J. Appl. Phys. 34, 2040 (1963).